Main Group Hydrogen-Bond Donors and Pyridyl Ligands for Supramolecular and Coordination Chemistry

Alex Johannes Plajer
Selwyn College
July 2019

A dissertation submitted to the University of Cambridge as part of the Doctor of Philosophy

Declaration

I hereby declare that this dissertation, entitled ‘Main Group H-bond Donors and Pyridyl Ligands for Supramolecular and Coordination Chemistry’, is the result of work that I have undertaken in the University Chemical Laboratory at the University of Cambridge between October 2017 and July 2019. Except where stated to the contrary, this dissertation is my own work; credit for results obtained from collaboration with other parties is referenced to directly in the text. Figures that have been reproduced or adapted from other sources are indicated as such in their corresponding caption references. Aspects of the results presented herein have been published in peer-reviewed journals; a list of publications is included. This dissertation has not been, nor is currently being, submitted for any other degree, diploma or other academic qualification at this or any other university. It does not exceed 60,000 words in length.

Alex J. Plajer, 19.7.2019

Abstract

The thesis involves the investigation of two main areas in which new ligands based on main group frameworks are developed. In the first part of this thesis we explore the host-guest chemistry of a range of non-carbon frameworks based on P-N bonds. In the first chapter we develop strategies for enhancing the anion binding properties of phosphazanes of the type $[(RNH)(E)P(\mu\text{-}N^tBu)]_2$ (E = O, S, Se) which are bench stable, H-bond receptors that can be regarded as inorganic analogues of squaramides (a key class of organic anion receptor). We find that there are distinct advantages of these inorganic receptors over organic counterparts such as the ease by which their functionality and electronic character can be altered (by means of the R-groups and chalcogenide present). Selenium substitution at the phosphine-centres, the presence of electron withdrawing R-groups and metal coordination to the soft donor centres can be used to modulate and enhance anion binding. The water stability and superior anion binding properties of the selenophosph(V)azanes gives them applications as synthetic anion transporters through phospholipid bilayers. Next, we establish synthetic methodologies for the rational design of bimetallic phosphazane coordination complexes of the type $[L_nM(PyridylNH)P(\mu\text{-}N^tBu)]_2$ (M = transition metal, L = supporting ligand). By optimisation of the NH bond polarity we achieve halide binding approximately one order of magnitude stronger than for organic analogues. We find that metal coordination renders these complexes robust enough to function as synthetic anion transporters through phospholipid bilayers and reveal how metal coordination affects the transport activity. We also investigate the general coordination chemistry of the parent ligand and the effect of quinolyl substitution. Finally, we investigate the host-guest chemistry of pentameric phosphazane macrocycle $\{[NHP(\mu\text{-}N^tBu)]_2\}_5$. The polar coordination site of this system promotes new modes of guest encapsulation via H-bonding with the π-systems of unsaturated bonds, and with reactive anionic phosphorus centres. Guests can be kinetically locked within the structure, with halide anions displaying stronger effective binding than in any classical organic or metal-organic receptor reported to date.

The second part of the thesis moves on to explore the coordination properties of main group bridged trispyridyl ligands. The new 6-methyl substituted ligands $E(6\text{-}Me\text{-}2\text{-}py)_3$ (E = As, Sb, Bi) are synthesised, allowing the assessment of the effects of bridgehead

modification alone on descending a single group in the periodic table. We show that the primary influence on coordination behaviour is the increasing Lewis acidity and electropositivity of the bridgehead atom as group 15 is descended, which not only modulates the electron density on the pyridyl donor groups but also introduces the potential for anion selective coordination behaviour. We then continue to investigate the structural consequences of bridgehead change and derivatisation in a range of transition metal complexes and also demonstrate the effect of bridgehead oxidation going from E = As to As=O. Having revealed that the presence of a 6-Me group is crucial for the synthesis of trispyridyl main group ligands we explore the coordination chemistry of the silicon derivative E= PhSi, for which coordination studies were previously hindered by the inefficient synthesis of the ligand. In the final chapter we expand the scope of ligand modification of the trispyridyl aluminate E = EtAl by reaction with organic acids and aldehydes.

Acknowledgements

While trying to write this I found it impossible to accurately remember and thank everybody enough who has helped and supported me during the past three years. So please don't be offended if I don't sing my praises high enough or I'm forgetting to mention you. Be sure that I'm genuinely grateful for what you did, thank you!

First, I want to thank my parents, who have always supported me in the things that matter and have been and are there for me in hard times, I feel lucky to be your son. Then I'd like to thank my girlfriend for her constant support, patients and advice. I´m so glad we met in life.

Next I want to thank my supervisor, who really was the wright choice. Thank you for accepting me in the first place, letting me come back to the group, teaching me and granting me the freedom I had.

Special thanks go to the people I have collaborated with. You allowed me to explore all kinds of chemistry and taught me how to be a better scientist and co-worker. Thank you: Felix Rizzuto, Patrick Pröhm, Jinbo Zhu, Ulrich Keyzer, Jonathan Goodman, Sanha Lee, Markus Enders and Andrew Bond.

Also, I've been very lucky to work with two talented Erasmus students who directly and indirectly contributed with their hard and independent work to this thesis. Thank you, Daniel Crusius, Kevin Bold and Sara Kopf.

I also need to thank the people who also taught me 'how to research" and discussed data and ideas with me. The list is too long to remember… however some I haven't forgotten include: Evan Keyzer, Andrew Peel, Duncan Howe, Peter Grice, Tanya Ronson, Edmundo Guzmán Percástegui, John Carpenter, Cally Haynes, Roy Lavedomme, Larissa von Krebk, Annie Colebatch, Sebastian Pike, Raul Garcia Rodriguez and many others.

Finally, I'd like to thank all members of the Wright group for the great work environment during the years of my PhD. Even when things were not working the morning coffee break kept me motivated to come in day by day.

Publications

‘Designing the Macrocyclic Dimension in Main Group Chemistry’; **Chem. Eur. J.** 2018, 24, 3037-3082; H-C. Niu, A. J. Plajer, Rh. Garcia-Rodriguez, S. Singh, D. S. Wright

‘How Changing the Bridgehead Can Affect the Properties of Tripodal Ligands’; **Angew. Chem. Int. Ed.** 2018, 57, 6648-6652; A. J. Plajer, A. L. Colebatch, F. J. Rizzuto, P. Pröhm, A. D. Bond, R. García-Rodríguez, D. S. Wright

‘Formation and Selection of the Macrocycle $[\{(tBuN=)P(\mu\text{-}N^tBu)\}_2(\mu\text{-}Se)_2\{P(\mu\text{-}N^tBu)\}_2]_3$’; **Dalton Trans.** 2018, 47, 6675-6678; A. J. Plajer, H-C. Niu, F. J. Rizzuto, D. S. Wright

‘The Coordination Chemistry of the Neutral Trispyridyl Silicon Ligand $[PhSi(6\text{-}Me\text{-}2\text{-}py)_3]$’; **Dalton Trans.** 2018, 47, 7036-7043; A. J. Plajer, A. L. Colebatch, M. Enders, Á. García-Romero, A. D. Bond, R García-Rodríguez, D. S. Wright

‘Deprotonation, Insertion and Isomerisation in the Post-functionalisation of Trispyridyl Aluminates’; **Dalton Trans.** 2019, 48, 5692-5697; A. J. Plajer, S. Kopf, A. L. Colebatch, A. D. Bond, R. García-Rodríguez, D. S. Wright

‘Tailoring the Binding Properties of Phosphazane Anion Receptors’; **J. Am. Chem. Soc.** 2019, 141, 8807-8815**;** A. J. Plajer, J Zhu, P. Pröhm, A. D. Bond, U. F. Keyser, D. S. Wright

‘Guest Binding via N-H-π-Bonding and Kinetic Entrapment by an Inorganic Macrocycle’; **Angew. Chem. Int. Ed.** 2019, in press; A. J. Plajer, F. J. Rizzuto, H-C. Niu, S. Lee, J. M. Goodman, D. S. Wright

‘Conformational Control in Main Group Phosphazane Receptors and Transporters’; **in preparation**; A. J. Plajer, J. Zhu, P. Pröhm, F. J. Rizzuto, U. F. Keyzer, D. S. Wright

‘Charge assisted Selenophosphazane Anion Receptors’; **in preparation**; A. J. Plajer, S. Lee, A. D. Bond, J. M. Goodman, D. S. Wright

‘Coordination Chemistry of the Bench-stable Trispyridyl Pnictogen Ligands [E(6-Me-2-py)$_3$] (E = As, As=O, Sb)’; **in preparation**; A. J. Plajer, D. Crusius, A. D. Bond, D. S. Wright

‘Controlling the Coordination Chemistry of the Pyridyl Substituted Phosphazane [(2-py)NHP(μ-^{t}BuN)]$_2$’; **in preparation**; A. J. Plajer, A. D. Bond, D. S. Wright

Any work included in this dissertation that has been published has been reproduced herein with permission. Additional work that was carried out to some extent during the time of this PhD, but not included in this dissertation, has been published in the following peer-reviewed journals:

‘A Modular Approach to Inorganic Phosphazane Macrocycles’; **Angew. Chem. Int. Ed.** 2017, 56, 9087-9090; A. J. Plajer, R. García-Rodríguez, C. G. M. Benson, P. D. Matthews, A. D. Bond, S. Singh, L. H. Gade, D. S. Wright

‘Isomerisation, Reactivity and Coordination Chemistry of a New Hybrid, Multi-functional Phosphazane’; **Dalton Trans.** 2017, 46, 12775-12779; A. J. Plajer, K. Bold, F. J. Rizzuto, R. García-Rodríguez, T. K. Ronson, D. S. Wright

‘Flexible Bonding of the Phosph(V)azane Dianions [S(E)=P(μ-N^{t}Bu)]$_2^{2-}$’; **Chem. Eur. J.** 2018, 24, 2013-2019; A. J. Plajer, R. Garcia-Rodriguez, F. J. Rizzuto, D. S. Wright

‘Different Selectivities in the Insertions into C(sp2)-H Bonds - Benzofulvenes by Dual Gold Catalysis Competition Experiments’; **Chem. Eur. J.** 2018, 24,10766–10772; A. J. Plajer, L. Ahrens, M. Wieteck, D. M. Lustosa, R. B. Ahmadi, B. Yates, A. Ariafard, M. Rudolph, F. Rominger, A. S. K. Hashmi

‘Post-functionalisation of Tris-pyridyl Aluminate Ligands: Chirality, Coordination and Supramolecular Chemistry’; **Chem. Eur. J.** 2018, 24, 17019–17026; Á. García-Romero, A. J. Plajer, L. Álvarez-Miguel, A. D. Bond, D. S. Wright, R. García-Rodríguez

‘Waterproof architectures through subcomponent self-assembly’; **Chem. Sci.** 2019, 10, 2006-2018, E. G. Percástegui, J. Mosquera, T. K. Ronson, A. J. Plajer, M. Kieffer, J. R. Nitschke

‘H-bond-assisted Symmetry Breaking in a Network of Chiral Metal-organic Assemblies’; **J. Am. Chem. Soc.** 2019, 141, 1707–1715, F. J. Rizzuto, P. Pröhm, A. J. Plajer, J. L. Greenfield, J. R. Nitschke

‘Fluorometric Recognition of Nucleotides within a Water-Soluble Tetrahedral Capsule’; **Angew. Chem. Int. Ed.** 2019, 58, 4200-4204, A. J. Plajer, E. G. Percástegui, M. Santella, F. J. Rizzuto, Q. Gan, B. W. Laursen, J. R. Nitschke

‘A Tris(3-pyridyl)stannane as a Building Block for Heterobimetallic Coordination Polymers and Supramolecular Cages’; **submitted,** E. S. Yang, A. J. Plajer, Á. García-Romero , A. D. Bond, T. K. Ronson, C. M. Álvarez, R. García-Rodríguez, A. L. Colebatch, D. S. Wright

Abbreviations

°	Degrees
°C	Degrees Celsius
Å	Ångstroem
δ	Chemical shift
μ	Bridging
μl	Microlitre
λ	Wavelength
$\tilde{\nu}$	Wavenumber
ν	Frequency
χ	Magnetic moment
av.	Average
a.u.	Atomic units
ax.	Axial
Ar	Aryl
ATR	Attenuated total reflection
br	Broad
Bu	Butyl
ca.	Circa
calcd.	Calculated
Cp	Cyclopentadienyl
Cp*	Pentamethylcyclopentadienyl
COSY	Correlation spectroscopy
d	Doublet, days
dd	Doublet of doublets
DCM	DCM
DFT	Density functional theory
DMS	Dimethylsulphide
DMSO	Dimethylsulphoxide
ESI-MS	Electrosprayionisation-masspectrometry
Et	Ethyl
EXSY	Exchange spectroscopy
FLP	Frustrated Lewis pair

FIA	Fluoride ion affinity
h	Hours
HMBC	Heteronuclear multiple bond correlation
HMQC	Heteronuclear multiple-quantum correlation spectroscopy
HOMO	Highest occupied molecular orbital
HR	High-resolution
HSQC	Heteronuclear single quantum coherence
IR	Infrared
J	Coupling constant
K	Kelvin
LUMO	Lowest unoccupied molecular orbital
LR	Low resolution
m	Multiplet (NMR), medium (IR)
ml	Millilitre
mmol	Millimole
mg	Milligram
min	Minutes
M	Molarity
Me	Methyl
MS	Mass spectrometry
NBO	Natural bond orbital
NMR	Nuclear magnetic resonance
NOESY	Nuclear Overhauser effect spectroscopy
OAc	Acetate
OTf	Triflate
ppm	Parts per million
py	Pyridyl
pz	Pyrazolyl
q	Quartet
qu	Quinolyl
RFX	Reflux
RT	Room temperature
s	Singlet (NMR), strong (IR), seconds (time)
t	Triplet

T	Temperature
Ter	Terphenyl
Ts	Tosyl
TBA	Tetrabutylammonium
TMEDA	N,N,N’,N’ -Tetramethylethylendiamine
TMS	Trimethylsilyl
THF	Tetrahydrofuran
THT	Tetrahydrothiophene
UV-Vis	Ultraviolet-visible
vdW	Van der Waal
VT	Variable temperature
W	Weak
XS	Excess

Content

Part 1:
Main Group Supramolecular Chemistry with Cyclodiphosphazanes

Chapter 1: Introduction to Part 1

Phophorus-Nitrogen Chemistry and Cyclodiphosphazanes

Phosphorus-nitrogen compounds are well established nowadays in various areas of synthesis, catalysis and materials science. Applied as neutral superbases, elastomeric and thermoplastic polymers and main group based catalysts in small molecule activation, phosphorus-nitrogen compounds have a range of reactivities and properties that have few analogues in carbon based chemistry.[1] Figure 1 shows some important examples of phosphorus(V)-containing P-N systems that have applications as non-nucleophilic superbases and as components that facilitate improved performance of solar cells, lithium ion batteries and membrane fuel cells.[2–4]

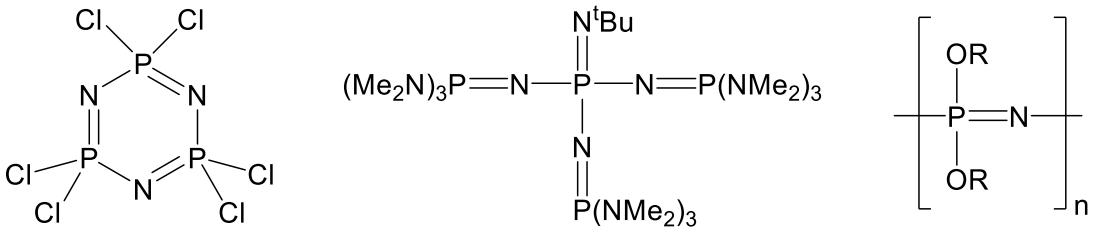

Figure 1: Examples of P-N based molecules.[1]

Phosphorus(III) and phosphorus(V) containing compounds of this type are typically obtained via similar synthetic methodologies from the condensation reactions of phosphorus halides and amines. The work presented in this thesis largely focuses on phosphorus(III) systems and their derivatives, hence the introduction will focus specifically on this area. The reactions of primary amines RNH_2 with PCl_3 results in the formation of phosph(III)azanes containing phosphorus(III)-nitrogen bonds, however, the exact outcome depends on the reaction conditions and the amine employed. Usually, cyclic products with alternating phosphorus and nitrogen centres of different ring sizes are obtained. The ring size is determined by the steric bulk of the organic amine (Figure 2).[5] These rings can be seen as the oligomerisation products of the transient imino-phosphine monomer RN=PCl, the product of a 1:1 condensation of RNH_2 and PCl_3 with the elimination of HCl. Larger substituents such as ^{t}Bu or Ph favour the formation of four membered P_2N_2 rings. Although this results in a certain

degree of ring strain, the four-membered ring minimises steric repulsion between the organic substituents. However, there is clearly a subtle balance between ring strain and steric effects as four membered rings can be converted into their six-membered homologues by chloride abstraction.[6,7] Six- and eight-membered rings are formed for small amine substituents, like Me or Et.[8] Polymeric phosphorus(III)-nitrogen chains are much harder to generate than phosphorus(V) analogues. Whereas the phosphorus(V) polymers like the polyphosphazene shown in Figure 1 can be formed by ring-opening polmerisation of cyclic phosphazenes, following a similar approach using cyclic phosph(III)azanes gives a mixture of products.[5] Figure 2 summarises the chemistry mentioned in this paragraph.

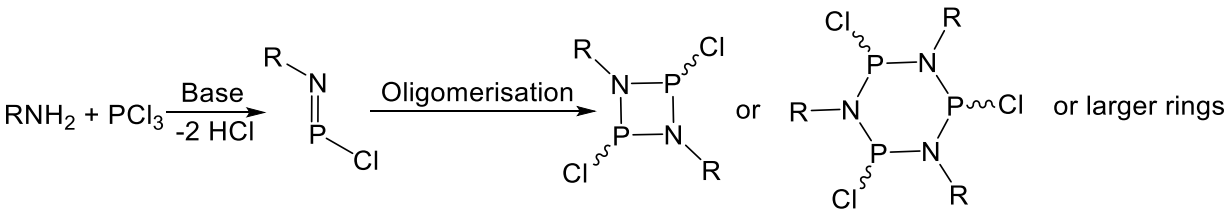

Figure 2: Polycondensation reaction generating phosphazanes.

Studies in this part of the thesis focus on dimeric cyclodiphosphazanes. Broadly speaking the chemistry of dimeric cyclodiphospazanes is far more developed than for the trimeric and higher homologues, as further derivatisation of the latter is problematic in terms of selectivity and stereochemistry. Cyclodiphosphazanes of the type $[ClP(\mu\text{-}NR)]_2$ are the formal [2+2] cycloaddition product of ClP=NR.[9,10] This dimerisation occurs very readily in practice and hence $[ClP(\mu\text{-}NR)]_2$ are obtained from the 1:1 reaction of RNH_2 with PCl_3 in presence of a Brønsted base, which scavenges HCl (Figure 3).[11]

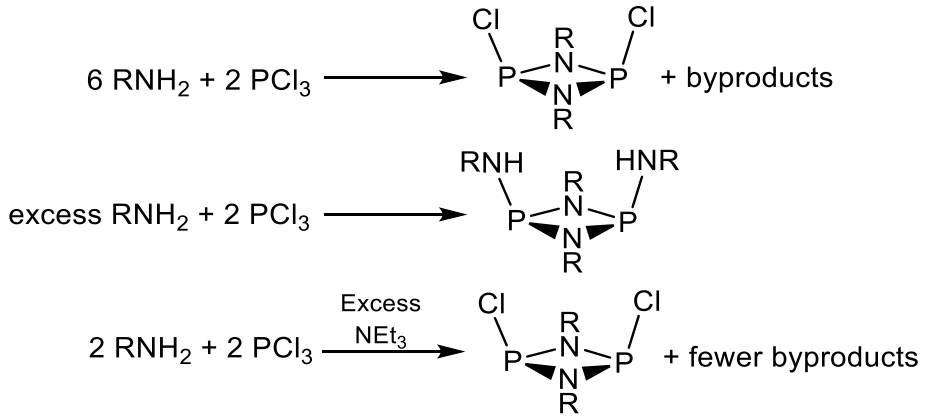

Figure 3: Different synthetic methodologies for the synthesis of cyclodiphosphazanes.

Where the amine RNH_2 is used in large excess it can act as a Brønsted base and also reacts further with the P-Cl bonds of $[ClP(\mu\text{-}NR)]_2$ to give diaminocyclodiphosph(III)azanes $[RNHP(\mu\text{-}NR)]_2$. These products are also commonly observed as byproducts in the synthesis of $[ClP(\mu\text{-}NR)]_2$. In order to avoid this competing pathway, low reaction temperature and the use of a non-nucleophilic Brønsted base like Et_3N in large excess is often needed.[11]

The family of $[ClP(\mu\text{-}NR)]_2$ phosph(III)azanes can form cis or trans-isomers, examples of which are shown in Figure 4. This isomerism also occurs in the derivatives of the type $[RP(\mu\text{-}NR)]_2$ in which Cl atoms are substituted by an organic group R. Generally, the cis-isomers are preferred for the majority of substituents, except where very large sterically-demanding R-groups are present.[12] However, the nature of the exocyclic substituents also influences the isomerism. In the cis-isomers, the P_2N_2 ring units are normally slightly puckered whereas these units are planar for the trans-isomers. Although there have been some theoretical investigations on this, prediction of this cis/trans-isomerism is still very difficult.[13,14]

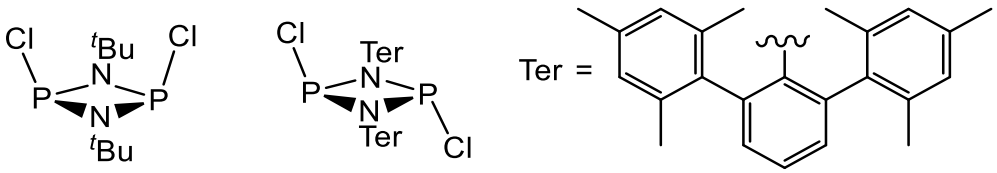

Figure 4: Cis/trans-isomerism in $[ClP(\mu\text{-}NR)]_2$.

The P-Cl functionalities as well as the phosphorus(III) centres of $[ClP(\mu\text{-}NR)]_2$ are reactive sites that can be further functionalised. Due to the marked stability of the P_2N_2 framework with an endocyclic ^{t}Bu, synthetic studies have overwhelmingly used $[ClP(\mu\text{-}N^tBu)]_2$ as a building block. $[ClP(\mu\text{-}N^tBu)]_2$ can be employed in condensation reactions with, e.g., RNH_2, ROH or RCOOH, giving the corresponding $[RXP(\mu\text{-}N^tBu)]_2$ (X = NH, O, COO) in high yields.[15] Particular attention has been paid to the chemistry of $[RNHP(\mu\text{-}N^tBu)]_2$. Stahl et al. as well as Chivers et al. have studied the condensation and deprotonation of the latter.[16,17] The NH group of ^{t}BuNHP$(\mu\text{-}N^tBu)]_2$ can be easily deprotonated with ^{n}BuLi, yielding $[^t$BuNP$(\mu\text{-}N^tBu)$Li(THF)$]_2$ in THF which adopts a heterocubane structure in the solid state (Figure 5). The $[^t$BuNP$(\mu\text{-}N^tBu)]_2^{2-}$ dianion can be transferred onto a variety of main group and transition metal centres in methathesis reactions. In the resulting complexes, $[^t$BuNP$(\mu\text{-}N^tBu)]_2^{2-}$ often acts as a tridentate donor using its two anionic exocyclic amide substituents as well as one of the endocyclic P_2N_2 nitrogen atoms.[16]

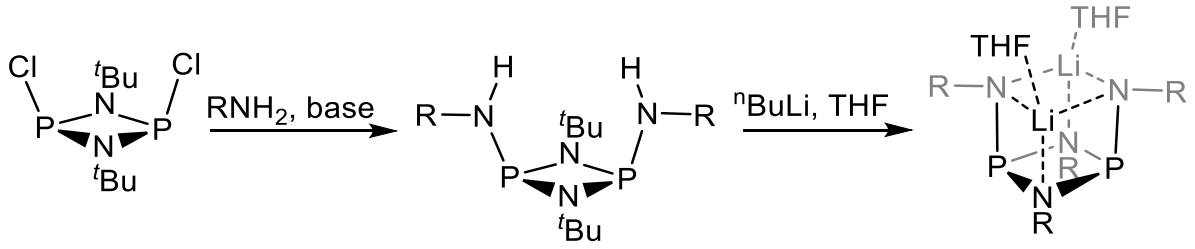

Figure 5: Synthetic protocol for the heterocubane $[^t$BuNP$(\mu\text{-}N^tBu)$Li(THF)$]_2$.

A further possibility for functionalisation is the oxidation of the phosphorus(III) positions. This is achieved using elemental chalcogens or peroxides.[18] Such oxidations have mainly been focusing on $[RNHP(\mu\text{-}N^tBu)]_2$ as the P(III) centres are particularly electron rich and hence prone to oxidation. There are different synthetic strategies for complete oxidation of diamino-substituted phosphazanes (Figure 6). The first approach involves direct oxidation of the neutral $[RNHP(\mu\text{-}N^tBu)]_2$ with peroxides or elemental chalcogen. Whereas full oxidation is achieved at room temperature with peroxides, such as ^{t}BuOOH or H_2O_2, prolonged reaction times at reflux conditions are often employed for the oxidation with elemental sulphur or selenium.[19] However, these conditions generate mixtures of the cis and trans-isomeric products.[20,21] It should be noted that the trans-isomer is often unwanted as its stereochemistry makes it unsuited as a supporting ligand for molecular complexes containing metal centres. Hence, Garcia et al. recently reported the use of ball-milling for cis-selective sulphur and selenium

oxidation. The resulting cis-[RNH(E=)P(μ-N^{t}Bu)]$_2$] (E = O, S, Se) are air and moisture stable.[21] The formation of the ditellurium derivative of [RNH(Te=)P(μ-N^{t}Bu)]$_2$] cannot be achieved via these methodologies. Only the unsymmetrical species [RNHP(μ-N^{t}Bu)$_2$P(=Te)NHR], with one P(III) and one P(V)=Te centre, are obtained as the products. Woollins et al. found that prior deprotonation accelerates the oxidation of the P(III) centres drastically (Figure 6).[22] Full tellurium oxidation to give the dianion [RN(Te=)P(μ-N^{t}Bu)]$_2^{2-}$ as its lithium or sodium salts readily occurs at room temperature due to an increase of overall electron density of the phosphazane backbone. Depending on the metal cation present and the presence of supporting ligands (such as TMEDA), a number of structural motifs are observed in complexes of the [RN(E=)P(μ-N^{t}Bu)]$_2^{2-}$ (E = O, S, Se, Te) dianions.[18]

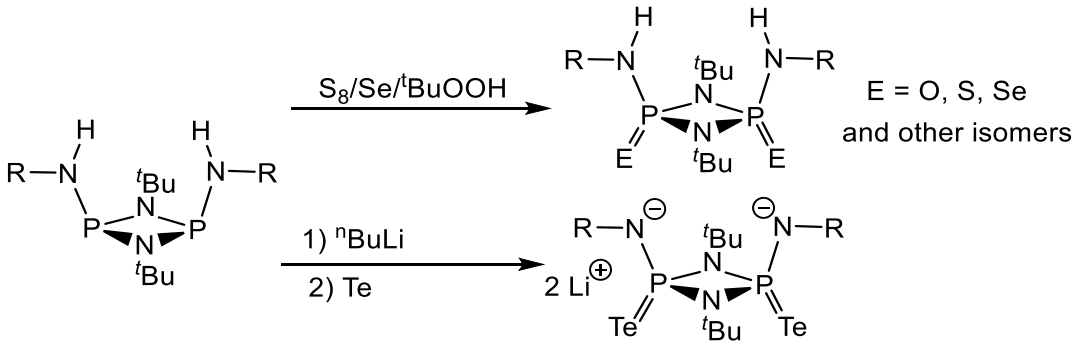

Figure 6: Synthetic protocol for phosphazane oxidation.

The family of the dianions [RN(E=)P(μ-N^{t}Bu)]$_2^{2-}$ (E = O, S, Se, Te) can be transferred intact to a variety of main group and transition metal centres. Transfer to metals can either be achieved directly via deprotonation of the neutral precursors [RNH(E=)P(μ-N^{t}Bu)]$_2$ (E = O, S, Se) with organometallic bases (e.g. ZnEt$_2$) or via salt metathesis reactions of M$_2$[RN(E=)P(μ-N^{t}Bu)]$_2$ (M= Li, Na, E = O, S, Se, Te) with transition and main group metal halides.[18,23,24] Employing the second synthetic strategy allowed access to a variety of coordination complexes summarised in Figure 7. Early work by Chivers et al. showed that nickel(II), palladium(II) and platinum(II) cations are coordinated using a bidentate S,S-mode via the sulphur face of cis-[RN(S=)P(μ-N^{t}Bu)]$_2^{2-}$. The same ligand can also be employed as a side-on S,N-ligand after single deprotonation of [RNH(S=)P(μ-N^{t}Bu)]$_2$ and transfer to a metal centre. On a similar note, Stahl and coworkers recently reported the face-on N,N-coordination mode of [RN(S=)P(μ-N^{t}Bu)]$_2^{2-}$ to early transition metals. [18] Clearly the coordination preference

of these phosh(V)azane ligands can be rationalised on the grounds of hardness and softness of the metals coordinated.

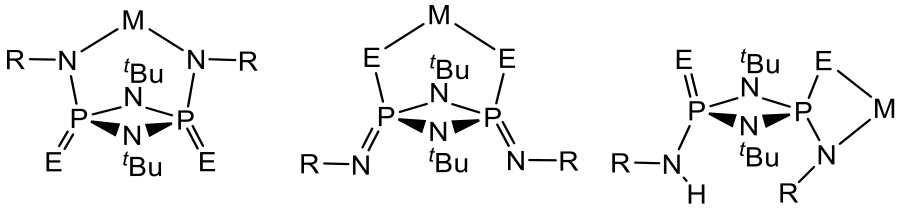

Figure 7: Different coordination modes of $[RNH(E=)P(\mu\text{-}N^tBu)]_2$] (E = O, S, Se) with metals M.

Recently work by Woollins et al. focused on the formation of bicyclic main group arrangements coordinated by the $P_2N_2E_2$ (E = S, Se, Te) framework. A variety of bridging main group metal atoms were incorporated such as $^tBu_2Sn$, $^tBu_2Ge$, Se-Se and PhSb.[23] Wright et al. recently showed a marked preference for Se,Se-coordination over S,S-coordination in the related $[Se(S=)P(\mu\text{-}N^tBu)]_2^{2-}$ ligand set.[25] Although the phosphazane chemistry presented in this introduction only highlights a small cross-section of the studies in this area, the main point made in all of these previous reports is that the P_2N_2 ring unit is a stable synthetic and structural building block. These features have allowed rational development in phosphazane chemistry. In particular, Wright et al. have been able to use the P_2N_2 fragment in the construction of larger supramolecular arrangements and this is the focus of the next section of the introduction.

Main Group Supramolecular Chemistry Using Cyclodiphosphazanes

While organic macrocycles based on thermodynamically stable carbon frameworks, are a central area of modern chemistry (with extensive applications in the fields of coordination chemistry, catalysis and extraction, to name a few), functional inorganic macrocycles whose frameworks are constructed solely from inorganic elements are rare.[26–28] In addition, few general families of inorganic systems have been identified, unlike organic counterparts which have been derivatised extensively and span a diverse range of structural and donor/acceptor types (for example crown ethers, calixarenes and porphyrins, Figure 8).[29]

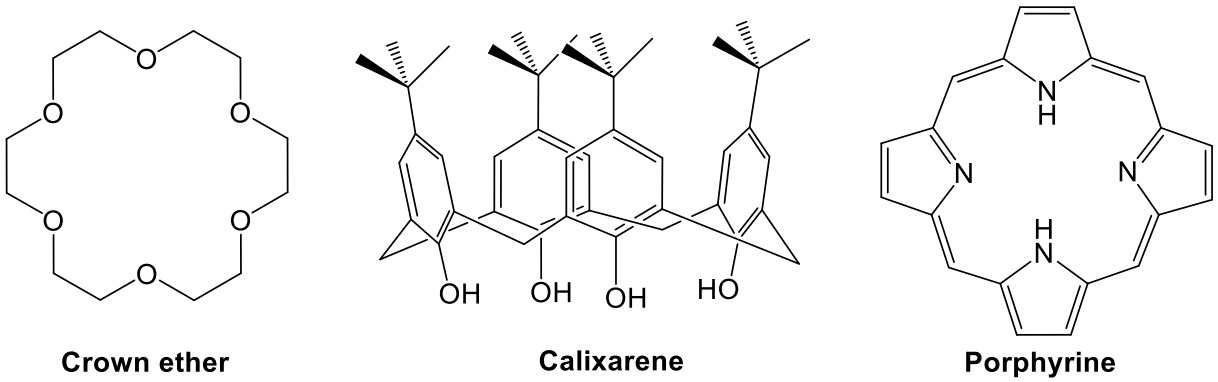

Figure 8: Examples of organic cavitands and macrocycles.

Since most of the elements in the periodic table are metals it is perhaps unsurprising that the vast majority of macrocyclic inorganic systems are metallocycles. In the limited cases in which their host-guest chemistry has been explored, behaviour is dominated by anion coordination through the electropositive metal centres of the macrocyclic hosts.[30–32] This is in contrast to the well-developed host-guest chemistry of organic macrocyles in which anion, cation and neutral guest coordination are commonplace.[26] The idea of supramolecular functionality, however, has not been entirely absent in main group chemistry. Contributions by Gabbai et al. focused on selective anion binding and extraction with Lewis acidic main group centres.[33] Examples of anion coordination by topologically-complex inorganic systems are seen in Hawthorne's metallacarborands and Mulvey's inverse crowns (Figure 9), which can exhibit both anion-selective behaviour as well as the ability to coordinate highly unusual anions (such as the double 2,5-CH arene deprotonation of toluene witnessed in the example shown in Figure 9).[30,34] The main point is that very few donor-type macrocycles have been reported. An early example is the twelve-membered phosph(V)azane $[(Me_2N)PN]_6$ which was found to coordinate Cu^{2+} within its cavity (Figure 10).[35] Other more recent examples of cation coordination have been found in the case of cyclic silicones, which are analogous to crown ethers (e.g., the potassium complex shown in Figure 10). Related to this, silsesquioxane cages and their germanium analogues have been reported to host anions within them.[36–38]

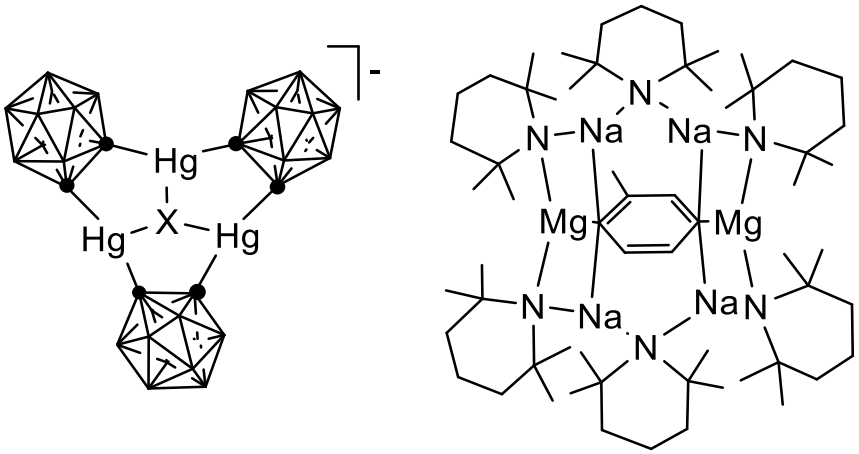

Figure 9: Left: Host-guest complex of a metallocarborand, in which the 1,2-$B_{10}C_2$ carborane units link the Hg(II) centres together in the host which coordinates halide ions (X = F, Cl, Br). Right: An inverse crown complex of a heterometallic Mg/Na amido host coordinating an unusual 2,5-deprotonated toluene dianion.

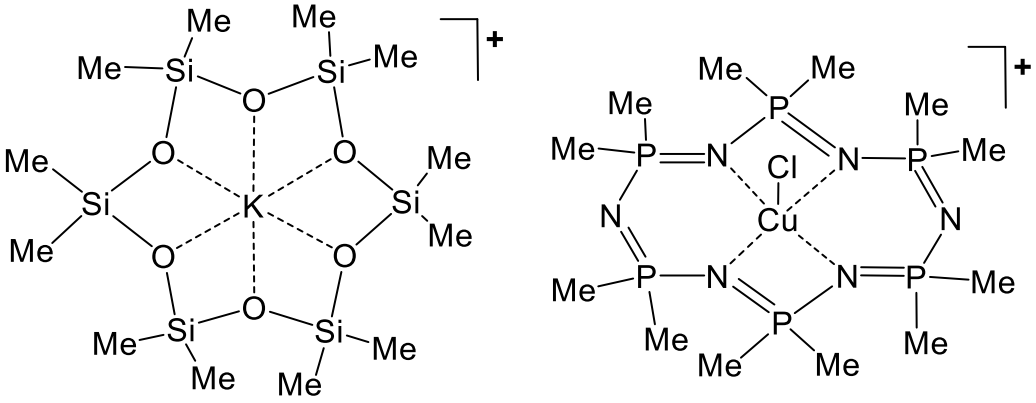

Figure 10: Left: A potassium complex of a cyclic silicone macrocycle. Right: A phosphazene macrocycle coordinating a Cu(II) ion.

Some of the fundamental issues to consider in the development of any stable inorganic macrocyclic system relate to bond energy and ionicity, since for any host macrocycle to exist in the absence of a guest, it is clear that bonding within its framework should be both stable and directional. A guide to both of these factors is a graph of the heteroatomic bond energy versus the ionic contribution to the bonds, derived from the definition of Pauling electronegativity (Figure 11, which shows a range of element-element, element-O and element-N bonds).[39,40] The kinetic and thermodynamic stability as well as the rigidity of carbon-based macrocycles can be seen to stem in large part from the high stability of the framework bonds (C-C, C-N, C-O) combined

with the relatively low ionic contribution to the bond character. For elements beyond the second period of the periodic table, however, as a particular p-block group is descended orbital energy/size mismatching will tend to lead to weaker bonds. Although this is offset to some extent by an increase in the ionic contribution to the bond energy, this contribution has the detrimental effect of increasing the polarity of the bonds (leading to kinetic instability and non-directionality of bonding, in particular). The 'sweet-spot' in the search for frameworks which are likely to support rigid macrocycles is located around the classical carbon area (as highlighted in Figure 11). This is largely borne out by a more extensive literature survey of constitutionally stable main group macromolecular systems, which are far more prevalent in this area, and provides a useful starting point in any planned synthesis of main group macrocycles.

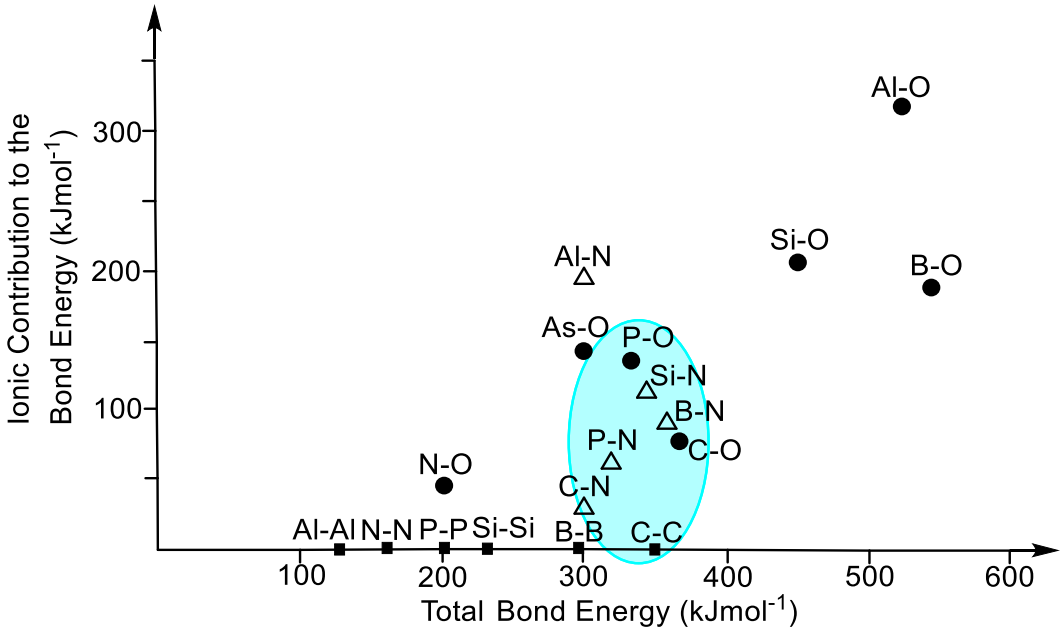

Figure 11: Background consideration of bond energy and bond polarity, showing the 'sweet spot' located around the classical organic area.

Work by Wright et al. in the area of inorganic macrocycles arose initially through a serendipitous discovery. With the intention of obtaining a heterometallic Sn(II)/Sb(III) cage, the lithium salt of the tris(amido)stannate anion $[Sn(2\text{-}MeO\text{-}C_6H_4NH)_3]^-$ was reacted with the potent base $Sb(NMe_2)_3$.The surprising product of this reaction is the hexameric Sb(III) macrocycle $[\{Sb(\mu\text{-}2\text{-}MeO\text{-}C_6H_4N)\}_2((\mu\text{-}2\text{-}MeO\text{-}C_6H_4N)]_6$, having a cyclic arrangement of six Sb_2N_2 ring units bridged by imido-N atoms (Figure 12).[41] The overall arrangement is toroidal, with the Sb_2N_2 ring units being roughly perpendicular to the Sb_{12} mean plane. A similar Sb(III) macrocycle was later obtained

by Norman and coworkers using a more direct approach.[42] The significance of this result was the potential that [{Sb(μ-2-MeO-C_6H_4N)}$_2$((μ-2-MeO-C_6H_4N)]$_6$ may represent the first recognisable example of a broader family of macrocyclic compounds of this type within the p-block. A clue to this was provided by the series of previously reported isoelectronic species [{P(μ-NR)}$_2$(μ-NR)]$_2$, [{Sn(μ-NR)}$_2$(μ-NR)]$_2^{4-}$ and [{MeAl(μ-NCy)}$_2$(μ-NR)]$_2^{4-}$ (Figure 13), which in the light of the structure of [{Sb(μ-2-MeO-C_6H_4N)}$_2$((μ-2-MeO-C_6H_4N)]$_6$ could be reappraised as 'dimeric' macrocycles with the same architecture.

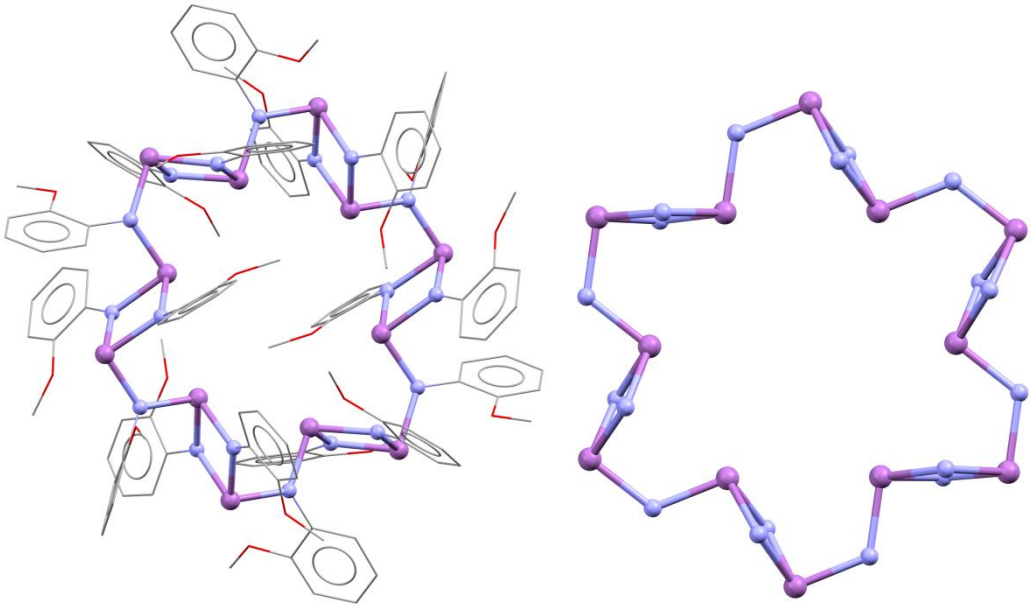

Figure 12: Left: Structure of the Sb(III) macrocycle [{Sb(μ-2-MeO-C_6H_4N)}$_2$((μ-2-MeO-C_6H_4N)]$_6$; Right: the core arrangement, showing only the Sb and N atoms. Colour code: purple = Sb, blue = N, grey = C, red = O.

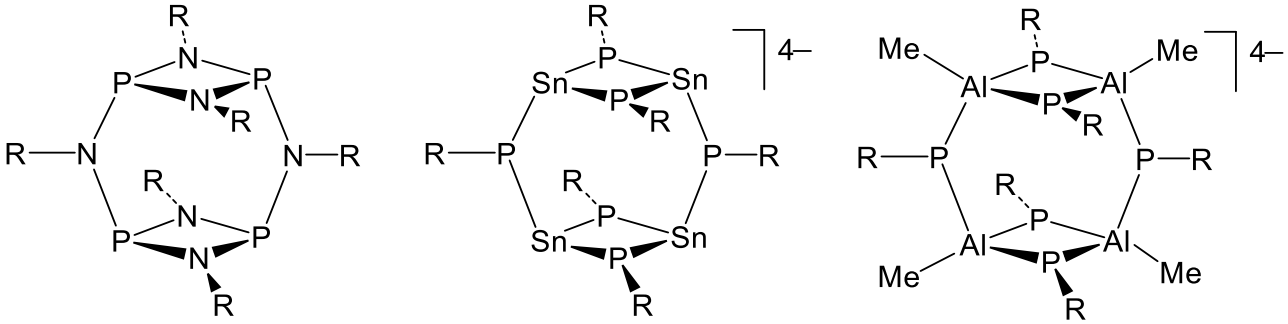

Figure 13: Isoelectronic 'dimeric' cage-like architectures.

Owing to the high bond energy and relatively low polarity of the P-N bonds (as seen diagrammatically in Figure 11), higher-order macrocycles related to [{Sb(μ-2-MeO-C_6H_4N)}$_2$((μ-2-MeO-C_6H_4N)]$_6$ based on P-N building blocks therefore became the

focus of future studies by Wright et al. in this area. It was reasoned that reduction of the steric demands of the P_2N_2- bridging groups of $[\{P(\mu\text{-}NR)\}_2(\mu\text{-}NR)]_2$ might be in itself enough to allow the expansion of the macrocyclic framework. As discussed above $[ClP(\mu\text{-}N^tBu)]_2$ was found to be particularly robust for the rational construction of larger supramolecular structures. It was reasoned that linking the P_2N_2 units is synthetically feasible via reacting nucleophilic and electrophilic P_2N_2 units such as $[(NH_2)P(\mu\text{-}N^tBu)]_2$ and $[ClP(\mu\text{-}N^tBu)]_2$. The novel nucleophilic synthetic building block $[(NH_2)P(\mu\text{-}N^tBu)]_2$ is obtained in good yield by the simple reaction of the phosph(III)azane dimer $[ClP(\mu\text{-}N^tBu)]_2$ with a solution of excess ammonia in THF (Figure 14).[43]

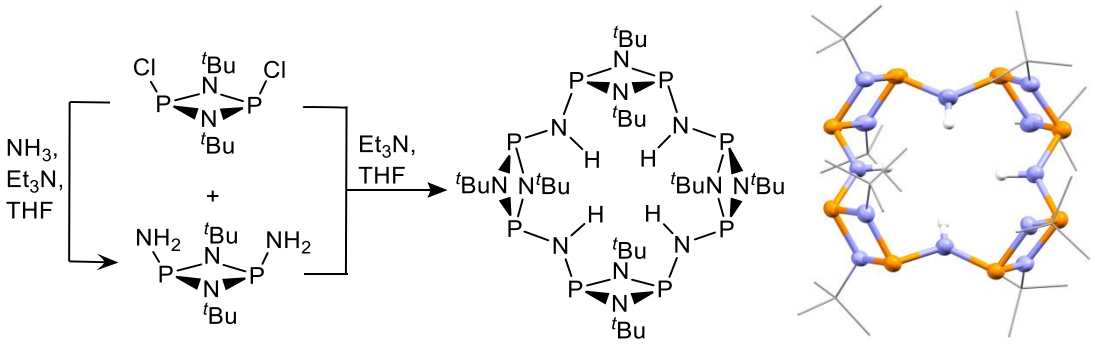

Figure 14: Left: Parallel synthesis of the tetrameric macrocycle $[\{P(\mu\text{-}NtBu)\}_2(NH)]_4$ from the electrophilic $[ClP(\mu\text{-}N^tBu)]_2$ and nucleophilic building blocks $[(NH_2)P(\mu\text{-}N^tBu)]_2$; Right: Structure of the tetramer $[\{P(\mu\text{-}N^tBu)\}_2(NH)]_4$. Colour code: orange = P, blue = N, grey = C, white = H.

Like $[ClP(\mu\text{-}N^tBu)]_2$ and the majority of phosph(III)azane dimers reported, $[(NH_2)P(\mu\text{-}N^tBu)]_2$ exhibits a preference for the cis-isomer in the solution and solid state. This is one of the key factors favouring the use of cyclodiphosphazanes in macrocycle synthesis, since the cis-conformation effectively preorganises the components for macrocyclisation during assembly. The nucleophilic precursor $[(NH_2)P(\mu\text{-}N^tBu)]_2$ is readily condensed with the electrophilic component $[ClP(\mu\text{-}N^tBu)]_2$ at -78 °C in the presence of excess Et_3N (as a Brønsted base) to give the tetrameric macrocycle $[\{P(\mu\text{-}N^tBu)\}_2(NH)]_4$ in an isolated yield of 67% (an overall yield of 30% starting from PCl_3 and $^tBuNH_2$) (Figure 14).

Although $[\{P(\mu\text{-}N^tBu)\}_2(NH)]_4$ is generated almost quantitatively, further in situ ^{31}P NMR investigation of the reaction at low temperature showed that another minor product is always formed (in variable amounts of about 1-5% of the total phosphorus signal). This species is the host-guest complex $[\{P(\mu\text{-}N^tBu)\}_2(NH)]_5(HCl)$, composed

of a pentameric $[H\{P(\mu\text{-}N^tBu)\}_2(NH)]_5^+$ macrocycle which coordinates a Cl^- anion at the centre of the planar $[\{P\bullet\bullet\bullet P\}N]_5$ core using the five NH groups (with a H-atom bonded to a P-centre of the macrocycle) (Figure 15). The macrocyclic cavity of $[\{P(\mu\text{-}N^tBu)\}_2(NH)]_5$ is ca. 6.8 Å in diameter (measured N•••N).[44]

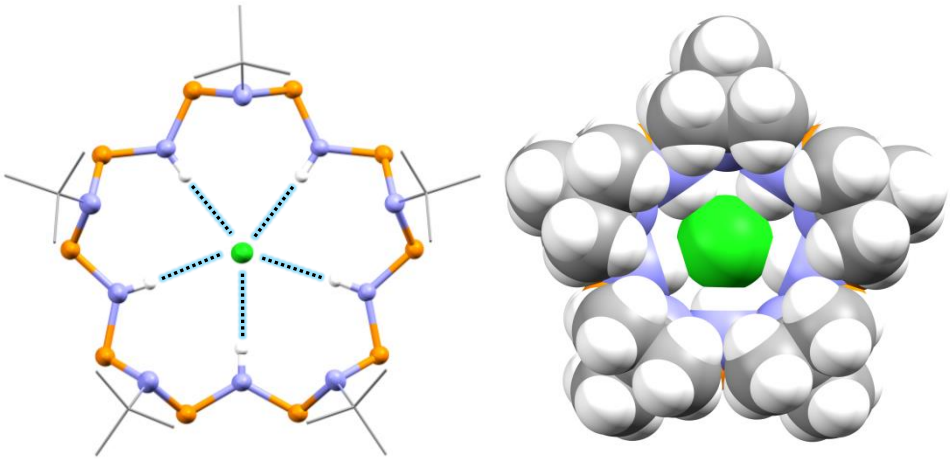

Figure 15: Structure of the host-guest complex $[\{P(\mu\text{-}N^tBu)\}_2(NH)]_5(HCl)$. Colour code: orange = P, blue = N, grey = C, white = H, green = Cl.

The structure of this minor product illustrates that, in addition to the preorganisation of the cis-building blocks, templating by Cl^- also directs the formation of macrocycles rather than polymers in these reactions. The formation of the pentameric macrocyclic core of $[\{P(\mu\text{-}N^tBu)\}_2(NH)]_5$, with an uneven number of P_2N_2 units, clearly cannot occur by the stepwise/alternate condensation of the building blocks $[ClP(\mu\text{-}N^tBu)]_2$ and $[(NH_2)P(\mu\text{-}N^tBu)]_2$, for which only macrocycles with an even number of P_2N_2 subunits could be constructed (like $[\{P(\mu\text{-}N^tBu)\}_2(NH)]_4$, Figure 14). Extensive ^{31}P NMR studies of the reactions of the precursors $[ClP(\mu\text{-}N^tBu)]_2$ and $[(NH_2)P(\mu\text{-}N^tBu)]_2$ under a range of conditions reveal the importance of Cl^- templating in this reaction and indicate that a common intermediate (Figure 16) is responsible for the formation of both the tetramer $[\{P(\mu\text{-}N^tBu)\}_2(NH)]_4$ and pentamer $[\{P(\mu\text{-}N^tBu)\}_2(NH)]_5$. While $[\{P(\mu\text{-}N^tBu)\}_2(NH)]_4$ results from ring closure of the common intermediate (with the elimination of Et_3NHCl), $[\{P(\mu\text{-}N^tBu)\}_2(NH)]_5$ results from the further insertion of a unit of the nucleophilic component $[(NH_2)P(\mu\text{-}N^tBu)]_2$ (with loss of NH_4Cl).

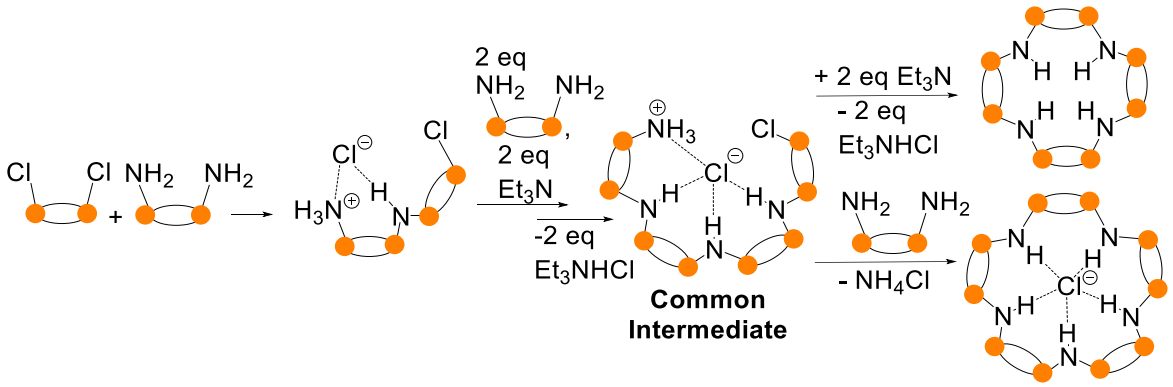

Figure 16: Proposed mechanism of formation of $[\{P(\mu\text{-}N^tBu)\}_2(NH)]_4$ and $[\{P(\mu\text{-}N^tBu)\}_2(NH)]_5$ through the common intermediate.

Insight into the mechanism of selection of the tetrameric or pentameric arrangements is revealed by the effects of addition of excess of different halide ions to the reaction.[45] While the tetramer $[\{P(\mu\text{-}N^tBu)\}_2(NH)]_4$ is formed almost quantitatively in the reaction shown in Figure 14, remarkably, pentamer $[\{P(\mu\text{-}N^tBu)\}_2(NH)]_5$ is produced almost quantitatively if the reaction is performed in the presence of excess LiI (with the order of selection of $[\{P(\mu\text{-}N^tBu)\}_2(NH)]_5$ being $I^- >> Br^- > Cl^-$). This is the opposite to the thermodynamic stability of the host-guest complexes $[[\{P(\mu\text{-}N^tBu)\}_2(NH)]_5 \subset X]^-$ ($X = Cl^- > Br^- >> I^-$) from DFT calculations, as expected on the basis of weaker N-H•••I^- H-bonding. The reasons for the observed selectivity with I^- are proposed to be entirely kinetic in origin (Figure 16). For the smaller halide ion Cl^- the rate of ring closing to the tetramer $[\{P(\mu\text{-}N^tBu)\}_2(NH)]_4$ is greater than that for further insertion of $[(NH_2)P(\mu\text{-}N^tBu)]_2$ to give the pentamer $[\{P(\mu\text{-}N^tBu)\}_2(NH)]_5$. This is an example of negative templation, in which selection of $[\{P(\mu\text{-}N^tBu)\}_2(NH)]_4$ is due to slowing of the rate of formation of $[\{P(\mu\text{-}N^tBu)\}_2(NH)]_5$.[46] In the case of I^-, however, the $-NH_3^+$ and -Cl termini of the intermediate are held further apart at optimum separation for insertion of $[(NH_2)P(\mu\text{-}N^tBu)]_2$ to give the pentamer $[\{P(\mu\text{-}N^tBu)\}_2(NH)]_5$. This is an example of positive templation, in which $[\{P(\mu\text{-}N^tBu)\}_2(NH)]_5$ is favoured due to the accelerated rate. Using a ten-fold excess of LiI and adjusting the stoichiometry to the required 3:2 ratio (of compounds $[(NH_2)P(\mu\text{-}N^tBu)]_2$ and $[ClP(\mu\text{-}N^tBu)]_2$, respectively) for the formation of $[\{P(\mu\text{-}N^tBu)\}_2(NH)]_5$ provides a preparative route to the pentamer, in the form of the host-guest complex $Li(THF)_4^+[\{P(\mu\text{-}N^tBu)\}_2(\mu\text{-}NH)]_5I^-$. Its solid-state structure reveals a highly distorted pentameric macrocyclic arrangement in which the I^- anion is located above one side of the macrocyclic mean plane (cf. the planar

structure $[[\{P(\mu\text{-}N^tBu)\}_2(NH)]_5\subset Cl]^-$ (Figure 15). The free pentamer $[\{P(\mu\text{-}N^tBu)\}_2(NH)]_5$ can be released by the reaction of $Li(THF)_4[[\{P(\mu\text{-}N^tBu)\}_2(NH)]_5\subset I]$ with MeONa (→ NaI + LiOMe + $[\{P(\mu\text{-}N^tBu)\}_2(NH)]_5$) in DCM). The X-ray structure of the product shows encapsulation of two DCM molecules in the solid state.[47]

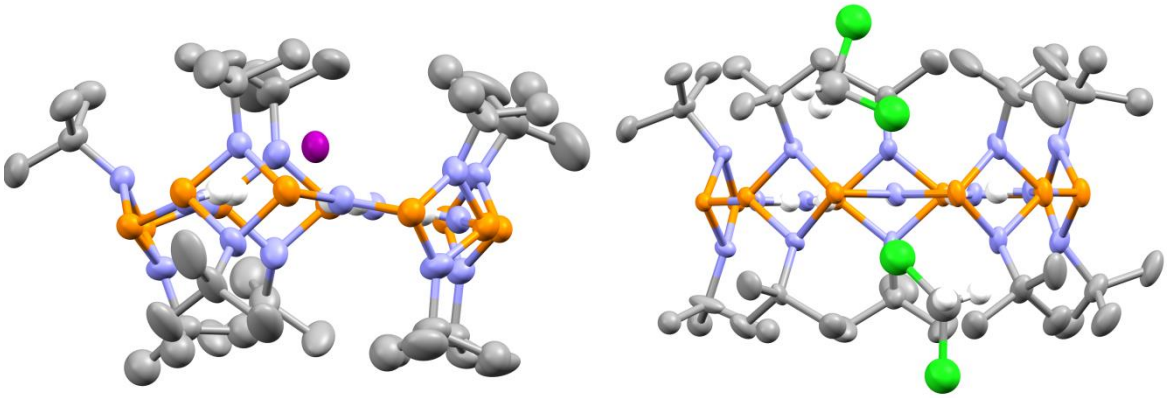

Figure 17: Left: Structure of the anion $[[\{P(\mu\text{-}N^tBu)\}_2(NH)]_5\subset I]^-$. Right: Structure of $[[\{P(\mu\text{-}N^tBu)\}_2(NH)]_5\subset(DCM)_2]$. Colour code: orange = P, blue = N, grey = C, white = H, green = Cl, purple = I.

In order to target macrocycles containing group 16 atoms, it is necessary to develop new nucleophilic precursors which are isoelectronic with $[(NH_2)P(\mu\text{-}N^tBu)]_2$**,** depicted in Figure 18. Simple consideration of the bond energies involved (NH/EH versus P=N/P=E-π plus PH) explains why whereas $[(NH_2)P(\mu\text{-}N^tBu)]_2$ is most stable as its P(III) tautomer, $[H(O=)P(\mu\text{-}N^tBu)]_2$ and $[H(S=)P(\mu\text{-}N^tBu)]_2$ will be most stable in their P(V) tautomers.[40]

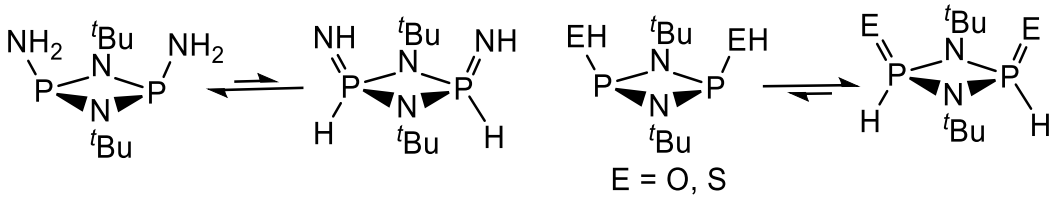

Figure 18: Isoelectronic nucleophilic building blocks and their preferred tautomers.

Precursor $[H(O=)P(\mu\text{-}N^tBu)]_2$ is readily obtained by the controlled hydrolysis of the $[ClP(\mu\text{-}N^tBu)]_2$ with H_2O in THF in the presence of excess Et_3N.[48] However, $[H(O=)P(\mu\text{-}N^tBu)]_2$ rapidly dimerises in to $[\{O=(H)P(\mu\text{-}N^tBu)]_2\}_2(\mu\text{-}O)]$ above 10 °C.Trapping of the framework of $[H(O=)P(\mu\text{-}N^tBu)]_2$ is achieved by the addition of excess ^{n}BuLi, resulting in deprotonation to give the dianion $[O\text{-}P(\mu\text{-}N^tBu)]_2^{2-}$ which can

be reacted in situ to give the O-bridge macrocyclic tetramer [{P(μ-N^{t}Bu)}$_2$(μ-O)]$_4$ (Figure 19).[49] The solid-state structure of [{P(μ-N^{t}Bu)}$_2$(μ-O)]$_4$ is very similar to the N-bridged analogue [{P(μ-N^{t}Bu)}$_2$(μ-NH)]$_4$, but with a noticeable contraction in the diameter of the cavity (from 5.2 Å to 5.05 Å), in line with the small decrease in bond length of the framework P-O bonds compared to P-N bonds.

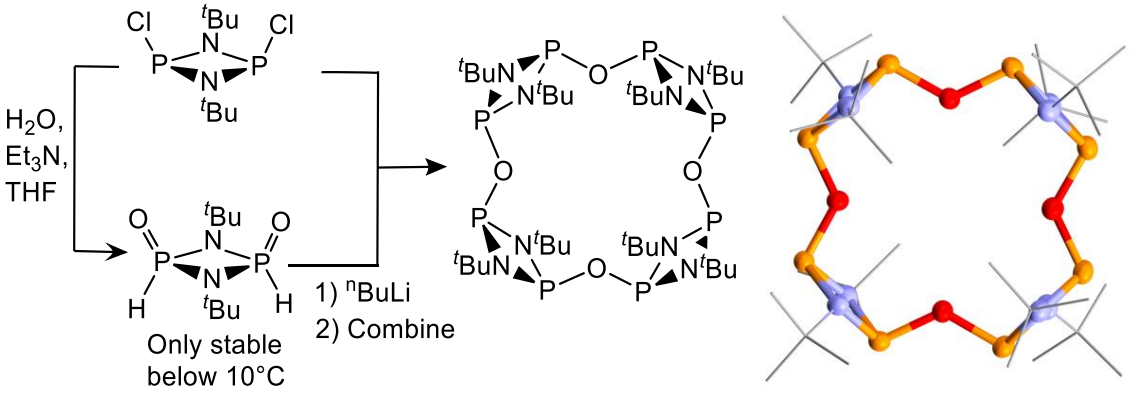

Figure 19: Left: Formation and trapping of the nucleophilic precursor [H(O=)P(μ-N^{t}Bu)]$_2$ and the formation of the O-bridge tetramer [{P(μ-N^{t}Bu)}$_2$(μ-O)]$_4$. Right: Solid-state structure of [{P(μ-N^{t}Bu)}$_2$(μ-O)]$_4$. Colour code: orange = P, blue = N, grey = C, red = O.

Direct evidence of the formation of the dianion [O-P(μ-N^{t}Bu)]$_2^{2-}$ is obtained by the isolation of the intermediate prior to reaction with [ClP(μ-N^{t}Bu)]$_2$, in the form a complex lithium cluster (Figure 20).[50] The cluster has three dianion units of [O-P(μ-N^{t}Bu)]$_2^{2-}$ which surround a central Li$_7$Cl$_7$ double-cubane unit. The presence of the cis conformation of the [O-P(μ-N^{t}Bu)]$_2^{2-}$ dianion and the overall metallocyclic arrangement of [O-P(μ-N^{t}Bu)]$_2^{2-}$ suggest that ligand preorganisation and cation templating are important in the assembly of macrocycle [{P(μ-N^{t}Bu)}$_2$(μ-O)]$_4$. However, attempts to template the formation of larger O-bridged macrocycles by the addition of bigger alkali metal ions to the reaction have only led to the formation of [{P(μ-N^{t}Bu)}$_2$(μ-O)]$_4$. A range of nucleophilic precursors [H(S=)P(μ-NR)]$_2$ (R = ^{t}Bu, Dipp, Mes, CHPh$_2$) can be readily accessed by reactions of the corresponding dichloride dimers [ClP(μ-NR)]$_2$ with LiSH at -78 °C in THF.[14] Double-deprotonation of the ^{t}Bu dimer [H(S=)P(μ-N^{t}Bu)]$_2$ with 2 equivalents benzylsodium yields the dianion [S-P(μ-N^{t}Bu)]$_2^{2-}$, which similarly to [O-P(μ-N^{t}Bu)]$_2^{2-}$ retains the cis orientation of the sulphide functionalities and crystallises as a cluster in the solid state (Figure 20).[51]

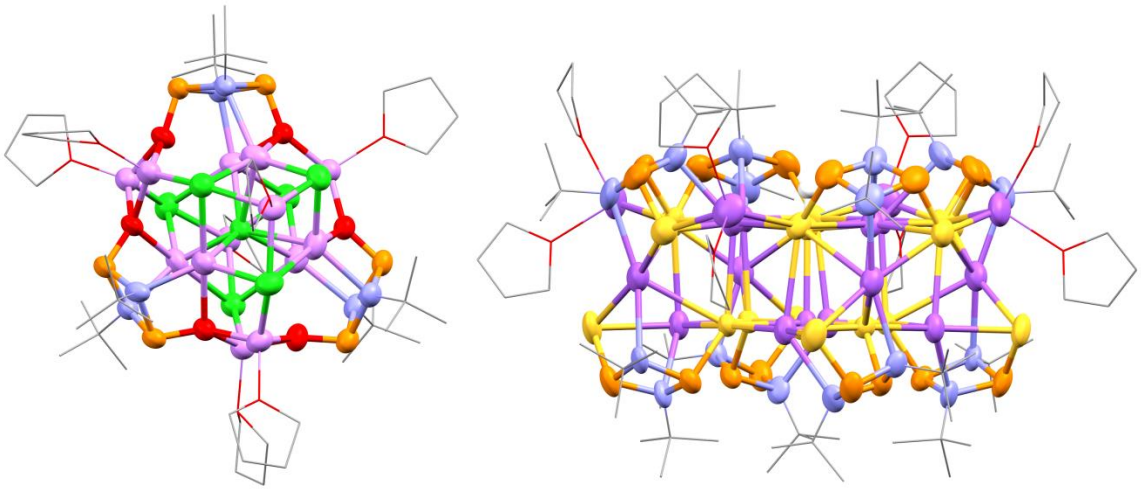

Figure 20: Left: Solid-state structure of the Li cluster formed by $[O\text{-}P(\mu\text{-}N^tBu)]_2^{2-}$. Right: Solid-state structure of Na cluster formed by $[S\text{-}P(\mu\text{-}N^tBu)]_2^{2-}$ in the solid state. Colour code: orange = P, blue = N, grey = C, red = O, purple = Li, dark purple = Na, green = Cl, yellow = S.

Unfortunately, dianions like $[S\text{-}P(\mu\text{-}N^tBu)]_2^{2-}$ are chemically too unstable to be used in the formation of S-bridged P(III) macrocycles. Instead, it is necessary to stabilise the P_2N_2 units of $[S\text{-}P(\mu\text{-}N^tBu)]_2^{2-}$ prior to cyclisation, by oxidation of the P-centres with elemental sulphur or selenium (Figure 21), producing the new P(V) dianions $[(E)(S)P(\mu\text{-}N^tBu]_2^{2-}$ [E = S, Se]. This approach provides the basis for a modular, one-pot synthesis of a range of S- and Se-bridged macrocycles.[52] Deprotonation of $[H(S=)P(\mu\text{-}N^tBu)]_2$, followed by room temperature in situ oxidation with S or Se, then addition of a range of dichlorides $[ClP(\mu\text{-}NR)]_2$ gives the macrocycles $[\{(S=)P(\mu\text{-}N^tBu)\}_2(\mu\text{-}S)\{P(\mu\text{-}NR)\}(\mu\text{-}S)]_3$ (E = S; R = ^{t}Bu, neopentyl, R-1-(2-napthyl)ethyl) or $[\{(S=)P(\mu\text{-}N^tBu)\}_2(\mu\text{-}Se)\{P(\mu\text{-}N^tBu)\}(\mu\text{-}Se)]_3$ in isolated yields of over 80%, having $P(III)_2P(V)_2$ backbones (Figure 21). Significantly, this method allows the synthesis of mixed-ligand macrocycles (containing ^{t}Bu and R' groups), as well as the incorporation of chiral R'-groups (as in the case of R-1-(2-napthyl)ethyl)).

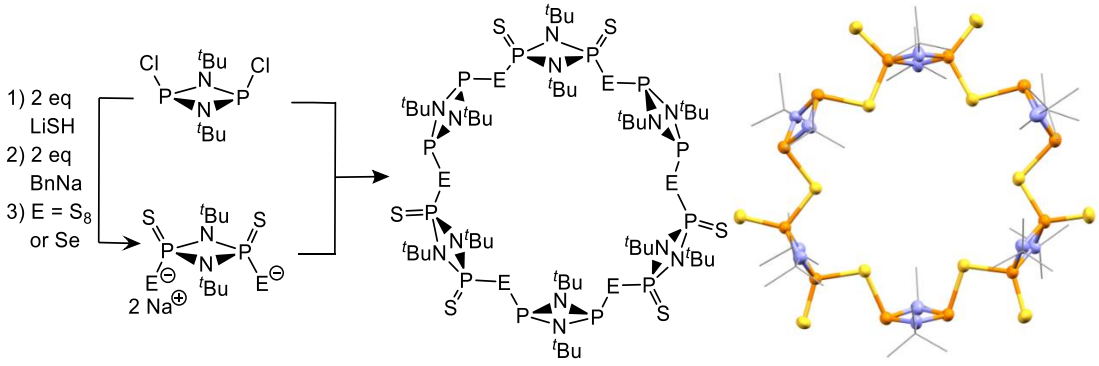

Figure 21: Left: Macrocyclisation to [{(S=)P(μ-N^{t}Bu)}$_2$(μ-S){P(μ-N^{t}Bu)}(μ-S)]$_3$ and [{(S=)P(μ-N^{t}Bu)}$_2$(μ-Se){P(μ-N^{t}Bu)}(μ-Se)]$_3$; note that the nucleophilic phosphazane [(S)$_2$P(μ-N^{t}Bu)]$_2^{2-}$ can also be cyclised with derivatives of [ClP(μ-N^{t}Bu)]$_2$ (see main text). Right: Solid-state structure of [{(S=)P(μ-N^{t}Bu)}$_2$(μ-S){P(μ-N^{t}Bu)}(μ-S)]$_3$ analogue. Colour code: orange = P, blue = N, grey = C, yellow = S.

These macrocycles can be derivatised further by S-oxidation of their frameworks. For example, [{(S=)P(μ-N^{t}Bu)}$_2$(μ-S){P(μ-NR)}(μ-S)]$_3$ is converted quantitatively into the all P(V) derivative [{(S=)P(μ-N^{t}Bu)}$_2$(μ-S)]$_6$ which shows improved air and moisture stability.

In addition to the pathway illustrated in Figure 21, dianion intermediate [(Se)(S)P(μ-N^{t}Bu]$_2^{2-}$ can be oxidised with I_2 to give -Se$_2$- bridged trimeric macrocycle [{(S=)P(μ-N^{t}Bu)}$_2$(μ-Se-Se)]$_3$ (Figure 22). This is directly related to the previously reported isoelectronic and isostructural trimers [{(^{t}BuN=)P(μ-N^{t}Bu)}$_2$(μ-Se-Se)]$_3$ (E = S, Se) which is obtained via I_2 oxidation of [(^{t}BuN=)(E-P(μ-N^{t}Bu)]$_2^{2-}$.[53]

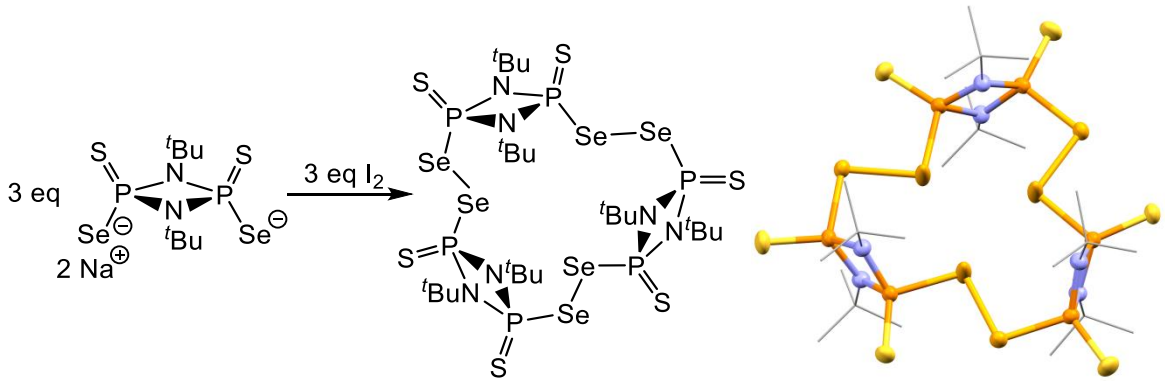

Figure 22: Left: Synthesis of [{(^{t}BuN=)P(μ-N^{t}Bu)}$_2$(μ-Se-Se)]$_3$. Right: Solid-state structure of [{(^{t}BuN=)P(μ-N^{t}Bu)}$_2$(μ-Se-Se)]$_3$. Colour code: orange = P, light orange = Se, blue = N, grey = C, yellow = S.

Macrocycles that are closely related to [{(S=)P(μ-N^{t}Bu)}$_2$(μ-S){P(μ-NR)}(μ-S)]$_3$ can also be constructed selectively via a one-pot Wurtz coupling procedure, involving the reaction of the P(V) dichlorides [(E=)(Cl)P(μ-^{t}Bu)]$_2$ (E = S, E = Se) in toluene.[54,55] The mechanism of formation of the macrocycles [{(S=)P(μ-N^{t}Bu)$_2$P}(μ-S)]$_6$ or [{(Se=)P(μ-N^{t}Bu)$_2$P}(μ-Se)]$_6$ probably involves the 'head-to-tail' reaction of a transient anionic intermediate [(E=)(Cl)P(μ-^{t}Bu)$_2$P(-E)]$^-$, which effectively acts as both the nucleophilic and electrophilic component. The solid-state structure of the Se-macrocycle [{(Se=)P(μ-N^{t}Bu)$_2$P}(μ-Se)]$_6$ is shown in Figure 23 and has a distinct, alternating P(III)P(V) backbone that can be compared to the P(III)$_2$P(V)$_2$ backbone in Figure 21. Interestingly, in respect to preorganisation in these systems, it appears from recent studies of the formation of the S-macrocycle [{(S=)P(μ-N^{t}Bu)$_2$P}(μ-S)]$_6$ that only the cis-isomer of the precursor [(S=)(Cl)P(μ-^{t}Bu)]$_2$ may be involved in the formation of the macrocycle, with the trans-isomer being doubly reduced to the singlet biradicaloid dianion [(S)(Cl)P(μ-^{t}Bu)]$_2^{2-\bullet}$ under the reaction conditions.

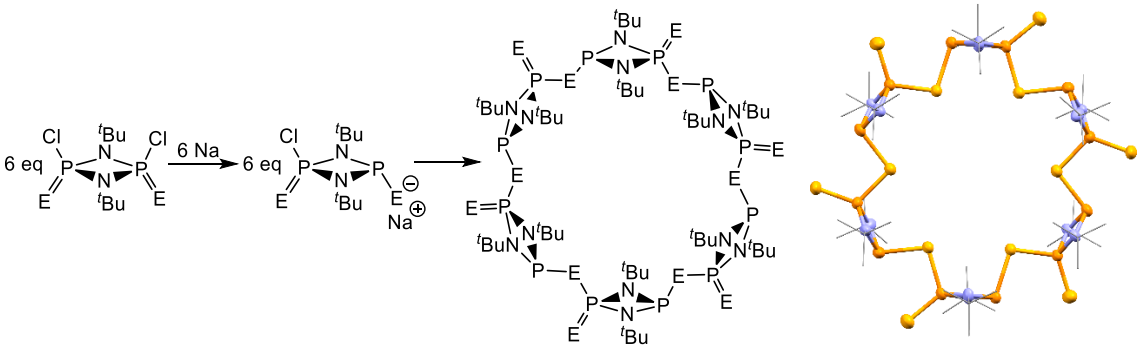

Figure 23: Left: Synthesis of [{(E=)P(μ-N^{t}Bu)$_2$P}(μ-E)]$_6$ (E = S, Se) Right: Solid-state structure of [{(Se=)P(μ-N^{t}Bu)$_2$P}(μ-E)]$_6$. Colour code: orange = P, light orange = Se, blue = N, grey = C.

Cyclodiphosphazanes can also form hybrid organic-inorganic macrocycles. Organic linkers such as diols, diamines or amino-thiophenols can be employed to link the P$_2$N$_2$ ring units together. Choosing linear aliphatic diols as the organic linkers yields dimers consisting of a hybrid organic-inorganic ring unit.[56,57] When diamino-naphthalene is used as the organic nucleophile, the trimeric macrocycle [{P(μ-N^{t}Bu)}$_2${1,8-(NH)$_2$C$_{10}$H$_6$}]$_3$, consisting of three P$_2$N$_2$ and three naphthalene units linked by NH bridges is formed (Figure 24).[58] The largest phosphazane macrocycle of this kind is obtained when para-diaminophenylene is used as the organic component.[59] This

tetrameric species [{P(μ-N^{t}Bu)}$_2${1,4-(NH)$_2$C$_6$H$_4$}]$_4$ adopts a folded conformation in the solid state and contains a roughly tetrahedral arrangement with regards to the P_2N_2 units. Moreover, the overall geometry is stabilised by NH•••π interactions between the bridges and the aromatic units of the framework. Various derivatives of these hybrid macrocycles have been synthesised in recent years although little structural variety is observed when changing the organic portion.

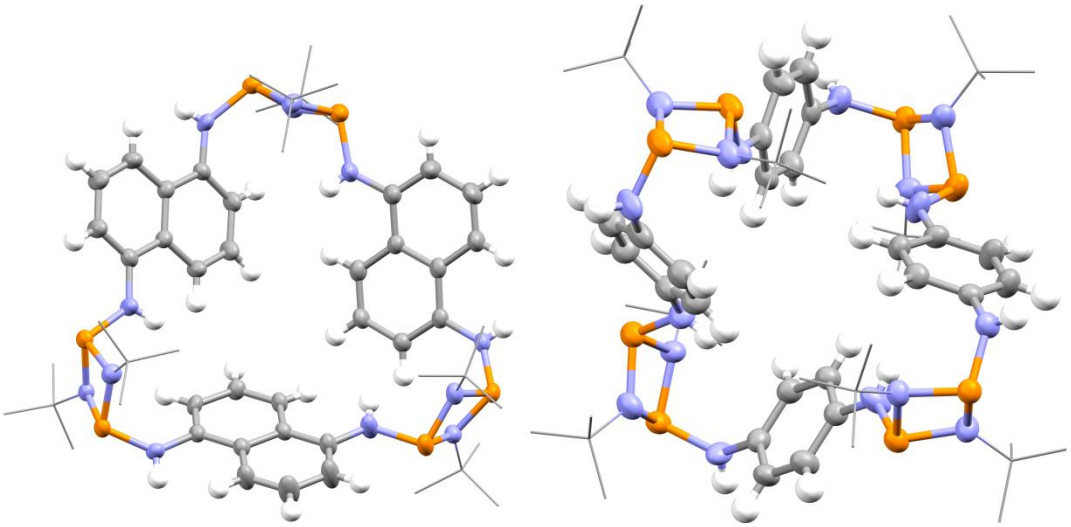

Figure 24: Left: Solid state structure of [{P(μ-N^{t}Bu)}$_2${1,8-(NH)$_2$C$_{10}$H$_6$}]$_3$; Right: Solid-state structure of [{P(μ-N^{t}Bu)}$_2${1,4-(NH)$_2$C$_6$H$_4$}]$_4$. Colour code: orange = P, blue = N, grey = C.

It should be noted that in most of the larger macrocyclic phosphazane topologies host-guest adduct formation with solvent molecules can be observed in the solid state. Although there has been no in detail study on the host-guest chemistry of phosphazane macrocycles yet, this observation highlights the potential of such systems for supramolecular applications.

Phosphazanes in Anion Binding and Catalysis

In recent years there have been related efforts to employ less topologically complex main group functionalities in anion binding and catalysis. The traditional strategy for main group anion-receptors has been the incorporation of Lewis acidic metal atoms, such as B(III) and Sb(V), for anion binding.[60–63] However, a range of H-bond donor receptors containing a variety of p-block functionalities has recently emerged, including phosphoramides R(O/S=)P(NHR)$_2$ and (O/S=)P(NHR)$_3$, sulfonamides

$(O=)_2S(NHR)_2$, boronic acids $RB(OH)_2$, borinic acids R_2BOH, silanols $R_2Si(OH)_2$ and phosphonium cations $(R_2N)_2P(NHR)_2^+$.[64–68] The acidity of the H-bond donor NH and OH groups increases when bonded to heavier main group elements, due to transfer of electron density from the lone-pairs on N or O into the σ*- or p-orbitals of the main group centre, e.g., the proton acidity of COH is less than SiOH.[69,70] Turning to main group elements therefore provides the potential means of tuning the strength of anion binding and affinity to a generally greater level than in a typical organic system.

Directly relevant to the work presented in this thesis, Goldfuss and coworkers have investigated the anion binding properties of the air-stable phosph(V)azane dimer $[ArNH(E)P(\mu\text{-}N^tBu)]_2$ (E = O, S, Ar = 3,5-$(CF_3)_2C_6H_3$) (Figure 25), whose bidentate H-bond donor arrangements are conceptually related to ureas and squaramides.[71–74] All of the presented receptors in Figure 25 possess positively polarised cis-oriented NH functionalities set up to act as H-bond donors to an anion.

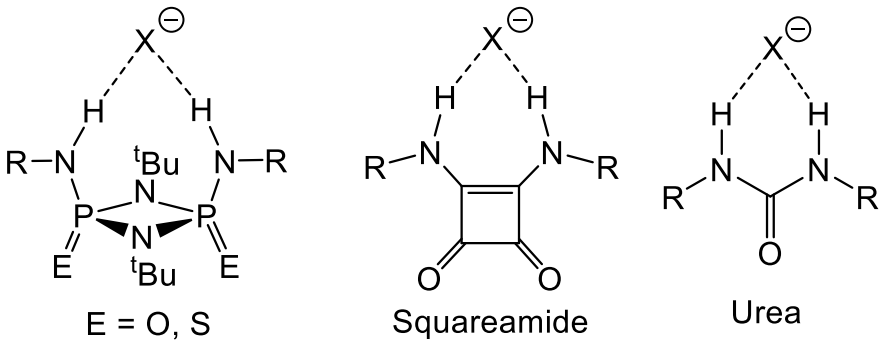

Figure 25: Comparison of phosphazane with squaramide and urea anion receptors.

Phosph(V)azane $[(3,5\text{-}(CF_3)_2C_6H_3)NH(O=)P(\mu\text{-}N^tBu)]_2$ binds particularly strongly to Cl^-, with logK = 5.44 being significantly higher than the corresponding diaryl urea (logK = 4.25 M^{-1}) and squaramides (logK = 5.13 M^{-1}) (containing the same 3,5-$(CF_3)_2C_6H_3$ groups, with K being the binding constant of the anion binding interaction in acetonitrile). However the obtained binding constant for the squareamide receptor deviated significantly from constants presented by other groups which makes these findings questionable.[75] The high anion affinity makes $[(3,5\text{-}(CF_3)_2C_6H_3)NH(O=)P(\mu\text{-}N^tBu)]_2$ useful in counterion-catalysis of the N-acyl-Mannich reaction. Related phosphazanes with less electron withdrawing exocyclic substituents have been employed in Knoevenagel-type condensation reactions. $[(3,5\text{-}(CF_3)_2C_6H_3)NH(O=)P(\mu\text{-}$

N^{t}Bu)]$_2$ is found to bind acetate OAc$^-$ approximately one order of magnitude stronger than Cl$^-$, as a consequence of the large NH•••NH bite distance in [(3,5-(CF$_3$)$_2$C$_6$H$_3$)NH(O=)P(μ-N^{t}Bu)]$_2$. The sulphur derivative [(3,5-(CF$_3$)$_2$C$_6$H$_3$)NH(S=)P(μ-N^{t}Bu)]$_2$ has a significantly lower affinity for Cl$^-$ and OAc$^-$. This difference when moving down the periodic table was ascribed, on the basis of structural and DFT studies, to the effect of stabilising ortho-C-H•••O=P interactions in the O-analogue on the conformation of the dimer, making the chelating NH exo-exo conformation (necessary for bifurcated Cl$^-$ coordination) more energetically accessible than the endo-exo conformation (Figure 26).

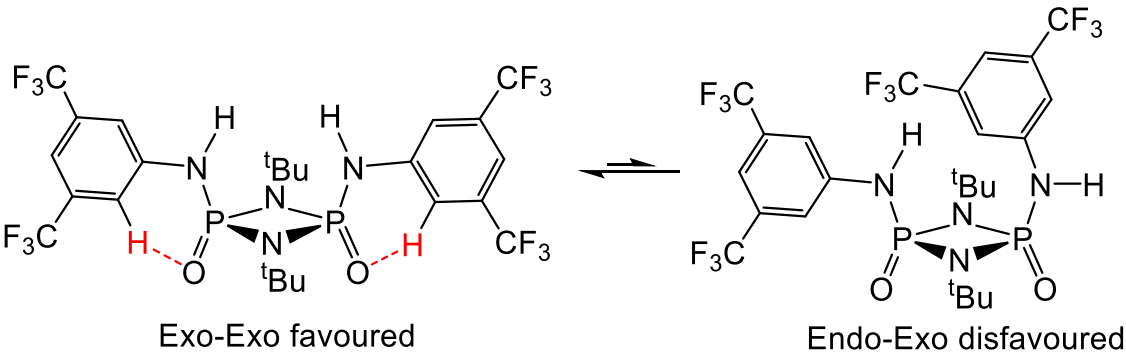

Figure 26: Conformational preference in Goldfuss phosphazane anion receptor.

In related work, Garcia et al. undertook a crystallographic study of solvate crystals of [^{t}BuNH(Se=)P(μ-N^{t}Bu)]$_2$.[76] It was found that when crystallised from donor solvents such as Me$_2$CO or CH$_3$CN 1:1 host-guest adducts can be observed with [^{t}BuNH(Se=)P(μ-N^{t}Bu)]$_2$ acting as a bidentate H-bond donor. However, the anion binding properties of such selenium derivatives have not been studied in detail in this area and there is, in particular, an absence of quantitative data which would allow the assessment of the relative anion-binding ability of the O-, S- and Se-phosph(V)azanes.

Generally speaking, the aims of the first part of this thesis are to expand the scope of cyclodiphosphazanes in supramolecular chemistry both structurally and in terms of applications. We were particularly interested to explore how the main group chemistry of the P$_2$N$_2$ backbone affects the supramolecular chemistry of such phosphazanes and to what extent main-group supramolecular chemistry differs from established organic systems.

Chapter 2: Tailoring the Binding Properties of Phosphazane Anion Receptors

This chapter will focus on understanding how the anion binding properties of small dimeric phosphazanes of the type $[RNH(X)P(\mu\text{-}NR)]_2$ can be improved, and which type of derivative is the most applicable to anion binding and transport (especially in aqueous media). In particular here we are focusing on the selenium derivatives and on phosphazane metal complexes which have not been considered previously in anion binding studies.

Results and Discussion

Exploring the Factors that Can be Used to Control Anion Binding in Cyclodiphosphazane Receptors

It was found in the initial stages of the current work that one aspect that makes Se-dimers $[RNH(Se)P(\mu\text{-}N^tBu)]_2$ particularly attractive synthetic precursors (and anion receptors), is that the cis-isomers (necessary for anion binding) can be obtained regioselectively by a new general modular approach from the readily prepared phosph(III)azane cis-$[ClP(\mu\text{-}N^tBu)]_2$ **2.1** via the diaminophosph(III)azanes cis-$[RNP(\mu\text{-}N^tBu)]_2$, without the formation of the trans- and other isomers in the final oxidation step with elemental Se (Figure 27). As mentioned in the introduction, similar oxidations have been performed in toluene at reflux.[21] This generally gives the cis- and trans-isomers which have to be separated by, e.g., column chromatography, resulting in overall yields < 40%.[72] Our new simple modification is to use THF at room temperature, which leads to quantitative formation of the cis-product alone. The new selenium cis-phosph(V)azane dimers **2.2 - 2.5** (which are key receptors studied in this chapter) were obtained after work-up in yields > 90% (see Experimental).

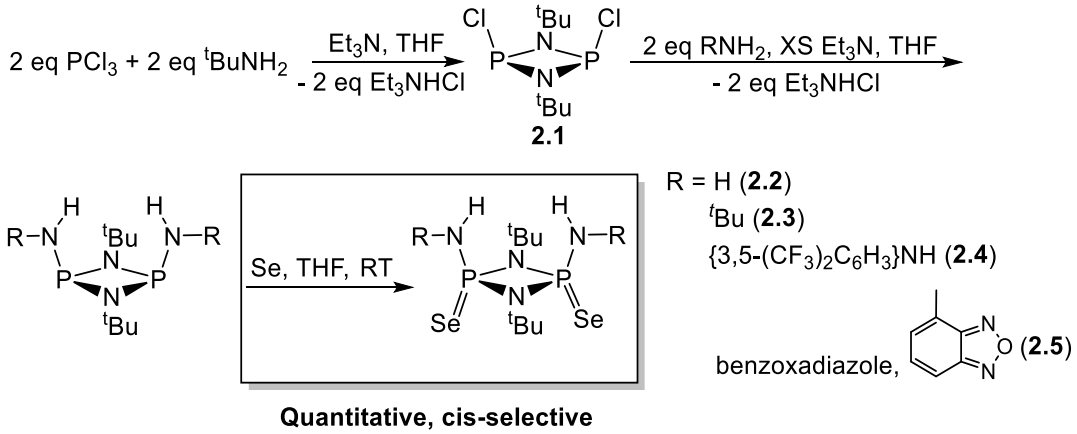

Figure 27: Synthesis of the key anion receptors in this chapter.

In contrast to **2.2** and **2.3** (Figure 27), which contain electron-donating R-groups (H and ^{t}Bu), **2.4** and its phosph(III)azane precursor [(3,5-$(CF_3)_2C_6H_3$)NHP(μ-N^{t}Bu)]$_2$ **2.6** are in fact isolated as their Et_3NHCl adducts from these reactions (**2.4**•Et_3NHCl and **2.6**•Et_3NHCl), due to the presence of the electron-withdrawing 3,5-$(CF_3)_2C_6H_3$ group and the resulting enhancement in H-bond donor ability. Free **2.6** is readily obtained by washing an Et_2O solution of **2.6**•Et_3NHCl with water.

Early on we realised that selenium oxidised phosp(V)azanes, which have not been explored previously in the context of anion binding systematically, should be particularly potent anion receptors. A direct indication of this is provided by the increase in the chemical shifts of the NH protons observed for the family of phospa(V)azane dimers cis-[^{t}BuNH(E)P(μ-N^{t}Bu)]$_2$ [E = O **2.7**, S **2.8**, Se **2.3**] (Figure 28) in their room temperature ^{1}H NMR spectra at similar concentrations in CD_3CN, being in the order **2.3** (δ = 4.00 ppm) > **2.8** (δ = 3.74 ppm) > **2.7** (δ = 3.15 ppm). Phosphazanes **2.7** and **2.8** were synthesised using the previously published procedures.[19]

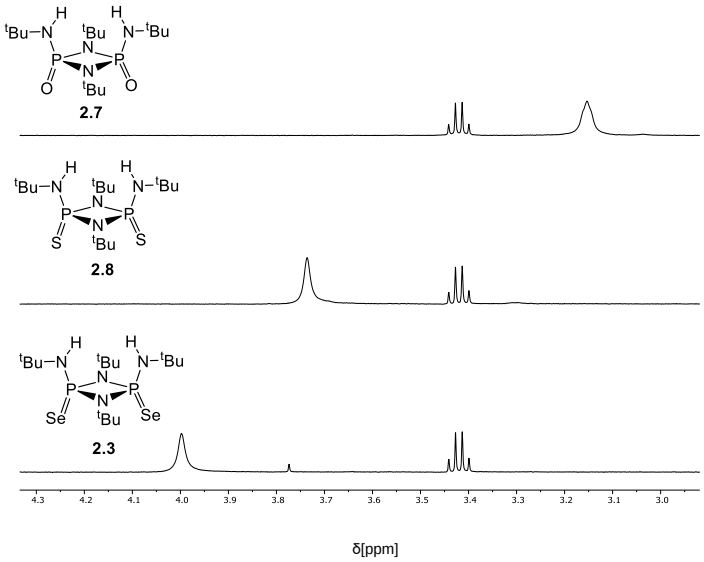

Figure 28: Overlaid ^{1}H NMR spectra (CD_3CN, 25 °C, 400 MHz) of **2.7**, **2.8** and **2.3**; residual ether at ca. 3.4 ppm.

We next measured the binding constants of cis-[^{t}BuNH(E)P(μ-N^{t}Bu)]$_2$ [E = O **2.7**, S **2.8**, Se **2.3**] (ca. 7 mM) with Cl^- in CD_3CN by titration with a standard solution of [$^{n}Bu_4N$]Cl (TBACl). Upon addition of increasing amounts of TBACl we observe gradual shifting of the NH resonance indicative of fast exchange anion binding in solution (Figure 29 shows this data for **2.3**).[77] The change in the NH resonances was monitored by ^{1}H NMR spectroscopy and could all be fitted to a 1:1 binding model using the Bindfit program suite.[78] In accordance with our initial NMR spectroscopic observations, the binding constants (K) follow the same order of **2.3** (235 ± 7 M^{-1}) > **2.8** (155 ± 3 M^{-1}) > **2.7** (18 ± 1 M^{-1}).

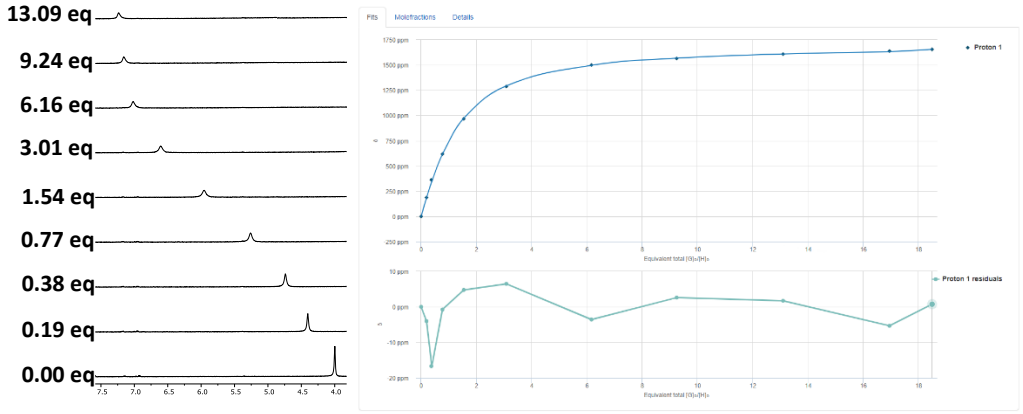

Figure 29: ^{1}H NMR titration (CD_3CN, 25 °C, 400 MHz) of **2.3** with TBACl and fit to a 1:1 binding isotherm with K = (235 ± 7 $M)^{-1}$; y-Axis in Hz (not ppm).

DFT calculations at the B3LYP-D3-BJ/def2-TZVPD level of theory were used to investigate the proton acidities and, hence, the relative anion binding properties of **2.3**, **2.7** and **2.8**. These were carried out by Patrick Pröhm at FU Berlin. A systematic decrease of the electron density at the bond critical point of the NH bonds is found moving from **2.7** (ρ = 0.3406 e/Å^3) to **2.8** (ρ = 0.3393 e/Å^3) to **2.3** (ρ = 0.3387 e/Å^3), which is in line with the observed greater acidity of the NH bonds, favorable for H-bonding. This, however, is not reflected in the charges on the N and H atoms, which remain almost the same in **2.3**, **2.7** and **2.8** (N, -1.01 e, H +0.40 e). The LUMO of **2.3**, **2.7** and **2.8** (Figure 30) is located at the position where anion binding occurs, with the main contribution to the LUMO being from the σ* CH and NH orbitals, and with the chalcogen contribution increasing going from **2.3** to **2.8** to **2.7**. The energy of the LUMO decreases going from **2.3** (-0.517 eV) to **2.8** (-0.571 eV) to **2.7** (-0.629 eV). This means that occupation of the LUMO with the electron density of a chloride anion upon binding will release more energy for **2.3** than **2.8** and **2.7**, consistent with the observed order of chloride binding constant. The lowering of the LUMO energies is a direct consequence of decreasing the HOMO-LUMO gap when moving from chemically hard to soft atoms (HOMO-LUMO gap **2.7** (5.07 eV), **2.8** (5.33 eV) and **2.3** (5.72 eV).[79]
The greater delocalisation of the chalcogen electron density moving from O to S and Se is seen in the electrostatic potential (ESP) maps (Figure 30), which show a decrease in the electron density of the chalcogen and a more homogeneous charge distribution moving from **2.7** to **2.8** and **2.3**, suggesting greater delocalisation and polarisability. A similar trend is observed for the natural charges. Here, the O-atom of **2.7** is calculated to carry a negative charge of -1.085 e, significantly higher that the S-atom of **2.8** (-0.576 e) and the Se-atom of **2.3** (-0.489 e). The calculations suggest that the selenium derivatives are in fact the most potent anion receptors on the basis of electronic factors associated with the inorganic framework.

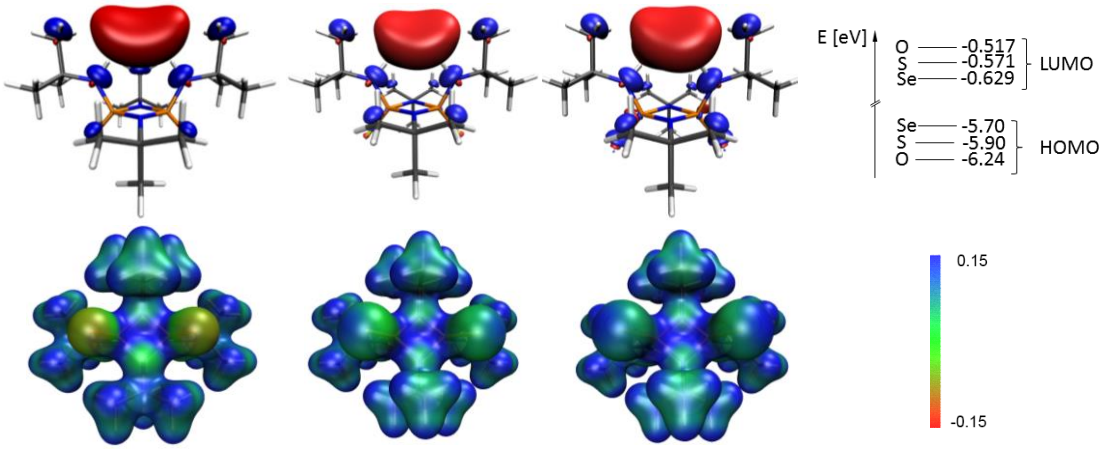

Figure 30: The LUMO (left to right) of **2.7**, **2.8** and **2.3** obtained at B3LYP-D3-BJ/def2-TZVPD level of theory.

The order of the binding constants for **2.8** (E = S) and **2.7** (E = O) is the opposite of that observed by Goldfuss and coworkers for [(3,5-$(CF_3)_2C_6H_3$)NH(O=)P(μ-N^{t}Bu)]$_2$ showing higher anion affinities than [(3,5-$(CF_3)_2C_6H_3$)NH(S=)P(μ-N^{t}Bu)]$_2$.[73] Intrigued by this difference, we determined the binding constant for the Se-receptor **2.4** using UV-Visible titration of a 1.5*10^{-5} M solution in CH_3CN with a standard solution of TBACl at 25 °C.Again, we were able to fit the change in the UV-Vis spectral data to a 1:1 binding isotherm with logK = 5.74 ± 0.05. This value can be compared to the previously reported value of logK for the O-receptor [(3,5-$(CF_3)_2C_6H_3$)NH(O=)P(μ-N^{t}Bu)]$_2$ of 5.43 ± 0.02. The value of logK reported for the S-receptor is 5.17 ± 0.02. On this basis, the binding constants for Cl^- in acetonitrile follow the order **2.4** > [(3,5-$(CF_3)_2C_6H_3$)NH(O=)P(μ-N^{t}Bu)]$_2$ > [(3,5-$(CF_3)_2C_6H_3$)NH(S=)P(μ-N^{t}Bu)]$_2$. The significant point being that the Se-receptor has a binding constant that is at least as high if not higher than the O-receptor. A possible explanation for the different behaviour observed for **2.3**, **2.7** and **2.8** [**2.8** (Se) > **2.7** (S) > **2.3** (O)] is that the effect of the chalcogen (O, S or Se) on the framework bonding and the polarity of the NH groups is offset in [(3,5-$(CF_3)_2C_6H_3$)NH(O=)P(μ-N^{t}Bu)]$_2$ by the preorganisation due to ortho-C-H•••O=P interactions (see Figure 26).

Next, we investigated how backbone modification other than change of the chalcogen affects the anion binding properties of phosphazanes. Comparison of the single crystal X-ray structures of **2.4**•Et_3NHCl and **2.6**•Et_3NHCl (Figure 31) provides the opportunity to explore how backbone modification by oxidation of the P atoms alters the Cl^- binding

properties of phosphazane anion receptors. Most importantly, oxidation of the P(III) centres of **2.6** results in significant shortening of the N-H•••Cl H-bonds in the P(V) adduct **2.4**•Et_3NHCl by ca. 0.17 Å (from N•••Cl av. 3.38 Å in **2.6**•Et_3NHCl to av. 3.21 Å in **2.4**•Et_3NHCl), signifying the greater H-bond donor properties of the receptor **2.4** upon selenium oxidation. The increased Cl-receptor interaction is accommodated by the reorientation of the 3,5-$(CF_3)_2C_6H_3$ units, which are mutually coplanar and perpendicular to the P_2N_2 mean plane in **2.6**•Et_3NHCl but tilted significantly from perpendicular in **2.4**•Et_3NHCl (by av. 52 °) (Figure 31). This change allows the closer engagement of the Et_3NHCl guest (in particular the ammonium cation) with the receptor pocket of **2.4**, but has the effect of reducing the potential for any stabilising ortho-C-H•••Se interactions with the 3,5-$(CF_3)_2C_6H_3$ groups. Such interactions have been proposed previously to be crucial to the exo-exo conformation of the NH groups in the closely related O- and S-receptors.[71,73] However, these interactions are at best weak in **2.4**•Et_3NHCl (2.87-2.93 Å, cf. 3.10 Å for the sum of van der Waals radii of Se and H), and the analysis of the structures of **2.4**•Et_3NHCl and **2.6**•Et_3NHCl strongly suggests that steric factors are more important in dictating the orientation of the 3,5-$(CF_3)_2C_6H_3$ groups in the Se receptors.[80]

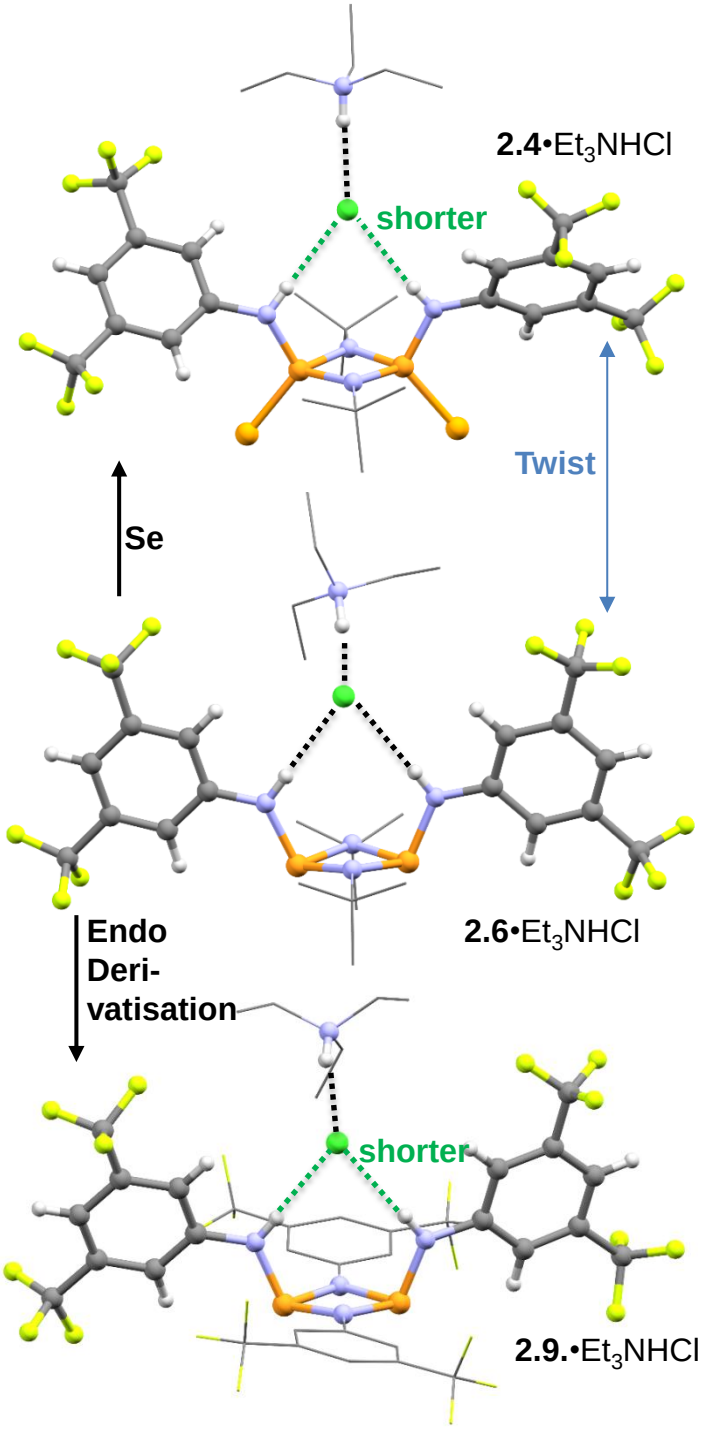

Figure 31: Comparison of the structural effects of oxidation of the P(III) centres **2.6** by Se in **2.4** and substitution of the P_2N_2-bridging ^{t}BuN-groups in **2.9** by $(CF_3)_2C_6H_3N$-groups on the 1:1 H-bond adducts with Et_3NHCl. Selected bond length [Å] and angles [°]: **2.6**•Et_3NHCl, N_{endo}-P av. 1.71, N_{exo}-P av 1.70, (receptor)N···Cl av. 3.38, $Et_3N(H)$···Cl 3.04, N_{exo}-P-N_{endo} av. 102.8, P-N-P av. 97.9; **2.4**•Et_3NHCl, N_{endo}-P av. 1.68, N_{exo}-P av. 1.65, P-Se av. 2.08, (receptor)N···Cl av. 3.21, $Et_3N(H)$···Cl 3.07, N_{exo}-P-N_{endo} av. 107.2, P-N-P av. 96.4, N_{endo}-P-Se av. 113.6; **2.9**•Et_3NHCl, N_{endo}-P av. 1.73, N_{exo}-P av. 1.67, (receptor)N···Cl av. 3.23, $Et_3N(H)$···Cl 3.05 N_{exo}-P-N_{endo} av. 104.5, P-N-P av. 101.2. Colour code, orange = Se, blue = N, green = Cl, yellow = F.

Similar receptor enhancement to selenium oxidation is also caused by replacing the endocyclic, electron-rich ^{t}Bu substituents by electron withdrawing 3,5-$(CF_3)_2C_6H_3$ substituents, in the solid-state structure of the 1:1 adduct of the phosh(III)azane [3,5-$(CF_3)_2C_6H_3$NHP(μ-N-3,5-$(CF_3)_2C_6H_3$)]$_2$ with Et_3NHCl **2.9**•Et_3NHCl, which was obtained by the 2:1 reaction of $(CF_3)_2C_6H_3NH_2$ with PCl_3 in Et_3N/THF. The result of the incorporation of this electron-withdrawing group within the P_2N_2 ring unit is the shortening of the NH•••Cl H-bonds by ca. 0.15 Å compared to those in **2.6**•Et_3NHCl, i.e., of a similar magnitude to the effect of Se-oxidation of **2.4**. Interestingly, no tilting of the exocyclic 3,5-$(CF_3)_2C_6H_3$ substituents of **2.9** is observed, presumably because the lower steric demands of the 3,5-$(CF_3)_2C_6H_3$ groups compared to the ^{t}Bu substituents in **2.4**•Et_3NHCl. Therefore, close approach of the Et_3NHCl guest can occur without significant distortion of the receptor ligand in this case.

The effects of H-bonding in **2.4**•Et_3NHCl and **2.6**•Et_3NHCl are also observed in their solution ^{1}H NMR spectra in $CDCl_3$ at room temperature. The strengthening of the phosphazane-chloride interactions causes deshielding of the phosphazane NH proton from δ = 7.13 ppm in **2.6**•Et_3NHCl to 8.80 ppm in **2.4**•Et_3NHCl and the concurrent weakening of the $Et_3NH^+\cdots Cl^-$ interactions, resulting in shielding of the ammonium NH resonances from δ = 11.85 ppm in **2.6**•Et_3NHCl to 10.98 ppm in **2.4**•Et_3NHCl. Therefore, oxidation can be seen to amplify the receptor properties of phosphazanes not only in the solid state but also in solution.

The Effect of Metal-Coordination and Charge on Anion Binding

One aspect of the receptor chemistry of phosph(III/V)azanes that has so far been ignored is the potential effect of metal coordination of the receptors on anion binding. Consequently, of the presence of soft donor atoms like P and Se in phosphazane receptors of this type, there is an intrinsic potential for receptor modulation via metal coordination. Only a few studies of this effect have been explored with conceptually similar organic receptors.[81–84] Since phosphazanes have been identified as potent class of ligands for transition metals over the last decades, we set out to investigate the relation between their ligand and supramolecular properties.[15]

An initial indication of cooperative anion and cation coordination was provided by the formation and solid-state structure of the complex $[(NH_2)(Se)P(\mu\text{-}N^{t}Bu)]_2$•CuCl•THF **2.10**, obtained from the reaction of **2.2** with CuCl in THF. The single crystal X-ray

structure shows a polymeric arrangement in which intact CuCl monomers are coordinated side-on by the Se and NH_2 groups of **2.2**, with the retention of CuCl bonding (Figure 32). In addition, **2.10** also employs its NH functionality in a bifurcated H-bonded interaction with a THF molecule. A similar coordination polymer is formed in the reaction of **2.9** with (DMS)AuCl, giving the AuCl complex **2.11** in low crystalline yield (Figure 32). The single crystal X-ray structure shows a polymeric arrangement in which each of the AuCl monomer units is coordinated by the P-atom of a molecule of **2.9** and the NH proton of a neighboring phosphazane. The polymeric arrangement is further reinforced by Au•••Au interactions [3.3817(4) Å] between adjacent AuCl monomers, which are at the upper end of aurophilic interactions previously reported.[85] The isomerisation of **2.9** to the trans-isomer in this case, has been reported previously for other cyclophosphazanes, although the low yield of **2.11** could indicate the polymer is formed from trans impurities in **2.9**.[14,86] The CuCl and AuCl coordination polymers **2.10** and **2.11** highlight the potential of phosphazanes to coordinate to ion pairs, a field that has also recently been the focus of synthetically elaborate organic systems.[87]

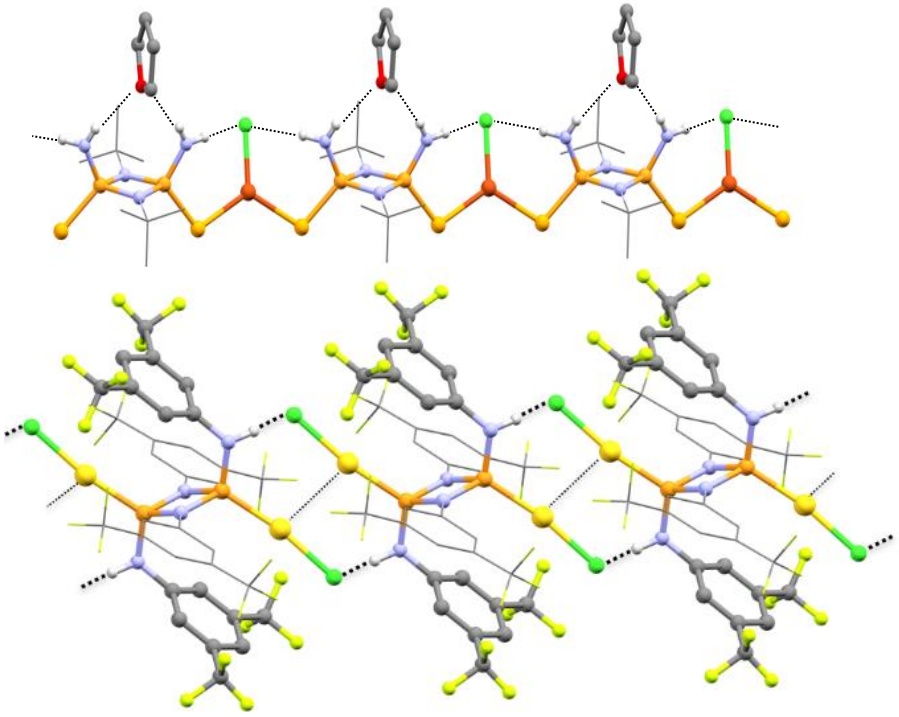

Figure 32: Molecular structures of top: **2.10** and bottom: **2.11**. H-atoms, except those involved in the H-bonding interactions, have been omitted for clarity. Selected bond length [Å] and angles [°]: **2.10**, N_{endo}-P av. 1.68, N_{exo}-P av. 1.61, P-Se av. 2.13, Se-Cu av. 2.35, N···Cl 3.18, N_{exo}-P-N_{endo} av. 112.0, P-N-P av. 96.2, N_{endo}-P-Se av. 118.1; **2.11**, N_{endo}-P av. 1.70, N_{exo}-P av. 1.65, P-Au av. 2.20, N···Cl 3.25, N_{exo}-P-N_{endo} av. 108.6, P-N-P av. 98.5, N_{endo}-P-Au av. 118.5. Colour code: orange = P, yellow = Au, blue = N, green = Cl, bright green = F, bright orange = Se, dark orange = Cu, red = O.

With these prototypes in mind, we next explored the effects of metal coordination by the P-atoms of the phosph(III)azane **2.6** on Cl^- binding. The 2:1 stoichiometric reaction of $(Me_2S)AuCl$ with the Et_3HNCl complex **2.6**•Et_3NHCl in DCM gives the crystalline complex **2.12**•Et_3NHCl in 68% yield after workup (Figure 33).

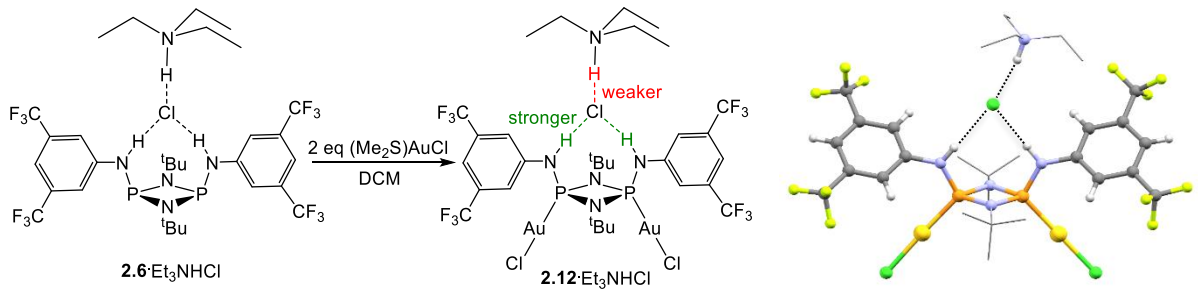

Figure 33: Left: Coordination of **2.6**•Et_3NHCl with AuCl to give complex **2.12**•Et_3NHCl. Right: Molecular structure of **2.12**•Et_3NHCl. H-atoms, except those involved in the H-bonding interactions, have been omitted for clarity. Selected bond length [Å] and angles [°]: **2.12**: N_{endo}-P av. 1.68, N_{exo}-P av. 1.64, P-Au av. 2.20, (receptor)N···Cl av. 3.19 $Et_3N(H)$···Cl 3.16, N_{exo}-P-N_{endo} av. 108.6, P-N-P av. 97.1, N_{endo}-P-Au av. 120.3. Colour code: orange = P, yellow = Au, blue = N, green = Cl, bright green = F.

The upfield shift of the room temperature ^{31}P NMR resonance from δ = 108.2 ppm in **2.6**•Et_3NHCl to 82.0 ppm in **2.12**•Et_3NHCl (in $CDCl_3$) indicates a significant increase in positive charge at the P atoms, consistent with transfer of electron density to Au(I). This results in an increase in the polarity of the NH bonds, with a large downfield shift found for these protons from δ = 7.13 to 9.38 ppm in the corresponding ^1H NMR spectra, indicating strengthening of the NH•••Cl interactions. The increase in the H-bond donor properties of the phosphazane **2.6** on coordination to Au(I) in **2.12**, anticipated on the basis of the NMR spectroscopic data, is seen in the solid-state structure of **2.12**•Et_3NHCl (Figure 33), in which there is a large increase in the Et_3N-H•••Cl distances (by ca. 0.12 Å with respect to the N•••Cl contact) and a large decrease in the N-H•••phosphazane H-bonding interactions (by ca. 0.19 Å with respect to the N•••Cl contact) moving from **2.6**•Et_3NHCl to **2.12**•Et_3NHCl. The extent of the strengthening of the H-bonding resulting from coordination of Au(I) is at least on par with the effect of Se-oxidation seen in **2.4**•Et_3NHCl (Figure 31), on the basis of a comparison of their solid-state structures. However, the ^1H NMR spectrum (Figure 34) of **2.12**•Et_3NHCl in solution actually suggests that coordination of the P-atoms amplifies the binding properties to a greater extent than Se-oxidation, with the NH proton resonance for **2.12**•Et_3NHCl (δ = 9.38 ppm) being significantly downfield of that

for **2.4**•Et_3NHCl (δ = 8.80 ppm) (accompanied by a large reduction of ca. 0.90 ppm in the Et_3NH NH resonance).

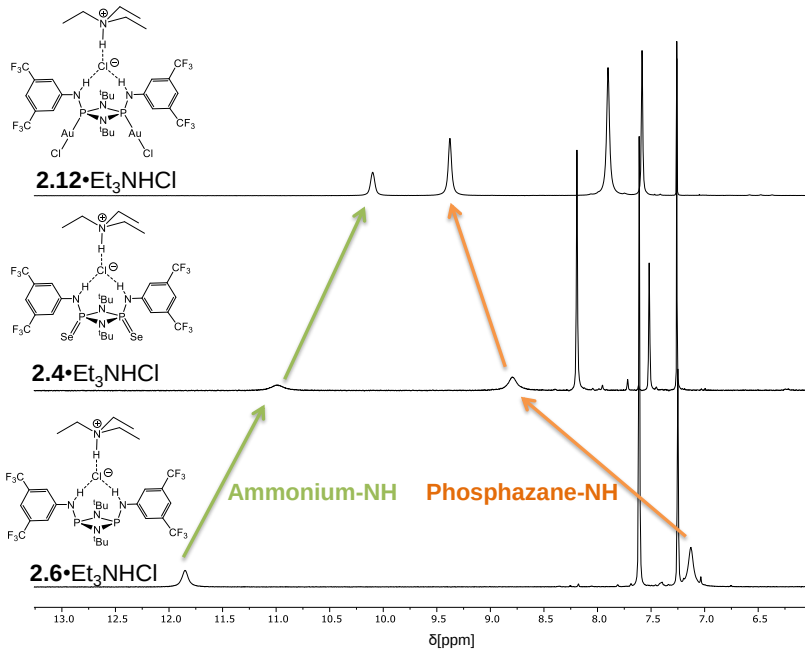

Figure 34: Overlaid ^1H NMR spectra ($CDCl_3$, 25 °C, 400 MHz) of **2.6**•Et_3NHCl, **2.4**•Et_3NHCl and **2.12**•Et_3NHCl.

Metal coordination by the Se-atoms of the Se-phosph(V)azane [^{t}BuNH(Se)P(μ-N^{t}Bu)]$_2$ **2.3** is also found to have a profound effect on the polarisation of the NH protons and its ability to H-bond to anions. The reactions of **2.3** with [(Ph_3P)Cu(CH_3CN)$_3$](BF_4) and [(Ph_3P)$_2$Pd(CH_3CN)$_2$](BF_4)$_2$ in DCM give the complexes [(Ph_3P)Cu(**2.3**)BF_4] **2.13** and [(Ph_3P)$_2$Pd(**2.3**)BF_4][BF_4] **2.14**, respectively, which were isolated in high crystalline yield after workup (74% for **2.13**, 95% for **2.14**). The solid-state structures of **2.13** and **2.14** (Figure 35) reveal the expected chelation of the Cu(I) and Pd(II) centres by the Se atoms of **2.3**, with a BF_4^- anion being chelated on the other side or the molecules by two NH•••F H-bonds. It should be noted in this respect, that there is some uncertainty concerning the precise coordination mode in both cases due to the extensive disorder of the BF_4^- anions. However, the NH•••F interactions involved are well within the sum of the van der Waals radii of h and F (ca 2.0 Å for **2.13** and **2.14** vs Σ_{cdW} = 2.5 Å).[80]

A measure of the effect of metal coordination on the polarisation of the NH protons of **2.3** is provided by the chemical shifts of the NH protons in the room temperature ^1H NMR spectra of **2.3** (in presence of 2 eq $TBABF_4$), **2.13** (in presence of 1 eq $TBABF_4$)

and **2.14**, with a large increase in the chemical shift in CD_2Cl_2 being observed moving from **2.3** (δ = 3.2 ppm), to **2.13** (δ = 5.3 ppm), to **2.14** (δ = 5.6 ppm), indicating that the increase in the polarisation of the phosphazane framework results in strengthening of the NH•••F interactions (in the same way as for **2.6**).

Whereas the room temperature ^{19}F NMR spectrum of a solution of 2 equivalents of $TBABF_4$ and **2.3** in CD_2Cl_2 shows only a negligible shift from that of $TBABF_4$ in CD_2Cl_2 (δ < 0.1 ppm), suggesting only weak H-bonding of BF_4^- to **2.3**, the ^{19}F NMR spectra of **2.13** and **2.14** in CD_2Cl_2 show significantly larger shifts of Δδ = 0.6 and 1.66 ppm, respectively, compared to free $TBABF_4$. The observed ^{19}F NMR shifts in **2.13** and **2.14** not only indicate that BF_4^- is H-bonded to the receptor in both, but also that metal coordination actually switches on anion coordination ability. This is probably largely due to the polarisation effect of metal coordination on the inorganic framework of **2.3**, which will increase with the charge on the metal, the net charge of the complex and the greater involvement of metal d-orbitals in bonding; hence the highest affinity for BF_4^- is found in the cation of the Pd(II) complex **2.14** in which the shortest H-bonding contacts to the BF_4^- anion are observed in the solid state. However, closer inspection of the solid-state structures of **2.13** and **2.14** indicates that the coordination of the Se-atoms to Cu(I) and Pd(II) has an additional geometric effect, resulting in buckling of the essentially planar P_2N_2 ring unit of **2.3**, with an associated increase in the bite of the $(NH)_2$ H-bond receptor site. The increase in the bite (**2.14** > **2.13** > **2.3**) can be traced directly to the metal geometry, with the trigonal planar geometry of Cu(I) in **2.13** (with Se-Cu-Se ca. 120 °) causing less distortion than the square-planar geometry of Pd(II) in **2.14** (with Se-Pd-Se ca. 103 °) (Figure 35). The flexibility of the phosphazane backbone therefore allows adaptation of the receptors upon metal coordination and hence activation for larger anions. This ability to adapt upon metal coordination is in stark contrast to the geometrically rigid squaramide and urea anion receptors.

In order to quantify the extent to which anion binding is enhanced in solution we carried out ^1H NMR titrations. We chose nitrate as the target anion since we reasoned that its relative chemical hardness would leave the Se-Palladium bonds intact. Addition of increasing amounts of $TBANO_3$ in $CDCl_3$ to **2.13** or **2.3** (in presence of 2 eq $TBABF_4$) results in gradual downfield shifting of the NH resonance indicative of fast exchange binding of nitrate. In both cases the binding equilibrium could be described with a 1:1 binding model with K = (661.3±51.6) M^{-1} for **2.14** and K = (6.6±0.2) M^{-1} for **2.3**; the copper(I) complex **2.13** is not stable in the presence of excess $TBANO_3$.

Taken together our observations show that palladium(II) coordination increases the receptor potential of selenophosphazanes in solution which can be partially attributed to the net positive charge of the receptor in addition to the above-mentioned backbone distortion.

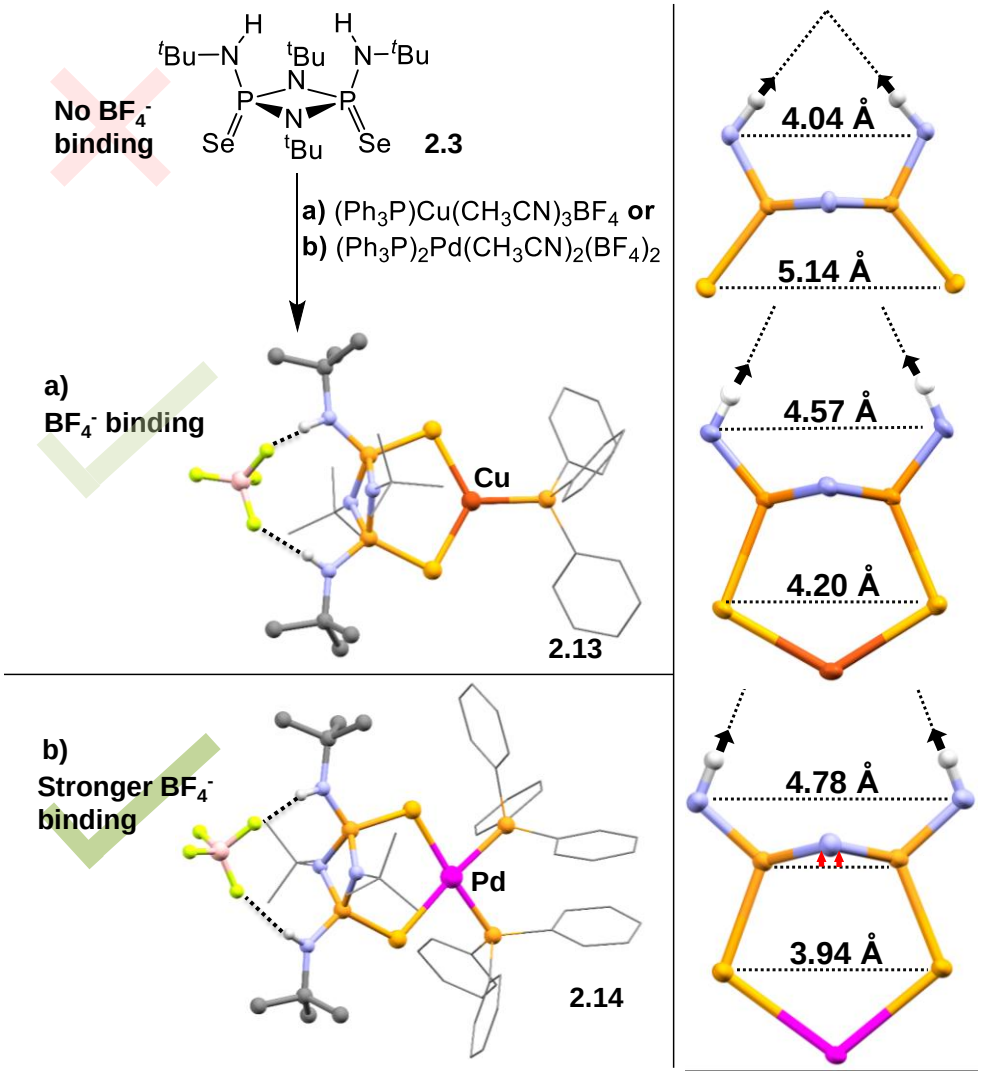

Figure 35: Left: Molecular structures of (a) **2.13** and (b) the cation of **2.14**. Disorder of the BF_4^- ions and H-atoms, except those involved in the H-bonding interactions, and DCM in the lattice of **2.14** have been omitted for clarity. Selected bond length [Å] and angles [°]: **2.13**: N_{endo}-P av. 1.68, N_{exo}-P av. 1.61, P-Se av. 2.14, av. 2.94, Se-Cu av. 2.40, P-Cu av. 2.24, N_{exo}-P-N_{endo} av. 114.4 P-N-P av 94.5 Se-Cu-Se; **2.14**: 122.1 P-Pd-P av. 118.8; N_{endo}-P av. 1.68, N_{exo}-P av. 1.61, P-Se av. 2.20, N···F (shortest) av. 2.94, Se-Pd av. 2.52, P-Pd av. 2.34, N_{exo}-P-N_{endo} av. 112.5, P-N-P av. 92.8, Se-Pd-Se av. 102.9, P-Pd-P av. 92.3. Colour code: orange = P, brown = Cu, purple = Pd, blue = N, pink = B, bright green = F, white = H. Right: Distortion of the P_2N_2 ring units of **2.3** (top, structural data from reference [76]) caused by metal coordination in **2.13** (middle) and **2.14**.

Addition of more coordinating anions such as chloride in the form of TBACl results in displacement of the palladium fragment as $(Ph_3P)_2PdCl_2$, which was shown via in situ

^{31}P NMR spectroscopy. Importantly, this results in release of the tetrafluoroborate anion as the activating effect of the complex fragment is reversed. The ^{19}F NMR spectrum after chloride addition shows free BF_4^- which is not shifted relative to a $TBABF_4$ reference solution. In a similar way, reduction of the Cl^- complex of $[(Se=)(^tBuNH)P(\mu\text{-}N^tBu)]_2$ **2.3** with excess $^tBu_3P$, giving the $[(^tBuNH)P(\mu\text{-}N^tBu)]_2$, also results in release of the H-bonded anion since $[(^tBuNH)P(\mu\text{-}N^tBu)]_2$ does not interact with Cl^- strongly.

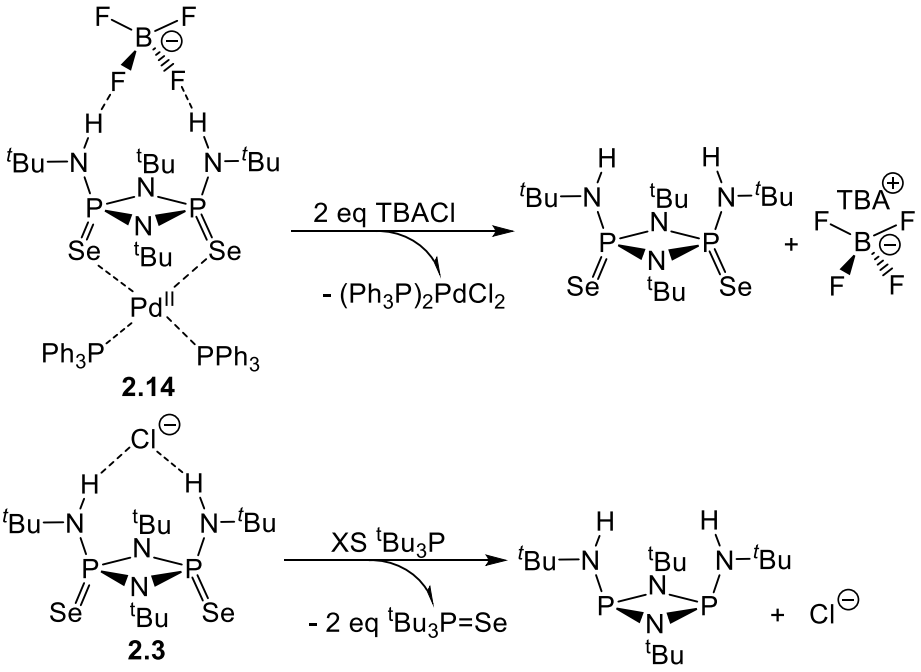

Figure 36: Top: Chloride triggered BF_4^- release using **2.14**. Bottom: $^tBu_3P$ triggered chloride release using **2.3**.

Encouraged by the potential charge induced binding enhancement found in the Pd complex **2.14**, we suspected that phosphonium derivatives of diaminophosphazanes could be particularly potent anion receptors. In order to investigate this we synthesised $[^tBuNH(Se=)P(\mu\text{-}N^tBu)_2P(Me)HN^tBu]BAr^F$ **2.15** (BAr^F = $[(3,5\text{-}CF_3)_2C_6H_3]_4B]^-$) in four synthetic steps using an improved synthetic protocol to that reported earlier by Balakrishna et al. for the iodide complex (Figure **37**).[88] We chose BAr^F as the counteranion to avoid anion coordination of the counteranion and to improve solubility in organic solvents. **2.15** is stable under benchtop conditions for at least 6 months and does not require the use of dried solvents. Importantly, the ^{1}H NMR spectrum of **2.15** in $CDCl_3$ shows

that both of the NH protons display similar shifts (δ(Se=PNH) = 3.43 ppm, δ(Me-PNH) = 3.30 ppm) from which we conclude that methylation of the phosphorus(III) centre results in comparable acidification of the NH proton to Se oxidation of the P(III) centres. The solid-structure of **2.15** reveals that the phosphazane adopts an endo-exo conformation regarding the exocyclic amine substituents (

Figure **37**). This is in contrast to the iodide salt reported by Balakrishna et al. which adopts an exo-exo conformation in order to bind to the iodide counteranion.

Addition of increasing amounts of $TBABF_4$ in $CDCl_3$ solution results in gradual downfield shifting of both NH resonances. Interestingly this process could be most accurately modelled using at non-cooperative 2:1 receptor:anion binding model with K = (6112.9±525.7) M^{-1}. Employing a 1:1 binding model produced an associated error of 158.1% (vs 2:1 model 8.6%). The ^{19}F NMR spectrum of a 1:1 mixture of **2.15** and $TBABF_4$ in $CDCl_3$ also indicates that BF_4^- is bound in solution, with Δδ = 1.60 ppm (compared to free BF_4). As mentioned above, [(Se=)(^{t}BuNH)P(μ-N^{t}Bu)]$_2$ **2.3** does not bind BF_4 in $CDCl_3$. We conclude that **2.15** is a better receptor on the basis of coulombic attraction between the cationic receptor and the BF_4^- anion. Although we also observe strong interaction between **2.15** and nitrate, ^1H NMR titration of **2.15** with $TBANO_3$ in $CDCl_3$ revealed that more than one binding process occurs which prevented quantitative analysis of the process.

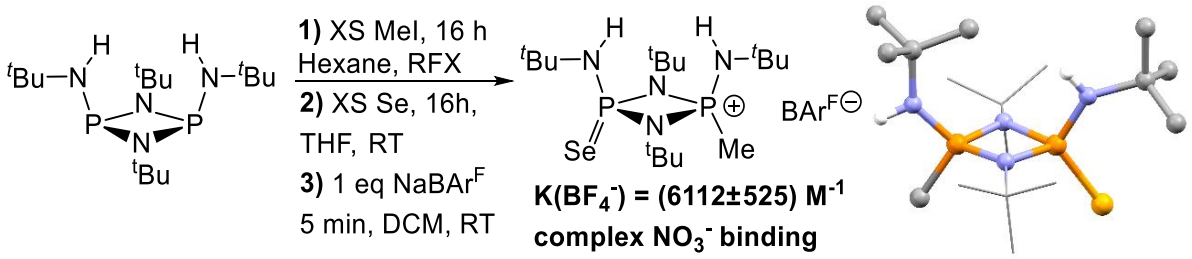

Figure 37: Left: Synthesis and binding behaviour of **2.15**. Right: solid-state structure of **2.15**; non-NH hydrogens and counteranion omitted for clarity. Quality of the dataset prevents detailed structural discussion. Colour code: orange = P , bright orange = Se, blue = N, grey = C, white = H.

Applications as Colourometric Reagents and in Anion Transport

We next looked at how the effects of anion binding might be used for anion sensing and the transport of anions through phospholipid bilayers. Although the P_2N_2 ring unit of $[^tBuNH(O)P(\mu\text{-}N^tBu)]_2$ **2.7** remains intact upon coordination of Cl^-, previous in situ ^1H and ^{31}P NMR spectroscopic studies showed that the P_2N_2 ring unit does not survive in the presence of F^-, presumably due to nucleophilic attack of the P-atoms and ring opening.[71] We wondered whether this effect could be harnessed as a means of sensing F^- anions. For this purpose, Se-phosphazane **2.5** (Figure 27), containing chromophoric benzoxadiazole groups, was chosen as a candidate for investigation. In accord with the previous report, addition of excess TBAX containing less nucleophilic halides X = Cl^-, Br^-, I^- to solutions of **2.5** in MeCN does not result in any significant colour change. However, addition of excess TBAF gives an immediate red colour change (Figure 38), so that **2.5** functions as a colourometric reagent for F^-.

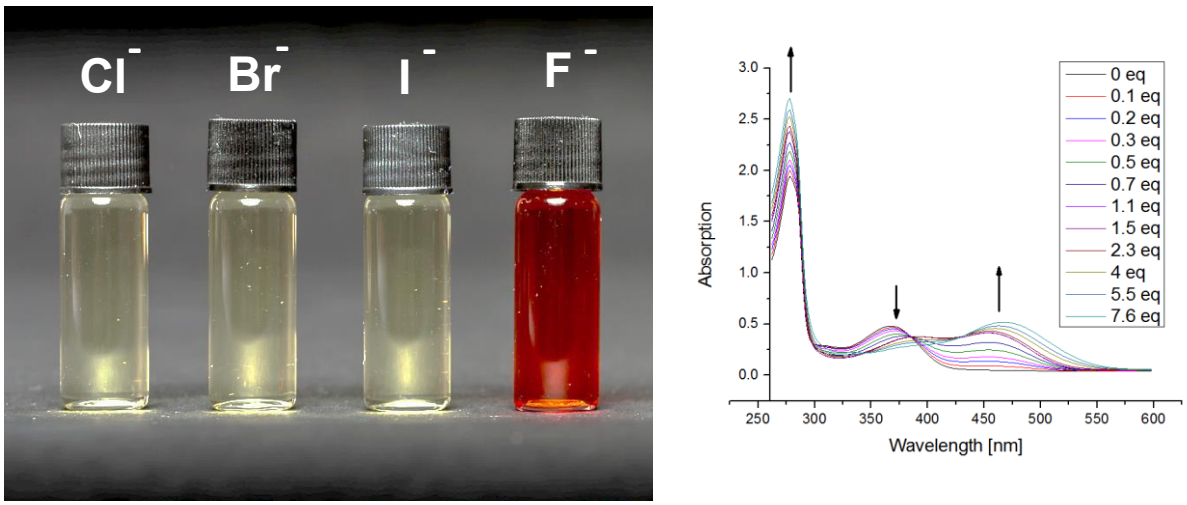

Figure 38: Left: observed effect of the addition of excess TBAX (X = F, Cl, Br, I) to MeCN solutions of **2.5**; Right: UV-VIS titration of a 27.5 µM solution of **2.5** in CH_3CN with TBAF.

The titration of TBAF into a MeCN solution of **2.5** was monitored by UV-Vis spectroscopy (Figure 38). Addition of 0.1-0.3 eq of TBAF results in a similar change in the UV-Vis spectrum as observed for titration with TBACl, including the observation of an isosbestic point which indicates the initial binding of F^- to intact **2.5**. Addition of further TBAF results in the eventual transition to a completely new species. Initial H-bonding followed by further reactivity has been also observed by Fabbrizzi et al. for the deprotonation of ureas by fluoride.[89] In situ ^{31}P NMR spectroscopy in CD_3CN also

supports the conclusion that **2.5** reacts with F^- at higher concentration, with the chemical shift changing by ca. 15 ppm on addition of 10 equivalents of TBAF (Figure 39). The single product formed contains one ^{31}P environment with isotopic coupling to a single ^{77}Se atom (and no ^{31}P-^{19}F coupling), indicating breakdown of the P_2N_2 ring of **2.5** into a mononuclear phosphorus species.

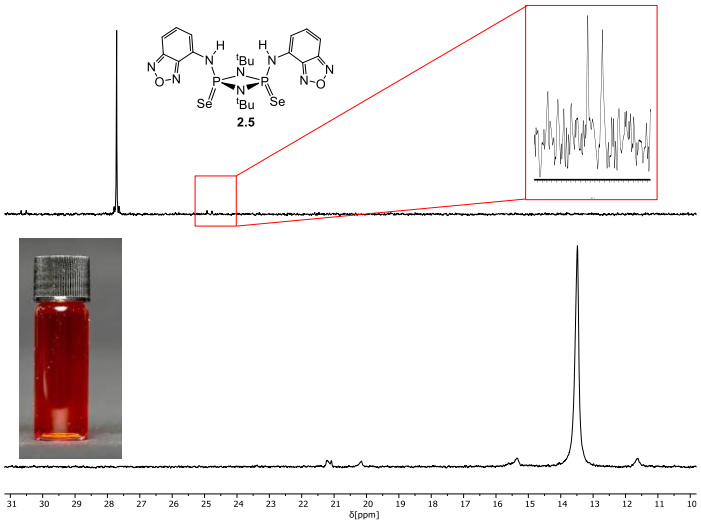

Figure 39: Overlaid ^{31}P NMR spectra (CD_3CN, 25 °C, 202 MHz) of **2.5** before and after addition of excess TBAF.

The fact that the phosphazane receptors can strongly bind Cl^- and are also soluble in a range of organic solvents (owing to the presence of apolar organic substituents) suggested that they may be of value as synthetic anion transporters through lipid bilayers, an area extensively investigated with organic receptors.[90] This area of research has been widely ignored as main group systems are rarely robust enough under the aqueous conditions used in membrane-transport experiments. Since all the receptors **2.3**, **2.4**, **2.7** and **2.8** are stable under benchtop condition we chose to investigate their activity as synthetic anion transporters. The closest work to the transporter ability of phosphazanes reported here is the investigation of the phosphoric triamide receptors $(E=)P(NHAr)_3$ (E = O, S; Ar = 3,5-$(CF_3)_2C_6H_3$) by Gale and coworkers.[68] The following transport study were carried out in collaboration with Dr. Jinbo Zhu and Prof. Ulrich Keyzer (Cambridge).

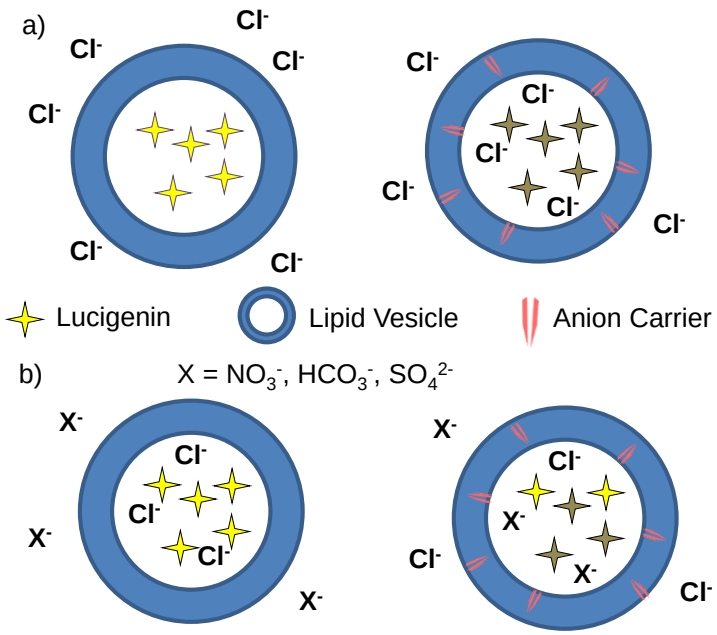

Figure 40: Schematics of (a) the lucigenin assay (POPC-LUVs⊃LU) used to assess anion carrier ability into a LUV, (b) the lucigenin assay exchange of Cl^- (inside) and other anions (X^- = NO_3^-, HCO_3^{2-}, SO_4^{2-}) outside the LUV.

Ion transport was assessed using lucigenin (LU, chloride-sensitive fluorescent dye) or 8-hydroxypyrene-1,3,6-trisulfonic acid (HPTS, pH sensitive fluorescent dye) encapsulated large unilamellar vesicles (LUVs) composed by 2-oleoyl-1-palmitoyl-sn-glycero-3-phosphocholine (POPC). The lucigenin assay (POPC-LUV⊃LU) was used to assess Cl^- transport (Figure 40a) and Cl^-/X^- exchange (Figure 40b) into and out of the LUVs, mediated by the phosph(V)azane anion carriers.[91,92] The HPTS assay (POPC-LUV⊃HPTS) was used to assess the ion transport activity and selectivity of cation and anion transport through the membrane.[93,94] All of the experiments were performed in aqueous media. For essay details see experimental section.

From Figure 41 it can be concluded that the Se- phosph(V)azane **2.4** (containing electron-withdrawing 3,5-$(CF_3)_2C_6H_3$ groups) is a better Cl^- anion carrier than **2.3** (containing electron-donating ^{t}BuNH substituents). The fluorescence of the encapsulate dye is quenched by chloride and hence greater quenching indicates a higher chloride concentration. The anion transport behaviour can at least in part be explained by the relative anion binding properties, with the values of LogK being in the same order as the observed Cl^- carrier ability (**2.4** > **2.3**). However, fluorination of synthetic anion transporters has also been previously reported to increase transport

activity.[95] Fluorination results in greater lipophilicity and better integration of the transporter into the lipid bilayer.

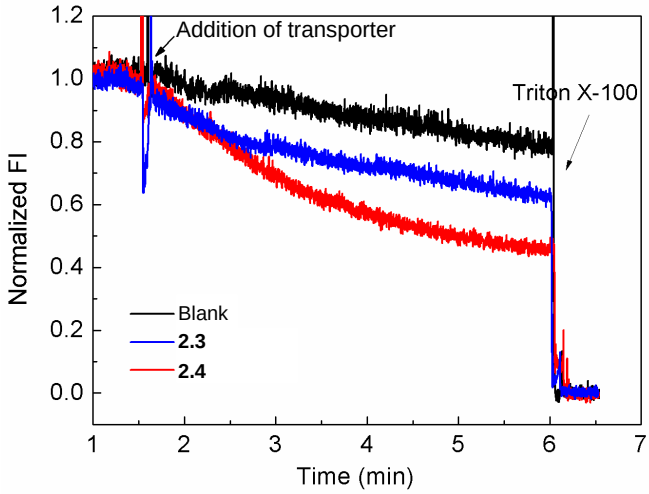

Figure 41: Chloride influx into POPC-LUVs⊃lucigenin mediated by different carriers added at 1.5 min with the same concentration (200 nm). FI = Fluorescence intensity. Triton X-100 = lysing agent. 10 µL of acetonitrile was added as the blank control. 1 mM lucigenin was encapsulated in the LUVs and 20 mM NaCl was in the extravesicular buffer solution.

In order to allow more accurate comparison of the most active phosphazane receptor **2.4** with organic counterparts, we determined the EC50 values (the concentration of transporter needed for 50% chloride efflux in 270 s) of **2.4** and the corresponding thiourea and squareamide containing 3,5-$(CF_3)_2C_6H_3$ substituents (Figure 42) using HPTS assay. Thiourea $[3,5\text{-}(CF_3)_2C_6H_3NH]_2C{=}S$ **2.16** and Squaramide $[3,5\text{-}(CF_3)_2C_6H_3NH]_2C_4O_2$ **2.17** were synthesised using literature protocols.[96] The Se-phosph(V)azane **2.4** has very similar activity to the thiourea, with the squaramide being the most active (**2.4** EC50 = 8.56 nm, **2.16** = 8.02 nm, **2.17** = 0.35 nm), in line with previous reports. Only a limited number of topologically simple anion transporters with competitive EC50 values to those of thioureas and squaramides have been reported previously.[97]

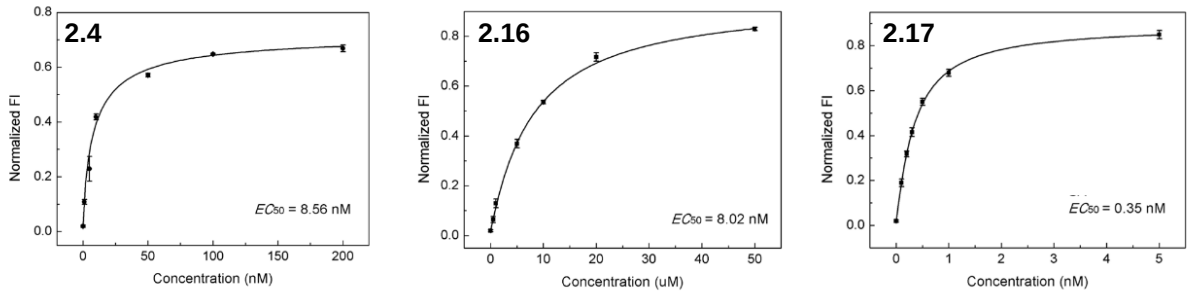

Figure 42: Change of the normalised fluorescence intensity of HPTS at 6 min as a function of carrier molecule concentrations across POPC-LUVs⊃HPTS. The data was collected from three repeated measurements. EC50 value for each carrier molecule gained from the Hill plot was given in the figure.

Since we had shown that the phosphazanes can mutually coordinate to cation-anion pairs, the question arised whether the transport mechanism across the membrane involves cation-anion symport or anion-anion antiport. Since anion transport into the LUV causes a build-up of negative charge inside the vesicle, this has to be counterbalanced by either simultaneous transport of a cation inside the vesicle or transport of an anion of the buffer solution inside the vesicle outside.

We employed an HPTS assay to investigate cation dependency. The POPC-LUVs⊃HPTS assay shows that changing the cation from Li^+ to Cs^+ has little effect on **2.4** assisted transport of H^+ or OH^- through the membrane (Figure 43), so that a symport mechanism is therefore unlikely. By following the fluorescence intensity of vesicles containing Cl^- upon addition of different anions outside the vesicle (Figure 43), transport of Cl^- anions outside the vesicle can clearly be observed upon NO_3^- addition. However, addition of SO_4^{2-} resulted in no fluorescence change and addition of HCO_3^- in only a minor change. The selectivity for nitrate and chloride over sulphate was confirmed in a separate HPTS assay (Figure 43). Such clear anion dependence is a strong indication of an anion-anion antiport mechanism and is similar to the transport mechanism observed for thioureas, squareamides and (E=)P(NHAr)$_3$ [E = O, S; Ar = 3,5-(CF$_3$)$_2$C$_6$H$_3$].[68,96]

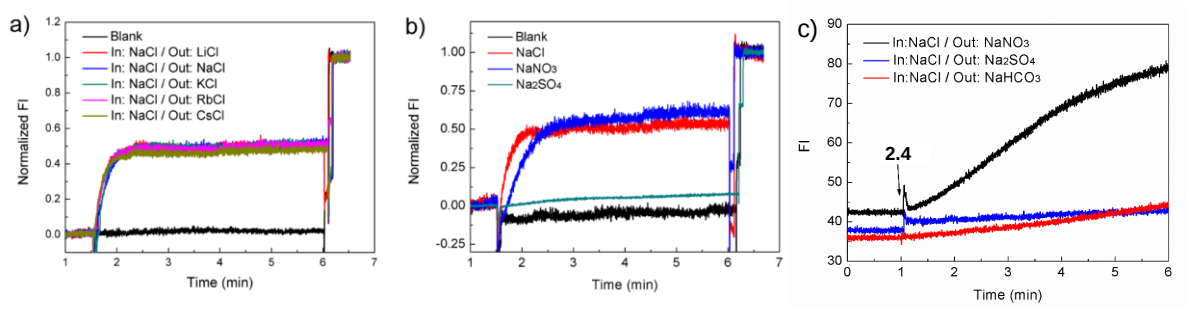

Figure 43: Left: Ion transport activity of **2.4** (0.1 µM) across NaCl contained POPC-LUVs⊃lucigenin compared in different extravesicular solution conditions. Inside: 100 mM NaCl, 1 mM lucigenin, PB buffer; outside: 100 mM NaX (X= NO_3, HCO_3, SO_4), PB buffer. The NaCl contained POPC-LUVs⊃lucigenin was diluted by NaX-PB buffer before measurement and **2.4** was added at 1 min ion transport activity of **2.4** (0.1 µM) across POPC-LUVs⊃HPTS compared in different intravesicular and extravesicular solution conditions. a) Cation investigation. Inside: 100 mM NaCl, pH 6.7, HEPES buffer; outside: 100 mM MCl (M = Li, Na, K), pH 7.5, HEPES buffer. b) Anion investigation. Inside: 100 mM NaX (X = Cl, NO_3, SO_4), pH 6.7, HEPES buffer; outside: 100 mM NaX, pH 7.5, HEPES buffer.

Finally, since our previous studies had identified significant differences in Cl^- binding to phosph(V)azanes of the type $[RNH(E)P(\mu\text{-}N^tBu)]_2$, containing different chalcogens (E = O, S, Se), we also looked at the effect of varying the chalcogen substitution on membrane transport. Comparing **2.3**, **2.7** and **2.8**, we observe an increase in transport activity moving to the heavier chalcogens (**2.3** > **2.8** > **2.7**) (Figure 44), with the O-transporter having almost no activity. Apart from the inherently lower anion binding ability of **2.7** which we determined previously in this report, a further reason for the poor transport properties of **2.7** is its hydrolytic sensitivity. Whereas solid **2.3** is completely insoluble but stable in D_2O at room temperature, contrary to previous reports **2.7** rapidly hydrolyses under these condition (Figure 44). The greater transport activity of the Se-receptor **2.3** over the S-receptor **2.8** can be attributed to the increase in anion affinity as well as the greater hydrophobicity of the heavier congeners.

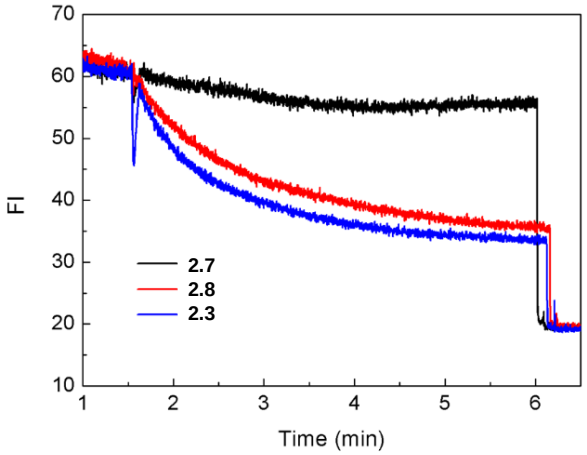

Figure 44: Chloride influx into POPC-LUVs⊃lucigenin mediated by carriers **2.3, 2.7, 2.8** (0.5 µM). Carriers were added at 1.5 min and Triton X-100 was added at 6 min.

Chapter Conclusion

One of the primary conclusions from this chapter is that seleno-phosph(V)azanes [RNH(Se)P(µ-N^{t}Bu)]$_2$ have superior anion binding and anion transport properties to O- and S-counterparts, stemming from their greater proton acidity. Se-substitution at the P(III)-atoms of phosph(III)azanes [RNH(Se)P(µ-N^{t}Bu)]$_2$ has a similar effect to the introduction of electron-withdrawing groups within the P_2N_2 rings or metal coordination by the P-lone pairs. A unique feature of phosphazane anion receptors is the ability of metal coordination to activate and modulate anion binding, a feature which makes them very different to common organic counterparts like squaramides and thioureas. Introduction of positive charge leads to binding of the weakly coordinating BF_4^- anion. The selective lability of the P_2N_2 ring units of seleno-phosph(V)azanes to ring cleavage by strong nucleophiles can be harnessed to develop F^- sensing capability by the incorporation of chromophoric substituents, while their water stability, hydrophobic character and strong anion binding properties lead to applications as synthetic anion transporters through phospholipid layers.

Experimental Details

General experimental details involving techniques, instruments and materials employed are provided in the appendix at the end of this thesis.

$[H_2NP(\mu\text{-}N^tBu)]_2$, $[^tBuNH(O)P(\mu\text{-}N^tBu)]_2$ **2.7**, $[^tBuNH(S)P(\mu\text{-}N^tBu)]_2$ **2.8**, $(Ph_3P)Cu(CH_3CN)_3(BF_4)$, $(Ph_3P)_2Pd(CH_3CN)_2(BF_4)_2$, $[^tBuNH(Me\text{-})P(\mu\text{-}N^tBu)_2PNH^tBu]I$, $[3,5\text{-}(CF_3)_2C_6H_3NH]_2C{=}S$ **2.16** and $[3,5\text{-}(CF_3)_2C_6H_3NH]_2C_4O_2$ **2.17** were synthesised using the literature protocols.[19,44,88,96,98,99] Adapted literature protocols and new protocols are summarised in the following section.

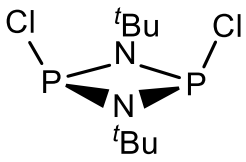

Synthesis of 2.1: 2.1 has been synthesised using an adapted literature protocol. An oven-dried 3 L Schlenk flask equipped with an overhead stirrer and a dropping funnel connected to a Schlenk line was charged with 1.5 L THF and 1 L Et_3N under a stream of nitrogen. The solution was degassed for 1 h with nitrogen. The solution was cooled to -78 °C and distilled PCl_3 (60 ml, 94.2 g, 0.69 mol) was added dropwise via the dropping funnel causing the formation of a fine white precipitate. Afterwards the funnel was flushed with 25 ml of THF. Tertiarybutylamine $^tBuNH_2$ (72.2 ml, 50.5 g, 0.69 mol) was added over the course of 1 h via the dropping funnel. The resulting mixture was stirred overnight during which it was allowed to slowly reach room temperature. After 16 hrs a thick faint yellow suspension formed. The mixture was filtered under a nitrogen atmosphere using a 2 L filter frit and a 10 mM cannula and the precipitate was washed with another 200 ml of THF. The combined yellow filtrate was connected to an external trap and afterwards all solvent was removed in vacuo yielding an orange oily residue. The residue was transferred into an oven dried 250 ml Schlenk flask which was connected to an external trap and heated in vacuo at 80 °C for 1 h. This step removes volatile byproducts and equilibrates the product mixture. 150 ml of toluene was added to the resulting thick oily residue yielding an orange suspension which was filtered to remove residual Et_3NHCl. All solvent was removed in vacuo yielding a thick orange oil which solidified upon standing, yielding $[ClP(\mu\text{-}N^tBu)_2]$ **2.1** as a light-orange solid (65 g, 0.24 mol, 68%). The spectral data was in agreement with the literature.[11]

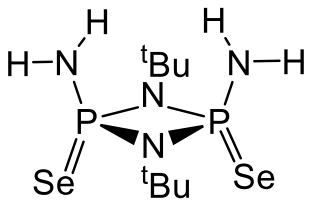

Synthesis of 2.2: Inside a N_2 filled glovebox a Schlenk tube was charged with $[H_2NP(\mu\text{-}N^tBu)]_2$ (236 mg, 1) and selenium (316 mg, 4 mmol, 4 eq) and transferred to a Schlenk line. 20 ml of THF were added and the resulting suspension was stirred overnight. Afterwards unreacted selenium was filtered off under ambient conditions and the solvent was removed in vacuo to yield **2.2** as a white powder (390 mg, 99%). **^{1}H NMR (25 °C, d$_6$-Acetone, 500.12 MHz):** δ [ppm] = 5.04 (s, 4H, NH_2), 1.67 (s, 18H, ^{t}Bu); **^{31}P NMR (25 °C, d$_6$-Acetone, 202.48 MHz)**: δ [ppm] = 33.8 (s, with two satellite doublets arising from [(^{77}Se=)H_2N-P(μ-N tBu)P-NH_2(=Se)], $^1J_{PSe}$ = 878 Hz, $^2J_{PP}$ = 20 Hz); **Elemental analysis (%)** calcd. for **2.2:** calcd. C 24.4% H 5.6% N 14.2% found C 24.0% H 5.6% N 13.9%.

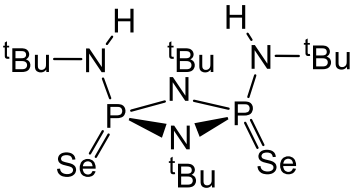

Synthesis of 2.3: **2.3** has been synthesised using an adapted literature protocol. An oven-dried 500 ml Schlenk flask equipped was connected to a Schlenk line and was charged with 200 ml THF and 100 ml dried and distilled ^{t}BuNH$_2$ under a stream of nitrogen. The solution was cooled to -78 °C and distilled PCl_3 (10 ml, 15.7 g, 0.12 mol) was added dropwise via the dropping funnel causing the formation of a white precipitate. The resulting mixture was stirred overnight during which it was allowed to slowly reach room temperature. After 16 h a thick faint yellow suspension formed. Under a stream of nitrogen dried powdered Selenium (20 g, excess) was added and the suspension was stirred at room temperature overnight. Afterwards all volatiles were removed in vacuo and the resulting grey solid was extracted with 500 ml of toluene yielding a faint yellow clear filtrate. The solvent was removed in vacuo until the precipitation of a colourless solid was observed which was dissolved by gentle heating. Storage of the solution at -14 °C overnight yielded **2.3** as colourless crystals which were isolated by filtration and dried in vacuo. Concentration of the mother liquor and storage yielded a second batch of analytically pure product. Overall yield (20 g, 66%). The spectral data was in agreement with the literature.[76] In a control study we observed via in situ ^{31}P NMR that oxidation in fact occurs quantitatively and cis-selective.

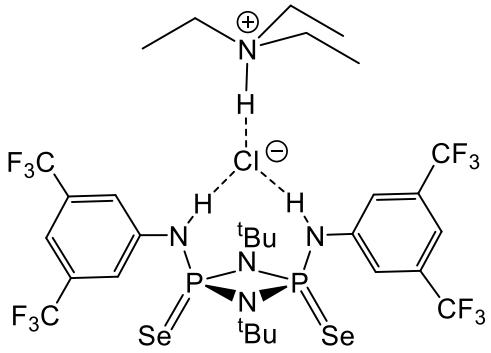

Synthesis of 2.4•Et_3NHCl**:** Inside a N_2 filled glovebox a Schlenk tube was charged with **2.1** (275 mg, 1 mmol) and transferred to a Schlenk line. 20 ml of THF and 3,5-Bis(trifluoromethyl)aniline (458 mg, 2 mmol, 2 eq) were added. The solution was cooled to 0 °C and 2 ml of dry NEt_3 were added dropwise. The resulting mixture was allowed to warm to room temperature and then stirred overnight at 40 °C. Afterwards selenium (316 mg, 4 mmol, 4 eq) was added and the mixture was stirred at room temperature. The reaction progress was monitored by in situ ^{31}P NMR spectroscopy. After completion of the reaction the solvent was removed in vacuo and resulting solid mixture was extracted with 20 ml toluene. The solvent was removed in vacuo to yield **2.4•**Et_3NHCl as a yellow powder (872 mg, 0.91 mmol, 91%). Crystals suitable of the solvate **2.4•**Et_3NHCl for X-ray crystallography were obtained by layering an Et_2O solution of **2.4•**Et_3NHCl with pentane. **^{1}H NMR (25 °C, CD_3Cl, 500.12 MHz):** δ [ppm] =10.98 (s, 1H, **H**NEt_3), 8.80 (s, 2H, HNAr), 8.20 (s, 4H, o-Ar), 7.52 (s, 2H, m-Ar), 3.13 (q, $^3J_{HH}$ = 7.2 Hz, 6H, HN(**CH_2**$CH_3)_3$),), 1.62 (s, 18H, ^{t}Bu), 1.37 (t, $^3J_{HH}$ = 7.2 Hz, 9H, HN(CH_2**CH_3**$)_3$; **^{31}P NMR (25 °C, CD_3Cl, 202.48 MHz)**: δ [ppm] =31.51 (s, with two satellite doublets arising from [(^{77}Se=)HRN-P(μ-N^{t}Bu)P-NRH (=Se)], $^1J_{PSe}$ = 908 Hz, $^2J_{PP}$ = 20 Hz); **Elemental analysis (%)** calcd. for **2.4•**Et_3NHCl**:** calcd. C 37.7%, H 4.4%, N 7.3% found C 37.8%, H 4.5%, N 7.4%; **LRESI-MS (-ve ion)**: simul (Phosphazane·Cl^-) 854.95 found 854.90.

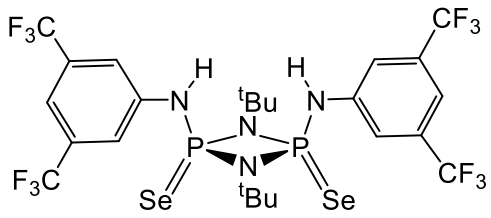

Synthesis of free 2.4: 2.4•Et_3NHCl (100 mg, 0.1 mmol) was dissolved in 20 ml of Et_2O. The solution was washed three times with 10 ml of water and afterwards dried with anhydrous $MgSO_4$. The solvent was removed in vacuo to yield **2.4** as a yellow powder (84 mg, 85%); **^{1}H NMR (25 °C, CD_3Cl, 500.12 MHz):** δ [ppm] =7.71 (s, 4H, o-Ar), 7.68 (s, 2H, m-Ar), 5.78 (s, 2H, NH), 1.65 (s, 18H, ^{t}Bu); **^{31}P NMR (25 °C, CD_3Cl, 202.48 MHz)**: δ [ppm] =30.38 (s, with two satellite doublets arising from [(^{77}Se=)HRN-P(μ-N tBu)P-NRH (=Se)], $^1J_{PSe}$ = 927 Hz, $^2J_{PP}$ = 25 Hz); **Elemental analysis (%)** calcd. for **2.4:**

calcd. C 35.2%, H 3.2%, N 6.8%, found C 35.1%, H 3.4%, N 6.8%; **LRESI-MS (-ve ion)**: simul (Phosphazane·Cl^-) 854.95, found 854.90.

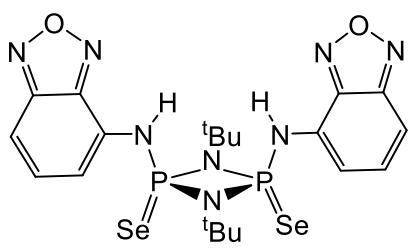

Synthesis of 2.5: Inside a N_2 filled glovebox a Schlenk tube was charged with **2.1** (275 mg, 1 mmol) and 4-amino-benzoxadiazole (316 mg, 4 mmol, 2 eq) and transferred to a Schlenk line. 20 ml of THF and 5 ml dry NEt_3 were added and the resulting suspension was stirred overnight at 50 °C. Afterwards selenium (316 mg, 4 mmol, 4 eq) was added and the mixture was stirred or 72 h at room temperature. The solvent was removed in vacuo and resulting solid mixture was extracted with 20 ml DCM. The solvent was removed in vacuo to yield **2.5** as a yellow powder (587 mg, 0.93 mmol, 97%). **^{1}H NMR (25 °C, CD_3Cl, 500.12 MHz):** δ [ppm] = 7.85 (d, $^3J_{HH}$ = 6.8 Hz, 2H, Ar), 7.63 – 7.45 (m, 4H, Ar), 6.74 (s, 2H, NH), 1.61 (s, 18H, ^{t}Bu); **^{31}P NMR (25 °C, CD_3Cl, 202.48 MHz)**: δ [ppm] = 27.7 (s, with two satellite doublets arising from [(^{77}Se=)HRN-P(μ-N^{t}Bu)P-NRH (=Se)], $^1J_{PSe}$ = 929 Hz, $^2J_{PP}$ = 25 Hz); no suitable elemental analysis could be obtained.

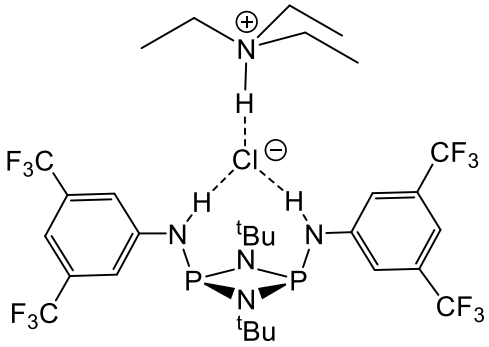

Synthesis of 2.6•Et_3NHCl: Inside a N_2 filled glovebox a Schlenk tube was charged with **2.1** (275 mg, 1 mmol) and transferred to a Schlenk line. 20 ml of THF and 3,5-Bis(trifluoromethyl)aniline (458 mg, 2 mmol, 2 eq). The solution was cooled to 0 °C and 2 ml of dry NEt_3 were added dropwise. The resulting mixture was allowed to warm to room temperature and then stirred overnight at 40 °C.Afterwards the solvent was removed in vacuo and the resulting solid mixture was extracted with 40 ml of hexane. The solvent was removed in vacuo space until the precipitation of a white solid was observed which was gently heated back into solution. Storage of the solution at -20 °C led to the formation of colourless crystal suitable for X-ray diffraction which were isolated by filtration and dried in vacuo to yield **2.6•**Et_3NHCl as a colourless powder (240 mg, 0.30 mmol, 30%). **^{1}H NMR (25 °C, CD_3Cl, 500.12 MHz):** δ [ppm] =11.85 (s, 1H, **H**NEt_3), 7.62 (s, 4H, o-Ar), 7.26 (s, 2H,

m-Ar), 7.13 (s, 2H, HNAr), 3.10 (q, $^3J_{HH}$ = 7.2 Hz, 6H, HN(**CH$_2$**CH$_3$)$_3$), 1.41 (t, $^3J_{HH}$ = 7.2 Hz, 9H, HN(CH$_2$**CH$_3$**)$_3$)), 1.28 (s, 18H, ^{t}Bu), **^{31}P NMR (25 °C, CD$_3$Cl, 202.48 MHz)**: δ [ppm] = 108.19 (s). **Elemental analysis (%)** calcd. for **2.6**•Et$_3$NHCl**:** calcd. C 45.2%, H 5.3%, N 8.8%, found C 45.1%, H 5.3%, N 8.7%; **LRESI-MS (-ve ion)**: simul (Phosphazane·Cl$^-$) 695.11, found 695.05

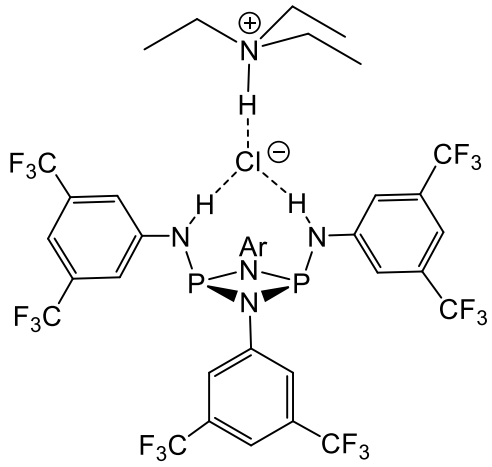

Synthesis of 2.9•Et$_3$NHCl**:** A Schlenk tube was charged with PCl_3 (0.44 g, 3.21 mmol) and 25 ml of toluene. The resulting solution was cooled to -78 °C and 25 ml of NEt_3 were added. To this (3,5-bistrifluoromethyl)aniline (1.47 g, 6.42 mmol) was added dropwise at -78 °C and mixture was slowly allowed to warm to room temperature overnight during which time a thick white suspension formed. All solvents were removed in vacuo and the resulting solid was extracted with 100 ml of hexane. The filtrate was concentrated in vacuo until the precipitation of a white solid was observed which was dissolved into solution by gentle heating. Storage at -14 °C yielded a white crystalline solid which was recrystallised twice from hexane to yield **2.9**•Et$_3$NHCl as colourless crystals suitable for single crystal X-ray diffraction (112 mg, 0.1 mmol, 6.3%); **^{1}H NMR (25 °C, CD$_3$Cl, 500.12 MHz):** δ [ppm] =11.10 (s, 1H, **H**NEt$_3$), 9.39 (s, 2H, HNAr), 7.86 (s, 4H, o-Ar), 7.47 (s, 2H, m-Ar), 7.40 (s, 2H, m-Ar), 7.30 (s, 4H, o-Ar), 3.02 (q, $^3J_{HH}$ = 7.2 Hz, 6H, HN(**CH$_2$**CH$_3$)$_3$),)), 1.31 (t, $^3J_{HH}$ = 7.2 Hz, 9H, HN(CH$_2$**CH$_3$**)$_3$; **^{31}P NMR (25 °C, CD$_3$Cl, 202.48 MHz)**: δ [ppm] =113.47 (s); **Elemental analysis (%)** calcd. for **2.9**•Et$_3$NHCl**:** calcd. C 41.1%, H 2.7%, N 6.3%, found C 41.5%, H 2.9%, N 6.2%; **LRESI-MS (-ve ion)**: simul (Phosphazane·Cl$^-$) 1007.00 found 1006.90.

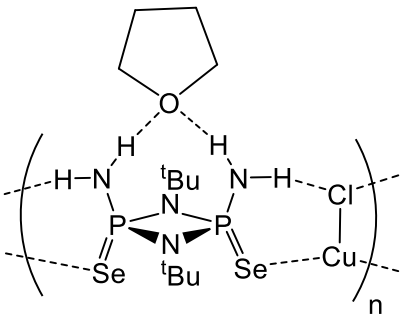

Synthesis of 2.10: Inside a N_2 filled glovebox a Schlenk tube was charged with **2.2** (100 mg, 0,25 mmol) and CuCl (25 mg, 0.25 mmol, 1 eq). The Schlenk tube was transferred to a Schlenk line and 10 ml of THF were added. The resulting orange/brown mixture was stirred at room temperature for 1 h. Afterwards the solution was reduced to approximately 5 ml in vacuo and stored at 4 °C for 3 days which lead to the formation of orange crystals suitable for X-ray crystallography. The crystals were isolated by filtration and dried in vacuo to yield **3**·CuCl as an orange/brown crystalline solid (113 mg, 0.20 mmol, 80%). Crystal lose THF when dried under vacuum. The following spectroscopic and analytical data refers to this material. **^{1}H NMR (25 °C, d_8-THF, 500.12 MHz):** δ [ppm] = 5.81 (s, 4H, NH_2), 1.71 (s, 18H, ^{t}Bu); **^{31}P NMR (25 °C, d_8-THF, 202.48 MHz)**: δ [ppm] = 30.36 (s); **Elemental analysis (%) calcd. for 2.10(-THF):** calcd. C 30.1%, H 6.0%, N 8.8%, found C 30.4%, H 6.5%, N 8.9%.

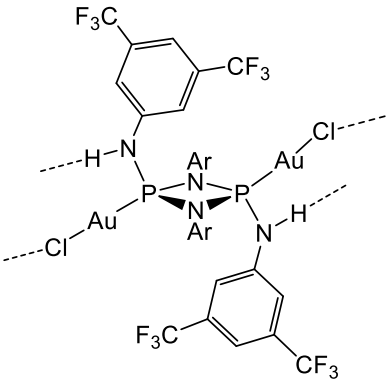

Synthesis of 2.11: Inside a N_2 filled glovebox a Schlenk tube was charged with **2.9**•Et_3NHCl (100 mg, 0,13 mmol) and $(Me_2S)AuCl$ (74 mg, 0.26 mmol, 2 eq). The Schlenk tube was transferred to a Schlenk line and 2 ml of DCM were added. The resulting solution was stirred at 10 min at room temperature and then layered with 15 ml of pentane. Over the course of 2 weeks a few single crystals of **2.11** grew alongside colourless precipitate. Due to the low yield **2.11** could only be characterised by single crystal X-ray diffraction.

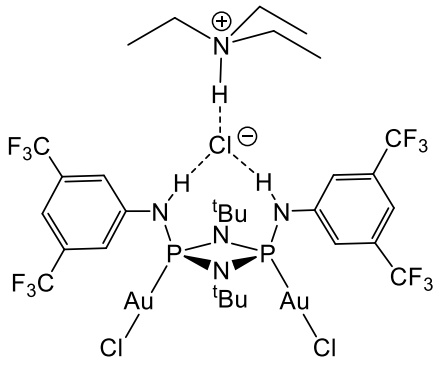

Synthesis of 2.12•Et_3NHCl**:** Inside a N_2 filled glovebox a Schlenk tube was charged with **2.6•**Et_3NHCl (100 mg, 0.13 mmol) and $(Me_2S)AuCl$ (74 mg, 0.26 mmol, 2 eq). The Schlenk tube was transferred to a Schlenk line and 2 ml of DCM were added. The resulting solution was stirred at 10 min at room temperature. Afterwards pentane was added dropwise until the formation then dissolution of a white precipitate was observed. The solution was stored at 4 ºC for 3 days which led to the formation of colourless crystals suitable for X-ray crystallography. The crystals were isolated by filtration and dried in vacuo to yield **2.12•**Et_3NHCl as a colourless solid (109 mg, 0.09 mmol, 66%); **^{1}H NMR (25 °C, CD_3Cl, 500.12 MHz):** δ [ppm] = 10.11 (s, 1H, **H**NEt_3), 9.38 (s, 2H, HNAr), 7.90 (s, 4H, o-Ar), 7.59 (s, 2H, m-Ar), 3.15 (dq, 6H, ^3J_H= 2.7 and 6.8 Hz, HN(**CH_2**$CH_3)_3$), 1.59 (s, 18H, ^{t}Bu), 1.40 (t, 9H, ^3J_H= 6.8 Hz, , HN(CH_2**CH_3**$)_3$); **^{31}P NMR (25 °C, CD_3Cl, 202.48 MHz)**: δ [ppm] = 81.97 (s); **Elemental analysis (%)** calcd. for **2.12•**Et_3NHCl**:** calcd. C 28.5%, H 3.3%, N 5.6%, found C 28.3%, H 3.4%, N 5.5%. **LRESI-MS (-ve ion)**: simul (Phosphazane·Cl^-) 1158.98 found 1158.90.

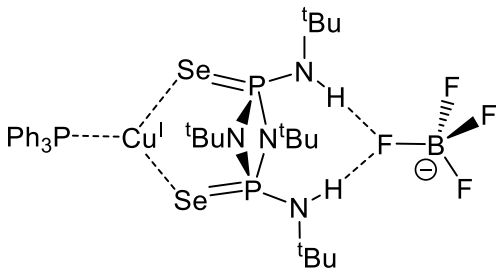

Synthesis of 2.13: To solution of **2.3** (50 mg, 0.1 mmol) in 1 ml DCM was added $(Ph_3P)Cu(CH_3CN)_3(BF_4)$ (55 mg, 0.1 mmol, 1 eq) in 1 ml CH_3CN. After 10 minutes the resulting mixture was transferred to a crystallisation tube and layered with approximately 10 ml of Et_2O. After 10 days at room temperature large colourless crystals formed which were suitable for X-ray crystallography. The crystals were isolated by filtration and dried in vacuo to yield **2.13** (69 mg, 0.75 mmol, 75%). **^{1}H NMR (25 °C, CD_2Cl_2, 500.12 MHz):** δ [ppm] =7.46 (t, $^3J_{HH}$= 7.4, 3H, PPh_3), 7.40 – 7.20 (m, 12H, PPh_3), 5.33 (s, 2H, NH), 1.71 (s, 18H, ^{t}Bu$_{endo}$), 1.54 (s, 18H, ^{t}Bu$_{exo}$); **^{31}P NMR (25 °C, CD_2Cl_2, 202.48 MHz)**: δ [ppm] =18.64 (s, with two satellite doublets arising from [(^{77}Se=)HRN-P(μ-N^{t}Bu)P-NRH (=Se)], $^1J_{PSe}$ = 732 Hz, $^2J_{PP}$ = 25 Hz); **^{19}F NMR (25 °C, CD_2Cl_2, 395.99 MHz)**: δ [ppm] = -150.59 (s), -150.63 (s); **Elemental analysis**

(%) calcd. for **2.13:** calcd. C 44.4%, H 5.8%, N 6.1%, found C 45.6%, H 6.1%, N 5.5%. **LRESI-MS (+ve ion)**: simul. (**2.13** - BF_4)$^+$ 848.13, found 848.10.

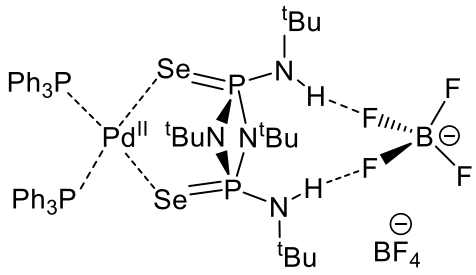

Synthesis of 2.14: To a solution of **2.3** (50 mg, 0.1 mmol) in 1 ml CH_2Cl was added $(Ph_3P)_2Pd(CH_3CN)_2(BF_4)_2$ (92 mg, 0.1 mmol, 1 eq) in 1 ml DCM. After 10 minutes the resulting orange mixture was transferred to a crystallisation tube and layered with approximately 10 ml of pentane. After 3 days at room temperature large orange crystals formed which were suitable for X-ray crystallography. The crystals were isolated by filtration and dried in vacuo to yield **2.14**·DCM. (126 mg, 0.95 mmol, 95%); **^{1}H NMR (25 °C, CD_2Cl_2, 500.12 MHz):** δ [ppm] = 7.62-7.51 (m, 6H, PPh_3), 7.40 -7.27 (m, 24H, PPh_3), 5.62 (s, 2H, NH), 1.69 (s, 18H, ^{t}Bu$_{endo}$), 1.19 (s, 18H, ^{t}Bu$_{exo}$); **^{31}P NMR (25 °C, CD_2Cl_2, 202.48 MHz)**: δ [ppm] = 27.3 (AA'XX'), 17.61 (AA'XX');**^{19}F NMR (25 °C, CD_2Cl_2, 395.99 MHz)**: δ [ppm] = -150.05 (s), -150.10 (s); **Elemental analysis (%)** calcd. for **2.14**·DCM**:** calcd. C 45.6%, H 5.0%, N 4.0%, found C46.0%, H 5.2%, N 3.7%; **LRESI-MS**: simul (**2.14**-BF_4)$^+$ 1255.23, found 1225.17

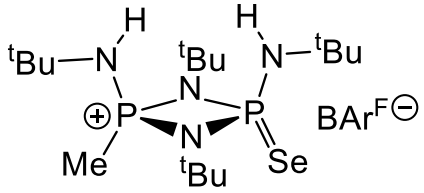

Synthesis of 2.15: Inside a N_2 filled glovebox, a Schlenk flask was filled with 491 mg [^{t}BuNH(Me-)P(μ-N^{t}Bu)$_2$PNH^{t}Bu]I (1 mmol, 1 equivalent) and 200 mg Selenium (excess) and transferred to a Schlenk line. 50 ml of THF were added and the resulting suspension was stirred at room temperature for 72 h. Afterwards the suspension was filtered in air to remove unreacted selenium. All volatiles were removed in vacuo yielding a white solid which was redissolved in 50 ml of 1:1 THF/DCM. $NaBAr^F$ (886 mg, 1 mmol, 1 equivalent) was added to the solution and the mixture was stirred for 2h at room temperature yielding a white suspension. The suspension was filtered and all solvent was removed in vacuum yielding **2.15** as a white solid (1.23g, 0.95 mmol, 95%); **^{1}H NMR (25 °C, $CDCl_3$, 400 MHz):** δ [ppm] = 7.69 (s, 8H, Bar^F), 7.53 (s, 4H, Bar^F), 3.43 (s, 1H, SePN**H**), 3.30 (d, J_{PH} = 18 Hz, 1H, MePN**H**)**,** 2.15 (d, J_{PH} = 20 Hz, 3H, **Me**P)**,** 1.59 (s, 18H, ^{t}Bu), 1.58 (s, 9H, ^{t}Bu), 1.47 (s, 9H, ^{t}Bu); **^{31}P NMR (25 °C, $CDCl_3$, 202.48 MHz)**: δ [ppm] =

25.3 (s), 25.1 (s);**^{19}F NMR (25 °C, $CDCl_3$, 395.99 MHz)**: δ [ppm] = 62.4 (s). **Elemental analysis (%)** calcd. for **2.15:** calcd. C 45.1%, H 4.1%, N 4.3%, found C 44.7, H 4.1%, N 4.1%.

Experiment details for Transport studies

Materials

POPC for vesicle preparation were purchased from Avanti Polar Lipids. HPTS, lucigenin and Sephadex G-50 were purchased from Sigma. Fluorescence measurements were performed on a Cary Eclipse Fluorescence Spectrophotometer (Agilent).

Cl^- transport activity studied by lucigenin assay

Preparation of POPC-LUVs⊃lucigenin

A thin lipid film in a glass vial was obtained by evaporating 0.4 ml of POPC (20 mg/ml in chloroform) under reduced pressure on a rotary evaporator at 45 °C and then in high vacuum under room temperature for 1 h. 0.4 ml of PB (phosphate buffer) with lucigenin (1 mM lucigenin, 5 mM sodium phosphate, 225 mM $NaNO_3$, pH 7.5) was added to rehydrate the lipid film. The resulting suspension was subjected to 5 freeze/thaw cycles and extruded through a polycarbonate membrane (pore size 200 nm) for 29 times. Unencapsulated lucigenin was removed by a Sephadex (G-50) column, and finally about 0.9 ml of POPC-LUVs⊃lucigenin solution (~ 11.6 mM POPC; solution in the liposomes: 1 mM lucigenin, 5 mM sodium phosphate, 225 mM $NaNO_3$, pH = 7.5) was gained.

For the preparation of NaCl contained POPC-LUVs⊃lucigenin, 0.4 ml of PB with NaCl and lucigenin (1 mM lucigenin, 5 mM sodium phosphate, 100 mM NaCl, pH 7.5) was used to rehydrate the lipid film. The other procedure was the same as above and a final volume of around 0.9 ml of POPC-LUVs⊃lucigenin solution (~ 11.6 mM POPC; solution in the liposomes: 1 mM lucigenin, 5 mM sodium phosphate, 100 mM NaCl, pH = 7.5) was gained.

Cl^- transport across POPC-LUVs⊃lucigenin

30 µL of vesicle solution mixed with 970 µL of PB (5 mM sodium phosphate, pH = 7.5, 225 mM $NaNO_3$ or 100 mM other salt) were mixed in a dry cuvette. 5 µL of 4 M NaCl was added to the extravesicular buffer to induce a 20 mM chloride gradient across the lipid membrane at t = 0.5 min after the start of the recording, and 10 µL anion carrier molecule in acetonitrile was added at t = 1.5 min to initiate the transport. 20 µL of 10 wt% Triton X-100 was added to lyse the vesicles for calibration at t = 6 min. The change of fluorescence intensity of the lucigenin with time was recorded at 505 nm with the excitation wavelength of 455 nm. Fluorescence time courses of lucigenin were also normalised to fractional emission intensity I_t according to equation [E1]:

$$I_t = (F_t - F_\infty) / (F_0 - F_\infty) \text{ [E1]},$$

where F_t is fluorescence intensity at time t, $F_0 = F_t$ before addition of NaCl and $F_\infty = F_t$ after complete leakage with Triton X-100.

Ion transport activity studied by HPTS assay

Preparation of POPC-LUVs⊃HPTS

A thin lipid film was gained by evaporating 0.4 ml of POPC (20 mg/ ml in chloroform) under reduced pressure on a rotary evaporator at 45 °C and then in high vacuum under room temperature for 1 h. After that the lipid film was rehydrated with 0.4 ml HEPES buffer containing HPTS (1 mM HPTS, 10 mM HEPES, 100 mM NaCl, pH 6.7) by vortexing and then sonicated for 15 min. Subsequently, the resulting suspension was subjected to 5 freeze/thaw cycles and extruded through a polycarbonate membrane (pore size 200 nm) for 29 times. Finally, the unencapsulated HPTS was removed by a Sephadex (G-50) column and a final volume of around 0.9 ml of POPC-LUVs⊃HPTS solution (~ 11.6 mM POPC; solution inside liposomes: 1 mM HPTS, 10 mM HEPES, 100 mM NaCl, pH = 6.7; solution outside liposomes: 10 mM HEPES, 100 mM NaCl, pH = 6.7) was obtained.

Ion transport activity studied across POPC-LUVs⊃HPTS

10 µL of POPC-LUVs⊃HPTS solution prepared as described above and 990 µL of HEPES buffer (10 mM HEPES, 100 mM NaCl, pH 6.7) were mixed in a dry cuvette.

8.5 µL of 0.5 M NaOH was added into the extravesicular buffer to induce a pH gradient (ΔpH = 0.8) across the lipid membrane at t = 0.5 min after the start of the recording, anion carrier molecule (20 µL in acetonitrile at varied concentration) was added to initiate the ion transport at t = 1.5 min, and 20 µL of 10 wt% Triton X-100 was added to lyse the vesicles for calibration at t = 6 min. The change of fluorescence intensity of the HPTS with time was recorded at 510 nm with the excitation wavelength of 450 nm. Fluorescence time courses were normalised to fractional emission intensity I'_t according to equation [E2].

$$I'_t = (F_t - F_0) / (F_\infty - F_0) \text{ [E2]},$$

where F_t is fluorescence intensity at time t, $F_0 = F_t$ before the addition of carrier molecule and $F_\infty = F_t$ at saturation after complete leakage achieved with the 10 wt% Triton X-100. Fractional emission intensity I_t at 6 min (the time point before the addition of Trition X-100) were plotted as a function of carrier molecule concentration and fitted to the Hill equation [E3] to give the effective concentration EC_{50} (the concentration of carrier molecule showing half activity respect to the maximum) and the Hill coefficient n.

$$I = I_\infty + (I_0 - I_\infty) / [1 + (c / EC_{50})^n] \text{ [E3]},$$

Where c is the concentration of carrier molecule, I_0 is fractional emission intensity without carrier molecule, and I_∞ is fractional emission intensity with excess of carrier molecule. As discussed earlier, we changed the buffer solution inside or outside of the vesicles to study the transport mechanism and test its selectivity for different ions.

Chapter 3: Conformational Control in Phosphazane H-bond and Pyridyl donors

As mentioned in the previous chapter, Goldfuss et al. have shown computationally that diaminophospha(V)zanes of the type $[RNH(E)P(\mu\text{-}NR)]_2$ (E = O, S, Se) intrinsically prefer an endo-exo conformation.[71,73] In order for anion binding to occur the receptor has first to preorganise to the exo-exo conformer (Figure 45). This is associated with an energy penalty which has the net result of decreasing the receptor's anion affinity. In this chapter we seek to design phosphazane anion receptors which are conformationally fixed in order to increase anion affinity and access alternative modes of binding. We initially envisaged that exocyclic 2-aminopyridyl groups of the receptor $[(2\text{-py})NHP(\mu\text{-}N^tBu)]_2$ (2-py = 2-pyridyl) **3.1** might result in a bidentate coordination motif in which the endo-endo conformation could be fixed by metal coordination to the pyridyl groups (Figure 45, bottom).

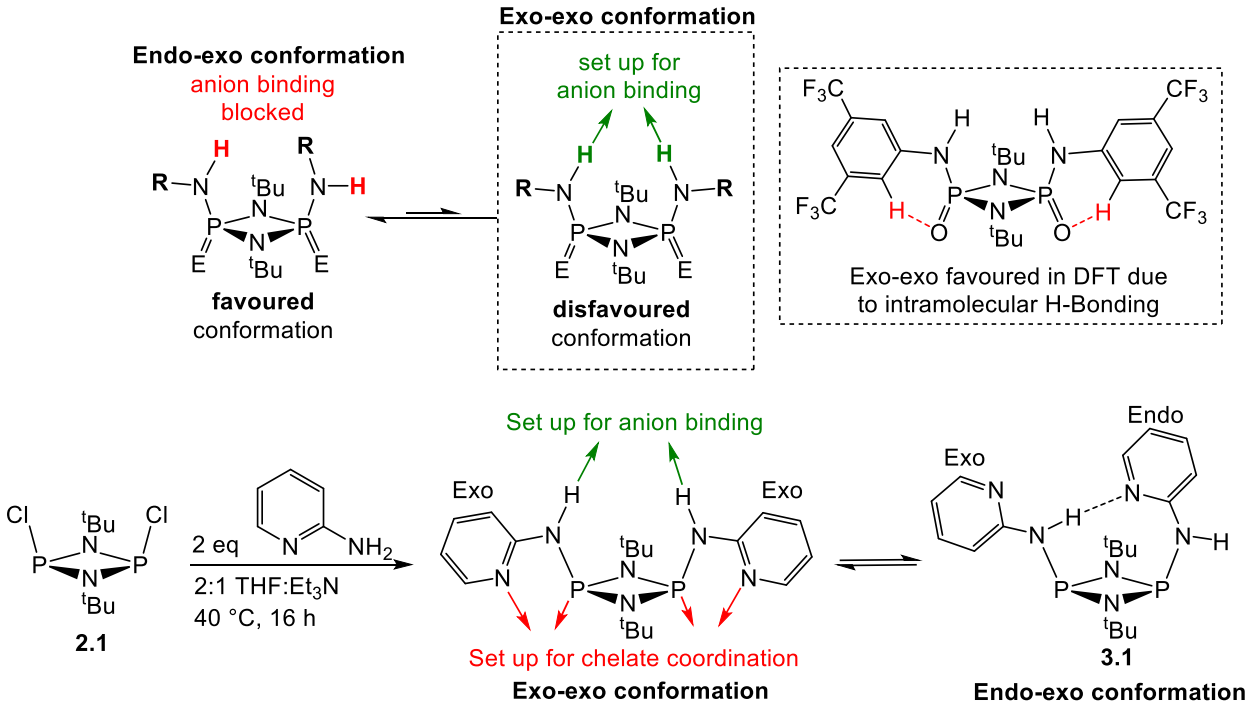

Figure 45: Top: Conformers of phosphazane anion receptors; Bottom: Synthesis of **3.1.**

Results and Discussion

Development and Binding Properties of New Receptors and Transporters

Condensation of 2-aminopyridine with $[ClP(\mu\text{-}N^tBu)]_2$ **2.1** in presence of excess NEt_3 yields $[PyNHP(\mu\text{-}N^tBu)]_2$ **3.1** in good yield after crystallisation from hexane. Although the ^{31}P and ^1H NMR spectra show single environments for the P and NH atoms, the solid-state structure reveals that **3.1** is present in the endo-exo conformation (Figure 46, top). This conformation is stabilised by an intramolecular H-bond between the NH proton of the endo-PyNH group and the N-atom of the exo-PyNH group ($N_{NH}\cdots N_{py}$ = 2.87 Å). Nevertheless, in solution the exo-exo and endo-exo conformers rapidly interconvert, which is indicated by the observation of broad NH and P resonances at room temperature in the ^1H and ^{31}P NMR spectra. The presence of an intramolecular H-bond provides the opportunity to explore how modification of the phosphazane backbone can affect the hydrogen donor strength of the NH functionalities. Since in the previous chapter we identified selenium oxidation as a way to enhance the receptor properties significantly, we subjected **3.1** to selenium oxidation via our optimised protocol yielding $[PyNH(Se{=})P(\mu\text{-}N^tBu)]_2$ **3.2**. Similarly to **3.1**, the solid-state structure of **3.2** reveals the preference for the endo-exo conformation (Figure 46). Although the $N_N\cdots N_{py}$ is slightly elongated to 2.92 Å in **3.2** (by ca. 0.05 Å compared to **3.1**), the room temperature ^{31}P and ^1H NMR spectra in d_6-DMSO or $CDCl_3$ show two phosphorus and pyridyl environments. This indicates that oxidation of the P(III) centres to P(V) results, as expected, in the increase in the favourability of the endo-exo conformation as a result of the increased H-bond donor strength. A variable-temperature (VT) ^{31}P NMR spectroscopic study of **3.2** in d_6-DMSO shows that both resonances coalesce to a broad singlet at approximately 100 °C.In comparison, the broad singlet observed in the ^{31}P NMR spectrum of the P(III) precursor **3.1** splits into two resonances at low temperature with a coalescence temperature of approximately 10 °C.The VT behaviour of **3.1** and **3.2** is consistent with the endo-exo conformer being enthalpically favoured and the exo-exo conformer being entropically favoured. DFT calculation on the B3LYP-D3BJ/def2-TZVPP level of theory (carried out in collaboration with Patrick Pröhm at FU Berlin) show that the endo-exo conformers of **3.1** and **3.2** are 26.8 kJ/mol and 72.3 kJ/mol more stable, respectively, than their exo-

exo conformers. We also found computationally that the endo-endo conformer is favoured by 43.7 kJ/mol for **3.1** and 35.1 kJ/mol for **3.2**.

Similar splitting of the P and H environments is observed in the room temperature ^{31}P and ^{1}H NMR spectra of the Au(I) complex [(ClAu)$_2$**3.1**] **3.3** in d_6-DMSO or $CDCl_3$, obtained from the reaction of **3.1** and 2 equivalents (DMS)AuCl in DCM at room temperature in 84% yield, suggesting the same endo-exo conformation. This is confirmed in the solid-state structure of **3.3** (Figure 46). Unfortunately, **3.3** is not thermally stable enough for a VT NMR study at higher temperature. The observed increase of the barrier for interconversion of the exo-exo and endo-exo conformers again confirms the increase of NH H-bond donor strength upon gold coordination to the P(III) centres of **3.1**.

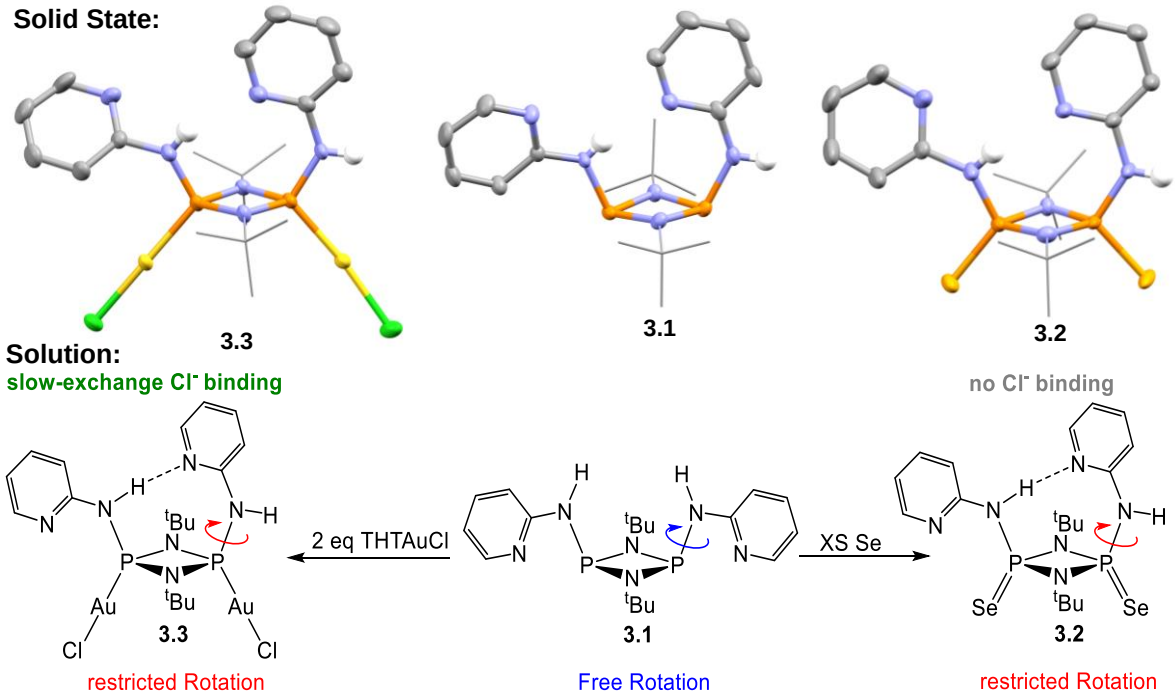

Figure 46: Top: solid state structures of **3.1**, **3.2** and **3.3**. Ellipsoids shown at 40% probability; non-NH hydrogen and lattice bound solvent molecules omitted for clarity. Selected bond length [Å] and angles [°]: **3.1:** N_{exo}-P av. 1.71, N_{exo}-P-N_{endo} av. 105.8, N_{exo}-$N_{pyridyl}$ 2.870(4); **3.2:** N_{exo}-P av. 1.64, N_{exo}-P-N_{endo} av. 109.2, N_{exo}-$N_{pyridyl}$ 2.924(5), P-Se 2.08; **Au:** N_{exo}-P av. 1.64, N_{exo}-P-N_{endo} av. 110.5, N_{exo}-$N_{pyridyl}$ 2.928(3), P-Au 2.21. Bottom: Synthesis and solution behaviour of **3.1**, **3.2** and **3.3**. Colour code: orange = P, yellow = Au, green = Cl, blue = N, white = H, grey = C, bright orange = Se.

Collectively, these initial results suggested for the first time that the energetic barrier between the conformations of the phosphazane unit can be manipulated by phosphazane backbone modification.

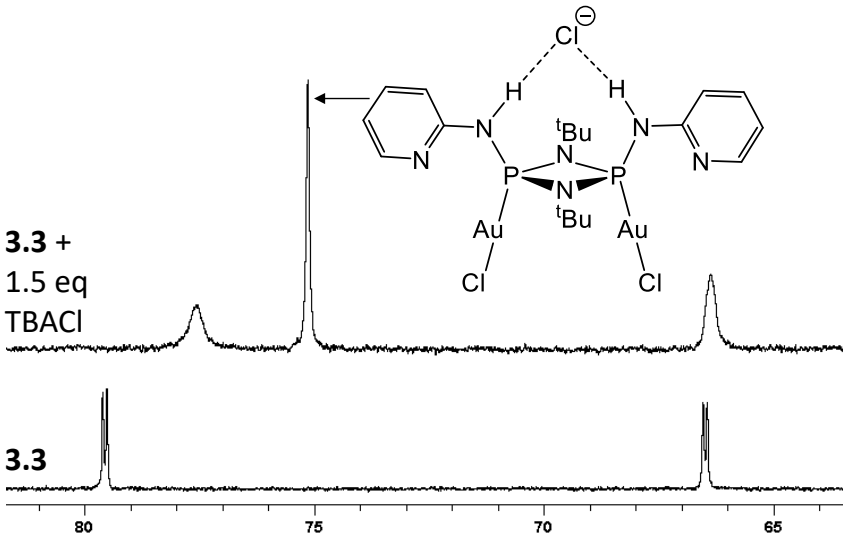

Figure 47: Overlaid ^{31}P NMR spectra of **3.3** ($CDCl_3$, 202 MHz, 25 °C) before and after the addition of TBACl.

Whereas **3.1** shows negligible interaction with chloride in $CDCl_3$, **3.2** interacts with chloride via its free endo-NH proton leaving the endo-exo conformation intact at room temperature. Addition of TBACl to **3.2** in $CDCl_3$ results in shifting of the NH proton which is not involved in the intramolecular H-bond. In contrast, gradual addition of TBACl to a $CDCl_3$ solution of **3.3** results in appearance of an additional symmetric set of signals in the ^1H NMR and a singlet resonance in the ^{31}P NMR spectrum (Figure 47) which is indicative of slow exchange chloride binding ($K = 30 \pm 5\ M^{-1}$). We conclude that the fact the **3.2** does not bind chloride face-on via both NH protons whereas **3.3** does, proves that AuCl coordination more effectively activates phosphazanes for anion binding than selenium oxidation. While we suspected in the previous chapter that this could be the case, we had not obtained quantitative support for this experimentally.

With these initial results in hand, we moved on to investigate further how the coordination of metals by the P(III) atoms of **3.1** can be used to fix the exo-exo arrangement, necessary for anion binding. Reaction of **3.1** with either one equivalent $[Rh(CO)_2Cl]_2$ or two equivalents $Mo(piperidine)_2(CO)_4$ results in coordination of the transition metal atoms of both by the P- and pyridyl-N atoms of **3.1** (Figure 48). The ^1H and ^{31}P NMR spectra of the resulting complexes $[Mo(CO)_4PyNHP(\mu\text{-}N^tBu)]_2$ **3.4**

and [Rh(CO)ClPyNHP(μ-N^{t}Bu)]$_2$ **3.5** show one environment for the P_2N_2 ring P centres together with only one pyridyl environment, indicating that the targeted exo–exo conformation of **3.1** is present in both. The ^{31}P NMR spectrum of **3.5** shows an AA´XX´ coupling pattern with J_{RhRh} = 0 Hz, similar to that observed by Reek et al. for dinuclear rhodium complexes.[100] X-ray quality crystals were grown from a concentrated 1:4 DMSO:CH_3CN solution in the case of **3.5** and CH_3CN in the case of **3.4** at 5 °C. The solid-state structures of the solvates **3.4**·CH_3CN and **3.5**·DMSO confirm the exo-exo receptor conformation (Figure 48). The structures also show the binding of the CH_3CN and DMSO molecules by the bidentate NH H-bond donor groups of the receptors. Metal coordination also significantly increases the polarity of the pendant NH protons. The ^{1}H NMR spectra show a downfield shift of approximately 2 ppm in CD_2Cl_2 in both **3.4** and **3.5** compared to **3.1**. Notably metal chelation also increases the stability of the phosphazane framework. Whereas **3.1** hydrolyses slowly under ambient conditions and in undried solvents, both **3.4** and **3.5** stay intact in wet DMSO for at least a week and are stable as powders under ambient conditions for at least 6 months.

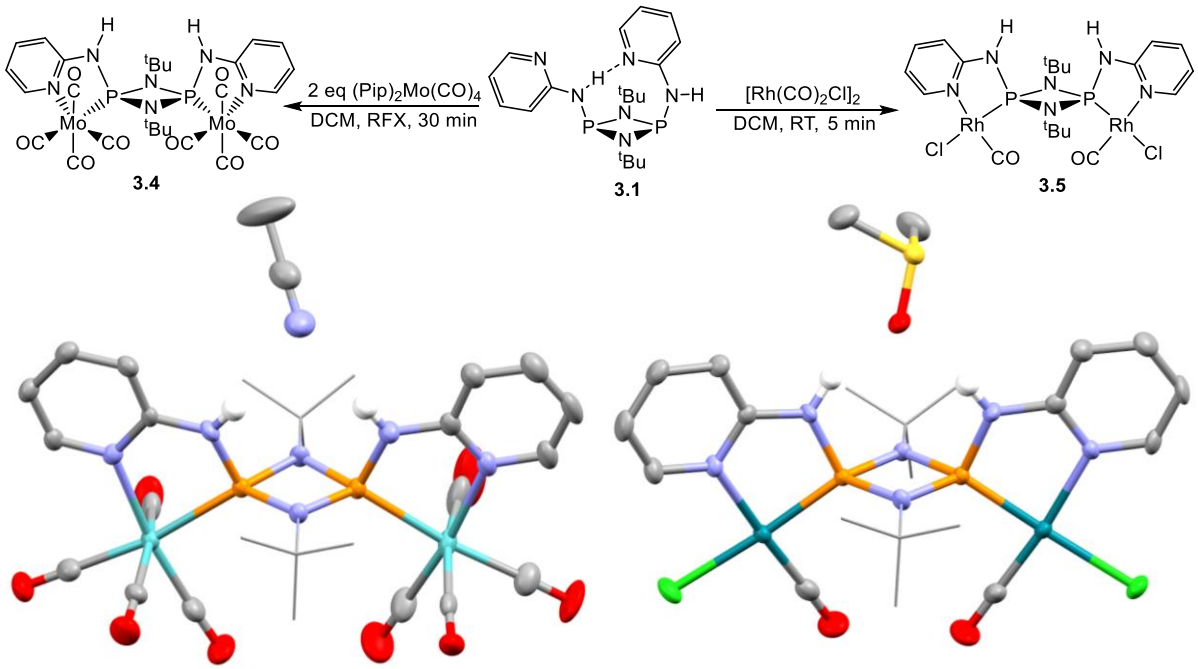

Figure 48: Top: Synthesis of **3.4** and **3.5**. Bottom: Solid state structure of **3.4** and **3.5**. Ellipsoids shown at 40% probability; non-NH hydrogens omitted for clarity. Selected bond length [Å] and angles [°]: **3.4**: N_{exo}-P av. 1.68, N_{exo}-P-N_{endo} 105.5, $N_{Acetonitrile}$-N_{exo} 3.17, P-Mo av. 2.47, $N_{pyridyl}$-Mo av. 2.29. **3.5**: N_{exo}-P av. 1.68, N_{exo}-P-N_{endo} 107.5, O-N_{exo} 2.85, P-Rh av. 2.16, $N_{pyridyl}$-Rh av. 2.11. Colour code: orange = P, dark green =Rh, green = Cl, yellow = S blue = N, white = H, grey = C, red = O.

Addition of increasing amounts of tetrabutylammonium chloride salts in d_6-DMSO results in gradual shifting of the NH resonances of **3.4** and **3.5**, indicative of fast-exchange halide binding (Figure 49). ^{1}H NMR titrations reveal that the anion binding processes are most accurately modelled using a 2:1 non-cooperative binding model for both receptors (using the BindFit program suite), indicating the formation of [(receptor)$_2$Cl$^-$] complexes (Figure 50). We observe the chloride binding to improve going from the molybdenum complex **3.4** with K = (416 ± 44) M^{-1} to the rhodium complex **3.5** with K = (1410 ± 91) M^{-1}. Hence the coordinated metal fragment does influence the binding properties of the receptors. Moving to the higher oxidation state metal from Mo(0) to Rh(I) increases the metal-ligand interaction in agreement with the spectrochemical series and therefore activates **3.1** more for anion binding.[101] It should be noted that a noticeable change in the chemical shift only occurs for the NH protons and not for the pyridyl environments. This indicates that only H-bonding interactions of the anion with the NH protons is occurring, not with the coordinated metal itself.

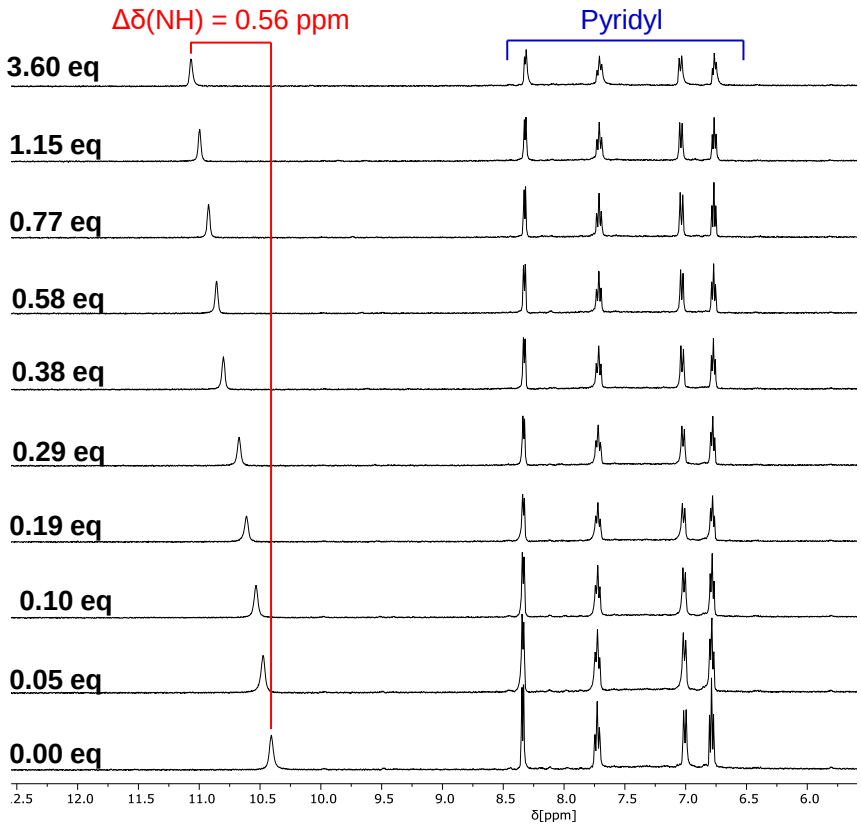

Figure 49: ^{1}H NMR titration (d$_6$-DMSO, 25 °C, 400 MHz) of **3.4** with TBACl.

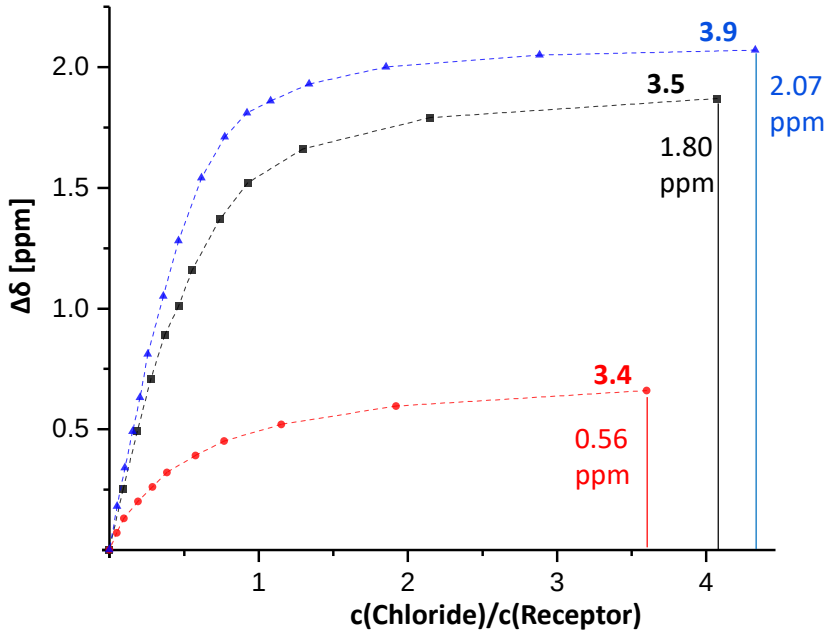

Figure 50: Shift of the NH proton signal in the ^{1}H NMR titration of **3.4**, **3.5** and **3.9** with increasing amounts of TBACl in d$_6$-DMSO.

Significantly, since the parent ligand **3.1** interacts with chloride only to a negligible extent, metal coordination actually switches on anion binding.

DFT calculations at the B3LYP-D3BJ/def2-TZVPP level of theory explain the activating effect of metal chelation (Figure 51). Modification of **3.1** either via selenium oxidation or metal coordination results in increased donation of the lone pair of the exocyclic nitrogen into the P-N(endo) σ*-orbitals. The delocalisation energy increases going from **3.1** (49.4 kJ/mol), to **3.2** (65.02 kJ/mol), **3.4** (54.44 kJ/mol) and **3.5** (54.31 kJ/mol) which also results in an increase of the P-N(exo) bond order, as is apparent from the increase of electron density in the bond critical points for **3.4** and **3.5**. In the case of **3.2**, this effect is counterbalanced by donation of the selenium lone pairs into the P-N(exo) σ*-orbitals. Hence, we conclude that delocalisation of the NH lone pair into the P_2N_2 ring is responsible for the activation of the NH protons for anion binding. Activation using our strategies can be compared to organic receptors in which there is no such mechanism for tuning the NH bond polarity.[89]

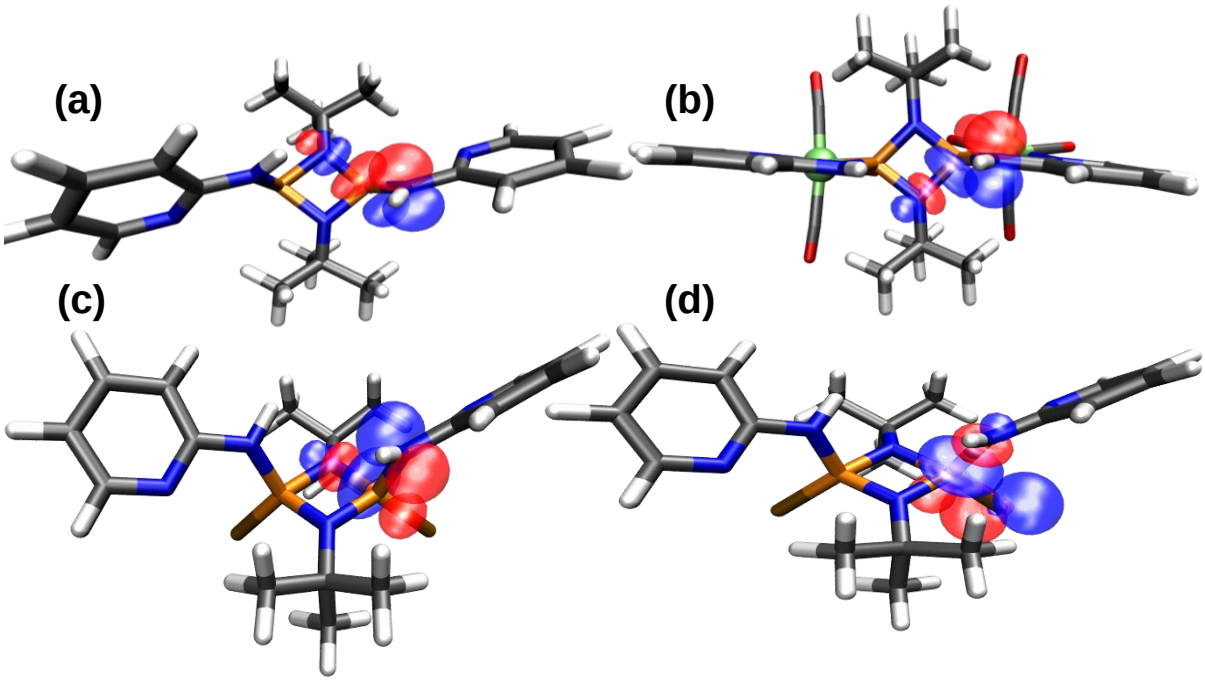

Figure 51: Donation of the N(exo) lone pair into the P-N(endo) σ*-orbitals in (a) **3.1**, (b) **3.4**, (c) **3.2**. (d) Donation of the Se lone pair into the P-N(exo) σ*-orbitals in **3.2**.

Calculations also reveal that metal chelation also activates **3.1** towards anion binding on geometric grounds. The optimised geometries of the exo-exo conformer for **3.1** and **3.2** show that the NH protons point away from each other. This results in improved alignment of the N(exo) lone pair with one P-N(endo) σ*-orbital. Upon molybdenum or rhodium chelation the NH protons are forced into the same plane pointing towards each other, in the correct geometry for anion binding. Notably this a

direct consequence of P,N chelation as opposed to P coordination alone. Additionally, calculations reproduce the greater affinity of **3.4** compared to **3.5**.

In order to increase the binding properties further, we installed electron withdrawing CF_3 groups onto the pyridyl substituents and prepared the Se receptor **3.7**, the AuCl receptor **3.8** and the RhClCO receptor **3.9** following the same synthetic methodologies outlined above (Figure 52). Again, the Se derivative **3.7** is found to only interact with chloride side-on, whereas the AuCl derivative **3.8** binds chloride in slow NMR exchange with K = (400±20) M^{-1}.

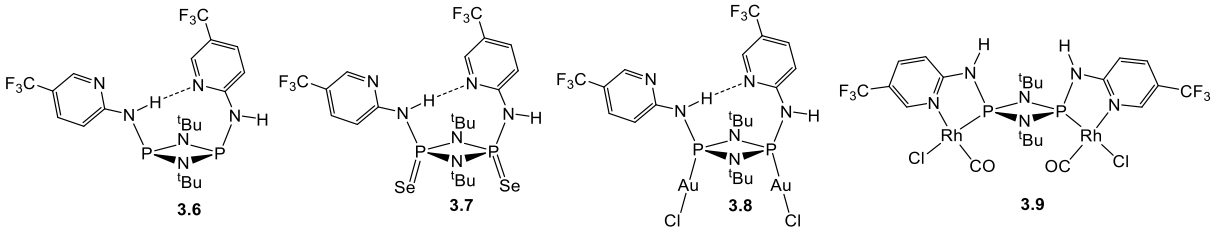

Figure 52: Labelling for **3.6**, **3.7, 3.8**, **3.9**.

Quantitative binding analysis of the Rh(I) complex [**3.6**{Rh(CO)Cl}$_2$] **3.9** shows that chloride binding (again best modelled as a 2:1 non-cooperative model) is further increased to K = (4948 ± 522) M^{-1} in d_6-DMSO. We attribute this increase to the greater protic nature of the NH proton in **3.9** compared to **3.5**, which correlates with the decrease of the CO stretching frequency from 2031 cm^{-1} in **3.9** to 2022 cm^{-1} in **3.5** (showing a decrease in electron density at the rhodium atom). In order to compare the receptor **3.9** with our previously best receptor **2.4** (in the previous chapter binding studies were only carried out in CH_3CN), we carried out ^{1}H NMR titrations for **2.4** with TBACl in d_6-DMSO revealing that a 2:1 non-cooperative binding process with K = (522 ± 11) M^{-1}**.** This reveals that in fact the halide affinities improve by an order of magnitude using the new receptor. Notably, **3.9** is better than the best structurally analogous double NH donor thiourea and squareamide receptors reported in the literature by one to two orders of magnitude (the best squaramide receptor binds chloride with K = 634 M^{-1} and thiourea with K = 41 M^{-1} under the same conditions).[96] It should be noted that previously the halide binding of phosphazanes in acetonitrile at lower concentration has been fitted to a 1:1 model, which gives a poorer fit to the data in DMSO. The reason for this difference is not clear at this stage.

Notably anion binding also affects the metal ligand interactions. Addition of excess TBACl (ca 10 eq) in CD_2Cl_2 to either **3.5** or **3.9** results in a decrease of the AX $^1J_{RhP}$ coupling constants by 11 Hz in **3.9** and 15 Hz in **3.5** respectively (Figure 53). The same effect on the $^1J_{RhP}$ coupling constant is also observed in d_6-DMSO. We also observe a decrease by 4 cm^{-1} for **3.4**, 5 cm^{-1} for **3.5** and 7 cm^{-1} for **3.9** in the CO stretching frequencies upon chloride addition. It has been suggested previously that N-H···X^- H-bonding represents an intermediate state of NH deprotonation by the anion.[89] Therefore anion binding should cause an accumulation of electron-density at the nitrogen atoms of the NH groups, resulting in a decrease of π-acceptor ability of the phosphine centres. The acidic nature of the NH protons in **3.9** is apparent from the deprotonation of **3.9** with more basic anions such as F^- or OAc^-, as shown by the loss of the NH resonance upon addition of excess these anions in d_6-DMSO.

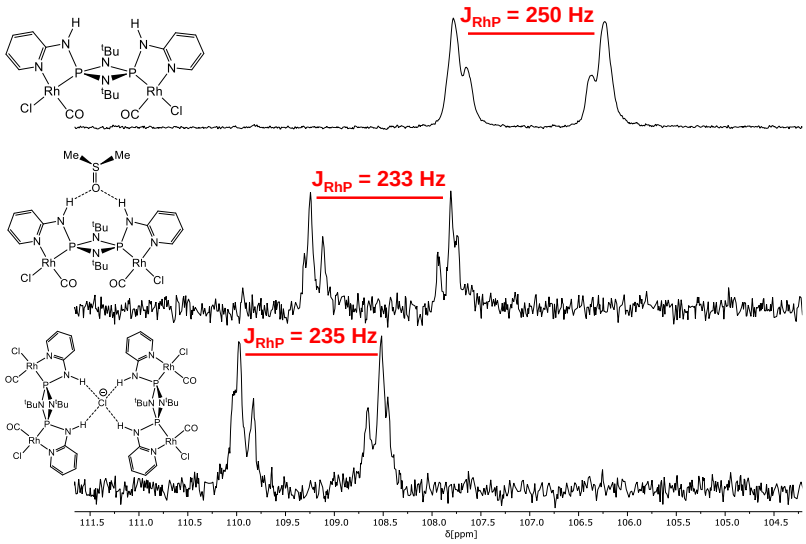

Figure 53: Overlaid ^{31}P NMR spectra of **3.5** ($CDCl_3$, 202 MHz, 25°C) before and after addition of excess TBACl and in d_6-DMSO.

DFT calculations support this hypothesis. Upon chloride binding to **3.5**, donation of the lone pair of the exocyclic nitrogen into the P-N(endo) σ*-orbitals increases from 54.3 kJ/mol to 63.8 kJ/mol which is accompanied by an increase of the electron density at the bond critical point of the P-N(exo) bond. We don't observe any changes in the NBO interactions between the endocyclic nitrogen lone pairs and the P-N(exo) σ*-orbitals upon chloride binding. **3.4** behaves analogously. Interestingly, this effect is less pronounced for the ligand **3.1** itself. Taken together, our results suggest that anion binding renders the phosphine centres less electron accepting. This is in line with the development of the $^1J_{PSe}$ coupling constants of **2.4** and **2.4**•Et_3NHCl discussed in the

previous chapter. Here chloride binding causes a decrease going from 927 Hz in **2.4**·Et_3NHCl to 908 Hz in **2.4** which also signals in increase in overall donor strength.[102]

Lastly, we found that anion binding also affects the solubility of **3.5** and **3.9** in non-donor solvents such as CD_2Cl_2. Whereas amorphous samples of **3.5** and **3.9** are soluble in CD_2Cl_2, prolonged storage of concentrated solutions causes the free receptors to crystallise which are then completely insoluble in CD_2Cl_2. However, addition of stoichiometric TBACl causes crystalline samples of **3.5** and **3.9** to dissolve. The solid-state structure of **3.9** obtained from CD_2Cl_2 helps explain this phenomenon (Figure 54). It reveals that **3.9** crystallises as a H-bonded network in which the NH hydrogens bind to a chloride ligand of a neighbouring rhodium complex. This behaviour is reminiscent of the self-association observed in ureas.[103] This network is reinforced by short intermolecular axial Cl-Rh contacts. We assume that addition of anions such as chloride breaks this network apart into discrete host-guest complexes which are then soluble in CD_2Cl_2. This network formation within the crystal lattice may also be responsible for the general insolubility of metal halide complexes of diaminophosphazanes $[RNHP(\mu\text{-}N^tBu)]_2$ often encountered during the work in this thesis.

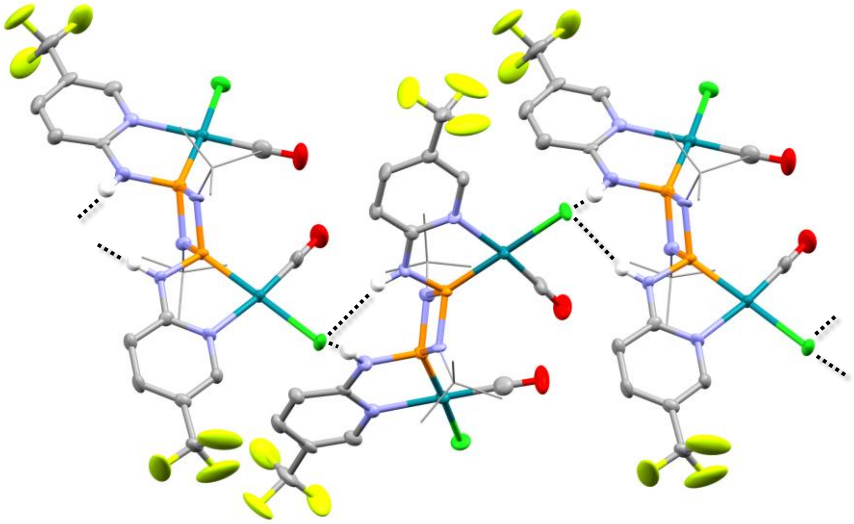

Figure 54: Solid-state structure of **3.9**. Ellipsoids shown at 40% probability; non-NH hydrogen atoms omitted for clarity. Selected bond length [Å] and angles [°]: N_{exo}-P av. 1.68, N_{exo}-P-N_{endo} 106.9, Cl-N_{exo} 3.32, P-Rh av. 2.15, $N_{pyridyl}$-Rh av. 2.11. Colour code: orange = P, dark green =Rh, green = Cl, yellow = S blue = N, white = H, grey = C, red = O, bright green = F.

Since we showed in the previous chapter that phosphazanes of the type [RNH(E)P(μ-N^{t}Bu)]$_2$ (E = S, Se) can transport anions across a lipid bilayer, we tested our new bimetallic phosphazanes for activity. These experiments were carried out in collaboration with Jinbo Zhu and Ulrich Keyser (Cambridge). Ion transport was assessed using lucigenin (LU, chloride-sensitive fluorescent dye) or 8-hydroxypyrene-1,3,6-trisulfonic acid (HPTS, pH sensitive fluorescent dye) encapsulated large unilamellar vesicles (LUVs) composed by 2-oleoyl-1-palmitoyl-sn-glycero-3-phosphocholine (POPC). The lucigenin assay (POPC-LUV⊃LU) was used to assess Cl^- transport (Figure 40a) and Cl^-/X^- exchange (Figure 40) into and out of the LUVs, mediated by the phosphazane anion carriers.[91,92] While the HPTS assay (POPC-LUV⊃HPTS) was used to assess the ion transport activity and selectivity of cation and anion transport through the membrane.[93,94] All of the experiments were performed in aqueous media. Figure 55 shows that the order of transport activity of the phosphazanes discussed in this chapter is **3.7** < **3.2** < **3.4** < **3.8** < **3.5** < **3.3** < **3.9** (Figure 55). This order does not follow the measured binding constants of the receptors involved but is complicated by a number of other potential factors such as poor inclusion into the bilayers (depending on solubility factors) and the possibility of the metal centres being involved in anion transport. Given that **3.7** shows no significant anion binding in solution it is unsurprising that no transport is observed. **3.2**, however,

transports chloride weakly. The large chloride concentration gradient probably drives reconstitution into the endo-exo conformation to bind chloride although this is not observed in solution. We infer that this does not occur for **3.7** because of the stronger intramolecular H-bond (due to the increased NH acidity caused by the electron withdrawing CF_3 group), hence anion transport is hindered on kinetic grounds.

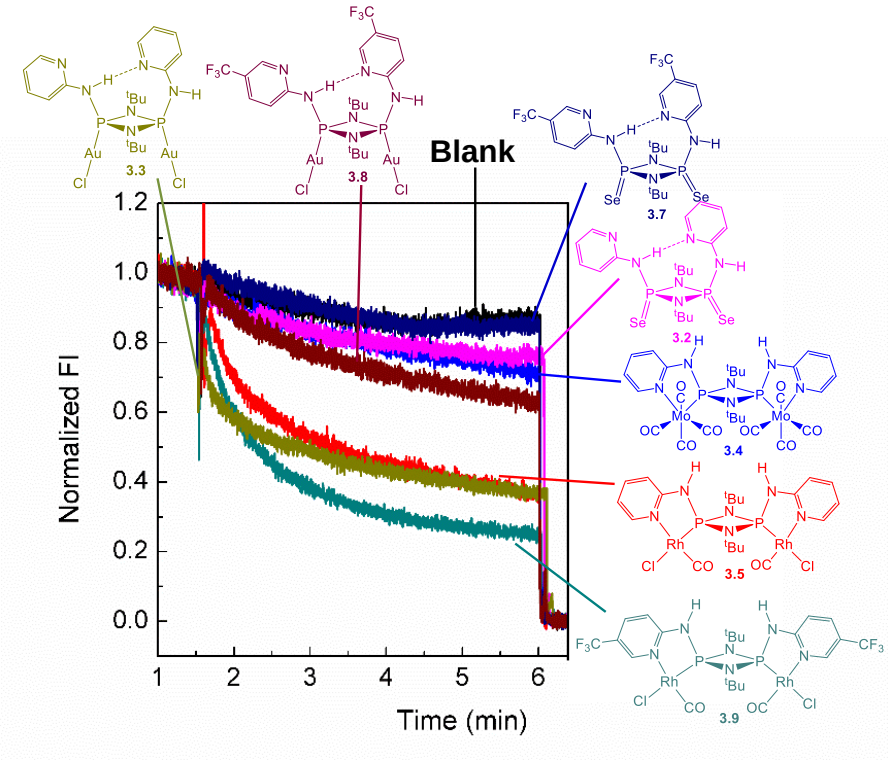

Figure 55: Chloride influx into POPC-SUVs⊃lucigenin mediated by different carrier molecules at the concentration of 2 µM as monitored by lucigenin assay.10 µL of acetonitrile was added as the blank control. 2 mM lucigenin was encapsulated in the SUVs and 20 mM NaCl was added at 0.5 min.

The next best transporter **3.4** probably shows comparatively small transport activity although being a relatively good receptor because of poor integration into the bilayer. Although hydrophobicity is favorable for integration into the bilayer transporter molecules must have some remaining solubility in the employed buffer solution in order to diffuse to the vesicles before precipitation. The two hydrophobic $Mo(CO)_4$ fragments in **3.4** probably prevent this. In comparison, the better receptor **3.5** which also features more polar RhCl(CO) complex fragments shows good transport activity which is further improved by fluorination going to **3.9**, probably as a consequence of improved chloride affinity and integration into the bilayer. The two remaining AuCl complexes **3.3** and **3.8** behave rather unexpectedly. Like **3.2** and **3.7**, fluorination

results in a decrease of transport activity which again could be a kinetic effect caused by the stronger intramolecular H-bond. However, the fact that **3.3** is the second best transporter in the investigated series is not easily explained given that it only showed weak chloride binding in $CDCl_3$ (a non-competitive solvent which should lead to stronger anion binding). However, Tecilla et al. reported that the simple palladium(II) complexes $[Ph_2P(CH_2)_3PPh_2]PdCl_2$ and $[Ph_2P(CH_2)_3PPh_2]Pd(OTf)_2$ transport anion via metal-ligand exchange.[104] This report and a report by Mao et al. on H-bonding iridium(III) complexes are, to the best of our knowledge, the only reports on lipid bilayer anion transport mediated by metal complexes.[105] This could mean that the complexes containing metal-bonded chloride ligands could transport chloride via metal-ligand exchange, in addition to transport via H-bonding. This could explain the surprising activity of **3.3**. We were able to demonstrate anion-exchange taking place at the rhodium centre of **3.5** by ^{31}P NMR spectroscopy. Addition of approximately 5 equivalents TBABr in d_6-DMSO results in significant broadening and shifting of the phosphine resonance ($\Delta\delta$ = ca. 3 ppm) which provides evidence for dynamic anion exchange on the NMR timescale (in contrast TBACl addition in d_6-DMSO leaves the ^{31}P NMR spectrum unchanged).

In order to accurately determine the activity of the best new transporters we determined their EC50 values using a HPTS assay revealing good to excellent activities (**3.5** EC50 = 26.2 nm, **3.3** = 2.97 nm, **3.9** = 0.35 nM; for comparison: **2.4** EC50 = 8.56 nm, **2.16** = 8.02 nm, **2.17** = 0.35 nm, see previous chapter). It is worth noting that **3.9** reaches the same activity as the best squaramide **2.17** even though it has only two rather than four CF_3 groups. Gale et al. reported the corresponding para-CF_3 substituted squareamide $[(4\text{-}CF_3\text{-}C_6H_4NH)C_2O]_2$ to be four times less active than **2.17** which means that **3.9** is four times more active than the squareamide $[(4\text{-}CF_3\text{-}C_6H_4NH)C_2O]_2$ for which comparison is more appropriate.

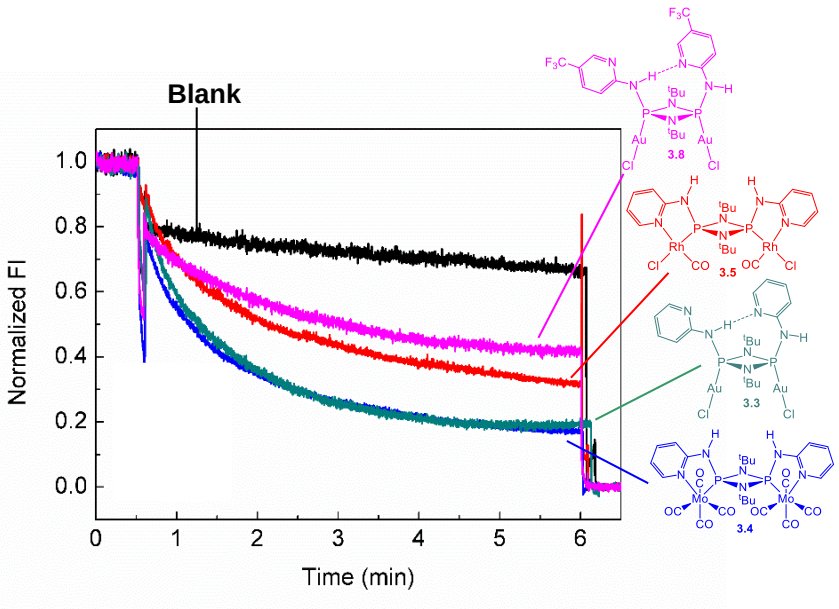

Figure 56: Chloride influx into POPC-SUVs⊃lucigenin via premixing method. The same amount of anion carriers were mixed with POPC before the formation of SUVs. 20 mM NaCl was added at 0.5 min and Triton X-100 was added at 6 min.

We conducted a series of control experiments in which the transporter molecules were preintegrated into the lipid before vesicle formation, in order to study how the nature of the phosphazanes influences its delivery properties to the bilayer (Figure 56). Interestingly using this method shows that **3.4** is a better transporter than **3.5** and shows similar activity to **3.3**. This confirms our earlier suggestion that the apolar $Mo(CO)_4$ fragments hamper integration into the bilayer. Importantly, this shows that the coordinated metal has a big influence on the functional behaviour of our transporters. Next, we compared **3.3** and **3.8** when preintegated into the bilayer and found that as before **3.3** exceeds the activity of **3.8**, showing that the decrease in transport activity upon fluorination does not stem from the transporters' ability to integrate into the bilayer. Notably, this contradicts the common observation that fluorination results in an increase in transport activity.[95]

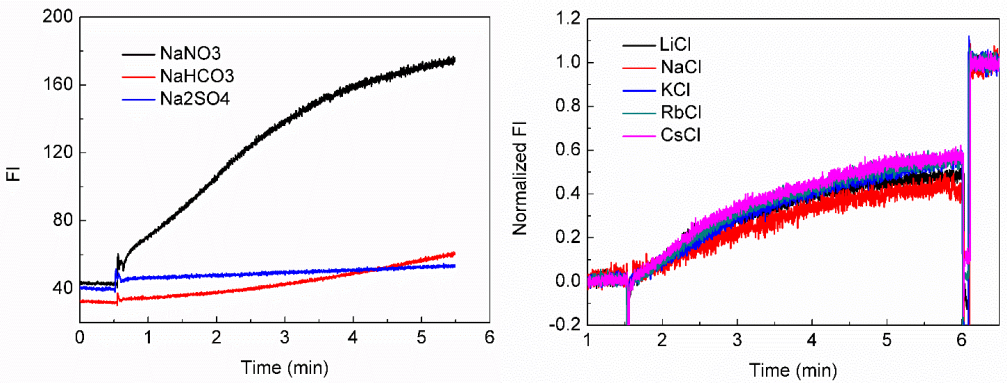

Figure 57: Ion transport activity of **3.9** (0.1 µM) across NaCl contained POPC-LUVs⊃lucigenin compared in different extravesicular solution conditions. Inside: 100 mM NaCl, 1 mM lucigenin, PB buffer; outside: 100 mM NaX (X= NO_3, HCO_3, SO_4), PB buffer. The NaCl contained POPC-LUVs⊃lucigenin was diluted by NaX-PB buffer before measurement and **3.9** was added at 1 min Ion transport activity of **3.9** (0.1 µM) across POPC-LUVs⊃HPTS compared in different intravesicular and extravesicular solution conditions. Left: Anion investigation. Inside: 100 mM NaX (X = Cl, NO_3, SO_4), pH 6.7, HEPES buffer; outside: 100 mM NaX, pH 7.5, HEPES buffer. Right: Cation investigation. Inside: 100 mM NaCl, pH 6.7, HEPES buffer; outside: 100 mM MCl (M = Li, Na, K, Rb, Cs), pH 7.5, HEPES buffer.

We employed an HPTS assay to investigate cation dependency of the best transporter **3.9**. The POPC-LUVs⊃HPTS assay shows that changing the cation from Li^+ to Cs^+ has little effect on transport of H^+ or OH^- through the membrane (Figure 57), so that a symport mechanism is therefore unlikely. By following the fluorescence intensity of vesicles containing Cl^- upon addition of different anions outside the vesicle (Figure 57), transport of Cl^- anions outside the vesicle can clearly be observed upon NO_3^- addition. However, addition of SO_4^{2-} resulted in no fluorescence change and addition of HCO_3^- in only a minor change. The selectivity for nitrate and chloride over sulphate was confirmed in a separate HPTS assay. Such clear anion dependence is a strong indication of an anion-anion antiport mechanism and is similar to the transport mechanism observed in the previous chapter. Nitrate binding to **3.9** was confirmed qualitatively in d_6-DMSO solution by ^1H NMR studies. Addition of excess $TBANO_3$ to **3.9** results in shifting of the NH resonance by $\Delta\delta$ = 0.25 ppm in d_6-DMSO (or $\Delta\delta$ = 2.0 ppm in CD_3CN). Notably, nitrate addition in d_6-DMSO leaves the ^{31}P NMR spectrum of **3.9** unchanged. This indicates that the active mode of anion antiport is H-bonding as opposed to metal-ligand exchange.

Further Exploration of the Coordination Chemistry

We continued to investigate the general coordination chemistry of [PyNHP(μ-N^{t}Bu)]$_2$ **3.1**. Given that the structure of **3.9** revealed that both cation and anion coordination can occur for **3.1**, we initially focused on coordination studies with [(Cymene)RuCl$_2$]$_2$ anticipating that the presence of chloride ligands might result in inter- and intramolecular H-bonding. Reaction of **3.1** with 0.5 eq of [(Cymene)RuCl$_2$]$_2$ gives rise to a 1:1 desymmetrised product as shown in the in situ ^{31}P NMR spectrum. Layering of the reaction mixture with pentane yields the product [(2-py)NHP(μ-^{t}NBu)]$_2$[RuCl$_2$(Cymene)] **3.10** as red crystals suitable for X-ray diffraction. The solid-state structure of **3.10** reveals coordination of **3.1** to one RuCl$_2$(Cymene) complex fragment (Figure 58). Surprisingly, this occurs only via one phosphine-ruthenium interaction, without any pyridyl coordination, with the endo-NH proton H-bonding to one of the Ru-bonded Cl atoms. This is probably due to the intrinsic preference of **3.1** for the endo-exo conformation as outlined above. The ^{1}H NMR spectrum of **3.10** in CD_2Cl_2 indicates the solid-state structure is retained in solution. Upon ruthenium coordination the NH resonances of **3.1** at 6.15 ppm (in $CDCl_3$) split into two significantly more deshielded NH resonances at 10.88 and 7.10 ppm which shows that both intramolecular H-bonds in the solid-state structure are also present in solution.

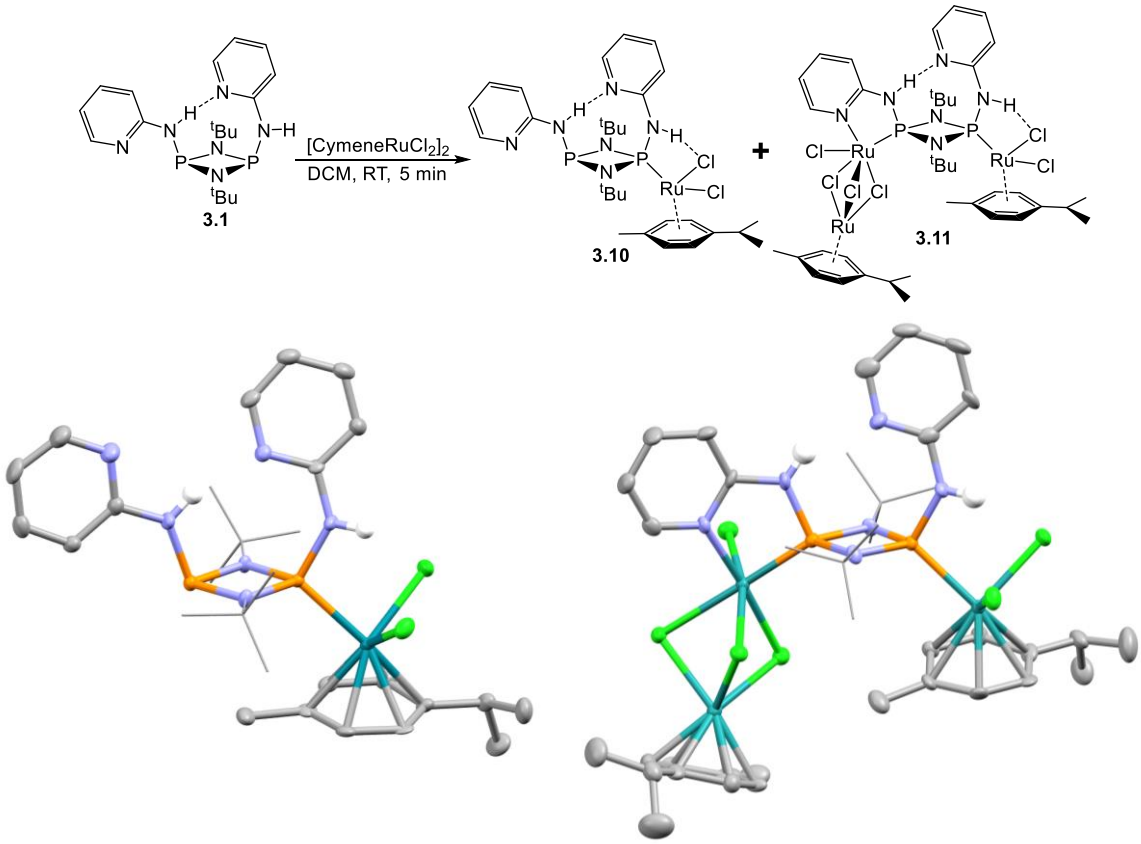

Figure 58: Top: Synthesis of **3.10** and **3.11.** Bottom: Solid state structures of **3.10** and **3.11**. Ellipsoids shown at 40% probability; non-NH hydrogen and lattice bound solvent molecules omitted for clarity. Selected bond length [Å] and angles [°]: **3.10**: N_{exo}-P av. 1.64, N_{exo}-P-N_{endo} 108.5, P_{mono}-Ru 2.334(5); **3.11**: N_{exo}-P av. 1.67, N_{exo}-P-N_{endo} 108.7, N_{exo}-$N_{pyridyl}$ 2.947(7), P_{mono}-Ru 2.353(8), $P_{chelate}$-Ru 2.176(5), $N_{pyridyl}$-Ru 2.057(1). Colour code: orange = P, dark green = Ru, green = Cl, blue = N, white = H, grey = C.

Since one phosphine centre remains uncoordinated in **3.10**, we investigated the 1:1 reaction between **3.1** and $[(Cymene)RuCl_2]_2$ targeting coordination of both phosphine centres of **3.1**. Interestingly the ^{1}H NMR spectrum in CD_2Cl_2 shows four resonances corresponding to two products one of which can be identified as **3.10** on the basis of the ^{31}P NMR shifts. Prolonged storage of a CD_2Cl_2 solution yielded a few single crystals of the second product which were suitable for single crystal X-ray diffraction. The solid-state structure shows a trinuclear ruthenium complex $[Ru_2Cl_4(Cymene)][(2\text{-}py)NHP(\mu\text{-}^tNBu)]_2[RuCl_2(Cymene)]$ **3.11** in which the vacant P,N binding pocket of **3.10** coordinates a Ru_2Cl_4Cymene fragment (Figure 58). Again, we observe two intramolecular H-bonds (between the N and NH proton of the pyridyl groups and between the exo-NH and the metal-bonded Cl atoms). The formation of **3.10** and **3.11**

highlight that the potential of **3.1** to undergo H-bonding dictates its coordination chemistry.

Spurred by the selective coordination found in **3.10** we investigated methylation of **3.1** to block one phosphine coordination site and potentially achieve direct coordination of the chelate P,N position to the metal atom. Gratifyingly the previously published procedure for the methylation of $[^tBuNHP(\mu\text{-}N^tBu)]_2$ also achieves selective monomethylation of **3.1**.[88] Reaction of **3.1** with excess methyliodide in refluxing hexane for 16 h results in the formation of a colourless precipitate. The ^{31}P NMR spectrum shows two indicative resonances, one in the phosphazane P(III) region at 97.1 ppm and one in the phosphazane P(V) region at 32.2 ppm, suggesting quaternisation of one phosphine centre of **3.1**. Single crystals suitable for X-ray diffraction could be grown from layer diffusion of a DCM solution of the product with pentane. The solid-state structure indeed confirms monomethylation of **3.1** yielding $[(2\text{-py})NHP(\mu\text{-}^tNBu)_2P(Me)NH(2\text{-py})]I$ **3.12)** (Figure 59).

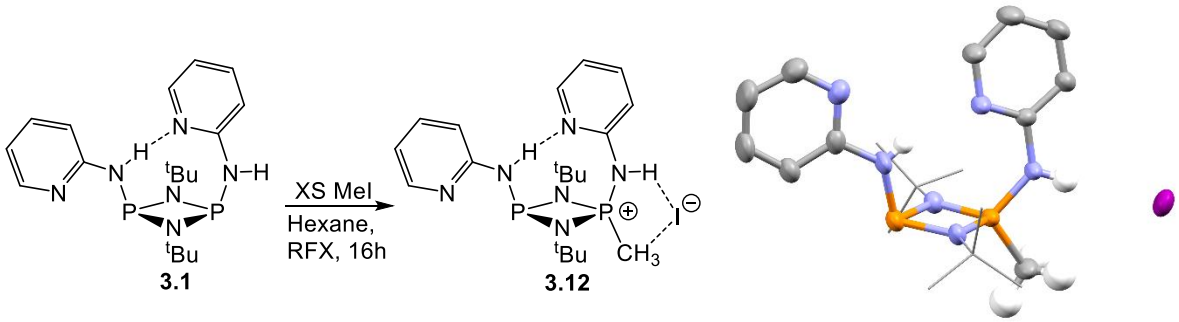

Figure 59: Left: Synthesis of **3.12.** Right: Solid state structures of **3.12**. Ellipsoids shown at 40% probability; non-NH and PMe hydrogen omitted for clarity. Selected bond length [Å] and angles [°]: N_{exo}-P(Me)-N_{endo} av. 108.5, N_{exo}-P(Me)-N_{endo} av. 102.0, N_{exo}-P(Me) 1.628(3), N_{exo}-P(III) 1.663(5), N_{endo}-$N_{Pyridyl}$ 2 N_{exo}-I 3.943, C-I 3.880. Colour code: orange = P, purple = I, blue = N, white = H, grey = C.

Interestingly, the iodide counteranion is coordinated side-on via H-bonding to one NH and potentially the methylphosphonium hydrogen atoms. In order to clarify whether the P-Me^+ protons participate in H-bonding to the iodide ion, we added excess tetrabutylammoniumiodide to a solution of **3.12** which results in a downfield shift of the NH and P-Me resonances to a greater extent than for the other protons. This behaviour is consistent with fast-exchange binding of iodide side-on in **3.12** in solution using the NH and P-Me^+ protons. With the methylated ligand **3.12** in hand we attempted coordination with a variety of transition metal complex precursors. Although metal coordination was achieved, most attempts resulted in inseparable mixtures or partial

decomposition as monitored via in situ ^{31}P NMR spectroscopy. However reaction with [Mo(Piperidine)$_2$(CO)$_4$] resulted in quantitative coordination (Figure 60). The in situ ^{31}P NMR spectrum shows a large downfield shift of the phosphorus(III) resonance from 97.1 ppm in **3.12** to 133.1 ppm in the reaction product. Layer diffusion of the reaction mixture with pentane yielded yellow crystals of [(2-py)NHP(μ-^{t}NBu)$_2$P(Me)N(2-py)]$_2$[Mo(CO)$_4$] **3.13** suitable for X-ray diffraction. The solid-state structure confirms chelate coordination of the Mo(CO)$_4$ fragment by the P,N pocket of the ligand. However, reaction with [Mo(Piperidine)$_2$(CO)$_4$] also resulted in deprotonation of the P(Me)-NH(2-py) group by the basic piperidine released in the reaction, yielding a P(Me)=N(2-py) group. This is apparent from the shortening of the P-N(exo) distance from 1.628(3) Å in **3.12** to 1.565(2) Å in **3.13.** In fact, closer inspection of the in situ ^{1}H NMR spectrum of the reaction mixture in CDCl$_3$ shows the formation of piperidine-hydrochloride.

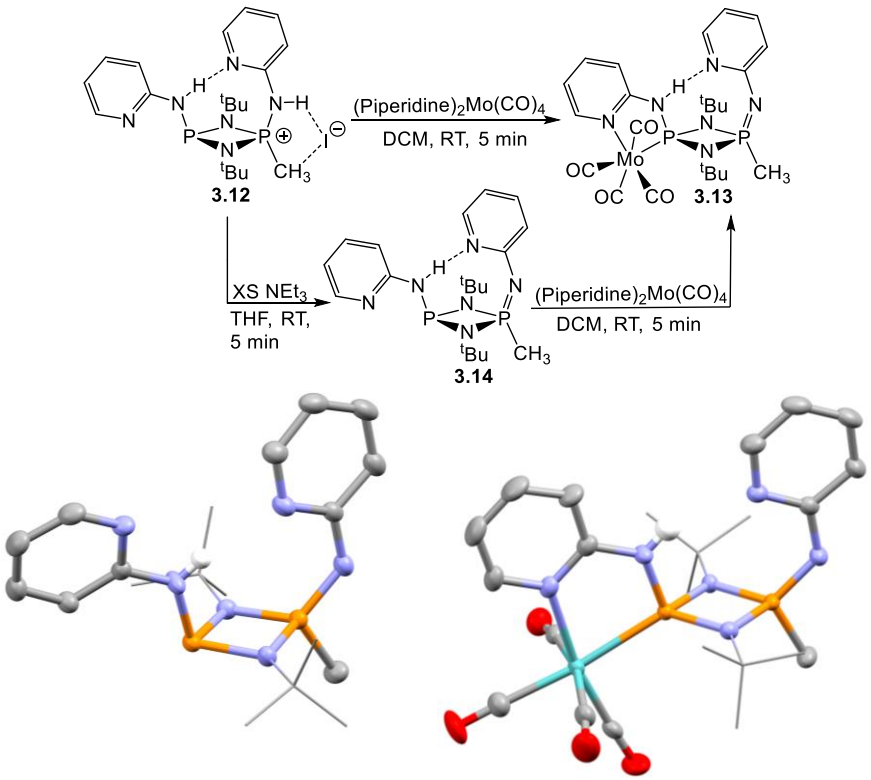

Figure 60: Top: Synthesis of **3.13** and **3.14.** Bottom: Solid state structures of **3.14**. Ellipsoids shown at 40% probability; non-NH hydrogens omitted for clarity. Selected bond length [Å] and angles [°]: **3.13**: N_{exo}-P(Me) 1.565(2), N_{exo}-P(III) 1.680(6), $N_{Pyridyl}$-N_{exo} 3.024(4), P-Mo 2.461(2), N-Mo 2.299(5), N-Mo-P 75.94(8), N-P(III)-N av. 104.5, N-P(V)-N av. 121.9. Low quality of the data set precludes detailed structural discussion of **3.14**. Colour code: orange = P, turquoise = Mo, blue = N, white = H, grey = C, red = O.

Deprotonation can also be performed without simultaneous metal coordination. Reaction of **3.12** with excess NEt_3 in DCM results in deprotonation of the exo-NH proton within 5 minutes (Figure 60, top). The in situ ^{31}P NMR spectrum shows a subtle shift of the phosphorus(V) resonance from 32.3 ppm in **3.12** to 24.6 ppm in [(2-py)NHP(μ-^{t}NBu)$_2$P(Me)=N(2-py)]$_2$ **3.14**. Removal of the solvents and extraction with hexane to remove the ammoniumiodide byproduct followed by crystallisation from hexane yields analytically pure **3.14** in 75% yield. The deprotonated ligand **3.14** can also be reacted with [Mo(Piperidine)$_2$(CO)$_4$] to yield **3.13** nearly quantitative (96% isolated yield).

In a further example, reaction of **3.14** with [RhCOCl$_2$]$_2$ occurs instantaneously (with CO evolution) in $CDCl_3$. The ^{31}P NMR confirms quantitative rhodium coordination. Notably, coordination of the phosphonium salt **3.12** with [RhCl(CO)$_2$]$_2$ was not successful, with no CO evolution being observed. While the phosphorus(V) resonance remains in a similar position to that in **3.14**, we observe a large shift in the phosphorus(III) resonance from 89.3 ppm to 104.4 ppm. Layer diffusion of the concentrated reaction mixture with pentane yields yellow crystals of [(**3.14**)RhCOCl] **3.15** suitable for X-ray diffraction. The solid-state structure confirms coordination of the RhCOCl complex fragment.

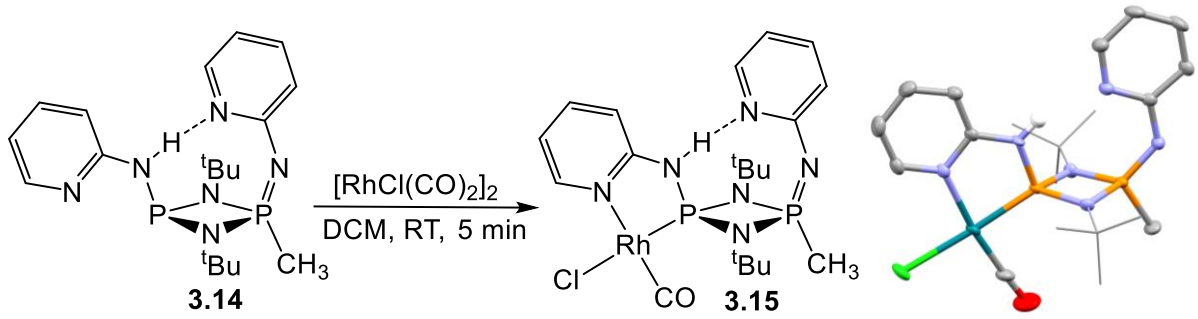

Figure 61: Left: Synthesis of **3.15.** Right: Solid-state structures of **3.15**. Ellipsoids shown at 40% probability; non-NH hydrogens omitted for clarity. Selected bond length [Å] and angles [°]: N_{exo}-P(Me) 1.562(4), N_{exo}-P(III) 1.679(2), $N_{Pyridyl}$-N_{exo} 2.948(3), P-Mo 2.153(5), N-Mo 2.118(4), N-Mo-P 82.68(2), N-P(III)-N av. 107.0, N-P(V)-N av. 122.1. Colour code: orange = P, green = Cl, dark green = Rh, blue = N, white = H, grey = C, red = O.

3.1 itself which we previously used in chloride binding and transport studies, can be deprotonated readily with strong organometallic bases (cf. deprotonation of **3.12** with much less basic NEt_3). Reaction of **3.1** with 2 equivalents of ^{n}BuLi in THF at room temperature occurs cleanly within 30 min. The in situ ^{31}P NMR spectrum shows a

singlet resonance at 120.5 ppm which is indicative of lithiation of diamino substituted cyclodiphosphazanes.[16] Storage of the concentrated reaction mixture at -14 °C for 48 h yielded crystals of the dilithiate **3.16** suitable for X-ray diffraction. In the solid-state structure, two [{(2-py)NP(μ-^{t}NBu)}$_2$Li$_2$] units form a double heterocubane (Figure 62). In each of the $P_2N_4Li_2$ units the lithium cations are coordinated by both exocyclic and one endocylic nitrogen atom of the [{(2-py)NP(μ-^{t}NBu)}$_2$]$^{2-}$ dianions. The cubane halves of the molecules are then bonded together by pyridyl-lithium interactions. This structure although related to that of previously reported [{(^{t}BuN)P(μ-N^{t}Bu)}Li$_2$]$_2$ (the lithiation product of [^{t}BuNHP(μ-N^{t}Bu)]$_2$ in toluene),[17] is subtly different, in that the presence of pyridyl donors result in a structure consisting of two separate cubane units. In [{(^{t}BuN)P(μ-N^{t}Bu)}Li$_2$]$_2$ the cubane units distort in order for two units to come together which results in breaking of two N_{exo}-Li interactions. In addition, [{(^{t}BuN)P(μ-N^{t}Bu)}Li$_2$]$_2$ is obtained from lithiation and crystallisation in non-donor toluene, whereas reaction and crystallisation in THF yields the heterocubane [^{t}BuNP(μ-N^{t}Bu)Li(THF)]$_2$ (which in the case of **3.16** yields the double cubane).

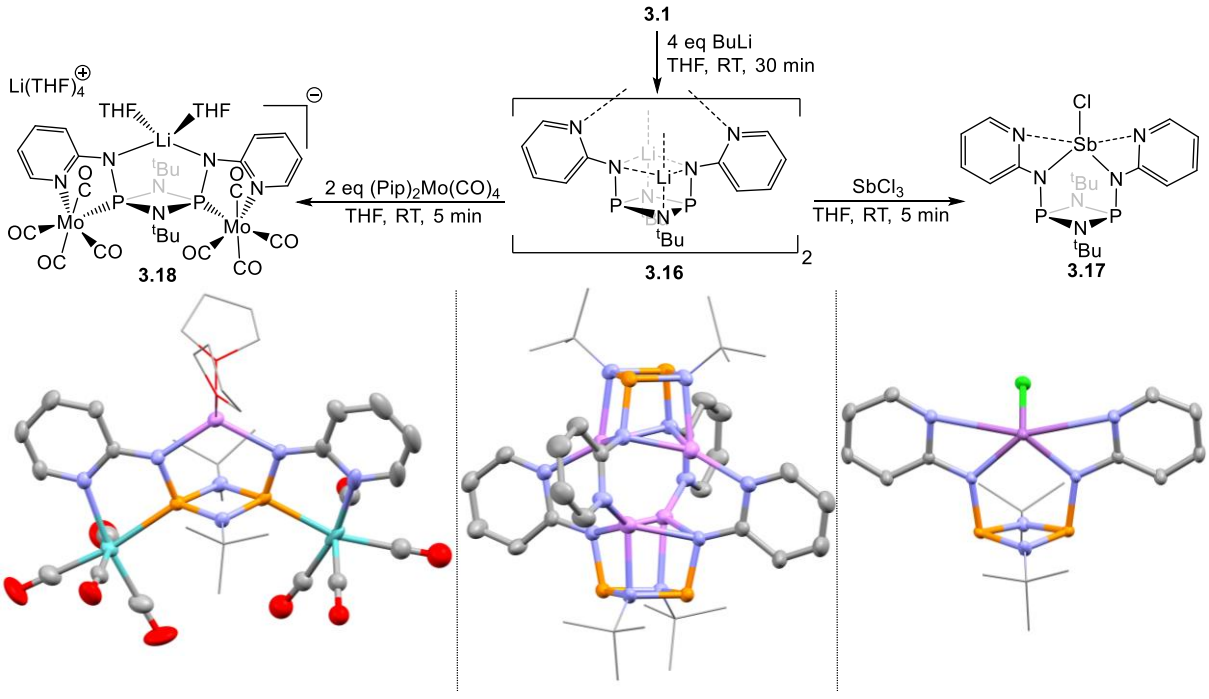

Figure 62: Top: Synthesis of **3.16**, **3.17** and **3.18**. Bottom: Solid-state structures of **3.16**, **3.17** and **3.18**. **3.17**: N_{exo}-P av. 1.71, N-Sb av. 2.10, $N_{Pyridyl}$-Sb av. 2.73, N_{endo}-Sb av. 3.45. **3.18**: N_{exo}-P av. 1.65, N_{exo}-Li av. 2.15, $N_{Pyridyl}$-Mo av. 2.28, P-Mo av. 2.50, N_{exo}-Li-N_{exo} 114.91(3), $N_{Pyridyl}$-Mo-P av. 73.5, N_{exo}-P-N_{endo} av. 105.3. Colour code: orange = P, purple = Li, dark purple = Sb, green = Cl, blue = N, white = H, grey = C, red = O.

The $[(2\text{-py})NP(\mu\text{-}^tNBu)]_2^{2-}$ dianion in **3.16** can be transferred intact to other metal centres. Reaction with $SbCl_3$ in THF quantitatively yields $\{[(2\text{-py})NP(\mu\text{-}^tNBu)]_2SbCl\}$ **3.17** as seen in the in situ ^{31}P NMR spectrum. Upon antimony coordination we observe a subtle downfield shift by ca. 8 ppm for **3.17** compared to **3.16**. The solid-state structure reveals teracoordination of a SbCl fragment by the exocyclic amido and pyridyl groups, giving a pseudo-octahedral Sb(III) centre in which one coordination site is occupied by a lone pair (Figure 62). This contrasts with the behaviour of the related derivative $\{[PhNP(\mu\text{-}^tNBu)]_2SbCl\}$ synthesised by Stahl et al. in which a tridentate N_{exo},N_{exo},N_{endo} coordination mode is observed, resulting in a trigonal bipyramidal geometry (with one position occupied by a metal lone pair).[106] However in **3.17** both N_{endo}-Sb distances (i.e, to the P_2N_2 ring nitrogens) lie outside the sum of the vdW radii, precluding such an interaction. This result shows that the $[(2\text{-py})NP(\mu\text{-}^tNBu)]_2^{2-}$ dianion can in fact act as a 8-electron donor in metal coordination.

The double cubane **3.16** can also be reacted with $(Piperidine)_2Mo(CO)_4$ achieving P,N-coordination to the $[(2\text{-py})NP(\mu\text{-}^tNBu)]_2^{2-}$ dianion which results in separation of the two heterocubanes in **3.16**. The in situ ^{31}P NMR spectrum shows a singlet at 158.8 ppm indicating quantitative molybdenum coordination. Interestingly, the solid-state structure of $Li(THF)_4\{[(Mo(CO)_4(2\text{-py})NP(\mu\text{-}^tNBu)]_2Li(THF)_2\}$ **3.18** reveals formation of a $\{[(Mo(CO)_4(2\text{-py})NP(\mu\text{-}^tNBu)]_2Li(THF)_2\}^-$ anion, which is charge balanced by a $Li(THF)_4^+$ cation (Figure 62). Hence, molybdenum coordination causes decoordination of one lithium cation per heterocubane. The ^7Li NMR spectrum is consistent with this. Whereas **3.16** shows one resonance at 3.05 ppm in d_8-THF, the ^7Li NMR of **3.18** consists of two broad singlets at -1.35 and -2.65 ppm. We suggest that molybdenum coordination increases donation of the N(endo) lone pairs into the P-N(exo) σ*-orbitals, which causes decoordination of the Li^+ cations from the endocyclic nitrogens. Additionally, this result demonstrates that $[(2\text{-py})NP(\mu\text{-}^tNBu)]_2^{2-}$ can serve as a Janus-head type ligand system for simultaneous coordination of a hard metal centre via the N_{exo} amide donors and two soft metal centres via the P,N chelate pockets. Unfortunately, attempted metathesis of **3.18** with $SbCl_3$ or reaction of **3.17** with $(Piperidine)_2Mo(CO)_4$ results in decomposition as monitored by in situ ^{31}P NMR.

Coordinating groups other than the pyridyl group can also be installed on the P_2N_2 backbone via amine condensation with $[ClP(\mu\text{-}N^tBu)]_2$ **2.1**. Reaction of **2.1** with 8-aminoquinoline yields the quinolyl functionalised phosphazane [(8-Quinolin)NHP(μ-

N^{t}Bu)]$_2$ **3.19** in 35% yield after crystallisation from toluene (Figure 63, top). The ^{31}P NMR spectrum of **3.19** in $CDCl_3$ shows a particularly broad singlet at 102.2 ppm which similarly to **3.1** results from rapid interconversion of the endo-exo and exo-exo conformers in solution. Cooling to 0 °C results in the appearance of a second broad resonance, which sharpens at -30 °C into two resonances as expected for the endo-exo conformer. Subsequent reaction of **3.19** with [RhCl(CO)$_2$]$_2$ in DCM results in near quantitative precipitation of [RhClCO(8-Quinolin)NHP(μ-N^{t}Bu)]$_2$ **3.20** (Figure 63, top). Again, we observe an AA'XX' pattern with J_{RhRh} = 0 Hz at 95.5 ppm in the ^{31}P NMR spectrum. However, in contrast to **3.5** or **3.9**, **3.20** is only soluble in DMSO, which makes it less attractive for potential applications. X-ray quality crystals of **3.20** could be obtained from a saturated 1:1 DMSO:CH_3CN mixture at 5 °C.Comparison of the solid-state structure of **3.20** with **3.5** reveals that the NH···NH distance is shortened significantly from 2.95 Å in **3.5** to 2.59 Å in **3.20**, as is the ortho-CH···CH distance from 6.74 Å in **3.5** to 5.33 Å in **3.20**, which results in a net decrease of anion-binding site volume.

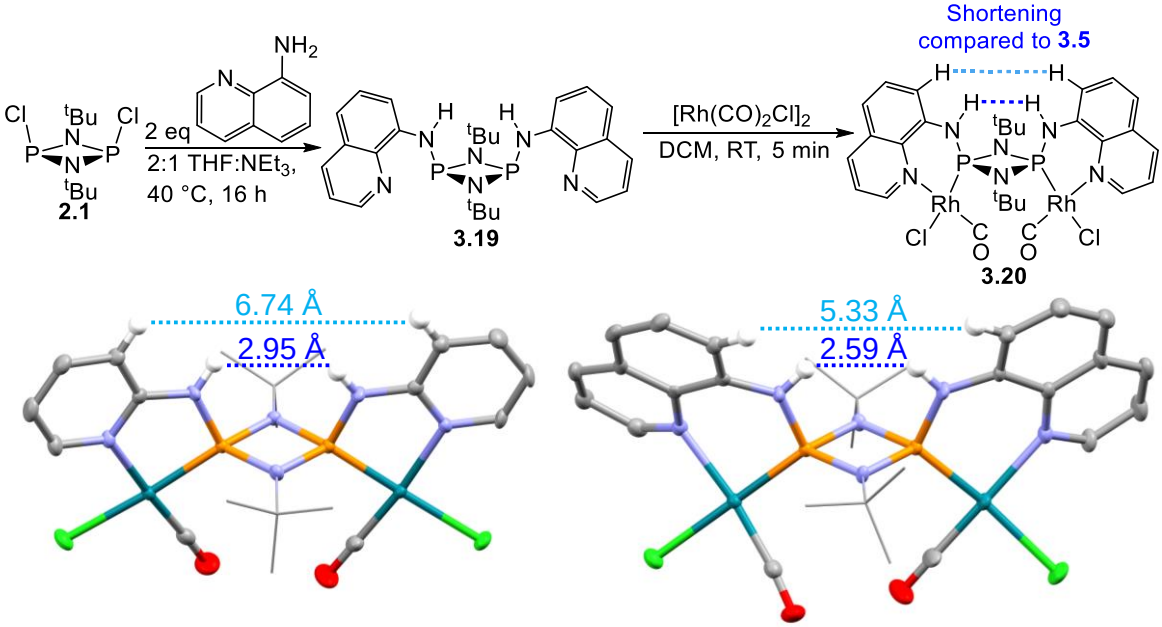

Figure 63: Top: Synthesis of **3.19** and **3.20**. Bottom: Comparison of the solid-state structures of **3.5** and **3.20**. Ellipsoids shown at 40% probability; most hydrogens omitted for clarity. Selected bond length [Å] and angles [°] of **3.20**: N_{exo}-P av. 1.66, N_{exo}-P-N_{endo} av. 106.4, P-Rh av. 2.16, $N_{Quinolyl}$-Rh av. 2.12, $N_{Quinolyl}$-Rh-P av. 91.0.

The development of the NH resonance upon ^{1}H NMR titration of **3.20** with TBACl in d_6-DMSO could be fitted to a 2:1 non-cooperative binding isotherm with K = (329 ± 11) M^{-1} (cf. **3.5** K = (1410 ± 91) M^{-1}). We conclude that **3.20** is a worse

chloride receptor than **3.5** due to the lower positive polarisation of the NH protons which is apparent from the ^{1}H NMR spectra of both in d_6-DMSO (δ(NH) = 9.35 ppm for **3.5** versus δ(NH) = 8.46 ppm for **3.20**). However, the ^{1}H NMR titration profile of **3.20** shows shifting (Δδ = 0.6 ppm) of the arylic resonance closest to the chloride binding site (highlighted in bright blue in Figure 63) which is less significant in the ^{1}H NMR titration profile of **3.5** (Δδ = 0.06 ppm). This means that aryl CH···Cl^- interactions probably contribute more to the overall binding interaction in **3.20** than in **3.5**. Hence, moving to different coordination motives directly influences the binding properties of our bimetallic phosphazane anion receptors.

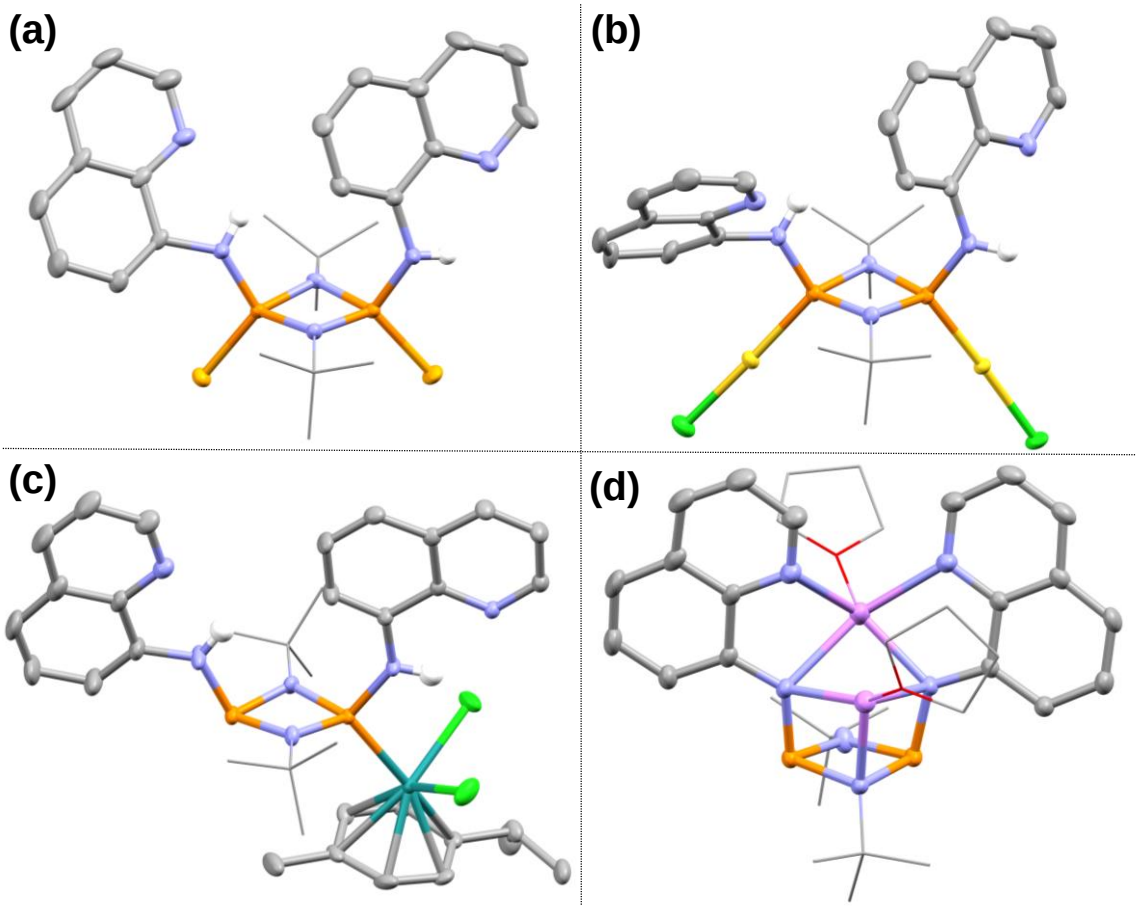

Figure 64: Solid-state structure of (a) **3.21**, (b) **3.22**, (c) **3.23** and (d) **3.24**. Thermal ellipsoids shown at 40% probability; non-NH hydrogens and lattice bound solvent molecules omitted for clarity. Selected bond length [Å] and angles [°]: (a) **3.21**: P-Se av. 2.08, P-N_{exo} av. 1.65, $C_{Quinolyl}$-N-P av. 131.3, N_{exo}-P-Se av. 111.2. (b) **3.22**: P-Au av. 2.21, P-N_{exo} av. 1.64, $C_{Quinolyl}$-N-P av. 126.7, N_{exo}-P-Au av. 111.2. (c) **3.23**: P-Ru 2.338(2), P-N_{exo} av. 1.67, $C_{Quinolyl}$-N-P av. 130.5, N_{exo}-P-Ru 107.03(3). (d) **3.24**: $N_{Quinolyl}$-Li av. 2.28, N_{exo}-Li_{penta} av. 2.18, N_{exo}-Li_{tetra} av. 2.08, P-N_{exo} 1.68, N_{endo}-Li av. 94.29(4), $N_{Quinoly}$-Li-$N_{Quinolyl}$ 97.55(2), $N_{Quinoly}$-Li-N_{exo} av. 74.0, N_{exo}-Li_{penta}-N_{exo} 88.95(3), N_{exo}-Li_{tetra}-N_{exo} 94.29(4), P-N_{endo}-Li_{tetra} av. 91.9.

The general coordination chemistry of **3.19** also differs significantly from its pyridyl analogue **3.1**. Oxidation of **3.19** with elemental Selenium quantitatively yields [(8-Quinolin)NH(Se=)P(μ-N^{t}Bu)]$_2$ **3.21**. Although the solid-state structure (Figure 64) shows that **3.21** adopts an endo-exo conformation, the ^{1}H and ^{31}P NMR spectrum show a single environment which split into two environments upon cooling to -30°C. In contrast, the ^{31}P NMR spectrum of the AuCl complex [(8-Quinolin)NH(ClAu)P(μ-N^{t}Bu)]$_2$ **3.22** (obtained from the reaction of **3.19** and 2eq (Me$_2$S)AuCl) consists of two broad singlet resonances at room temperature, which sharpen into a singlet and a doublet resonance upon cooling to -20 °C or merge into a singlet upon heating to 50 °C. Given that the solid-state structure of **3.21** and **3.22** (Figure 64) show no intramolecular H-bond between the exocyclic NH proton and the opposite quinolyl group, our results show that acidification of the NH protons by AuCl protons also shifts the conformer equilibrium in absence of a stabilising H-bond. This is probably due to increased repulsion of the NH dipoles upon AuCl coordination. Importantly these results confirm that AuCl coordination acidifies the NH protons to a greater extent than Se oxidation.

Reaction of **3.19** with 0.5 eq [(Cymene)RuCl$_2$]$_2$ results in single coordination of one phosphine centre of **3.19**. The solid-state structure of [(8-Quinolyl)NHP(μ-^{t}NBu)]$_2$[RuCl$_2$(Cymene)] **3.23** (Figure 64) shows the presence of an intramolecular H-bond between one NH proton and the chloride ligand of the (Cymene)RuCl$_2$ fragment similar to **3.10**, which is in line with the observed NH shifts in the ^{1}H NMR specrum of **3.23**. However, in contrast to **3.10**, the remaining P,N chelate pocket of **3.23** is not accessible for another ruthenium complex fragment as in the case of **3.11**. We don't observe any reaction between **3.23** and 0.5 eq [(Cymene)RuCl$_2$]$_2$ which is probably an effect of the altered geometry of **3.19** compared to **3.1**.

Finally, we subjected **3.19** to lithiation with 2 eq ^{n}BuLi in THF. Addition of ^{n}BuLi to **3.19** results in an immediate colour change of the yellow solution of **3.19** to deep red (in comparison the lithiate **3.16** is colourless). The in situ ^{31}P NMR indicates clean lithiation after 5 min at room temperature. In contrast to the lithiate **3.16**, [(8-Quinolin)NP(μ-N^{t}Bu)Li(THF)]$_2$ **3.24** does not dimerise in the solid-state (Figure 64) but forms a monomeric structure related to the heterocubane [^{t}BuNP(μ-N^{t}Bu)Li(THF)]$_2$. Whereas one Li$^+$ cation is tetracoordinated by both exocyclic amide nitrogens, one endocyclic P$_2$N$_2$ nitrogen and a THF solvent molecule, the other Li$^+$ cation is pentacoordinated by both exocyclic amide nitrogens, both quinolyl nitrogens and a THF solvent molecule.

Chapter Conclusion

In conclusion we have shown that integration of a N-donor in pyridyl functionalised phophazanes provides a means of controlling the conformation of diaminophosphazanes, via metal coordination to the P-atoms. This conformational control was first indicated by Se oxidation or AuCl coordination, which shifts the observed conformation away from the exo-exo towards the endo-exo conformation. Choosing the right metal fragment can fix the receptor in the exo-exo form, efficiently polarising the NH H-bond donor atoms and stabilising the P_2N_2 backbone for applications under ambient and biologically relevant conditions. We also find that anion coordination affects the donor properties and solubility of the phosphazane receptors. Our new strategy results in halide affinity constants approximately one order of magnitude higher than the previously best phosphazane receptor. Lastly, our design allowed us to apply phosphazane metal complexes in anion transport across a lipid bilayer exceeding the transport activities of the corresponding thioureas, selenophosphazanes and squareamides in the case of **3.9**. Our study also revealed that the integration of a metal complex into the bilayer heavily depends on the coordinated complex fragment. Furthermore, we showed that the potential of **3.1** to undergo H-bonding dictates its coordination chemistry. Methylation allows selective chelate coordination to one P,N binding pocket, whereas the presence of exocyclic pyridyl donors leads to the formation of an unprecedented double cubane structure upon lithiation, tetradentate Sb and Janus-head type Li,Mo,Mo coordination. Installation of quinolyl donors subtly modulates the chloride binding pocket which results in greater participation of the arylic protons in anion binding and significantly different coordination chemistry.

Experimental Details

General experimental details involving techniques, instruments and materials employed are provided in the appendix at the end of this thesis

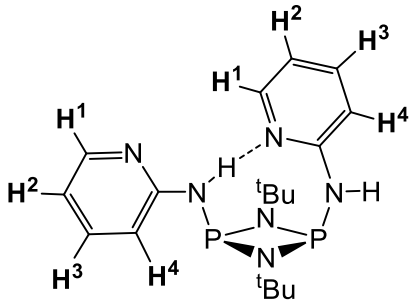

Synthesis of 3.1: Inside a N_2 filled glovebox a Schlenk tube was charged with **2.1** (2.75 g, 10 mmol) and transferred to a Schlenk line. 20 ml of THF and 2-Aminopyridine (1.88 g, 20 mmol, 2 equivalents) in 20 ml THF and 20 ml Et_3N were added subsequently at room temperature. The resulting mixture was then stirred overnight at 40 °C. Afterwards the solvent was removed in vacuo and the resulting solid mixture was extracted with 80 ml of hexane. The solvent was removed in vacuo until the precipitation of a white solid was observed which was gently heated back into solution. Storage of the solution at -20 °C led to the formation of colourless crystal suitable for X-ray diffraction which were isolated by filtration and dried in vacuo to yield **3.1** as a colourless crystalline powder (1.25 g, 3.23 mmol, 32%); **^{1}H NMR (25 °C, CD_3Cl, 500 MHz):** δ [ppm] = 8.18 (d, 2H, $^3J_{HH}$ = 5.1 Hz, H1), 7.51 – 7.43 (m, 2H, H3), 6.94 (d, 2H, $^3J_{HH}$ = 8.5 Hz, H4), 6.72 (dd, 2H, $^3J_{HH}$ = 7.1 Hz, $^3J_{HH}$ = 5.0 Hz,H2), 6.15 (bs, 2H, NH), 1.25 (s, 18H, ^{t}Bu); **^{31}P NMR (25 °C, CD_3Cl, 202 MHz)**: δ [ppm] = 106.38 (s); **Elemental analysis (%)**: calcd. for **3.1**: C 55.4, H 7.2, N 21.5; found: C 55.7, H 7.4, N 21.3

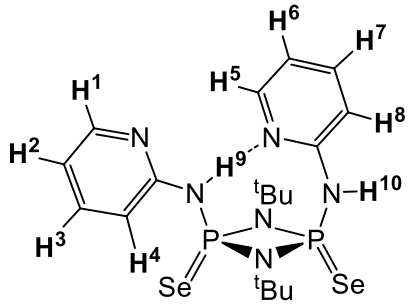

Synthesis of 3.2: Inside a N_2 filled glovebox a Schlenk tube was charged with **3.1** (200 mg, 0.52 mmol) and Selenium (156 mg, 2 mmol) and transferred to a Schlenk line. 20 ml of THF were added and the mixture was stirred at room temperature. The progress of the oxidation was monitored via in situ ^{31}P NMR spectroscopy. After completion excess Selenium was removed via filtration and the solvent was removed in vacuo yielding **3.2** as an air stable white solid (275 mg, 98%). **^{1}H NMR (25 °C, d_6-DMSO, 500 MHz):** δ [ppm] = 10.68 (d, $^4J_{HH}$ = 7.0 Hz, 1H, NH), 9.46 (d, $^3J_{HH}$ = 18 Hz, 1H, H1), 8.72 (d, J_{HH}= 3.9 Hz, 1H, H7), 8.32 (d, J_{HH}= 3.9 Hz, 1H, H4), 8.14 (d, J_{HH}= 8.5 Hz, 1H, H8), 7.85 – 7.69 (m, 2H, NH, H5), 7.21 -7.00 (m, 3H,

remaining), 1.41 (s, 18H, ^{t}Bu); **^{31}P NMR (25 °C, d$_6$-DMSO, 202 MHz)**: δ [ppm] = 27.8 (d accompanied by ^{77}Se satellites, $^{1}J_{PSe}$ = 434.5 Hz,$^{2}J_{PP}$ = 18.7 Hz), 21.5 (d accompanied by ^{77}Se satellites, $^{1}J_{PSe}$ = 437.1 Hz,$^{2}J_{PP}$ = 18.7 Hz); **Elemental analysis (%)**: calcd. for **3.1**: C 39.4, H 5.1, N 15.3; found: C 39.4, H 5.2, N 14.7

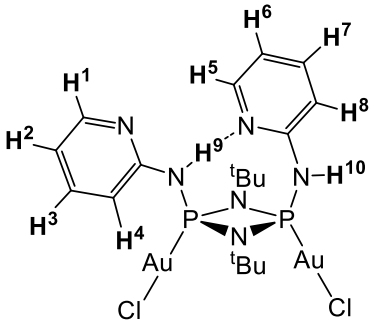

Synthesis of 3.3: Inside a N_2 filled glovebox a Schlenk tube was charged with **3.1** (50 mg, 0.13 mmol) and $(Me_2S)AuCl_2$ (76 mg, 0.26 mmol) and transferred to a Schlenk line. 3 ml of THF were added and the mixture was stirred at room temperature for 10 min. Afterwards the reaction mixture was concentrated to approximately 1 ml and layered with 10 ml of Pentane. Storage of this mixture at room temperature for 72h in the dark yields colourless crystals suitable for X-ray diffraction which where isolated by filtration and dried in vacuo to yield **3.3** as a white crystalline solid (94 mg, 0.11 mmol, 84%). **^{1}H NMR (25 °C, d$_8$-THF, 400 MHz):** δ [ppm] = 10.14 (d, $^{4}J_{HH}$ = 7.0 Hz, 1H, H9), 9.01 (d, $^{3}J_{HH}$ = 18 Hz, 1H, H5), 8.60 (d, J_{HH}= 3.9 Hz, 1H, H2), 8.30 (bs, 1H, H10), 7.80 – 7.62 (m, 3H, H4, H2, H6), 7.17 – 7.94 (m, 3H, remaining), 1.54 (s, 18H, ^{t}Bu); **^{31}P NMR (25 °C, d$_8$-THF, 202 MHz)**: δ [ppm] = 80.7 (bs), 69.1 (bs); No suitable elemental analysis could be obtained.

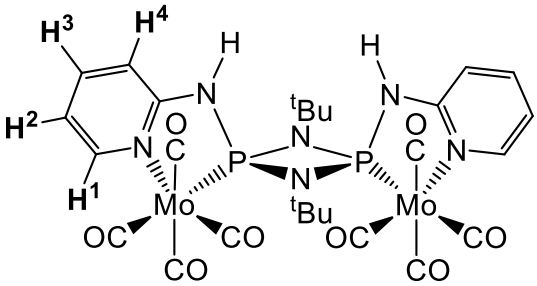

Synthesis of 3.4: Inside a N_2 filled glovebox a Schlenk tube was charged with **3.1** (200 mg, 0.52 mmol) and $(CO)_4Mo(Piperidine)_2$ (412 mg, 1.10 mmol) and transferred to a Schlenk line. 50 ml of DCM were added and the mixture was stirred at 40 °C for 2h . Afterwards all solvent was removed in vacuo and the resulting yellow residue was dissolved in 40 ml of warm CH_3CN. The solvent was removed in vacuo until the precipitation of a yellow solid was observed which was gently heated back into solution. Storage of the solution at -20 °C led to the formation of yellow crystals suitable for X-ray diffraction which were isolated by filtration and dried in vacuo to yield **3.4·CH$_3$CN** as a yellow crystalline powder (152 mg, 0.19 mmol, 36.3%). **^{1}H NMR**

(25 °C, d_6-DMSO, 500 MHz): δ [ppm] = 9.10 (bs, 2H, NH), 8.41 (d, 2H, $^3J_{HH}$= 5.5 Hz, H1), 7.79 (t, 2H, $^3J_{HH}$ = 7.3 Hz, H3), 6.95 (d, 2H, $^3J_{HH}$= 5.5 Hz, H4), 6.88 (t, 2H, $^3J_{HH}$ = 6.8 Hz, H2), 1.48 (s, 18H, ^{t}Bu); **^{31}P NMR (25 °C, d_6-DMSO, 202 MHz)**: δ [ppm] = 137.9 (s); **Elemental analysis (%)** calcd. for **3.4·CH_3CN:** C 39.7, H 3.7, N 11.5; found C 41.0, H 4.5, N 10.9

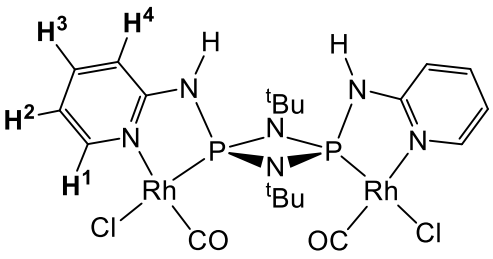

Synthesis of 3.5: Inside a N_2 filled glovebox a Schlenk tube was charged with **3.1** (100 mg, 0.26 mmol) and $Rh_2(CO)_4Cl_2$ (101 mg, 0.26 mmol) and transferred to a Schlenk line. 20 ml of DCM were added and the mixture was stirred at room temperature for 30 min. All volatiles were removed in vacuo yielding **3.5** as a yellow powder which was recrystallised from CH_3CN/DMSO solution yielding **3.5·DMSO** as yellow crystals suitable for X-ray diffraction (110 mg, 0.15 mmol, 59%). **^{1}H NMR (25 °C, CD_2Cl_2, 500 MHz):** δ [ppm] = 8.96 (bs, 2H, H1), 8.86 (bs, 2H, NH), 7.69 (pt, 2H, $^3J_{HH}$= 7.7 Hz, H3), 7.25 (d, 2H, $^3J_{HH}$= 7.7 Hz, H4), 7.69 (pt, 2H, $^3J_{HH}$= 7.7 Hz, H2), 1.65 (s, 18H, ^{t}Bu);**^{31}P NMR (25 °C, CD_2Cl_2, 202 MHz)**: δ [ppm] = 106.0-108.0 (m); **Elemental analysis (%)** calcd. for **3.5·DMSO:** C 33.0, H 4.3, N 10.5; found: C 33.3, H 4.3, N 10.7.

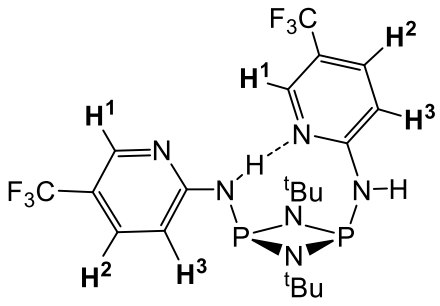

Synthesis of 3.6: Inside a N_2 filled glovebox a Schlenk tube was charged with **2.1** (2.75 g, 10 mmol) and transferred to a Schlenk line. 20 ml of THF and 2-Amino-5-(trifluoromethyl)pyridine (3.24g, 20 mmol, 2 equivalents) in 20 ml THF and 20 ml Et_3N were added subsequently at room temperature. The resulting mixture was then stirred overnight at 40 °C. Afterwards the solvent was removed in vacuo and the resulting solid mixture was extracted with 80 ml of hexane. The solvent was removed in vacuo until the precipitation of a white solid was observed which was gently heated back into solution. Storage of the solution at -20 °C led to the formation of colourless crystal suitable for X-ray diffraction which were isolated by filtration and dried in vacuo to yield **3.6** as a colourless crystalline powder (1.81 g, 3.48 mmol, 35%). **^{1}H NMR (25 °C, CD_3Cl, 500 MHz):** δ [ppm] = 8.48 (s, 2H, H1), 7.70 (dd, 2H, $^2J_{HH}$= 8.6 Hz, $^4J_{HH}$= 2.6 Hz H2), 7.02 (d, 2H, $^3J_{HH}$ = 8.6 Hz, H3), 6.62 (bs, 2H,

NH), 1.26 (s, 18H, ^{t}Bu); **^{31}P NMR (25 °C, CD_3Cl, 202 MHz)**: δ [ppm] = 109.79 (s); **Elemental analysis (%)** calcd. for **3.6:** C 45.6, H 5.0, N 15.9; found: C 45.6, H 5.1, N 15.8.

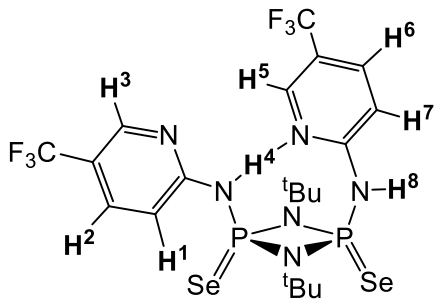

Synthesis of 3.7: Inside a N_2 filled glovebox a Schlenk tube was charged with **3.6** (100 mg, 0.19 mmol) and selenium (150 mg, excess) and transferred to a Schlenk line. 20 ml of THF were added and the mixture was stirred at room temperature. The progress of the oxidation was monitored via in situ ^{31}P NMR spectroscopy. After completion excess Selenium was removed via filtration and the solvent was removed in vacuo yielding **3.6** as an air stable white solid (130 mg, quantitative). **^{1}H NMR (25 °C, CD_3Cl, 400 MHz):** δ [ppm] = 10.67 (d, $^{2}J_{PH}$ = 6.3 Hz, 1H, H4), 9.23 (s, 1Hm H7), 8.56 (s, 1H, H3), 8.50 (d, $^{3}J_{HH}$ = 8.8 Hz, 1H, H2), 7.93 (d, $^{3}J_{HH}$ = 8.5 Hz, 1H, H6), 7.83 (d, $^{3}J_{HH}$ = 8.8 Hz, 1H, H1), 7.83 (d, $^{3}J_{HH}$ = 8.5 Hz, 1H, H7), 6.56 (d, $^{2}J_{PH}$ = 15.5 Hz, 1H, H8) , 1.59 (s, 18H, ^{t}Bu); **^{31}P NMR (25 °C, CD_3Cl, 202 MHz)**: δ [ppm] = 26.3 (d accompanied by ^{77}Se satellites, $^{1}J_{PSe}$ = 914.5 Hz,$^{2}J_{PP}$ = 19.3 Hz), 21.9 (d accompanied by ^{77}Se satellites, $^{1}J_{PSe}$ = 916.5 Hz,$^{2}J_{PP}$ = 19.0 Hz); **Elemental analysis (%)** calcd. for **3.7:** C 35.1, H 3.8, N 12.3; found: C 35.1, H 3.9, N 11.6.

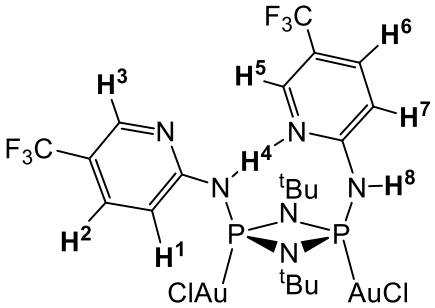

Synthesis of 3.8: Inside a N_2 filled glovebox a Schlenk tube was charged with **3.6** (100 mg, 0.19 mmol) and (THT)AuCl (121 mg, 0.38 mmol) and transferred to a Schlenk line. 5 ml of DCM were added and the mixture was stirred at room temperature for 10 minutes. Afterwards all volatiles were removed in vacuo and the product was washed with pentane yielding **3.8** as a colourless solid (185 mg, 99%). **^{1}H NMR (25 °C, $CDCl_3$, 400 MHz):** δ [ppm] = 10.12 (d, $^{2}J_{PH}$ = 9.1 Hz, 1H, H4), 8.88 (s, 1H,H7), 8.64 (s, 1H, H3), 8.58 (d, $^{2}J_{PH}$ = 22.5 Hz, 1H, H8), 8.00 (d, $^{3}J_{HH}$ = 8.8 Hz, 1H, H2), 7.94 (d, $^{3}J_{HH}$ = 8.5 Hz, 1H, H6), 7.79 (d, $^{3}J_{HH}$ = 8.8 Hz, 1H, H1), 7.24 (d, $^{3}J_{HH}$ = 8.5 Hz, 1H, H7), 1.56 (s, 18H, ^{t}Bu); **^{31}P NMR (25 °C,**

$CDCl_3$, 202 MHz): δ [ppm] =80.5 (d, J_{PP}= 14 Hz), 68.1 (d, J_{PP}= 14 Hz); **Elemental analysis (%)** calcd. for **3.8:** C 24.2, H 2.6, N 8.4; found: C 24.9, H 2.8, N 7.7.

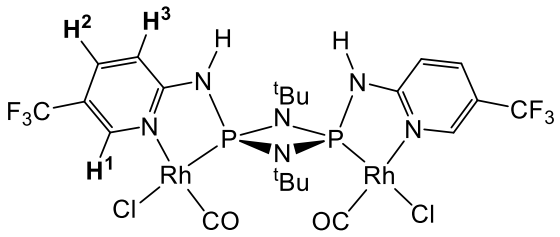

Synthesis of 3.9: Inside a N_2 filled glovebox a Schlenk tube was charged with **3.6** (100 mg, 0.18 mmol) and $Rh_2(CO)_4Cl_2$ (70 mg, 018) and transferred to a Schlenk line. 20 ml of DCM were added and the mixture was stirred at room temperature for 30 min. All volatiles were removed in vacuo yielding **3.9** as a yellow powder (141 mg, 0.16 mmol, 88%). **^{1}H NMR (25 °C, d_6-DMSO, 500 MHz):** δ [ppm] = 9.94 (s, 2H, NH), 9.35 (s, 2H, H1), 8.29 (dd, 2H, $^3J_{HH}$ = 8.8 Hz, $^4J_{HH}$ = 1.9 Hz, H2), 7.27 (d, 2H, $^3J_{HH}$ = 8.8 Hz, H3), 1.53 (s, 18H, ^{t}Bu); **^{31}P NMR (25 °C, d_6-DMSO, 202 MHz)**: δ [ppm] = 110.1-108.4 (m); **Elemental analysis (%)** calcd. for **3.9:** C 30.9, H 3.1, N 9.8; found C 30.8, H 3.1, N 9.2.

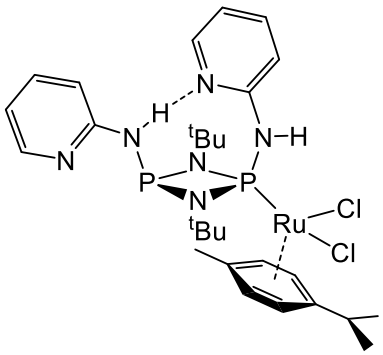

Synthesis of 3.10: Inside a N_2 filled glovebox a Schlenk tube was charged with **3.1** (20 mg, 0.05 mmol) and Dichloro(cymene)ruthenium(II)dimer (16 mg, 0.025 mmol) and then transferred to a Schlenk line. 2 ml of DCM were added and the resulting red solution was stirred for 10 minutes at room temperature. All volatiles were removed in vacuo yielding **3.10** as a red solid (36 mg, quantitative). X-ray quality crystals were grown from layer diffusion of a concentrated DCM solution with Hexane. **^{1}H NMR (25 °C, CD_2Cl_2 , 400 MHz):** δ [ppm] = 10.88 (d,$^2J_{PH}$ = 4.0 Hz, 1H, NH), 8.50 (dd, $^3J_{HH}$ = 5.0 Hz, $^4J_{HH}$ = 1.7 Hz, py), 8.22 (dd, $^3J_{HH}$ = 5.0 Hz, $^4J_{HH}$ = 1.7 Hz, py), 7.58 – 7.49 (m, 2H, py), 7.11 – 6.95 (m, 2H, NH, py), 6.91 (ddd, $^3J_{HH}$ = 7.1 Hz, $^3J_{HH}$ = 5.0 Hz, $^4J_{HH}$ = 1.0 Hz, py), 6.77 (ddd, $^3J_{HH}$ = 7.1 Hz, $^3J_{HH}$ = 5.0 Hz, $^4J_{HH}$ = 1.0 Hz, py), 6.48 (d,$^2J_{PH}$ = 6.5 Hz, 1H, py), 5.65 (d,$^2J_{PH}$ = 6.0 Hz, 2H, ArH), 4.96 (d,$^2J_{PH}$ = 6.0 Hz, 2H, ArH), 3.19 (dq, $^3J_{HH}$ = 7.0 Hz, $^4J_{HH}$ = 1.5 Hz, 1H, ^{i}PrCH), 2.30 (s, 3H, Me), 1.38 (d, $^3J_{HH}$ = 7.0 Hz, 6H, ^{i}PrMe), 1.34 (s, 18H, ^{t}Bu); **^{31}P NMR (25 °C, CD_2Cl_2 , 202 MHz):** δ [ppm] = 111.6 (d, $^2J_{PP}$ = 23.1 Hz), 89.5 (d, $^2J_{PP}$ = 23.1 Hz). **Elemental analysis (%)** calcd. for **3.10:** C 48.2, H 6.0, N 12.0; found C 47.2, H 6.0, N 10.9.

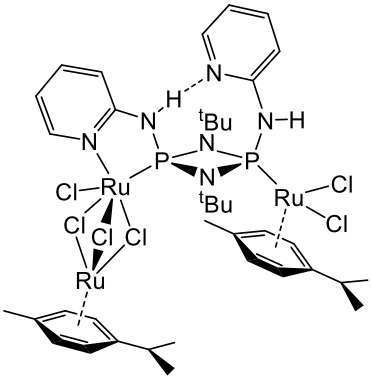

Synthesis of 3.11: Inside a N_2 filled glovebox a Youngs tab NMR tube was charged with **3.1** (20 mg, 0.05 mmol) and dichloro(cymene)ruthenium(II)dimer (32 mg, 0.05 mmol) and 0.7 ml CD_2Cl_2 were added. The resulting mixture was analysed by NMR showing two environments in the **^{1}H NMR (25 °C, $CDCl_3$, 400 MHz)** and the **^{31}P NMR (25 °C, $CDCl_3$, 202 MHz)**. After 24h at room temperature dark red crystals of **3.11** suitable for X-ray diffraction formed at the bottom of the NMR tube.

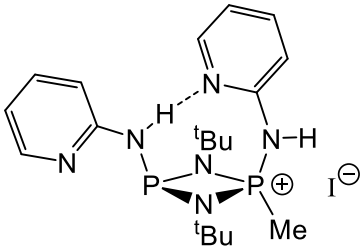

Synthesis of 3.12: Inside a N_2 filled glovebox a Schlenk tube was charged with **3.1** (1.0 g, 2.56 mmol) and then transferred to a Schlenk line. 25 ml of hexane and 1 ml of iodomethane (excess) were added and the resulting solution was stirred for 16 hours at 60 °C during which a colourless precipitate formed. The precipitate was isolated by filtration, washed with 50 ml pentane and dried in vacuo yielding **3.12** (1.0 g, 1.92 mmol ,75%) as a colourless solid. X-ray quality crystals were grown from layer diffusion of a concentrated DCM solution with hexane. **^{1}H NMR (25 °C, $CDCl_3$, 400 MHz):** δ [ppm] = 10.42 (s, 1H, NH), 9.45 (d, $^2J_{HP}$ = 3.6 Hz, 1H, NH), 8.48 (d, $^3J_{HH}$ = 4.5 Hz, 1H, py), 8.23 (d, $^3J_{HH}$ = 4.5 Hz, 1H, py), 7.91 (d, $^3J_{HH}$ = 8.2 Hz, 1H, py), 7.73 (t, $^3J_{HH}$ = 7.8 Hz, 1H, py), 7.57 (t, $^3J_{HH}$ = 7.8 Hz, 1H, py), 7.17 (t, $^3J_{HH}$ = 5.8 Hz, 1H, py), 6.92 (d, $^3J_{HH}$ = 7.9 Hz, 1H, py), 6.86 (t, $^3J_{HH}$ = 5.9 Hz, 1H, py), 2.62 (d, $^2J_{PH}$ = 15.4 Hz, 3H, PMe), 1.32 (s, 18H, ^{t}Bu); **^{31}P NMR (25 °C, $CDCl_3$, 202 MHz):** δ [ppm] = 97.1 (d, $^2J_{PP}$= 7.0 Hz, P(III)), 32.3 (d, $^2J_{PP}$= 7.0 Hz, P(V)); **Elemental analysis (%)** calcd. for **3.12:** C 42.8, H 5.8, N 15.7; found: C 41.4, H 5.8, N 14.9.

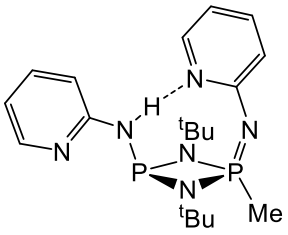

Synthesis of 3.14: Inside a N_2 filled glovebox a Schlenk tube was charged with **3.12** (532 mg, 1.00 mmol) and then transferred to a Schlenk line. 25 ml of THF and 5 ml of NEt_3 (excess) were added and the resulting solution was stirred for 30 min at room temperature during which a colourless precipitate formed. All volatiles were removed in vacuo and the the mixture was extracted with 25 ml of

toluene to remove the Et_3NHI. The filtrate was collected and all volatiles were removed in vacuo yielding **3.12** as a colourless solid (400 mg, 99%). **^{1}H NMR (25 °C, $CDCl_3$, 400 MHz):** δ [ppm] = 9.92 (d, $^2J_{PH}$ = 2.5 Hz, 1H, NH), 8.29 (d, $^3J_{HH}$ = 5.0 Hz, 1H, py), 8.22 (d, $^3J_{HH}$ = 5.0 Hz, 1H, py), 7.47 (t, $^3J_{HH}$ = 7.5 Hz, 1H, py), 7.42 (t, $^3J_{HH}$ = 7.5 Hz, 1H, py), 6.85 (d, $^3J_{HH}$ = 8.0 Hz, 1H, py), 6.75 – 6.64 (m, 3H, py), 1.89 (d, $^2J_{PH}$= 16.1 Hz, 3H, PMe), 1.27 (s, 18H, ^{t}Bu); **^{31}P NMR (25 °C, $CDCl_3$, 202 MHz):** δ [ppm] = 89.3 (s, P(III)), 24.6 (s, P(V)); **Elemental analysis (%)** calcd. for **3.14:** C 56.4, H 7.5, N 20.7; found: C 56.6, H 7.5, N 20.3.

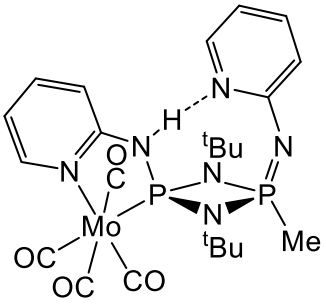

Synthesis of 3.13: Inside a N_2 filled glovebox a Schlenk tube was charged with **3.14** (100 mg, 0.25 mmol) and $(Piperidine)_2Mo(CO)_4$ (94 mg, 0.25 mmol, 1 eq) and then transferred to a Schlenk line. 25 ml of DCM were added and the resulting solution was stirred for 30 min at room temperature. Afterwards all volatiles were removed in vacuo and the resulting solid was washed with 25 ml of Pentane and dried in vacuo yielding **3.13** as a yellow solid (150 mg, 0.24 mmol, 96%). X-ray quality crystals were grown from layer diffusion of a DCM solution with hexane. **^{1}H NMR (25 °C, $CDCl_3$, 400 MHz):** δ [ppm] = 10.08 (s, 1H, NH), 8.46 (d, $^3J_{HH}$ = 5.0 Hz, 1H, py), 8.12 (d, $^3J_{HH}$ = 5.0 Hz, 1H, py), 7.60 – 7.35 (m, 2H, py), 6.85 – 6.70 (m, 3H, py), 6.64 (t, $^3J_{HH}$ = 6.5 Hz, 1H, py), 2.05 (d, $^2J_{PH}$= 15.8 Hz, 3H, PMe), 1.42 (s, 18H, ^{t}Bu); **^{31}P NMR (25 °C, $CDCl_3$, 202 MHz):** δ [ppm] = 133.1 (d, $^2J_{PP}$ = 18 Hz, P(III)), 22.2 (d, $^2J_{PP}$ = 18 Hz, P(V)); no suitable elemental analysis could be obtained.

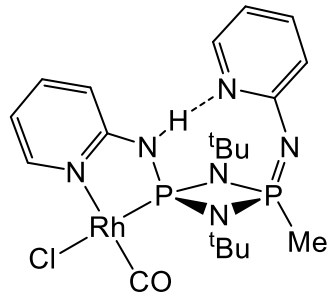

Synthesis of 3.15: Inside a N_2 filled glovebox a Schlenk tube was charged with **3.14** (100 mg, 0.25 mmol) and $Rh_2Cl_2(CO)_4$ (50 mg, 0.13 mmol, 0.5 eq) and then transferred to a Schlenk line. 25 ml of DCM were added and the resulting solution was stirred for 30 min at room temperature. Afterwards the mixture was filtered and the concentrated filtrated was layered with hexane. After 4 days large yellow crystals were obtained suitable for X-ray crystallography, which were isolated and dried in vacuo yielding **3.15** as a yellow crystalline solid (81 mg, 0.14 mmol, 57%). **^{1}H NMR (25 °C,**

$CDCl_3$, 400 MHz): δ [ppm] = 9.79 (s, 1H, NH), 9.16 (d, $^3J_{HH}$ = 5.8 Hz, 1H, py), 8.10 (d, $^3J_{HH}$ = 5.8 Hz, 1H, py), 7.69 (tt, $^3J_{HH}$ = 7.0 Hz, ^4J = 1.5 Hz, 1H, py), 7.53 (t, $^3J_{HH}$ = 7.5 Hz, 1H, py), 6.95 – 6.75 (m, 4H, py), 2.01 (d, $^2J_{PH}$= 15.8 Hz, 3H, PMe), 1.45 (s, 18H, ^{t}Bu). **^{31}P NMR (25 °C, $CDCl_3$, 202 MHz):** δ [ppm] = 104.4 (dd, $^1J_{RhP}$ = 229 Hz, $^2J_{PP}$ = 16 Hz, P(III)), 15.7 (s, P(V)); no suitable elemental analysis could be obtained.

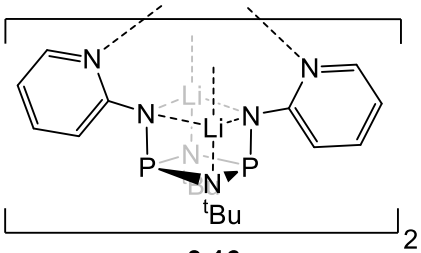

3.16

Synthesis of 3.16: Inside a N_2 filled glovebox a Schlenk tube was charged with **3.1** (390 mg, 1 mmol) and then transferred to a Schlenk line. 25 ml of THF were added and 1.25 ml of ^{n}BuLi (1.6M in hexane, 2 mmol, 2 eq) were added dropwise. The resulting yellow solution was stirred at room temperature for 30 min. Afterwards all volatiles were removed in vacuo yielding **3.16** as a faint yellow solid (405 mg, quantitative). X-ray quality crystals were grown from a concentrated THF solution at -14 °C.**^{1}H NMR (25 °C, d_8-toluene , 400 MHz):** δ [ppm] = 7.78 (d, $^3J_{HH}$ = 7.5 Hz, 2H, py), 7.50 (t, $^3J_{HH}$ = 7.5 Hz, 2H, py), 7.24 (d, $^3J_{HH}$ = 7.5 Hz, 2H, py), 7.01 (d, $^3J_{HH}$ = 7.5 Hz, 2H, py), 1.40 (s, 18H, ^{t}Bu); **^{31}P NMR (25 °C, d_8-toluene, 202 MHz):** δ [ppm] = 120.5 (s); **^{7}Li NMR (25 °C, d_8-toluene, 194 MHz):** δ [ppm] = 2.95 (s); no suitable elemental analysis could be obtained.

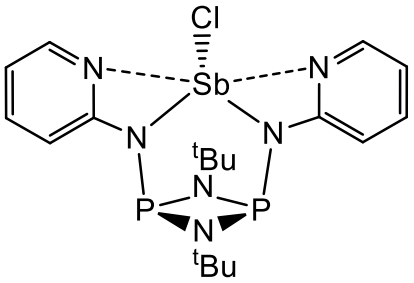

Synthesis of 3.17: Inside a N_2 filled glovebox a Schlenk tube was charged with **3.1** (390 mg, 1 mmol) and then transferred to a Schlenk line. 25 ml of THF were added and 1.25 ml of ^{n}BuLi (1.6 M in hexane, 2 mmol, 2 eq) were added dropwise. The resulting yellow solution was stirred at room temperature for 30 min. Afterwards a solution of $SbCl_3$ (228 mg, 1 mmol, 1 eq) in 10 ml THF was added dropwise causing the formation of a fine white precipitate. The resulting suspension was stirred for 5 min at room temperature. Afterwards all volatiles were removed in vacuo and the solid residue was extracted with 40 ml of toluene and filtered. All volatiles were removed in vacuo yielding **3.17** as an off-white powder (542mg, quantitative). X-ray quality crystals were grown from a saturated toluene solution at -14 °C.**^{1}H NMR (25 °C, d_8-toluene , 400 MHz):** δ [ppm] = 7.65 (d, $^3J_{HH}$ = 7.5 Hz, 2H,

py), 7.41 (t, $^3J_{HH}$ = 7.5 Hz, 2H, py), 7.32 (d, $^3J_{HH}$ = 7.5 Hz, 2H, py), 6.93 (d, $^3J_{HH}$ = 7.5 Hz, 2H, py), 1.42 (s, 18H, ^{t}Bu); **^{31}P NMR (25 °C, d$_8$-toluene, 202 MHz):** δ [ppm] = 129.2 (s); **Elemental analysis (%)** calcd. for **3.17:** C 39.6, H 4.8, N 15.4; found: C 39.5, H 4.8, N 14.9.

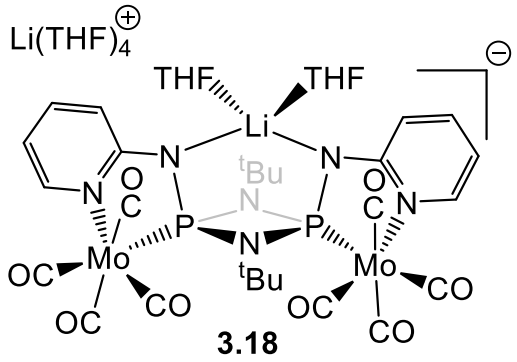

3.18

Synthesis of 3.18: Inside a N_2 filled glovebox a Schlenk tube was charged with **3.16** (50 mg, 0.06 mmol) and (Piperidine)$_2$Mo(CO)$_4$ (47 mg, 0.12 mmol, 2 eq) and then transferred to a Schlenk line. 5ml of THF were added and the resulting solution was stirred for 10 min at room temperature during which the colour turned orange. The reaction mixture was concentrated in vacuo to ca. 1.5 mol and then layered with 20ml of hexane. Storage over 3 d yielded yellow crystals suitable for X-ray diffraction which were isolated and dried in vacuo yielding **3.18** as a yellow crystalline solid (62 mg, 0.05 mmol, 79%). **^{1}H NMR (25 °C, d$_8$-THF, 400 MHz):** δ [ppm] = 8.34 (d, $^3J_{HH}$ = 7.4 Hz, 2H, py), 7.01 (t, $^3J_{HH}$ = 7.5 Hz, 2H, py), 7.43 (d, $^3J_{HH}$ = 7.5 Hz, 2H, py), 5.88 (d, $^3J_{HH}$ = 7.5 Hz, 2H, py), 3.61 (m, 24H, THF), 1.77 (m, 24H, THF), 1.50 (s, 18H, ^{t}Bu); **^{31}P NMR (25 °C, d$_8$-THF, 202 MHz)**: δ [ppm] = 158.8 (s); **^{7}Li NMR (d$_8$-THF, 25 °C, 194 MHz):** δ[ppm] = -1.35 (s), -2.65 (s); **Elemental analysis (%)** calcd. for **3.18:** C 49.4, H 5.8, N 6.5; found: C 49.0, H 5.8, N 5.9.

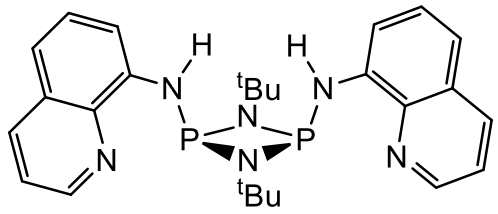

Synthesis of 3.19: Inside a N_2 filled glovebox a Schlenk tube was charged with **2.1** (1.0 g, 3.6 mmol) and transferred to a Schlenk line. 20 ml of THF and 8-Aminoquinolin (1.2 g, 7.2 mmol, 2 equivalents) in 20 ml THF and 20 ml Et_3N were added subsequently at room temperature. The resulting mixture was then stirred overnight at 40 °C.Afterwards the solvent was removed in vacuo and the resulting solid mixture was extracted with 80 ml of hexane. The solvent was removed in vacuo until the precipitation of a faint yellow solid was observed which was gently heated back into solution. Storage of the solution at -20 °C led to the formation of faint yellow crystals which were isolated by filtration and dried in vacuo to yield **3.19** as a colourless crystalline powder (0.90 g, 1.86 mmol, 52%); **^{1}H NMR (25 °C, CD$_3$Cl, 500 MHz):** δ

[ppm] = 8.86 (d, 2H, $^3J_{HH}$ = 4.5 Hz, Qu), 8.10 (d, 2H, $^3J_{HH}$ = 7.0 Hz, Qu), 7.87 (bs, 2H, Qu), 7.74 (bs, 2H, Qu), 7.50 (t, 2H, $^3J_{HH}$ = 7.0 Hz, Qu), 7.40 (dd, 2H, $^3J_{HH}$ = 7.5 Hz, $^3J_{HH}$ = 6.9 Hz, Qu), 7.28 (d, 2H, $^3J_{HH}$ = 7.0 Hz, Qu), 1.23 (s, 18H, ^{t}Bu); **^{31}P NMR (25 °C, CD_3Cl, 202 MHz)**: δ [ppm] = 102.20 (s); no suitable elemental analysis could be obtained.

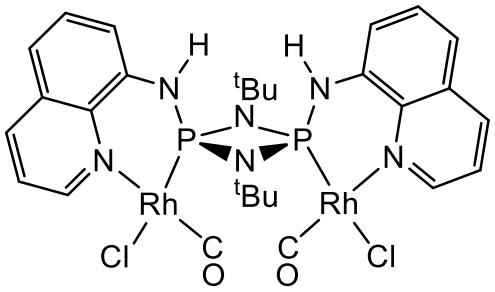

Synthesis of 3.20: Inside a N_2 filled glovebox a Schlenk tube was charged with **3.19** (100 mg, 0.21 mmol) and $Rh_2(CO)_4Cl_2$ (80 mg, 0.21 mmol) and transferred to a Schlenk line. 10 ml of DCM were added and the mixture was stirred at room temperature for 30 min during which a yellow powder precipitated. The precipitate was isolated by centrifugation and dried in vacuo yielding **3.20**·DCM as a yellow powder (163 mg, 0.20 mmol, 95%). **^{1}H NMR (25 °C, d_6-DMSO, 500 MHz):** δ [ppm] = 9.82 (d, 2H, $^3J_{HH}$ = 6.0 Hz, Qu), 8.60 (d, 2H, $^3J_{HH}$ = 7.0 Hz, Qu), 8.46 (bs, 2H, NH), 7.72-7.58 (m, 3H, Qu), 7.47 (d, 2H, $^3J_{HH}$ = 7.0 Hz, Qu),1.60 (s, 18H, ^{t}Bu);**^{31}P NMR (25 °C, d_6-DMSO, 202 MHz)**: δ [ppm] = 96.3-94.6 (m); **Elemental analysis (%)** calcd. for **3.20:** C 38.3, H 3.7, N 9.2; found: C 37.9, H 3.8, N 9.0.

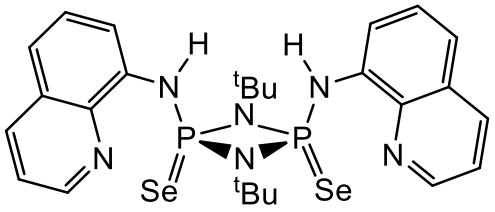

Synthesis of 3.21: Inside a N_2 filled glovebox a Schlenk tube was charged with **3.19** (200 mg, 0.40 mmol) and Selenium (200 mg, excess) and transferred to a Schlenk line. 20 ml of THF were added and the mixture was stirred at room temperature. The progress of the oxidation was monitored via in situ ^{31}P NMR spectroscopy. After completion excess Selenium was removed via filtration and the solvent was removed in vacuo yielding **3.2** as an air stable white solid (265 mg, quantitative). **^{1}H NMR (25 °C, $CDCl_3$, 400 MHz):** δ [ppm] = 8.83 (d, 2H, $^3J_{HH}$ = 4.7 Hz, Qu), 8.75 (bs, 2H, Qu), 8.39 (bs, 2H, NH), 8.18 (d, 2H, $^3J_{HH}$ = 6.5 Hz, Qu), 7.50 – 7.47 (m, 6H, Qu), 1.60 (s, 18H, ^{t}Bu); **^{31}P NMR (25 °C, CD_3Cl, 202 MHz)**: δ [ppm] = 26.7 (d accompanied by ^{77}Se satellites, $^1J_{PSe}$ = 903.9 Hz,$^2J_{PP}$ = 27.4 Hz); **Elemental analysis (%)** calcd. for **3.21:** C 48.2, H 5.0, N 13.0; found: C 47.9, H 5.0, N 12.7.

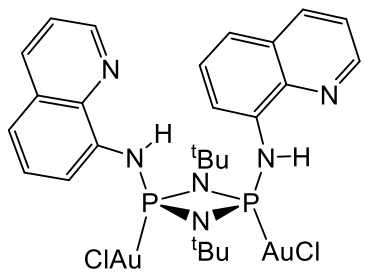

Synthesis of 3.22: Inside a N_2 filled glovebox a Schlenk tube was charged with **3.19** (50 mg, 0.1 mmol) and (THT)AuCl (64 mg, 0.2 mmol) and transferred to a Schlenk line. 5 ml of DCM were added and the mixture was stirred at room temperature for 10 minutes. Afterwards the reaction mixture was layered with 10 ml of Pentane. Storage over 72h at room temperature yielded yellow crystals suitable for X-ray diffraction which where isolated by filtration and dried in vacuo yielding **3.22** as a crystalline solid (90 mg, 0.09 mmol, 95%).**^{1}H NMR (25 °C, $CDCl_3$, 400 MHz):** δ [ppm] = 8.88 (d, $^2J_{HH}$ = 3.7 Hz, 1H, Qu), 8.49 (bs, 1H, NH), 8.29 (bs, 1H, NH), 8.24 (d, $^3J_{HH}$ = 8.3 Hz, 1H, Qu), 7.70 - 7.50 (m, 3H, Qu), 1.56 (s, 9H, ^{t}Bu); **^{31}P NMR (25 °C, $CDCl_3$, 202 MHz)**: δ [ppm] = 74.8 (bs), 71.2.1 (bs); No suitable elemental analysis could be obtained.

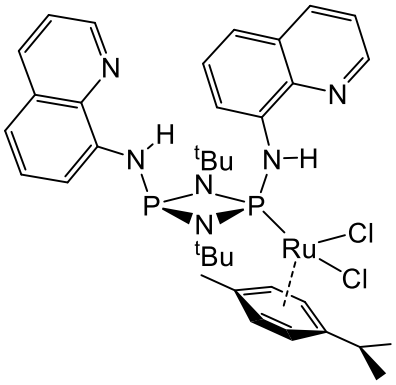

Synthesis of 3.23: Inside a N_2 filled glovebox a Schlenk tube was charged with **3.19** (50 mg, 0.1 mmol) and Dichloro(cymene)ruthenium(II)dimer (32 mg, 0.05 mmol) and then transferred to a Schlenk line. 2 ml of DCM were added and the resulting red solution was stirred for 10 min at room temperature. Afterwards the reaction mixture was layered with 10 ml of Pentane. Storage over 72h at room temperature yielded red crystals suitable for X-ray diffraction which where isolated by filtration and dried in vacuo yielding **3.23**·2DCM as a crystalline solid (75 mg, 0.09 mmol, 92%). **^{1}H NMR (25 °C, $CDCl_3$, 400 MHz):** δ [ppm] = 9.15 (d, $^2J_{PH}$ = 22.8 Hz, 1H, NH), 8.89 (d, $^3J_{HH}$ = 3.8 Hz, 2H, Qu), 8.61 (d, $^3J_{HH}$ = 7.9 Hz, 1H, Qu), 8.47 (d, $^3J_{HH}$ = 7.9 Hz, 1H, Qu), 8.14 (d, $^3J_{HH}$ = 7.9 Hz, 1H, Qu), 8.02 (d, $^3J_{HH}$ = 7.9 Hz, 1H, Qu), 7.80 – 7.70 (m, 2H, Qu), 7.52 – 7.38 (m, 5H, NH, Qu), 5.66 (d, $^3J_{HH}$ = 5.9 Hz, 2H, Cymene), 5.13 (d, $^3J_{HH}$ = 5.9 Hz, 2H, Cymene), 3.33 (quin, $^3J_{HH}$ = 7.0 Hz, 1H, CymeneCH), 2.39 (s, 3H, CymeneCH$_3$), 1.47 – 1.35 (m, 24H, ^{t}Bu, CymeneCH$_3$); **^{31}P NMR (25 °C, $CDCl_3$, 202 MHz):** δ [ppm] = 97.3 (d, $^2J_{PP}$ = 26.0 Hz), 88.5 (d, $^2J_{PP}$ = 26.0 Hz). **Elemental analysis (%)** calcd. for **3.23**·2DCM**:** C 47.7, H 5.4, N 8.6; found: C 46.6, H 5.5, N 9.5.

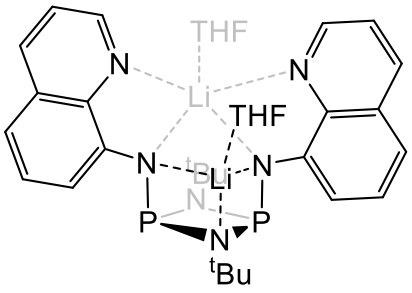

Synthesis of 3.24: Inside a N_2 filled glovebox a Schlenk tube was charged with **3.19** (400 mg, 0.82 mmol) and then transferred to a Schlenk line. 20 ml of THF were added and 1.02 ml of ^{n}BuLi (1.6 M in hexane, 1.64 mmol, 2 eq) were added dropwise. The resulting red solution was stirred at room temperature for 30 min. All volatiles were removed in vacuo yielding **3.24** as a red solid (525 mg, quantitative). Single crystals suitable for X-ray diffraction were grown from a THF:hexane mixture at -14°C. **^{1}H NMR (25 °C, d$_8$-THF, 400 MHz):** δ [ppm] = 8.04 (d, 2H, $^{3}J_{HH}$ = 4.0 Hz, Qu), 7.62 (d, 2H, $^{3}J_{HH}$ = 7.2 Hz, Qu), 7.10 (bs, 2H, Qu), 7.05 (t, 2H, $^{3}J_{HH}$ = 7.2 Hz, Qu), 6.55 – 6.35 (m, 4H, Qu), 1.30 (s, 18H, ^{t}Bu); **^{31}P NMR (25 °C, CD$_3$Cl, 202 MHz)**: δ [ppm] = 120.1 (s); **^{7}Li NMR (d$_8$-THF, 25 °C, 194 MHz):** δ[ppm] = 2.50 (s); no suitable elemental analysis could be obtained.

Chapter 4: Formation and Selection of the Macrocycle [{^{t}BuN=)P(μ-N^{t}Bu)}$_2$(μ-Se)$_2${P(μ-N^{t}Bu)}$_2$]$_3$

Having shown that phosphazanes of the type [RNH(Se)P(μ-N^{t}Bu)]$_2$ can be functional anion receptors (Chapter 2), we were curious to see whether they can also be structural building blocks in the formation of macrocycles. This chapter explores this potential.

Results and Discussion

With a new methodology in hand which selectively yields the cis-isomer of [^{t}BuNH(Se=)P(μ-N^{t}Bu)]$_2$ **2.3** (see Chapter 2) we investigated the use of this molecule as a precursor for macrocycle formation. Deprotonation of **2.3** with NaHMDS in THF followed by the addition of the electrophilic P(III) building block [ClP(μ-N^{t}Bu)]$_2$ **2.1** gives regioselective formation of the new Se-bridged macrocycle [{(tBuN=)P(μ-N^{t}Bu)}$_2$(μ-Se)2{P(μ-N^{t}Bu)}$_2$]$_3$ **4.1**, as revealed by in situ ^{31}P NMR spectroscopy (Figure 65). Crystalline **4.1** is obtained as the solvate **4.1**·4toluene from a toluene solution at -20 °C.

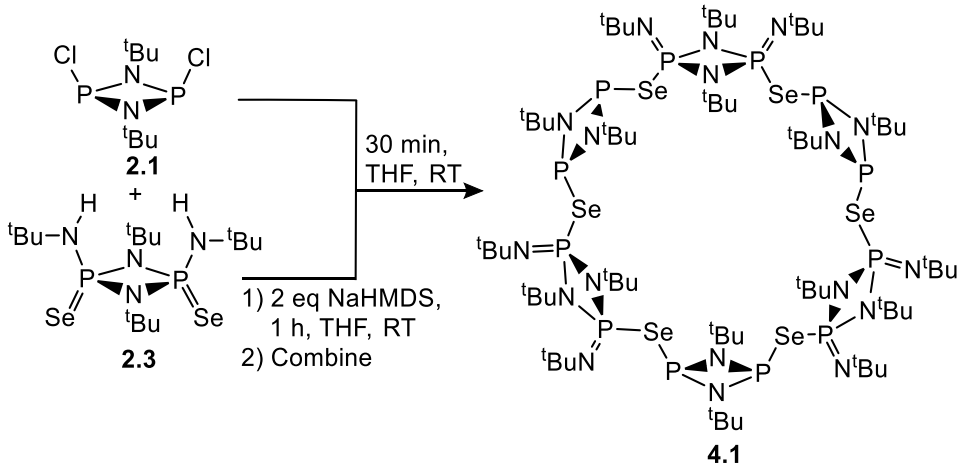

Figure 65 :Formation of the macrocycle **4.1** from the nucleophilic and electrophilic components **2.3** and **2.1**.

The incorporation of P(III) and P(V) units into the backbone of **4.1** is seen by the presence of two distinct (1:1), pseudo-triplet resonances at δ = 243.4 P(III) and -66.4 ppm P(V) in the room temperature ^{31}P NMR spectrum in CD_3Cl

($^2J_{PP}$ = 7.9 Hz), together with doublet ^{77}Se satellites (Figure 66). The single crystal X-ray structure of **4.1** confirms the main conclusions drawn from the NMR spectroscopic studies. The molecular structure consists of six P_2N_2 ring units bridged by Se atoms into a macrocyclic arrangement (Figure 67). The disposition of the P_2N_2 ring constituents, roughly perpendicular to the macrocyclic mean plane, and the overall connectivity of **4.1** are very similar to the features observed previously in the closely related macrocycles derived from Se-functionalised (see Chapter 1). The roughly cylindrical cavity of **4.1** measures ca. 8.08 Å in diameter (measured Se•••Se) and 6.3 Å in depth (i.e., ^{t}Bu to ^{t}Bu) and has similar dimensions to the previously reported Se-bridged macrocycle [{(S=)P(μ-N^{t}Bu)}$_2$(μ-Se)$_2${P(μ-N^{t}Bu)}$_2$]$_3$ (Figure 23) (with corresponding dimensions 8.18 and 6.6 Å).[52]

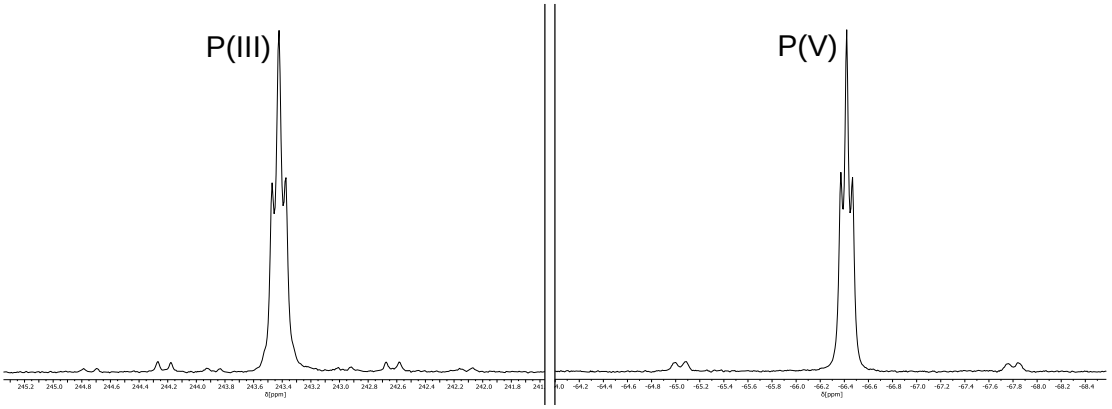

Figure 66: ^{31}P NMR spectra of **4.1** ($CDCl_3$, 25 °C, 202 MHz).

The observed Se-bridging in **4.1** is, at least on a kinetic level, not surprising since the dianion [(^{t}BuN)(Se)P(μ-N^{t}Bu)]$_2^{2-}$ has been shown previously to react as a facial, Se-centred nucleophile with a range of electrophiles.[23] The selective formation of a large [{P_2N_2}(μ-Se)]$_6$ arrangement is due to the preference for P-Se-P angles that are well below the normal value for sp^3 hybridisation at Se (reflecting the higher s-character of the Se lone pairs). The result is that smaller P-Se-P bridged macrocycles are disfavoured due to ring strain. However, this assembly is clearly entropically-disfavoured compared to the alternative formation of a ^{t}BuN-bridged arrangement containing a [{P_2N_2}(μ-N)]$_2$ core, as is seen (for example) in the formation of [{P(μ-N^{t}Bu)}$_2$(μ-N^{t}Bu)]$_2$ in the reaction of **2.1** with the phosph(III)azane dianion [(^{t}BuN)P(μ-N^{t}Bu)]$_2^{2-}$ (with ca. 130.2 ° macrocyclic N-bridge angles).[17] The reason for the preference for the Se-bridged macrocycle over the ^{t}BuN bridged arrangement is probably due to a desire to minimise ring strain, while at the same time maximise bond

energy (with stronger P=N double and P-Se single bonds in **4.1** compared to a weaker P-N single and P=Se double bond combination in the ^{t}BuN-bridged alternative).

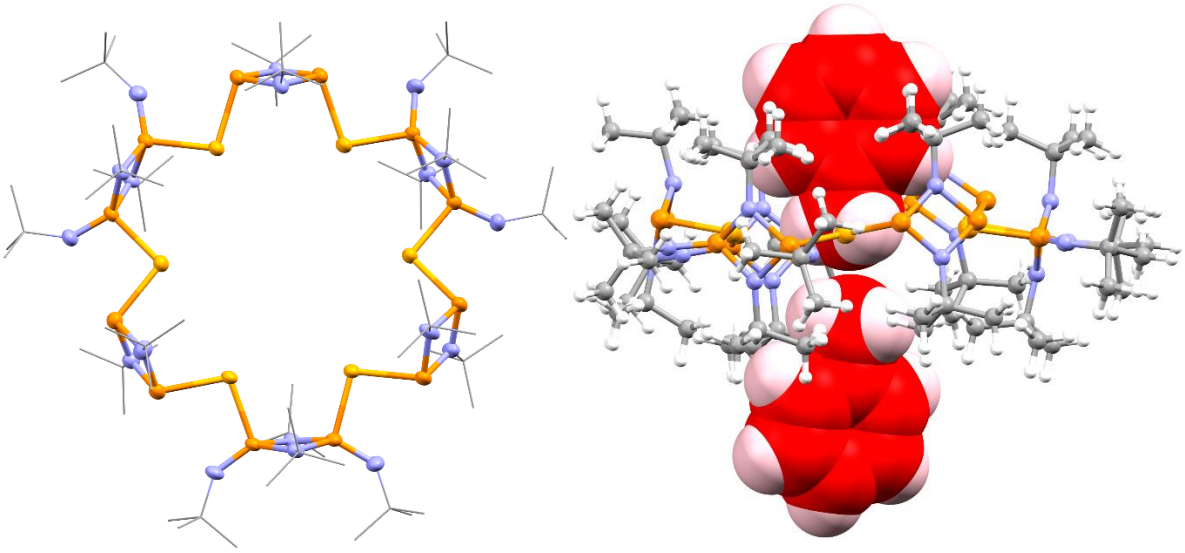

Figure 67: Left: Structure of the macrocycle **4.1**. H-atoms and toluene molecules in the lattice are omitted for clarity. Selected bond lengths [Å] and angles [°]: P(III)-Se range 2.3392(9)-2.3485(1), P(V)-Se range 2.2402(9)-2.2475(9), P(III)-μ-N range 1.702(3)-1.728(3), P(V)-μ-N range 1.697(3)-1.717(3), P=N^{t}Bu$_{terminal}$ range 1.510(3)-1.518(3), Se•••Se range (opposite) range 7.84-8.18 (mean 8.08), P(III)-μ-N-P(III) range 97.8(1)-99.4(1), (μ-)N-P(III)-(μ-)N range 80.7(1)-81.6(1), P(V)-μ-N-P(V) range 96.6(1)-97.1(1), (μ-)N-P(V)-(μ-)N range 82.5(1)-83.0(1), P(V)-N-C(^{t}Bu) range 138.6(3)-144.4(3), P(III)-Se-P(V) range 99.11(3)-101.07(3). Colour code: orange = P, blue = N, dark orange = Se, grey = C; Right: Host-guest complex formed in the solid state, guest toluene molecules highlighted in red.

Although for steric reasons the P_2N_2 ring units of **4.1** are buckled out of the mean plane of the macrocyle, the six Se-atoms are within 0.04 Å of a plane. The arrangement provides the host environment for two of the four toluene molecules in the solvate (Figure 67), with the remaining two residing in the lattice. This provides a possible reason for the greater lability of two of the four toluene molecules of the solvate when placed under vacuum. The host-guest interactions in **4.1** appear to be largely hydrophobic in origin. Similar toluene inclusion has also been found in related S-bridged phosphazane macrocyles and is analogous to toluene clatherates of calixarenes, such as in [p-^{t}Bu-OH-calix[4]arene•toluene], with the toroidal environment in **4.1** being conceptually similar to a cucurbituril.[27,107]

Chapter Conclusion

In summary, we have shown that the strategy of combining electrophilic and nucleophilic phosphazane components can be extended to the valence isoelectronic $[(^tBuN=)SeP(\mu\text{-}N^tBu)]_2^{2-}$ building block. There are a number of advantages in this, (i) the key starting material $[(^tBuNH)(Se=)P(\mu\text{-}N^tBu)]_2$ **2.3** is readily prepared, highly stable and can be stored indefinitely, it can be activated simply by deprotonation and (ii) the presence of ^{t}BuN groups at the periphery of **4.1** makes it highly soluble in an extended range of solvents (including pentane), which should greatly aid in further studies of host-guest chemistry.

Experimental Details

General experimental details involving techniques, instruments and materials employed are provided in the appendix at the end of this thesis

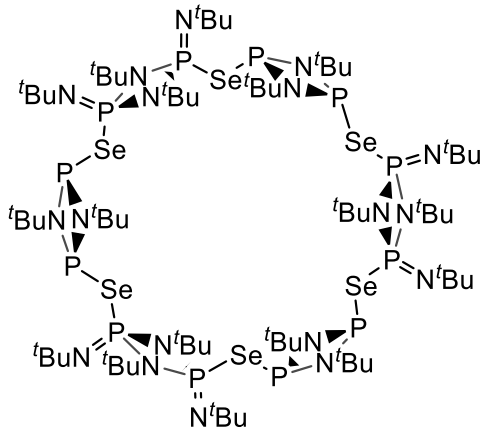

Synthesis of 4.1: A Schlenk tube was charged with **2.3** (506 mg, 1 mmol) which was dissolved in 20 ml THF. To this 2 ml (2 mmol) of a 1 M NaHMDS solution in THF was added dropwise at room temperature. The resulting yellow solution was stirred for 30 min at room temperature. To this **2.1** (275 mg, 1 mmol) in 5 ml THF was added dropwise. The reaction mixture was stirred for 30 min at room temperature; afterwards THF was removed in vacuo. The solid residue was extracted with 20 ml of toluene and filtered in order to remove NaCl. The toluene solution was concentrated in vacuo until the precipitation of a precipitate was observed which was redissolved by gentle heating. Storage at -20 °C afforded **4.1** as colourless crystals which was isolated by filtration and dried in vacuo. Subjecting the crystalline material to prolonged vacuum (0.1 bar, ca. 20 min) results in complete desolvation of the crystalline material (**4.1**·4toluene), giving **4.1** (250 mg 0.35 mmol, 35% yield), on which the following data were obtained; **^{1}H NMR (25 °C, CD_3Cl, 500.12 MHz)**: δ(ppm) = 1.32 (s, 9H, P(III)N^{t}Bu), 1.44 (s, 9H, P(V)N^{t}Bu), 1.70 (s, 9H, P=N^{t}Bu); **^{13}C NMR (25 °C, CD_3Cl, 125.78 MHz)**: δ(ppm) = 29.9, 31.6, 33.9 (d, $^{2}J_{CP}$ = 10.0 Hz, P=N^{t}Bu), 53.12, 53.7, 55.7; **^{31}P{^{1}H}NMR (25 °C, CD_3Cl, 161.7 MHz):** δ [ppm] = -66.4 (t, $^{2}J_{PP}$= 7.9 Hz, accompanied with a set doublet ^{77}Se sattelites $^{1}J_{PSe}$= 406 Hz, $^{3}J_{PSe}$= 14.1 Hz, P(V) unit), 243.4 (t, $^{2}J_{PP}$= 7.9 Hz, accompanied with a set doublet ^{77}Se sattelites $^{1}J_{PSe}$= 347 Hz, $^{3}J_{PSe}$= 14.1 Hz, P(III) unit); **^{77}Se NMR (25 °C, CD_3Cl, 95.4 MHz):** δ [ppm] = 526.8 (ddd, $^{1}J_{PSe}$= 406 Hz, $^{1}J_{PSe}$= 347 Hz, $^{3}J_{PSe}$= 14.1 Hz); Satisfactory elemental analysis could only be obtained on the partially desolvated material **4.1**·2toluene, isolated after subjecting the crystalline material **4.1**·4toluene to a vacuum for ca. 5–10 min, calc. C 44.7%, H 7.7%, N 10.9%; found C 45.7%, H 7.8%, N 11.1%.

Chapter 5: The Supramolecular Chemistry of NH Bridged Phosphazane Macrocycles

Although a multitude of phosphazane macrocycles are now synthetically available, the solution host-guest chemistry of this new class of encapsulants has not been fully explored. Although there is crystallographic evidence for the encapsulation of Cl^-, Br^-, I^- and DCM using the NH H-bond donor macrocyle $[\{P(\mu\text{-}N^tBu)\}_2(NH)]_5$ **5.1**, little is known about the host-guest chemistry of this and related phosphazane macrocycles.[45] Since we established in Chapters 2 and 3 that NH functionalities render phosphazanes potent in anion binding we were particularly interested in the binding properties of **5.1**.

Results and Discussion

The previously reported synthesis of $[\{P(\mu\text{-}NtBu)\}_2(NH)]_5$ **5.1** involves a multistep reaction sequence in which the nucleophilic component $[NH_2P(\mu\text{-}N^tBu)]_2$ is condensed with the electrophilic building block $[ClP(\mu\text{-}N^tBu)]_2$ **2.1** in the presence of Et_3N and an excess of LiI, product of this reaction being the host-guest complex $Li(THF)_4$[**5.1**⊂I] obtained in 44% yield (see Chapter 1). However, this is a time-consuming procedure and the synthesis of **5.1** also involves the use of NH_3 gas.[44] Our first objective at the beginning of studies in this thesis was therefore to develop a more direct protocol. An in situ ^{31}P NMR study shows that the 1:2 reaction of **2.1** with $LiNH_2$ in THF at 70 °C for 16 h in the presence of excess anhydrous LiI (2 eq per **2.1**) gives a mixture containing 90% $Li(THF)_4$[**5.1**⊂I] and 10% other unidentified byproducts; The complex can be recovered as a powder by extraction with pentane, in 40% yield (Figure 68). Treatment with NaOMe in DCM and crystallisation from THF gives the halide free macrocycle **5.1**•THF. The solid-state structure of **5.1**•Et_2O, obtained by crystallisation of **5.1**•THF from Et_2O, provides the first glimpse of the free macrocycle, in the absence of a guest solvent or anion within its cavity (Figure 68). This reveals that molecules of **5.1** have C_s symmetry (as opposed to C_{5v} symmetry as in some previously published host guest complexes). This is in agreement with previous gas-phase DFT calculations.[45] The approximately cylindrical coordination cavity of **5.1** determined from the solid-state

structure measures ca. 5.3 Å in diameter (NH···HN) by ca. 4.7 Å in height (with a volume of 105 Å^3), making it accessible for H-bonding to a range of common anions. A key difference between **5.1** and the closest organic relatives calixpyrrols is that the H-bonding binding site is sterically shielded by the ^{t}Bu groups of the backbone.[108]

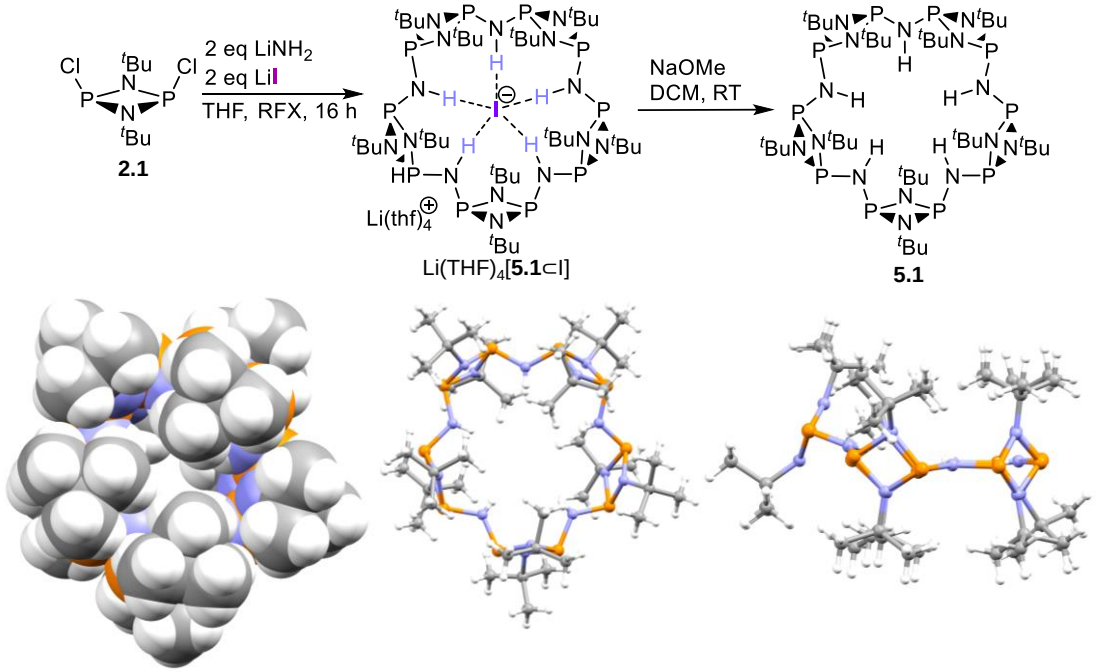

Figure 68: The new synthetic route and molecular structure of **5.1** in the solvate **5.1**•Et_2O. Top: Synthesis of **5.1**. Bottom: X-ray crystal structure of **5.1**•Et_2O; the lattice Et_2O molecule is omitted for clarity. Colour code: blue = N, orange = P, white = H, grey = C.

The presence of iodide as a template in the synthesis of **5.1** (as in the previously reported synthesis) proves to be crucial. In the absence of LiI we observe that also the tetrameric macrocyle [{P(μ-N^{t}Bu)}$_2$(NH)]$_4$ **5.2** is formed alongside other unidentified byproducts (Figure 69). We were able to further investigate the mode of templation of the pentamer **5.1** at this point. During the course of this study we found that the previously reported synthesis of tetramer **5.2** from the reaction of [ClP(μ-^{t}BuN)]$_2$ **2.1** and [H_2NP(μ-^{t}BuN)]$_2$ **5.3** in fact yields an initial mixture of products from which **5.2** is then crystallised out. The in situ ^{31}P NMR spectrum of the crude reaction mixture of **2.1** and **5.3** shows a sharp singlet for **5.2** alongside multiple resonance which we tentatively assign to linear oligomeric species (Figure 70). We conclude that these are N-terminated as we observe no resonances above 150 ppm which would be characteristic of P-Cl termini. Upon addition of an excess of variety of anions (Cl^- , Br^-, I^-, OAc^-, OCN^-,SCN^-, OCP^-) at room temperature in THF we observe the spontaneous

formation of the pentamer **5.1** exclusively from the cyclisation of the chain oligomers. This was confirmed by integration versus an internal PPh_3 reference to rule out formation of **5.1** from **5.2**. From this result we conclude that the primary mode of formation in our new synthesis of **5.1** is thermodynamic templation from chain oligomers which initially form from **2.1** and $LiNH_2$. Notably, the fact that pseudohalides and acetate template the formation of **5.1** hints at the encapsulation of these anions in solution.

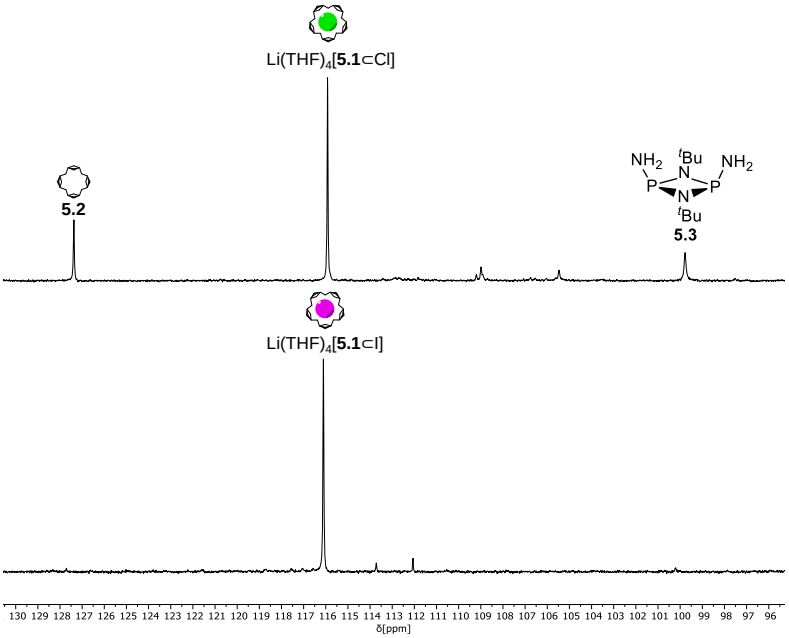

Figure 69: In situ ^{31}P NMR (THF, d_6-acetone capillary, 25 °C, 202 MHz) of the product mixture in absence (top) and presence (bottom) of excess LiI.

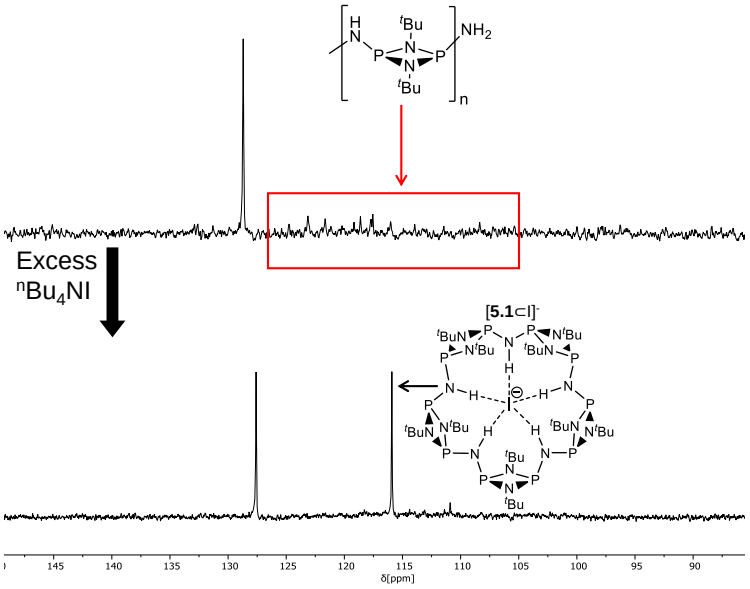

Figure 70: In situ ^{31}P NMR (THF, d_6-acetone capillary, 25 °C, 202 MHz) spectra before and after addition of TBAI to oligomeric byproducts.

Consequently, we then explored the coordination of common anionic guests by **5.1**. There has been an indication of relative binding of anions from previous DFT calculations which suggested the order $Cl^- > Br^- > I^-$.[45] Unfortunately, **5.1** proved too unstable for quantitative measurement of binding constants by NMR spectroscopic methods. However, negative-ion LRESI-MS of THF solutions of **5.1** containing excess $^nBu_4N^+X^-$ ($X^- = F^-, Cl^-, Br^-, I^-, OCN^-, SCN^-, AcO^-$) shows that the 1:1 complexes [**5.1**⊂X]$^-$ are formed. Examples are given in Figure 71 . Assuming similar ESI response factors for the host-guest complexes, we conducted a series of competitive binding experiments. This is a reasonable assumption given the geometry similarity of these complexes.

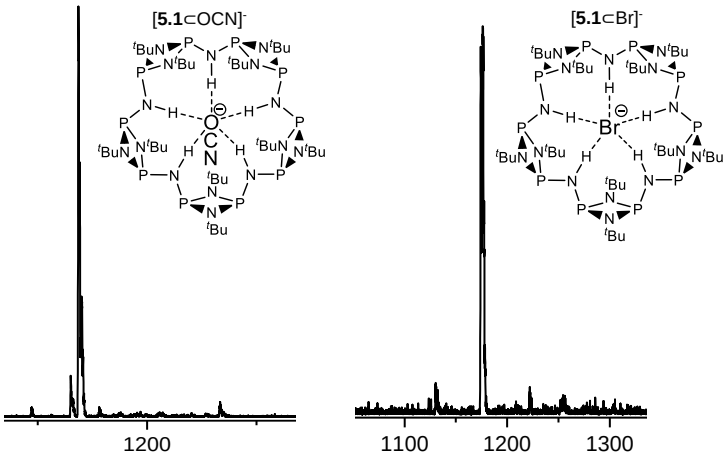

Figure 71: Examples of negative mode LRESI-mass spectra of **5.1** in presence of excess TBAX (X = OCN^- and Br^-) salts.

We collected negative-mode LRESI-mass spectra of **5.1** in presence of 10 equivalents of two different anions as their TBA salts under the same conditions as above (concentration and MS voltage). In some cases we observed a clear preferences for binding of **5.1** to one anion whereas in others we observed the formation of both host-guest species at similar signal intensity. Combining the results of multiple experiments with competing anion coordination by **5.1** revealed the hierarchy of anion binding is $Cl^- > Br^- > I^- \approx NCS^- \approx NCO^- \approx OAc^-$. Interestingly, we also find that the smaller tetramer **5.2** selectively binds F^- over larger halides, as seen by LRESI-MS in which formation of the host-guest complex [**5.2**⊂F]$^-$ is observed (Figure 72). Since we found **5.2** to be more chemically robust than **5.1**, we were able to confirm that anion encapsulation

follows a 1:1 binding isotherm by NMR titration (Figure 72).[78] Fitting the development of the NH NMR resonance over the course of a titration TBAF in DCM revealed the association constant to be K = (9.5 ± 1.2) x 10^2 M^{-1}. The ^{31}P NMR resonance is also observed to shift upfield by approximately 1 ppm over the course of the titration. Crucially, these preliminary studies confirm that **5.1** and **5.2** act as structurally robust, size-selective anion-hosts in a similar way to H-bonding organic counterparts, and indicate that their ^{t}Bu peripheries are sufficiently flexible to allow entry of guests into their binding sites.

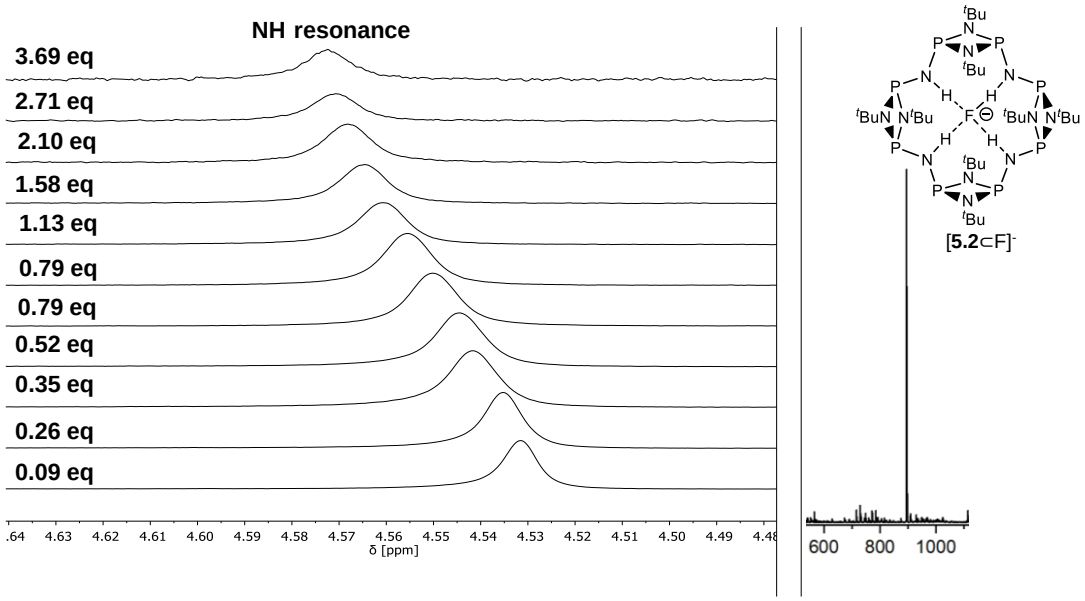

Figure 72: Binding of F^- within **5.2**. Left: ^{1}H NMR titration ($CDCl_3$, 400 MHz, 25 °C) of **5.2** with increasing amounts of TBAF Right: Low resolution negative mode ESI-MS of **5.2** in presence of excess TBAF.

Since **5.1** is stable towards nucleophilic attack it is a good candidate for the encapsulation of the 2-phosphaethynolate PCO^- anion. This anion has recently been the focus of considerable interest owing to its use as a synthon for P^-.[109] However, the high reactivity of this anion means that its supramolecular chemistry has not been explored previously. The negative-ion ESI-MS of a THF solution of **5.1** with approximately 5 equivalents of the sodium complex NaPCO(dioxane)$_{2.5}$ shows the formation of the 1:1 host guest complex [**5.1**⊂PCO]$^-$. The ^{31}P NMR spectrum at 298 K in d_8-THF shows only one broad resonance for the P-atom which is shifted upfield (Δδ = ca. 6 ppm) from NaPCO(dioxane)$_{2.5}$, indicating fast exchange between the coordinated and uncoordinated anion on the NMR timescale (Figure 73). Cooling to 243 K results in sharpening of the P resonance as well as the NH resonance of the

host in the ^{31}P and ^{1}H NMR spectrum, as a consequence of slowing down the intramolecular binding dynamics. Notably variable temperature NMR shift of free NaPCO(dioxane)$_{2.5}$ is smaller than in presence of **5.1** further supporting encapsulation. The ^{31}P-^{1}H HOESY NMR spectrum at 243 K shows a strong correlation between the NH protons of **5.1** and the P centre of the PCO^- anion, showing that the P centre which is a better size match for the cavity is H-bonded, rather than the more electronegative O atom (Figure 73). Further support for this conclusion is the absence of a through-space correlation between the ^{t}Bu protons of **5.1** and the P-centre of the PCO^- anion. DFT calculations (carried out in collaboration with Sanha Lee and Jonathan Goodman at the University of Cambridge) at the M06-2X/6-31g(d,p) level of theory show a clear energetic preference of ΔE = ca. 9 kJ/mol for binding to the P atom over O. The calculations also reveal that the preference for P binding by **5.1** is reinforced by weak ^{t}Bu C-H•••O interactions with the surrounding ^{t}Bu groups at the coordinated face of the host, which is splayed open to accommodate the anion.

Tilting of the PCO^- guest within the coordination site of **5.1** in the calculated structure suggested the participation of the π-orbitals of the anion in H-bonding. To investigate this we carried out NBO analysis which reveals that that N-H(σ*)···P=C(π) interactions contribute 49%, N-H(σ*)···P(lone pair) 26%, and C-H(σ*)···O(lone pair) 14% to the overall host-guest binding (Table 1).

Interaction Type	Interaction Strength [kJmol^{-1}]
nO→σ*NH	0.54
nO→σ*CH	29.50
nP→σ*NH	54.64
nP→σ*CH	3.05
πC-P→σ*NH	104.31
πC-P→σ*CH	19.00

Table 1: The six π → σ* and n → σ* interaction types and the interaction energies found between the pentamer **5.1** and the PCO^- guest found via NBO analysis.

Thus, the size-selective polar NH cavity and the hydrophobic ^{t}Bu periphery act in concert with each other in a unique way in this host-guest complex. Relevant to the bonding of the P-atom of the PCO^- anion by **5.1**, recent studies of the protonation of

PCO^- show that protonation occurs at the P atom, producing HPCO not PCOH.[110] Although previous gas-phase IR spectroscopic study have shown the existence of N-H···P H-bonds in the adduct $Me_2NH\cdots PMe_3$ and similar loose adducts, H-bonding to an anionic phosphorus centre as well as guest encapsulation via N-H···P H-bond has not been reported previously.[111,112]

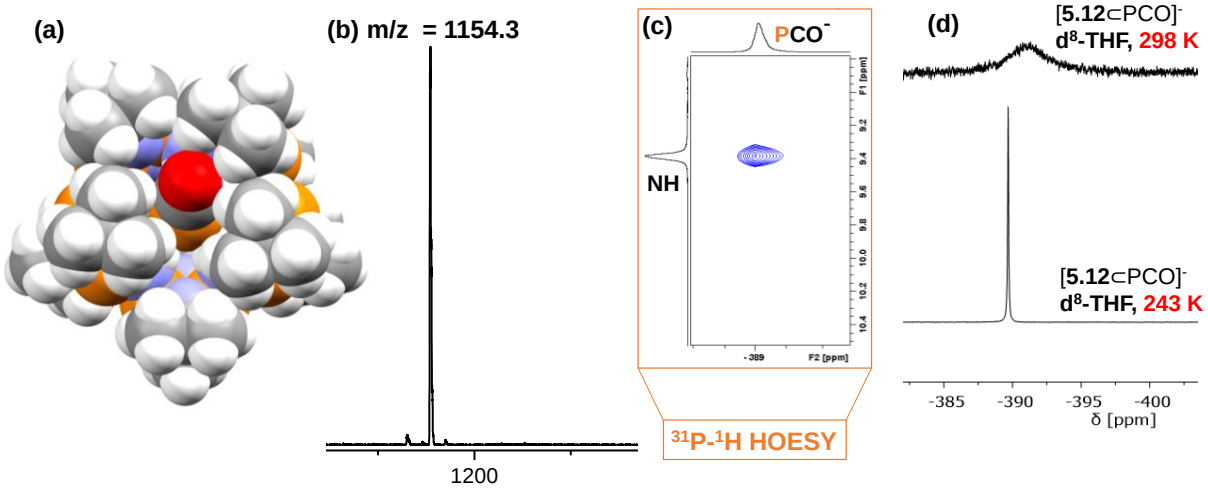

Figure 73: Binding of PCO^- within **5.1**. (a): The optimised P-bound structure of [**5.1**⊂PCO^-] and space-filling model of [**5.1**⊂PCO]$^-$ at the M06-2X/6-31g(d,p) level. Colour code: blue = N, orange = P, white = H, grey = C, red = O. (b): LRESI-MS of [**5.1**⊂PCO]$^-$. (c): The low-temperature ^{1}H-^{31}P HOESY NMR (243 K, d_8-THF) spectrum, confirming the orientation of the P atom into the cavity. (d): VT-^{31}P-NMR of the PCO^- resonance.

Next, we investigated the interaction of **5.1** with neutral guests. ^{1}H NMR titrations of **5.1** with acetone, benzonitrile and phenylactetylene in non-competitve solvents such as benzene and hexane result in significant downfield shifts in the NH protons of the host (ca. 0.4 ppm), indicating H-bonding of the neutral guests. In each case, the data can be fitted to 1:1 isotherms with K(Acetone) = (55.3 ± 5.4) M^{-1}, K(Phenylacetylene) = (66.7 ± 7.9) M^{-1} and K(Benzonitrile) = (150.8 ± 18.1) M^{-1}.[78] Subsequent crystallisation from these guests as the solvents at low temperature give the 1:1 adducts [**5.1**⊂Acetone], [**5.1**⊂Benzonitrile] and [**5.1**⊂Phenylacetylene], the single crystal X-ray structures of which are shown in Figure 74. A common feature in all of these arrangements is the responsive nature of the host **5.1**, in which the ^{t}Bu periphery opens up to accept the binding of the functional groups of the guests at the H-bond donor site (seen also in the previous DFT calculations of [**5.1**⊂PCO^-]). The effect of this can be seen most dramatically in the space-filling representation of [**5.1**⊂Acetone],

[**5.1**⊂Benzonitrile], in which binding of the guest at one face closes the opposite face of the host and prevents coordination of another guest molecule.

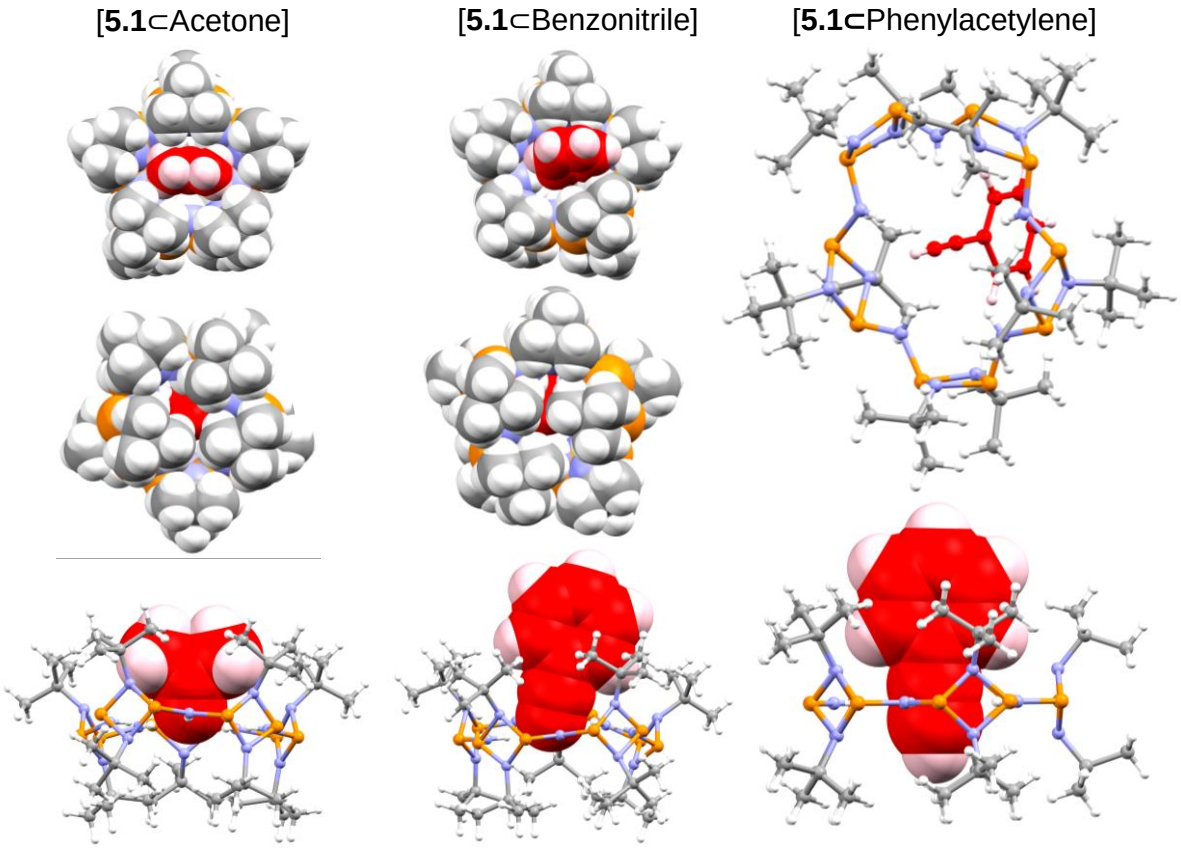

Figure 74: X-ray crystal structures of host-guest complexes of **5.1**. Left column: Space-filling diagram of [**5.1**⊂Acetone] (top and bottom view) and local environment of acetone. Middle column: Space-filling diagram of [**5.1**⊂Benzonitrile] (top and bottom view) and local environment of benzonitrile. Right column: The local environment of phenylacetylene in [**5.1**⊂Penylacetylene]; all the figures are obtained from the single crystal X-ray structures of the host-guest complexes. Carbon atoms of guest molecules are coloured red. Colour code: blue = N, orange = P, white = H, grey = C.

In [**5.1**⊂Acetone], the framework of **5.1** distorts in order for all of the nitrogen-bound hydrogens to bond to the electron-rich O atom of acetone; the O-atom resides above the mean plane of the five NH groups. The presence of H-bonding interactions is also confirmed by the reduction in the C=O stretching frequency from 1716 cm^{-1} for free acetone to 1680 cm^{-1} in a solid sample of [**5.1**⊂Acetone].

The solid-state structure of [**5.1**⊂Benzonitrile] confirms a similar inward orientation of the benzonitrile guest and structural adaptation of the framework of **5.1**. Additionally, it indicates that again encapsulation is achieved via a combination of H-bonding to the nitrile lone pair as well as the π-orbitals although there is some uncertainty due to

crystallographic disorder of the benzonitrile guest in the crystal. Hence we carried out DFT M06-2X/6-31g(d,p) calculations to probe the nature of the host-guest interactions. These revealed that the cavity centroid defined by the NH units lies approximately on the nitrile nitrogen. NBO analysis shows that the N-H(σ*)···π-C≡N interactions have the greatest contribution to host-guest binding, forming 63.5% of the total host-guest interaction (see Table 2).

Interaction Type	**Interaction Strength [kJmol^{-1}]**
πC-C→σ*C-H	11.34
πC-N→σ*C-H	0.33
πC-N→σ*N-H	54.18
nN→σ*C-H	11.67
nN→σ*N-H	7.70

Table 2: The five π → σ* and n → σ* interaction types and the interaction strengths found between the pentamer **5.1** and the benzonitrile guest via NBO analysis.

Such N-H•••π interactions are in stark contrast to other H-bonded adducts involving nitriles, which typically act as exclusive H-bond acceptors using their HOMO sp-type lone pairs, as opposed to the lower energy π-orbitals of the C≡N bond.[113]

Shifting the centre of electron density from the N in benzonitrile to the triple bond of phenylacetylene results in deeper penetration of the guest into the cavity of **5.1**. The middle of the triple bond in [**5.1**⊂Phenylacetylene] is found exactly at the centroid of the five N-atoms of the host in the crystal structure, with fully-developed N-H•••π-C≡C H-bonding (N•••centroid 3.46 Å) and apolar (^{t}Bu)H···phenyl interactions involved. The presence of N-H•••π H-bonding in solution is further confirmed by the ^{1}H-^{1}H NOESY NMR of **5.1** with excess phenylacetylene in hexane, which shows a through-space correlation between the alkynyl proton and the NH protons (Figure 75).

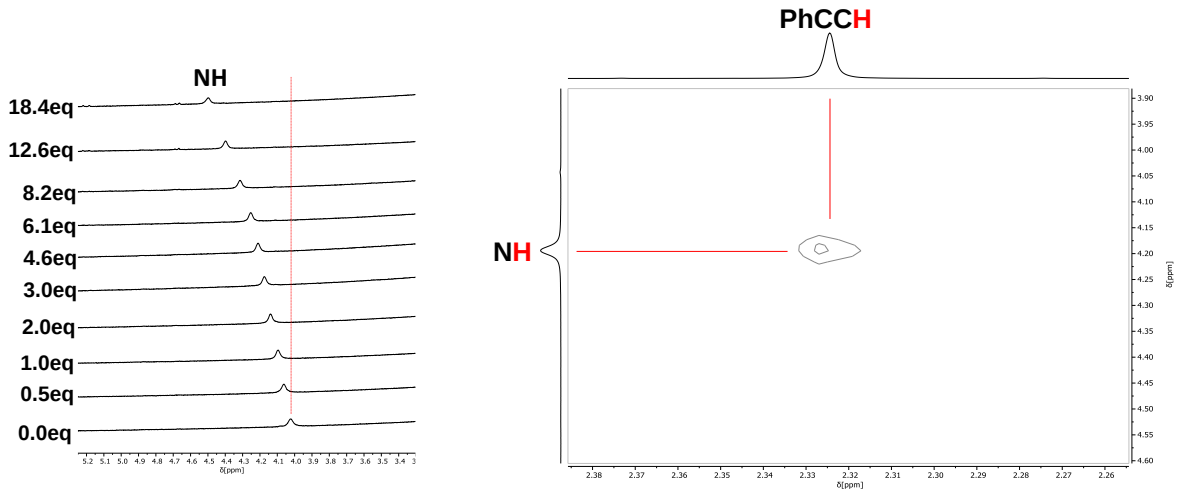

Figure 75: Left: ^{1}H NMR titration (hexane, d_6-Acetone capillary, 400 MHz, 25 °C) of **5.1** with increasing amounts of Phenylacetylene. Right: ^{1}H-^{1}H NOESY NMR correlation between acetylene and NH proton.

Direct observation of XH•••π(alkyne) H-bonding between two different chemical species to this extent is rare.[114] To the best of our knowledge, this is the first example of guest encapsulation via XH•••π H-bonding. Gas-phase DFT M06-2X/6-31g(d,p) calculations replicate the structure of [**5.1**⊂Phenylacetylene] closely, although the structure is slightly more distorted than in the solid state. NBO analysis reveals that encapsulation occurs predominantly via N-H•••π-C≡C (84.9%, 70.08 kJmol^{-1}) bonding and only to aminor extent via classic C-H•••π (aryl) (15.1%, 12.43 kJmol^{-1}) bonding. The similar computed binding energies of the guests of 110-111 kJmol^{-1} for [**5.1**⊂Benzonitrile] and [**5.1**⊂Phenylacetylene] support the conclusion that both complexes are predominantly bound via N-H•••π interactions with the guests. These values are in line with the experimentally determined binding constants for [**5.1**⊂Benzonitrile] and [**5.1**⊂Phenylacetylene] obtained from NMR titrations, which are also similar to each other.

As with many organic and metal-organic hosts, the host-guest behaviour of **5.1** is dynamic and reversible.[26] This was confirmed by an exchange experiment where excess NaPCO(dioxane)$_{2.5}$ was added to [**5.1**⊂I]$^{-}$ and binding was observed by ^{31}P NMR as discussed above.

The presence of a reactive phosphorus backbone in **5.1** enables post-synthetic modification of the macrocyclic backbone to trap guests irreversibly.[115,116] The reaction of [**5.1**⊂X]$^{-}$ (X = I, Cl) with ten equivalents of sulphur at 363 K gives the fully

oxidised P(V) host-guest complex [**5.4**⊂X]$^-$. Multi-gram synthesis of [**5.4**⊂I]$^-$ as its Li(THF)$_4^+$ salt is achieved by treatment of the crude reaction mixture of **2.1**, $LiNH_2$ and LiI (20 equivalents) with sulphur in 85% yield (Figure 76).

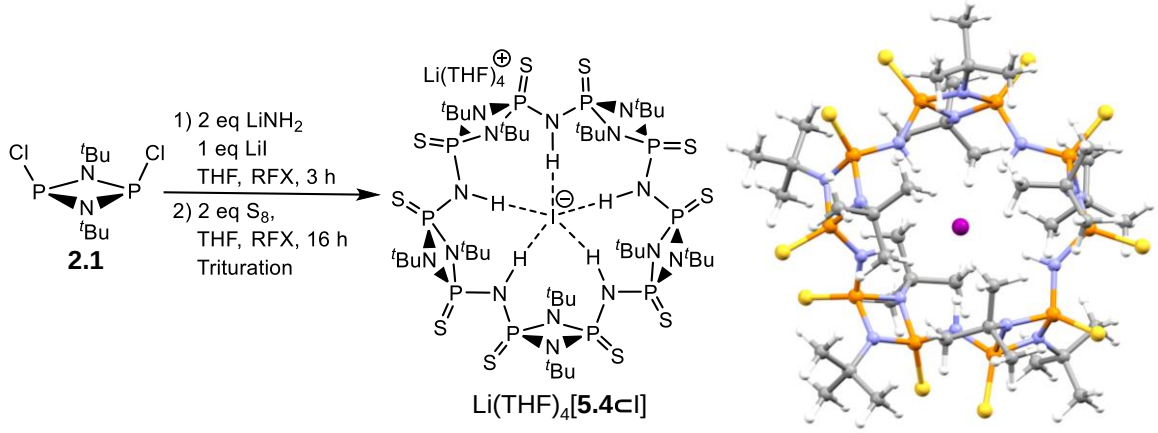

Figure 76: Left: Synthetic procedure for Li(THF)$_4$[**5.4**⊂I]. Right: Solid-state structure of Li(THF)$_4$[**5.4**⊂I]. Cation could not be identified due to high crystallographic disorder. Lattice bound solvent molecules omitted for clarity. Colour code: blue = N, orange = P, white = H, grey = C, Sulphur =S, purple = I.

Unlike [**5.1**⊂I]$^-$, which is water- and air-sensitive, [**5.4**⊂I]$^-$ is water- and air-stable for at least six months. Li(THF)$_4$[**5.4**⊂I] was fully characterised by negative mode ESI-MS, X-ray crystallography (vide infra), multinuclear NMR spectroscopy. The chloride complex could be synthesised via treatment of the crude reaction mixture of **2.1** and $LiNH_2$ in THF with Sulphur, removal of the solvent THF and trituration of crude Li(THF)$_4$[**5.4**⊂Cl] with hot toluene. Li(THF)$_4$[**5.4**⊂Cl] was characterised via ESI-MS and multinuclear NMR spectroscopy.

Contrasting with the behaviour of **5.1**, the halide guests within **5.4** are not bound dynamically and cannot be removed or exchanged from the host. For example, the iodide complex [**5.4**⊂I]$^-$ does not exchange its guest for chloride and (vice versa) the chloride complex [**5.4**⊂Cl]$^-$ does not exchange for iodide. In a series of NMR experiments we did not observe interconversion of [**5.4**⊂I]$^-$ into [**5.4**⊂Cl]$^-$ upon treatment with >10 eq TBACl in d_6-DMSO and or of [**5.4**⊂Cl]$^-$ into [**5.4**⊂I]$^-$ upon treatment with >10 eq TBAI. The chloride and iodide complex consequently appear as two chemically distinct species in the ^{1}H and ^{31}P NMR (

Figure **77**). Similar behaviour is observed with other anions such as attempted exchange of [**5.4**⊂I]$^-$ with NaPCO(dioxane)$_{2.5}$ which was monitored by ^{31}P NMR.

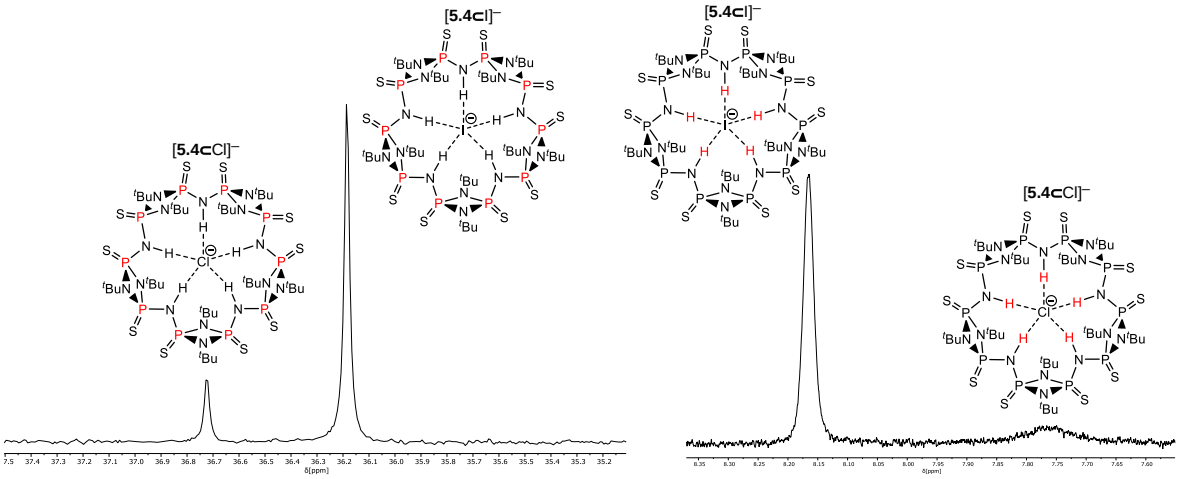

Figure 77: Left: ^{31}P NMR (d_6-DMSO, 202 MHz, 25 °C) of a mixture of [**5.4**⊂Cl]$^-$ and [**5.4**⊂I]$^-$. Right: ^{1}H NMR (d_6-DMSO, 500 MHz, 25 °C) of the same mixture.

Even treatment with MeOTf (> 500 equivalents) only results in mono-methylation of the framework of Li(THF)$_4$[**5.4**⊂I] to **5.5** (Figure 78), with no formation of MeI (note that 'free' iodide or chloride reacts spontaneously with MeOTf under nucleophilic substitution forming MeCl or MeI). **5.5** was characterised by positive mode ESI-MS, and ^{1}H and ^{31}P NMR spectroscopy. In the ESI-MS no free methylated macrocycle was observed. Only the overall cationic doubly methylated species can be observed which appears to be generated during the measurement. The ^{31}P NMR spectrum in $CDCl_3$ shows ten distinct doublet-of-doublets for **5.5**, with the ^{1}H NMR showing five distinct triplet NH resonances as a result of the desymmetrisation (Figure 78). Analogous methylation over abstraction is observed for [**5.4**⊂Cl]$^-$. Methylation results in increase of the chemical shift of the closest NH proton which is in line with strengthening of the NH-halide H-bond interaction due to polarisation of the NH bond. The proton second closest to the methylation site shows the same effect. Strengthening of the H-bond to these NH protons results in weakening of the other three which is in line with a decrease of chemical shift for the remaining protons compared to [**5.4**⊂I]$^-$.

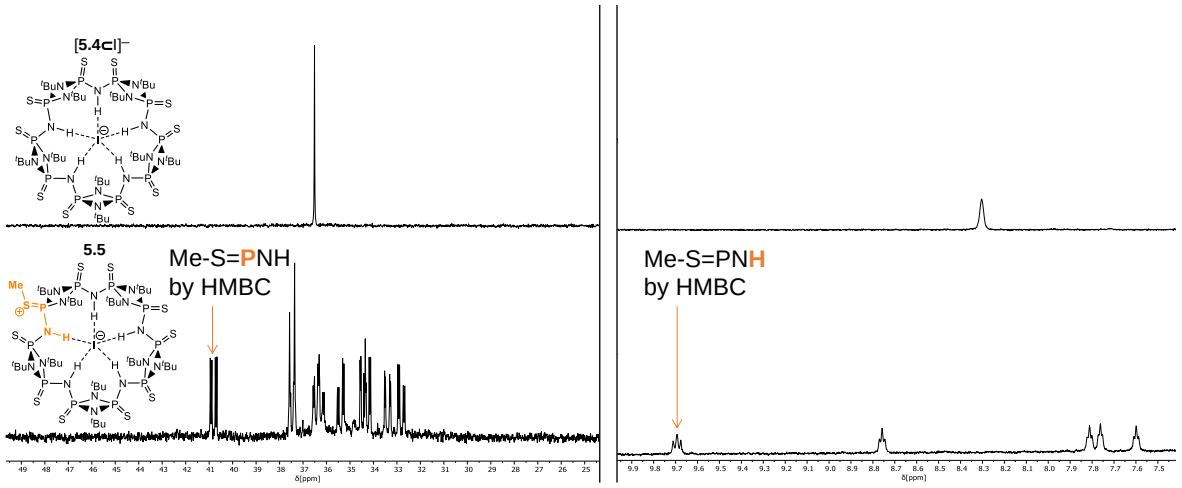

Figure 78: Stacked $^{1}H/^{31}P$ NMR spectra ($CDCl_3$,400 MHz/202 MHz, 25 °C) of [**5.4**⊂I]$^-$ showing the five-fold/ten-fold splitting upon mono-methylation; note that resonance at 9.7 ppm could be assigned via ^{31}P-^{1}H HMBC to the P=S-Me functionality.

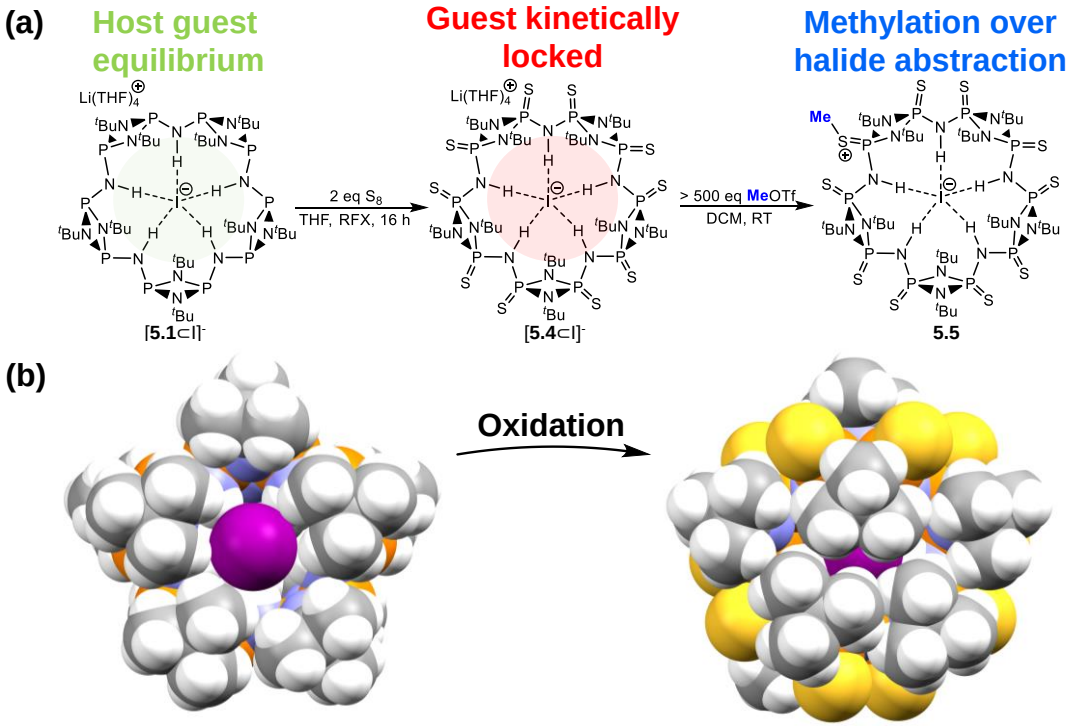

Figure 79: (a) Oxidation of **5.1** yields **5.4**. Attempts to remove the bound I^- anion lead instead to methylation of the macrocycle. (b) Comparison of the solid-state structures of [**5.1**⊂I]$^-$ and [**5.4**⊂I]$^-$; single crystal structure [**5.1⊂I**] $^-$ from reference [45]. Colour code: blue = N, orange = P, white = H, grey = C, yellow = S, purple = I.

Halide guests are thus locked in place within **5.4**. The solid-state structure of [**5.4**⊂I]$^-$ provides the key to understanding the highly robust nature of this halide binding. Single crystals were grown by slow evaporation of a saturated DMSO solution of

$Li(THF)_4$[**5.4**⊂I]$^-$. As seen in Figure 79, oxidation of the phosphorus periphery causes distortion of the macrocyclic framework due to P-N bond shortening and repulsion between the peripheral sulphur atoms. Before oxidation, halide guests are sterically accessible from one face of **5.1** since the P-N framework and the orientation of the ^{t}Bu groups are flexible. The cavity of **5.4**, however, is completely concealed by the surrounding ^{t}Bu groups, with a significant shortening of the N-H•••I distances in [**5.4**⊂I]$^-$ compared to those in [**5.1**⊂I]$^-$ (by ca. 0.2 Å). In contrast to **5.1**, **5.4** does not adapt its structure to different guests; whereas **5.1** adapts C_{5v} symmetry in its´ chloride and C_s symmetry in its´ iodide host guest complex, the overall geometry of host guest complexes of **5.4** appears to be determined by the inorganic backbone. This was confirmed by the cocrystallisation of iodide- and chloride-bound complexes from a mixture of both which showed that the macrocycle backbone is isomorphous for both bound guests and that the N-H•••halide distances do not change when moving to the more electron dense chloride guest. This configuration is echoed in our DFT modelling of [**5.4**⊂I]$^-$ and [**5.4**⊂Cl]$^-$ which also yields near identical macrocycle geometries for the different host guest complexes.

Cumulatively, our observations indicate that halides are kinetically locked within **5.4** due to the buckling of the macrocycle and the preferential orientations of ^{t}Bu groups, which prevent release of the halide guest. Backbone oxidation thus presents a novel method for modulating guest kinetics and reactivity. Furthermore, the best supramolecular organic halide receptor described so far can be obtained in its free form by washing with water, whereas the best metal-organic receptors either exchange halide guests for other anions or release the anion upon treatment with excess MeOTf. Applying these same strategies to [**5.4**⊂I]$^-$ leaves the host-guest complex intact.[117–119] Our inorganic macrocycle is effectively the best halide receptor known to date.

Chapter Conclusion

The dramatic illustration of some of the fundamental differences between organic and inorganic hosts that we present in this chapter leads to some important general conclusions. Above all, moving from the well-trodden area of organic hosts to inorganic frameworks introduces greater polarity and the prospect of molecular architectures that have no parallels in conventional organic arrangements. These features can lead to host-guest phenomena that have not been seen before. The unusually polar coordination site of this ring system promotes new modes of guest encapsulation: via H-bonding with the π-systems of unsaturated bonds, and with reactive anionic phosphorus centres. Guests can be kinetically locked within our structure, with anions displaying stronger effective halide binding than in any classical organic or metal-organic receptor. Expanding the horizons of this new area of supramolecular inorganic chemistry is made all the more accessible by the straightforward methods in which inorganic hosts can be synthesised. Our results show that main group systems can provide new tools for stabilising reactive species and employing a wider set of intermolecular interactions in supramolecular chemistry.

Experimental Details

General experimental details involving techniques, instruments and materials employed are provided in the appendix at the end of this thesis.

Synthesis of **5.2** and **5.3** was carried out according to the literature procedure.[43]

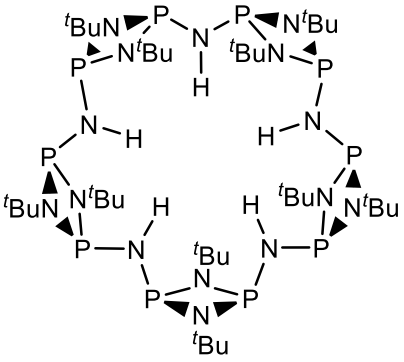

Synthesis of 5.1: Inside a N_2 filled glovebox a 250 ml Schlenk flask was charged with **2.1** (2.75 g, 10 mmol), LiI (1.34 g, 10 mmol) and $LiNH_2$ (460 mg, 20 mmol). The flask was connected to a Schlenk line and cooled to -78 °C.100 ml of THF was added and the resulting suspension was warmed to room temperature and then heated overnight at 70 °C. Afterwards the solvent was removed under vacuum and the resulting semi-solid was extracted with 3x100 ml of boiling hexane. The extracts were combined and the solvent was removed under vacuum to yield a white solid which was dried thoroughly under vacuum. The resulting solid was extracted with 3x100 ml of pentane. The extracts were combined and the solvent was removed in vacuum to yield a white solid (crude $Li(THF)_4$[**5.1⊂I**]) which was weighed out inside an N_2 filled glove box. The solid was dissolved in 50 ml of DCM and a 0.1 M solution of NaOMe in MeOH (freshly prepared from sodium and methanol; 1 eq NaOMe per $Li(THF)_4$[**5.1⊂I**]) was added dropwise. The resulting suspension was stirred for 30 min at room temperature. The precipitate was filtered off and the solvent was removed under vacuum to yield crude **5.1** (yield typically 1.2g, 1.1 mmol, 54%). The yield and purity of this material depends on how well exposure to air and moisture is avoided during the synthesis. For purification for analysis, **5.1** can be crystallised from minimum THF (typical crystalline yield 500 mg, 0.46 mmol, 23% based on **2.1**). The spectral data was in agreement with the literature.**^{1}H NMR (d_8-toluene, 400 MHz, 25 °C):** δ[ppm] = 4.49 (s, NH), 1.43 (s, ^{t}Bu), **^{31}P NMR (d_8-toluene, 202 MHz, 25 °C):** δ[ppm] = 114.5 (s);**LRMS (ESI-MS):** m/z =1130.2 (**5.1**·Cl^-); **HRESI-MS:** m/z = (**5.1**·Cl^-) calc = 1030.4965 (**5.1**·Cl^-) exp = 1030.5027; Note: Elemental analysis generally proved unhelpful for the phosphazane macrocycles in this chapter as the nitrogen content was measured to be up to 10% lower than the

expected content. This is probably due to ceramic formation and has been noted previously in the literature.[14]

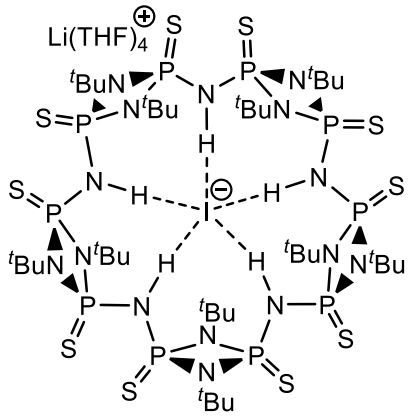

Synthesis of Li(THF)$_4$[5.4⊂I] : Inside a N_2 filled glovebox a 250 ml Schlenk flask was charged with **2.1** (2.75g, 10 mmol), LiI (1.34g, 10 mmol) and $LiNH_2$ (460 mg, 20 mmol). The flask was connected to a Schlenk line and cooled to -78 °C. 100 ml of THF were added and the resulting suspension was warmed to room temperature and then heated overnight at 70 °C. Afterwards the solvent was removed in vacuo and 100 ml of toluene was added. Under a stream of nitrogen solid sulphur (1g, 3.9 mmol) was added and the resulting suspension was stirred overnight at 90 °C during which more precipitate formed. The resulting precipitate was isolated by filtration under aerobic conditions and subsequently washed with 200 ml of water and 100 ml of pentane. The product was dried in vacuo to yield Li(THF)$_4$[**5.4**⊂I] as a colourless powder (3.1 g, 1.6 mmol, 80%, THF content was calculated on the basis of the ^{1}H NMR). **^{1}H NMR (d$_6$-DMSO, 400 MHz, 25 °C):** δ[ppm] = 8.17(s, NH), 2.08(s, ^{t}Bu);**^{31}P NMR (d$_6$-DMSO, 202 MHz, 25 °C):** δ[ppm] = 36.2 (s);**^{127}I NMR (d$_6$-DMSO, 25 °C):** δ[ppm] = 273.5 (bs);**^{7}Li NMR (d$_6$-DMSO, 25 °C):** δ[ppm] = -0.89 (s); **LRESI-MS:** m/z =1542.0 (**5.4**·I$^-$);**HRESI-MS:** m/z = (**5.4**·I$^-$) calc = 1542.1523 exp = 1542.1330.

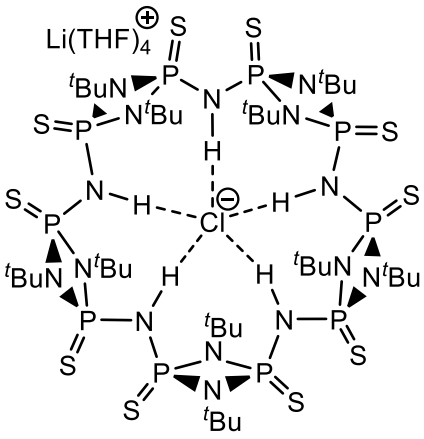

Synthesis of Li(THF)$_4$[5.4⊂Cl]: Inside a N_2 filled glovebox a 50 ml Schlenk flask was charged with **2.1** (275g, 1 mmol) and $LiNH_2$ (46 mg, 2 mmol). The flask was connected to a Schlenk line and cooled to -78 °C.10 ml of THF were added and the resulting suspension was warmed to room temperature and then heated overnight at 70 °C. Under a stream of nitrogen solid sulphur (200 mg, excess) was added and the resulting suspension was stirred for 72 h at 70 °C. Afterwards all solvent was removed in vacuo yielding a sticky yellow solid. 100 ml of toluene were added and the resulting suspension was heated at 90 °C for

1h in order to dissolve excess sulphur. After 1h a clear yellow solution and a white precipitate formed which was isolated by filtration under aerobic conditions and subsequently washed with 100 ml of hot toluene, 200 ml of water and 100 ml of pentane. The product was dried in vacuo to yield Li(THF)$_4$[**5.4**⊂Cl] as a colourless powder (110 mg, 1.6 mmol, 20%, amount of THF was calculated on the basis of the ^{1}H NMR).;**^{1}H NMR (d$_6$-DMSO, 400 MHz, 25 °C):** δ[ppm] = 7.50 (s, NH), 3.60 (m, THF), 1.68 (s, ^{t}Bu), 1.60 (m, THF); **^{31}P NMR (d$_6$-DMSO, 202 MHz, 25 °C):** δ[ppm] = 36.7 (s), **LRESI-MS:** m/z = calcd. 1450.22 ([**5.4**⊂Cl]$^-$) measured 1450.07.

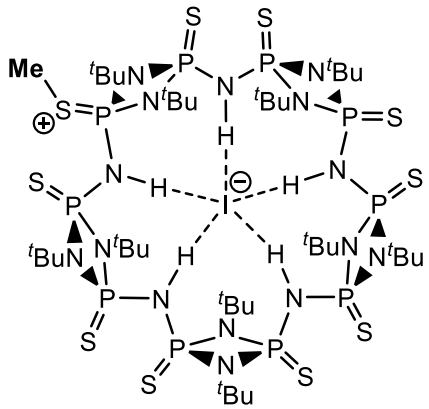

3

Synthesis of 5.5⊂Cl: Inside a N_2 filled glovebox a 100 ml Schlenk flask was charged with Li(THF)$_4$[**5.4**⊂I] (200 mg, 0.13 mmol) which was then transferred to a Schlenk line. 50 ml of dry DCM were added, followed by 50 µL MeOTf (excess). The resulting suspension was stirred for 2h at room temperature during which the suspended solid dissolved. All volatiles were removed in vacuo and the resulting white solid was extracted with 25 ml of toluene and filtered in order to remove LiOTf byproduct. All volatiles were removed in vacuo yielding **5.5** a colourless powder (160 mg, 0.1 mmol, 77%):**^{1}H NMR (CDCl$_3$, 400 MHz, 25 °C):** δ[ppm] = 9.79 (pt, $^2J_{PH}$ = 6.6 Hz, 1H, NH), 8.81 (pt, $^2J_{PH}$ = 4.2 Hz, 1H, NH), 7.80 (pt, $^2J_{PH}$ = 3.6 Hz, 1H, NH), 7.73 (pt, $^2J_{PH}$ = 3.2 Hz, 1H, NH), 2.71 (d, $^2J_{PH}$ = 21.8 Hz, 3H, P=S-Me), 1.88-1.60 (m, 180H, ^{t}Bu); **^{31}P NMR (CDCl$_3$, 202 MHz, 25 °C):** δ[ppm] = 41.4 (dd, $^2J_{PP}$ = 34.2 Hz, $^2J_{PP}$= 10.0 Hz), 38.6 – 38.2 (m), 37.4 (dd, $^2J_{PP}$ = 33.1 Hz, $^2J_{PP}$= 9.3 Hz), 37.1 (dd, $^2J_{PP}$ = 33.6 Hz, $^2J_{PP}$= 10.0 Hz), 36.3 (dd, , $^2J_{PP}$ = 35.4 Hz, $^2J_{PP}$= 9.5 Hz), 35.6 – 34.8 (m), 34.5 (dd, $^2J_{PP}$ = 34.3 Hz, $^2J_{PP}$= 5.6 Hz), 33.7 (dd, $^2J_{PP}$ = 35.9 Hz, $^2J_{PP}$= 10.1 Hz); **LRESI-MS:** m/z = calcd. 1572.20 (Me**5.5**)$^+$ measured 1572.23.

Part 2: Trispyridyl Main Group Ligands for Coordination Chemistry

Chapter 6: Introduction to Part 2

The development of homogeneous catalysis relies heavily on effective ligand design for the tuning of both sterics and electronics of the coordinated metal centres.[120] Among others, tripodal C_3-symmetric ligands have evolved as popular spectator ligands. Typically, three donor sites D, as shown in Figure 80, are connected by a non-donor bridging unit E coordinate facially to, for example, an octahedral or tetrahedral transition metal centre, providing a high degree of stereochemical control and highly stable complexes due to the chelate effect.

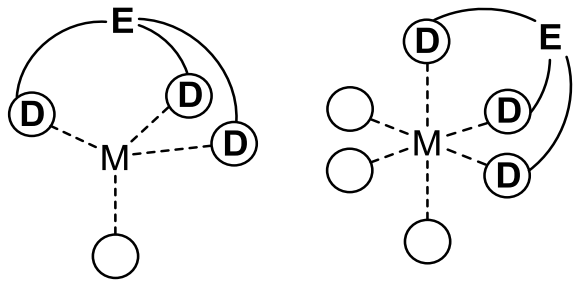

Figure 80: Tripodal ligand coordinating to tetrahedral and octahedral transition metal centres.

A great variety of tripodal ligands have been designed in the past on the basis of combining various bridgeheads with established donor functionalities.[101,121] Figure 81 shows a selection of established C_3-symmetric tripodal ligands.

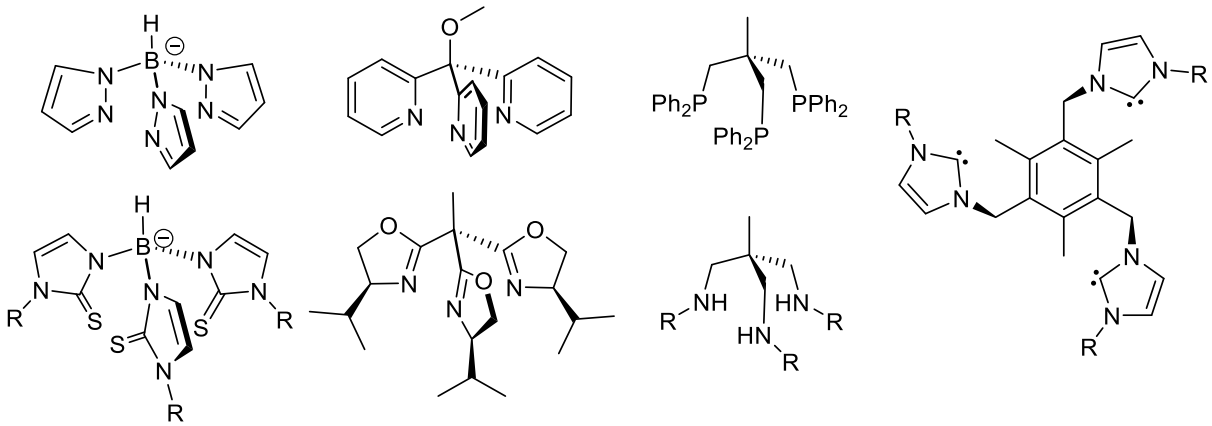

Figure 81: Tripodal ligands featuring different bridgeheads and donor groups.

Arguably, one of the most commonly used tripodal ligands is the trispyrazolylborate system, $HB(pz)_3^-$ (pz = pyrazolyl), established by Troflimenko in the 1970s which

serves as a 6-electron donor as well as a counter-anion with regard to a coordinated metal centre.[122] Due to their facile synthesis from pyrazoles and borohydrate BH_4^- and strong donor capacity (similar to cyclopentadienyl, Cp^-) trispyrazolylborates have found countless applications in coordination chemistry, homogeneous catalysis and even in bioinorganic chemistry, where they serve as supporting ligands for models of enzymatic active sites.[123,124]

Earlier, Wright et al. and others explored the chemistry of trispyridyl ligands of the type $E(2\text{-py})_3$ (2-py = 2-pyridyl) which are closely related to trispyrazolyl borates.[125] Similar to the latter, these ligands are generally available in a one-step procedure from methathesis of $REX_{2/3}$ or EX_3 with 2-Li-pyridine (or substituted 2-Li-pyridines, X = halide), with the elimination of the lithium halides LiX (Figure 82). Hence, these systems represent a synthetically readily accessible family of tripodal ligands which allow the rational design and tuning of the ligand properties through variations of the bridging group E or the pyridyl substitution pattern.

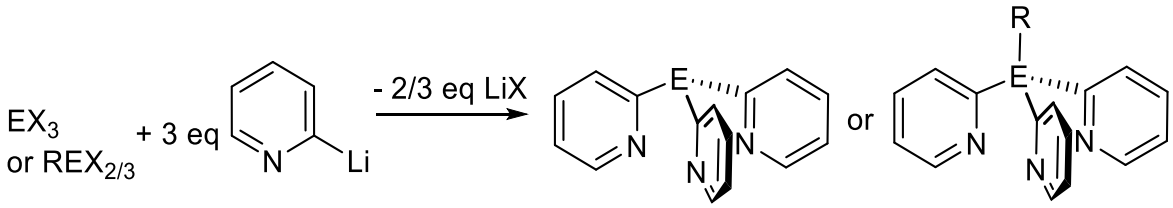

Figure 82: Generalised synthesis of main group trispyridyl ligands. E = BR^-, AlR^-, InR^-, CR, SiR, SnR, Sn^-, N, P, P=O/S/Se, As, As=O; X = Cl, Br.

Over the last 3 decades a range of trispyridyl ligands with various bridgeheads E have been synthesised and explored. Known trispyridyl $E(2\text{-py})_3$ ligands include those with E = BR^-, AlR^-, InR^-, CR, SiR, SnR, Sn^-, N, P, P=O/S/Se, As, As=O. The following introduction will focus on recent advances in the chemistry of trispyridyl main group ligands and in particular on the functional changes that come with bridgehead derivatisation with more metallic p-block elements.

Group 13

Since aluminium is in group 13, the related mononuclear trispyridyl ligand is only stable as its aluminate anion $RAl(2\text{-py})_3^-$.[126] The family of trispyridyl aluminates is synthesised from the reactions of $RAlCl_2$ with three equivalents of 2-Li-py as their Li^+ salts, $RAl(2\text{-py})_3Li$. Early on a variety of derivatives $RAl(2\text{-py'})_3^-$ (R = Me, Et, ^{i}Bu, ^{t}Bu ;

py' = 3/4/6-Me-2-py) were synthesised and employed in coordination studies.[127] The trispyridyl aluminates $RAl(2\text{-}py)_3^-$ are unique within the trispyridyl ligand family as the ligand is anionic, similar to trispyrazolylborate. This often favours the formation of sandwich complexes of the type L_2M, such as $[(MeAl(2\text{-}py)_3)_2Fe(II)]$ which is obtained from salt metathesis with $FeCl_2$.[128–130] However, introduction of steric bulk through substitution of the 6-position of the pyridyl group can disfavour the formation of sandwich complexes.[131] This subtle interplay between metal-ligand bonding to metals and steric repulsion is highlighted in the reactions of $^{i}BuAl(2\text{-}py)_3Li(THF)$ or $EtAl(6\text{-}Me\text{-}2\text{-}py)_3Li(THF)$ with $MnCl_2$, the first reaction forming a sandwich complex and the second forming a half-sandwich complex. Modification of the bridgehead substituent or substitution at the 3-, 4- or 5-positions of the pyridyl groups showed no or little effect on the chemistry of the corresponding trispyridyl aluminate. Taken together these studies underline the modular nature of the synthesis of trispyridyl ligands and the way in which steric effects can be used to modify their coordination behaviour. Both Lewis base solvation of the Li^+ cations and sterically demanding groups present on the pyridyl substituents can drastically affect the formation of monomeric or dimeric lithium aluminates. For example, removal of the THF ligand in monomeric $RAl(2\text{-}py)_3Li(THF)$ under vacuum gives dimers of the type $[(RAl(2\text{-}py)_3)_2Li_2]$, but this dimerisation can be supressed by installing substituents in the 6-position of the pyridyl substituents. This is illustrated dramatically in the case of removal of THF ligand in monomeric $RAl(6\text{-}R\text{-}2\text{-}py)_3Li(THF)$ which gives monomeric $RAl(6\text{-}R\text{-}2\text{-}py)_3Li$, containing three coordinated lithium. [132]

The aluminium-carbon bond is sufficiently polar for trispyridyl aluminates to undergo reactions other than metal ligand coordination. This reactivity persists in its coordination complexes with a range of metals. On this basis, it was found early that the sandwich L_2M complex $[(MeAl(2\text{-}py)_3)_2Fe(II)]$ acts as a remarkably selective epoxidation catalyst for styrene with only oxygen as the oxidant (Figure 83).[128] The catalytically active species was suggested to be $[(MeAl(2\text{-}py)_2(O))_2Fe(II)]$, formed by the reaction of one of the Al-C bonds of the aluminate with O_2. Hence, the reactivity of the bridgehead can play a crucial role in the activity and selectivity of catalysts.

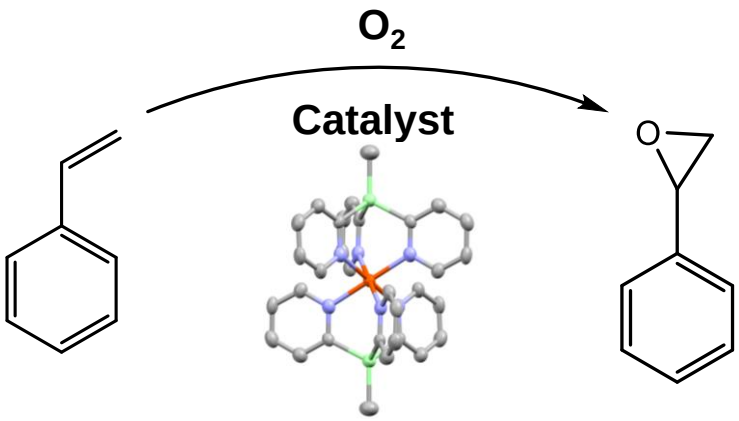

Figure 83: Catalytic epoxidation of styrene with the sandwich complex [(MeAl(2-py)$_3$)$_2$Fe(II)] and the solid-state structure of the catalyst. Colour code: grey = C, blue = N, orange = Fe, green = Al.

It was also found that the aluminate anion MeAl(2-py)$_3^-$ can serve as a soft pyridyl transfer reagent.[126] The reaction between MeAl(2-py)$_3$Li(THF) and CuCl yields the trimeric organometallic [Cu(2-py)]$_3$**.** Surprisingly this species is not synthetically accessible from the reaction of 2-Li-pyridine with CuCl. Analogously, reaction of EtAl(6-Me-2-py)$_3$Li(THF) with $SnCl_2$ yields the Janus-head like hexapyridyl ligand (6-Me-2-py)$_3$Sn-Sn(6-Me-2-py)$_3$ containing two tridentate coordination sites (Figure 84).[133] Since the hexahalide precursors Sn_2X_6 are either difficult to prepare or highly unstable, metathesis of 2-Li-pyridine with Sn_2X_6 is not feasible.[134] Hence, pyridyl transfer from EtAl(6-Me-2-py)$_3$Li(THF) represents a synthetic opportunity in main group chemistry to access polypyridyl system which cannot be synthesised via traditional routes.

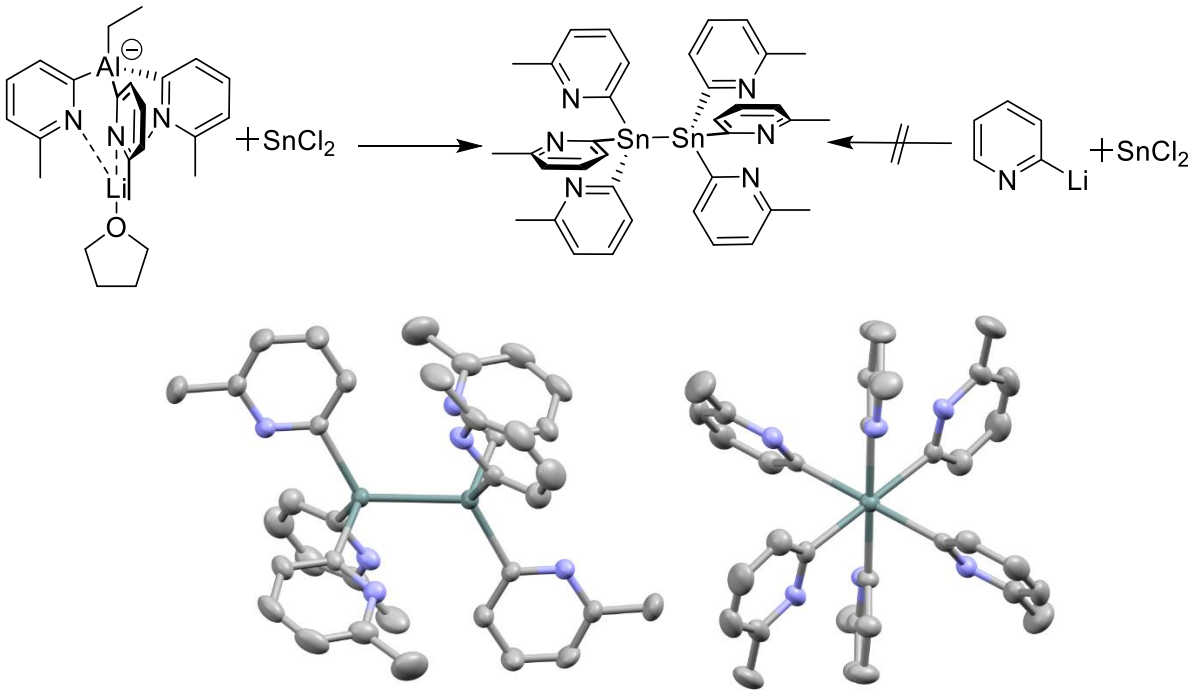

Figure 84: Formation and solid-state structure of (6-Me-2-py)$_3$Sn-Sn(6-Me-2-py)$_3$. Colour code: grey = C, blue = N, dark green = Sn.

In a related study it was shown that the CAl bonds are sufficiently polar to deprotonate acids in a controlled fashion. Reaction of EtAl(6-R-2-py)$_3$Li(THF) (R = H, CH_3, CF_3, Br) with one equivalent H_2O results in the loss of one pyridyl group and formation of a terminal AlOH group stabilised in a dimeric arrangement.[132] The presence of the terminal AlOH hydroxide was confirmed by ^{1}H NMR and IR spectroscopy. Its stability can be explained by the sterically protected location of the AlOH hydroxyl group within the cleft of the dimer. Interestingly, the hydroxide remains acidic and can be deprotonated by the bridgehead ethylate group or, for example, $ZnEt_2$ which was shown by in situ NMR monitoring. In the case of reaction with $ZnEt_2$, deprotonation is followed by pyridyl transfer to Zn(II) with the reaction product containing the [Zn(6-Br-2-py)$_3$]$_2^{2-}$ dianion, where the aluminate [EtAl(6-Br-py)$_3$]$^-$ is employed. More stable dimers of the type [EtAl(2-py)$_2$(R'O)Li$_2$(R'O)(2-py)$_2$AlEt] are produced when the aluminates are reacted with alcohols (Figure 85).

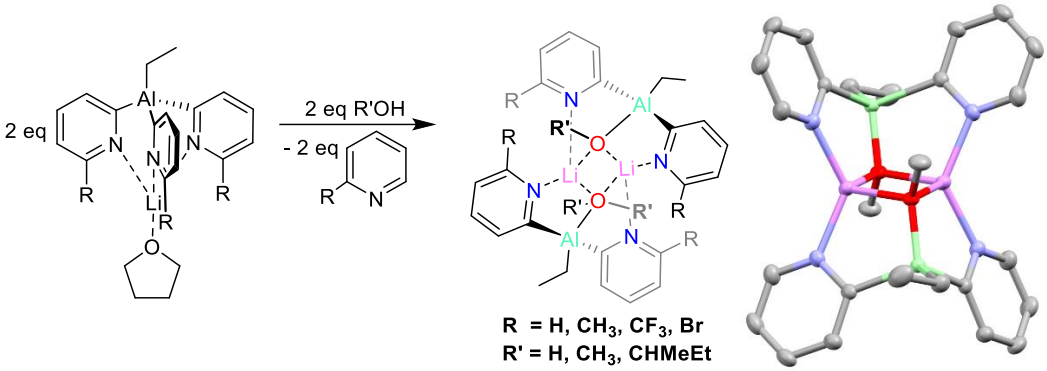

Figure 85: Controlled hydrolysis and alcoholysis of EtAl(6-R-2-py)$_3$Li(THF) to [EtAl(2-py)$_2$(R'O)Li$_2$(R'O)(2-py)$_2$AlEt]; solid state structure of EtAl(2-py)$_2$(MeO)Li$_2$(MeO)(2-py)$_2$AlEt]. Colour code: grey =C, blue = N, red = O, bright green = Al, purple = Li.

In a follow-up study of the reactions of aluminates with alcohols, Wright et al. developed a method to determine the enantiomeric excess of a mixture of chiral alcohols (Figure 85).[135] Reactions of [EtAl(6-Me-2-py)$_3$Li(THF)] with a chiral alcohols R*OH give dimers of the type [EtAl(2-py)$_2$(R*O)Li]$_2$. However, when a mixture of the R and the S alcohols is employed, the R and S monomers RAl(2-py)$_2$(R*$^{(R/S)}$O)Li form diastereomeric pairs of dimers (RR, SS and RS). These diastereomers can be easily distinguished by ^{1}H and ^{7}Li NMR spectroscopy using the 6-Me groups of the pyridyl ligands or Li^+ ions as reporters. For racemic mixtures this gives a 50:50 distribution of the RR\SS:SR\RS diastereomers, which do not interconvert on the NMR timescale. The ratio of the RR\SS:SR\RS diastereomers is representative of the initial enantiomeric excess of the employed alcohol. Consequently, the enantiomeric excess can be precisely determined via ^{1}H and ^{7}Li NMR spectroscopy by the use on this nonchiral agent.

Using the basicity of the pyridyl substituents also allows more elaborate functionalisation of trispyridyl aluminates.[136] Reactions of 2-HOCH$_2$py, 3-HOCH$_2$py or 4-HOCH$_2$py with [EtAl(2-py)$_3$Li.THF] introduces further complexity into the aluminate scaffold. For example, [EtAl(6-Me-2-py)$_2$(2-OCH$_2$py)Li] assembles into a Li$_2$O$_2$ centred dimer in which the pendent 2-OCH$_2$py groups form secondary pyridyl-N-Al interactions with the Al atoms of the aluminate anions. This backcoordination of the pendant alkoxy pyridyl ligands has been shown to be dynamic in solution. Functionalisation of the ligand with 3-HOCH$_2$py leads to the formation of an extended supramolecular structure in the double alcoholysis product [EtAl(6-Me-2-py)(3-OCH$_2$py)$_2$Li]. In the solid state the 3-OCH$_2$py substituents bridge Li$_2$O$_2$ centred dimers into an elaborate polymeric arrangement. Double alcoholysis was also used to synthesise the 'chiral-at- aluminium"

ligand [EtAl(6-Me-2-py)(OCH_3)(O^tBu)]$^-$ via sequential alcoholysis of [EtAl(6-Me-2-py)$_3$Li] with methanol and tert-butanol (Figure 86). Interestingly, dimers of the product [EtAl(6-Me-2-py)(OCH_3)(O^tBu)Li]$_2$ also statistically self-sort into diastereomers which can be identified by ^{1}H and ^{7}Li NMR spectroscopy in solution.

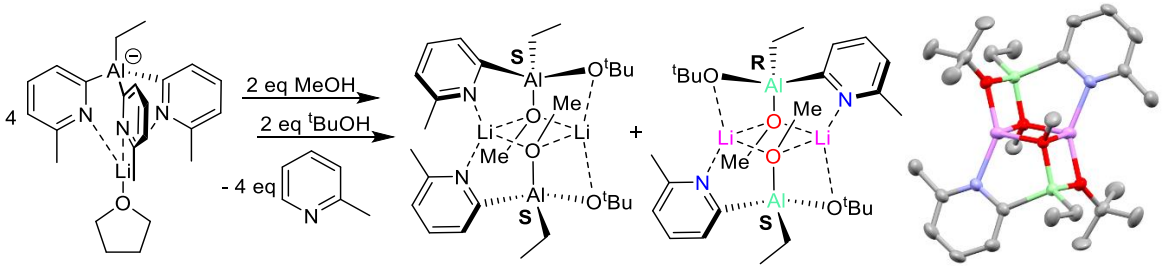

Figure 86: Generation of 'chiral-at-aluminium' dimeric diasteroemers by double alcoholysis. Colour code: grey =C, blue = N, red = O, bright green = Al, bright green = Li.

As mentioned earlier, reaction of the aluminates can also occur with oxygen. It was found that controlled oxidation of the transient complex [{EtAl(2-py)$_3$}$_2$Sm], which was obtained via metathesis of EtAl(2-py)$_3$Li(THF) and SmI_2, with molecular O_2 gives the Sm(III) compound [{EtAl(2-py)$_3$}{EtAl(2-py)$_2$O}Sm]$_2$ containing the ligand [EtAl(2-py)$_2$O]$^{2-}$ (Figure 87).[137] It was suggested that the dimeric Sm(III) complex can be seen as a model for the active species in the catalytic epoxide of styrene with O_2 using the Fe(II) complex [(MeAl(2-py)$_2$(O))$_2$Fe] mentioned earlier. Consequently, the epoxidation pathway of the styrene appears to involve cooperativity between the bridgehead and the coordinated metal.

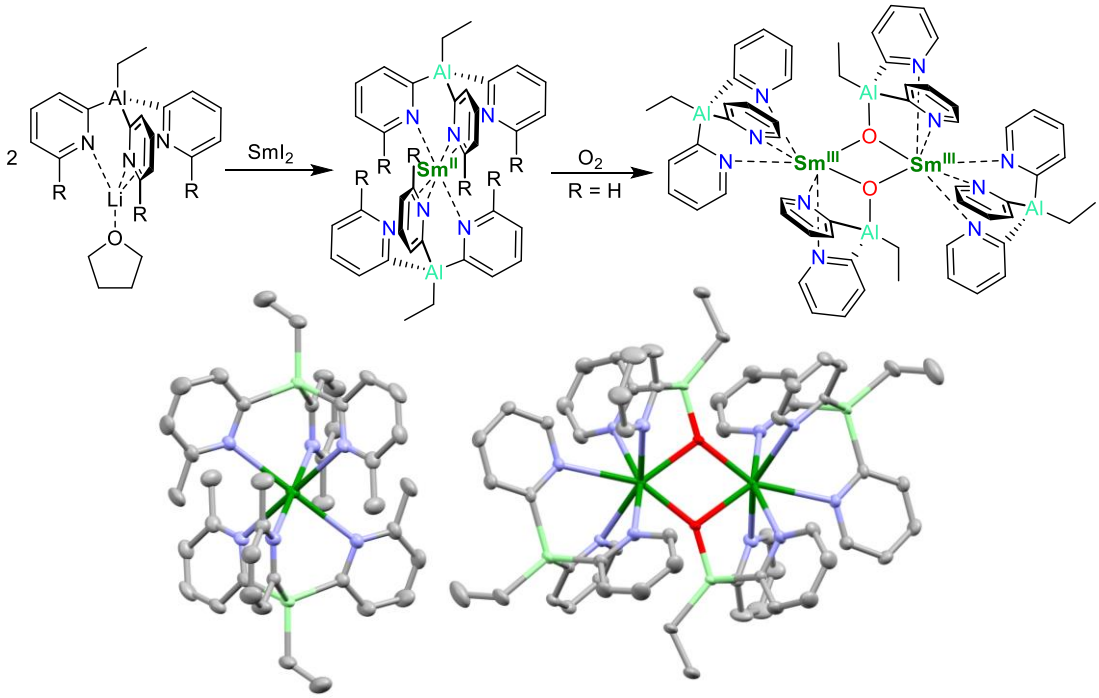

Figure 87: Oxidation of the samarium(II) complex [{EtAl(2-py)$_3$}$_2$Sm]. Colour code: grey =C, blue = N, red = O, bright green = Al, purple = Li, dark green = Sm.

Interestingly, the intermediate Sm(II) complex in this reaction could be stabilised by the sterically more demanding [EtAl(6-Me-2-py)$_3$]$^-$ ligand, producing [{EtAl(6-Me-2-py)$_3$}$_2$Sm] (Figure 87). It was shown that the coordination ability of [EtAl(6-R-2-py)$_3$]$^-$ to lanthanide(II) cations is highly dependent on the 6-R substituent. The presence of a 6-CF_3 group within the aluminate resulted in no coordination ability at all, in contrast to the 6-H, 6-Br and 6-Me substituted ligands.[138] Sandwich compounds of the type [{EtAl(6-Me-2-py)$_3$}$_2$Ln] are dynamic in solution. As a result, the half-sandwich [{EtAl(6-Me-2-py)$_3$}$_2$Y(THF)$_2$I] and the heteroleptic complex [{EtAl(6-Me-2-py)$_3$}Y{EtAl(6-Br-2-py)$_3$}] can be obtained by equilibriation from the homoleptic Yb sandwich compound.

As far as the rest of the heavier elements of group 13 are concerned, the [^{n}BuIn(2-py)$_3$]$^-$ anion can be formed in a similar fashion to the aluminates mentioned above, from the reaction of ^{n}BuInCl$_2$ and 2-Li-py.[129] However, little is known about its coordination chemistry apart from the complex with the Mo(CO)$_3$ complex fragment.

Jäkle et al. extensively investigated the chemistry of the trispyridyl borate ArB(2-py)$_3^-$, the pyridyl analogue of trispyrazolato borate.[139] Differently from all other trispyridyl main group ligands, reaction of the lithiate 2-Li-py with boron halides proved unsuccessful and ArB(2-py)$_3^-$ could only be isolated when the pyridyl-Grignard [(2-py)MgCl(THF)$_2$]$_2$ was employed as the nucleophile (Figure 88).[140] Trispyridyl borate was isolated as the ArB(2-py)$_3$H conjugated acid in which one pyridine group

is protonated. In contrast to the aluminates which are purified by crystallisation under inert atmosphere, $ArB(2\text{-}py)_3H$ is remarkably stable under benchtop conditions. It can be worked up aqueously and subjected to column chromatography and further functionalised by organic transformations. A number of transition metal complexes were obtained using established methodologies and it was found that the deprotonated form, $ArB(2\text{-}py)_3^-$, is a relatively strong sigma donor compared to trispyrazolato borate.[141] Similarly to trispyridyl aluminates, the borate analogue forms sandwich complexes of the type $[\{ArB(2\text{-}py)_3\}_2M]$ (M = Mg, Fe, Mn, Cu, Ru), some of which assemble into remarkably porous and shape persistent supramolecular structures in the solid state. Some of these complexes can be modified via organic transformations the pure ligand cannot undergo.

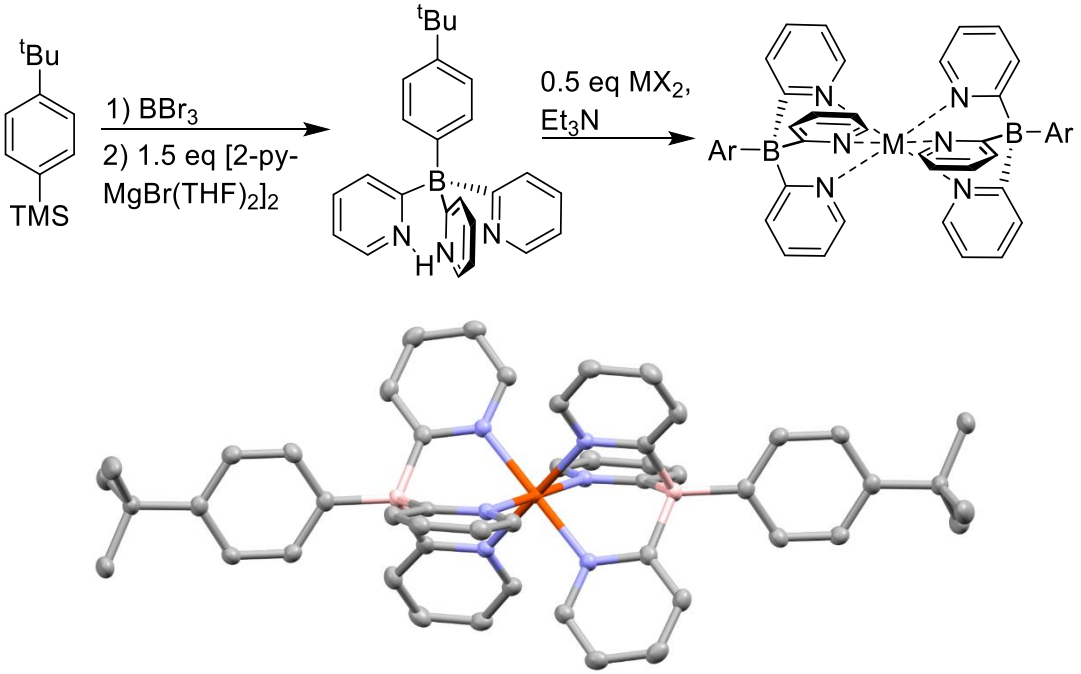

Figure 88: Synthesis and coordination chemistry of the trispyridyl borate $[(4\text{-}^tBu\text{-}C_6H_4)B(2\text{-}py)_3]^-$; Solid-state structure of the sandwich compound $[(4\text{-}^tBu\text{-}C_6H_4)B(2\text{-}py)_3]_2Fe$. Colour code: grey =C, blue = N, orange = Fe, pink = B.

Due to the high stability of the trispyridyl borate ligand, it can be incorporated into polymeric materials.[142,143] Vinyl or norbornyl bridgehead substituents allow polymerisation into homo- and co-block polymers via nitroxide mediated or ring-opening metathesis polymerisation. The trispyridyl borate units in these polymers can then be coordinated to $Cu(ClO_4)_2$. Copper(II) can be exchanged for iron(II), resulting in a change in the materials properties of the polymers.

Group 14

In the search for stable trispyridyl main group ligands Wright et al. reported the synthesis of $MeSi(2\text{-}py)_3LiCl$ from 2-Li-py and $MeSiCl_3$.[144] However, as in the case of trispyridyl borate, this route to the $MeSi(2\text{-}py)_3$ ligand was particularly low yielding which hindered further coordination studies. Following a similar procedure with $^nBuGeCl_3$ (obtained from the in situ reaction of $GeCl_4$ and ^{n}BuLi) yields the ^{n}BuGe(2-py)$_3$ ligand.[125] The tin(IV) derivative ^{n}BuSn(2-py)$_3$, however, was initially isolated from the reaction of 2-Li-py with Cp_2Sn (Figure 89).[145] In this reaction, ^{n}BuBr is generated in the initial lithium halogen exchange of ^{n}BuLi with 2-Br-py, the tin(IV) product is then formed by oxidative addition to the Sn(II) intermediate. The Sn(IV) ligand ^{n}BuSn(2-py)$_3$ can also be obtained in a similar fashion to the silicon and germanium analogue from preformed ^{n}BuSnCl$_3$ and 2-Li-py.[145] Cp_2Pb reacts under analogous conditions as in the Sn(II) case above to give the anionic plumbate $[Pb(2\text{-}py)_3]^-$ as the lithium-THF salt (Figure 89).[146] Therefore, it can be seen that the onset of the inert pair effect for group 14 bridgeheads leads to accessibility of both the +II and the +IV state of these heavy trispyridyl ligands.

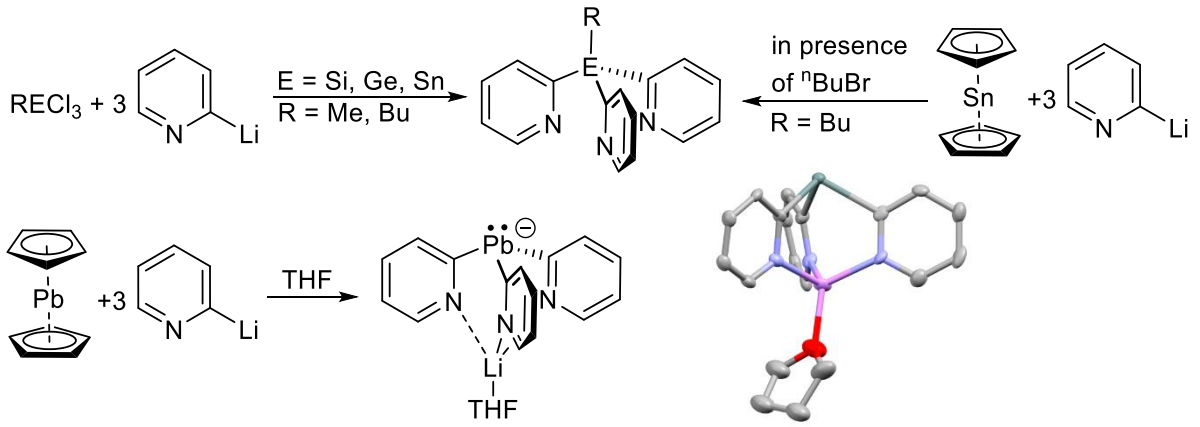

Figure 89: Synthesis of group 14 trispyridyl ligands and solid-state structure of [Pb(2-py)$_3$]Li(THF). Colour code: grey =C, blue = N, red = O, purple = Li, dark grey = Sn.

^{n}BuSn(2-py)$_3$ was found to coordinate in a classic tridentate fashion to CuBr and $Mo(CO)_3$.[145] Other than these examples, however, group 14 trispyridyl ligands with the bridgehead in +IV oxidation state have not been further investigated in coordination chemistry.

Group 14 ligands with +II oxidation state bridgeheads (like the plumbate mentioned above) show rich coordination chemistry through the pyridyl donors as well as the

bridgehead lone pair (Figure 90). This has allowed the formation of coordination polymers and the assembly of multimetallic coordination compounds, mostly investigated by Zeckert and coworkers. Reactions of $[Sn(5\text{-Me-2-py})_3Li(THF)]$, containing the $[Sn(5\text{-Me-2-py})_3]^-$ anion, with Cp^*_3Ln (Ln = La, Yb) yields the adduct $[Cp^*_3LnSn(5\text{-Me-2-py})_3Li(THF)]$ in which the Sn(II) lone pair coordinates to the Ln(III) centre of an intact Cp^*_3Ln moiety.[147] On the other hand, in reactions with Cp^*_2Ln (Ln = Eu, Yb) nucleophilic substitution of the Cp* ligands occurs.[148]

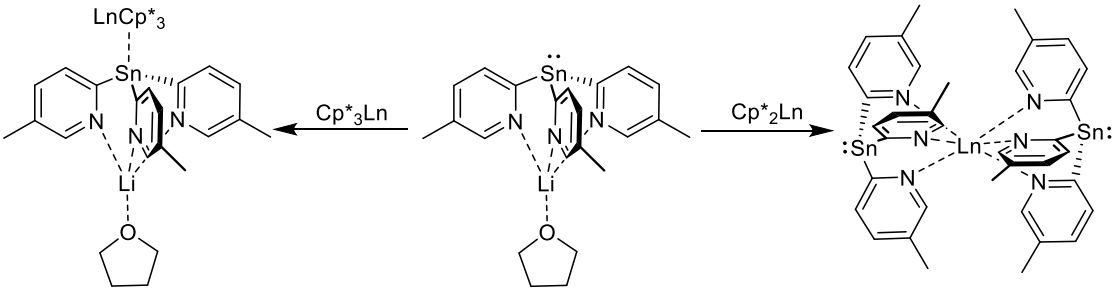

Figure 90: Reactivity of $[Sn(5\text{-Me2-py})_3Li(THF)]$ with Cp* lanthanide complexes.

$[Cp^*_3LnSn(5\text{-Me-2-py})_3Li(THF)]$ itself can be used as a ligand to substitute the Cp* groups of Cp^*_2Yb, yielding the trinuclear complex $[Cp^*_3LaSn(5\text{-Me-2-py})_3Yb(5\text{-Me-2-py})_3SnLaCp^*_3]$ with a central L_2M sandwich arrangement similar to what has been reported for the aluminate analogue $[\{EtAl(2\text{-py})_3\}_2Sm]$.[149] The Sn(II) lone pair can also be coordinated to main group centres. Lanthanide sandwich complexes of the type $[R_3E\text{-}Sn(5\text{-Me2-py})]_2Ln$ can be obtained.[150] Here the lone pair on Sn(II) is coordinatively saturated through Lewis acid base pair formation with, e.g., E = Et_3Al or Et_3Ga.

The lathanide coordination chemistry of $[Pb(5\text{-Me-2-py})_3Li(THF)]$ parallels that of the tin analogue to some extent although the lead lone pair is less coordinatively accessible. [151] Reaction of Cp^*_2Eu with $[Pb(6\text{-O}^t\text{Bu-2-py})_3Li(THF)]$ yields the L_2M sandwich compound in which the Eu(II) atom is coordinated by the six N-atoms of the two $[Pb(6\text{-O}^t\text{Bu-2-py})_3]^-$ ligands, with the Pb(II) centres remaining uncoordinated. However, it was observed that oxidative coupling of the lanthanide complexes can occur, yielding the diplumbane $(5\text{-Me-2-py})_3Pb\text{-}Pb(5\text{-Me-2-py})_3$. Therefore, lanthanide complexes are less stable for the Pb(II) ligands than for the Sn(II).

The use of tin bridgeheads also allows greater structural variety. It was found that an unusual hypervalent $[Sn(5\text{-Me-2-py})_6]^{2-}$ dianion featuring six Sn-C bonds can be formed as its $Li_2(THF)_2$ salt by the reaction of $Sn(5\text{-Me-2-py})_4$ (which itself is formed

by metathesis of $SnCl_4$ with 5-Me-2-Li-py) with 2 equivalents 5-Me-2-Li-py (Figure 91).[152] The Sn(IV) dianion is very thermally stable in solution and in the solid state. The authors suspected that this stability stems from the simultaneous coordination of the lithium cations in the lithium salt $[Li_2(THF)_2Sn(5\text{-Me-2-py})_6]$ by the trispyridyl faces. $[Li_2(THF)_2Sn(5\text{-Me-2-py})_6]$ can be seen as a Janus-head type ligand with two tridentate pockets for complex formation. However, its coordination chemistry remains unexplored.

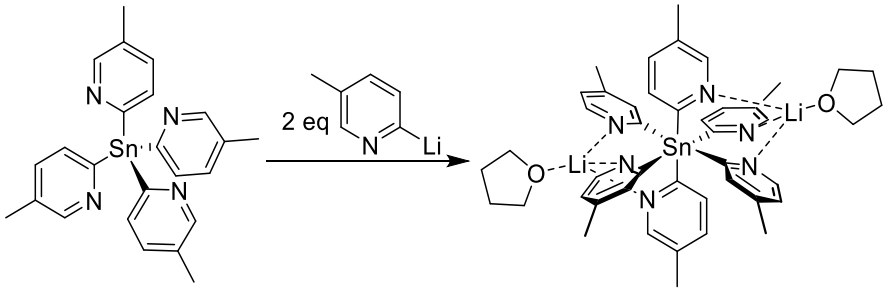

Figure 91: Synthesis of $[Sn(5\text{-Me-2-py})_6Li_2(THF)_2]$ from $Sn(5\text{-Me-2-py})_4$.

In a very recent study it was shown that a nonapyridyl framework can be obtained from the reaction of $[Sn(6\text{-O}^t\text{Bu-2-py})_3Li(THF)]$ and $Sn(HMDS)_2$ or $Pb(HMDS)_2$.[153] In the compound $[(Sn(6\text{-O}^t\text{Bu-2-py})_3)_3Sn/PbLi(THF)]$ three trispyridyl coordination pockets of which one is occupied by Li^+ are present.

Group 15

In group 15, trispyridyl phosphine $P(2\text{-py})_3$ and phosphine oxide $O{=}P(2\text{-py})_3$ are established ligands in coordination chemistry.[154–157] Since the phosphine bridgehead can also act as a donor in $P(2\text{-py})_3$, coordination modes involving the bridgehead are commonly observed. The work described in this section will deal with trispyridyl phosphine ligands which incorporate 6-Me-2-py groups, which have been recently explored in the Wright group (but which are representative of broader coordination chemistry in this area).[158] Three coordination modes have been observed so far for $P(6\text{-Me-2-py})_3$. In $[P(6\text{-Me-2-py})_3FeClOTf]$ (Figure 92, left) all three pyridyl groups are coordinating in a tridentate fashion to iron(II), whereas replacement of one triflate with chloride yields $(6\text{-Me-2-py})P(6\text{-Me-2-py})_2FeCl_2$ (Figure 92, centre), in which only two of the three pyridyl groups coordinate to the iron centre. It was shown that the presence of the 6-Me substituent supresses formation of sandwich type complexes [{P(6-Me-2-

py)$_3$}$_2$Fe], a mode which is encountered in the same study for the simpler P(2-py)$_3$ system. Finally, the phosphorus lone-pair can be accessed in the Janus-head like coordination mode observed in [(CH$_3$CN)$_3$CuP(6-Me-2-py)$_3$Cu(CH$_3$CN)]PF$_6$ (Figure 92, right). Here both the phosphine centre as well the pyridyl groups are coordinated to copper(I).

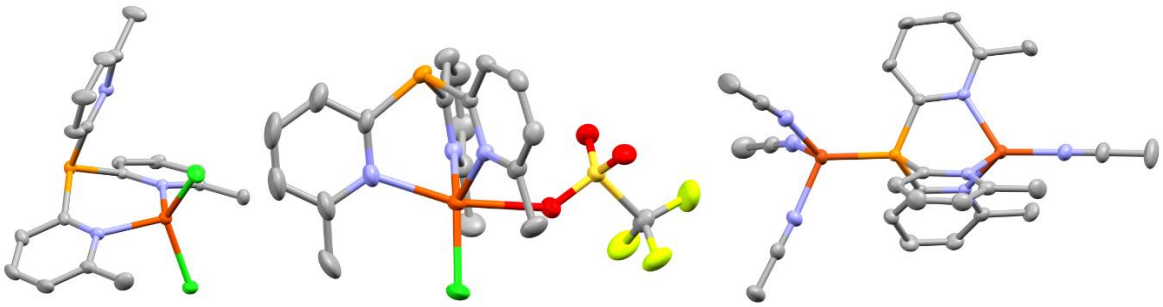

Figure 92: Coordination chemistry of P(6-Me-2-py)$_3$. Solid-state structure of left: [(6-Me-2-py)P(6-Me-2-py)$_2$FeCl$_2$], middle: [P(6-Me-2-py)$_3$FeClOTf] and right: [(CH$_3$CN)$_3$CuP(6-Me-2-py)$_3$Cu(CH$_3$CN)]PF$_6$. Colour code: grey = C, blue = N, orange = P, dark orange = Fe/Cu, green = Cl, red = O, bright green = F, yellow = S.

This P(N,N,N) coordination mode parallels what is found in other trisdonor substituted phosphines and has been shown previously to allow formation of heterobimetallic complexes in which the phosphorus and the pyridyl donors coordinate two different metals, e.g., in (C$_6$F$_5$)AuP(2-py)$_3$Rh(TFB) (TFB = tetrafluorobenzbicyclooctadiene).[159] Reek et al. utilised dual coordination of this type to build supramolecular hydroformylation catalysts. The 3-pyridyl derivative P(3-py)$_3$ can be coordinated to three zinc-porphyrins (and related systems), leaving the phosphorus centre available for coordination to Rh(I).[160–162] The coordinated rhodium is catalytically active in the hydroformylation of alkenes. Due to the supramolecular environment spanned by the porphyrin panels, the Rh(I) is sterically encumbered in a supramolecular capsule-like environment which has been shown to enhance selectivity for the formation of the branched over the terminal aldehyde in alkene hydroformylation. Modification of the panels increases the stability of the catalyst which ultimately yields systems applicable in highly polar industrially relevant solvents.

Similar to the alcoholysis of [EtAl(6-Me-2-py)$_3$Li(THF)] described previously, modification of framework of pyridyl-phosphine ligands has also been investigated recently. Unsymmetric pyridyl-phosphines of the type P(6-Me-2-py)$_x$(R$_2$N)$_{3-x}$ have been shown to react with organic acids and alcohols yielding P(6-Me-2-py)$_x$(RO)$_{3-x}$

with elimination of R_2NH.[163] In the case of P(6-Me-2-py)(R_2N)$_2$, alcoholysis can be controlled to substitute one or two amines enabling the synthesis of 'chiral-at-phosphurs" pyridyl phosphine ligands. Additionally, this development enables the synthesis of chiral pyridyl phosphines through reaction with chiral alcohols such as 2-butanol. Both the starting P(6-Me-2-py)$_x$(R_2N)$_{3-x}$ as well as the modified P(6-Me-2-py)$_x$(RO)$_{3-x}$ ligands tend to form dimeric coordination arrangements with copper salts. In those the alkoxide substituent is not involved in copper coordination, whereas the P-bound amine groups can be.

Artem´ev et al. recently realised the formation of larger cage-type structures based on trispyridyl phosphine. Reaction of P(2-py)$_3$ with AgOTf yields a silver-centred, P-face-capped [Ag@Ag$_4$(μ_3-P)$_4$] silver tetrahedron inscribed within a N_{12} icosahedron (Figure 93).[164] Multinuclear NMR studies revealed the cluster remains intact in solution. Additionally, the cluster shows solid-state luminescence with reported quantum yields up to 24%.

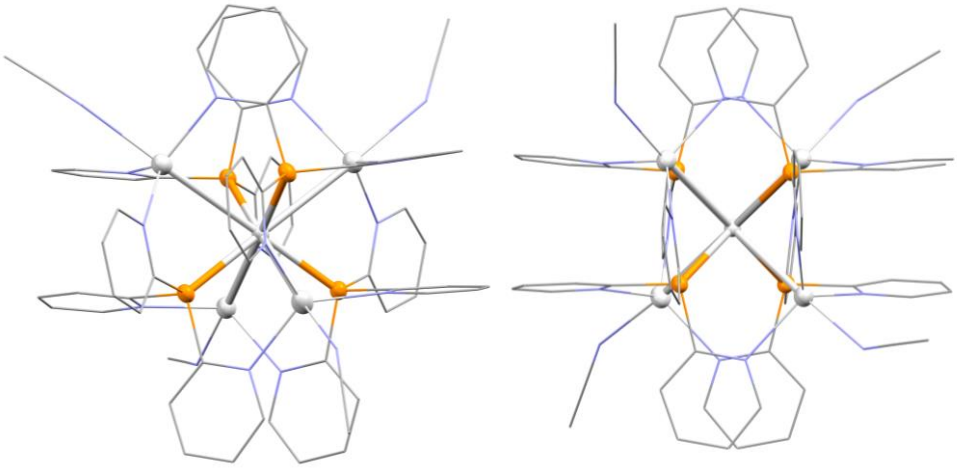

Figure 93: Different views of the solid-state structure of Ag_5 tetrahedron discussed above; OTf counteranions, hydrogen atoms and lattice bound solvent omitted for clarity. Colour code: grey = C, blue = N, silver = Ag, orange = P.

The same group also made creative use of P(2-py)$_3$ as a precursor to alpha-cationic facially coordinating ligands. Reaction of P(2-py)$_3$ with different alkyl iodides yields the phosphonium tripods [RP(2-py)$_3$]I.[165] In coordination studies with Cu(I) it was shown that changing the alkyl chain from Me to Pr to Bu yields either mononuclear or tetranuclear complexes of different structural types, as shown in Figure 94.

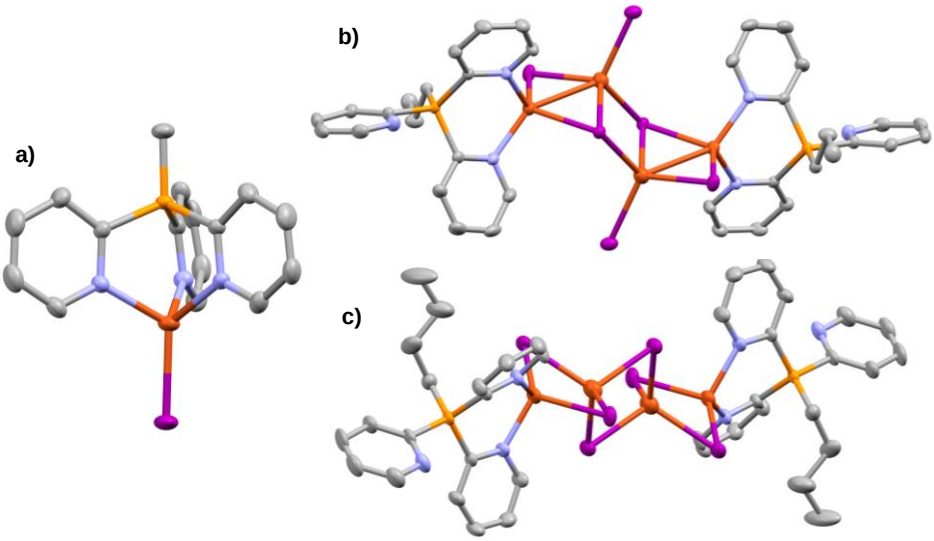

Figure 94: Different views of the solid-state structure of Cu(I) complexes of [RP(2-py)$_3$]I; a) R = Me, b) R = Pr and c) R = Bu. Colour code: grey = C, blue = N, purple = I, bright orange = P, dark orange =Cu.

In related work, Burford et al. recently made use of trispyridyl phosphine as a 6 electron donor for the stabilisation of pnictogen(III) trications (Figure 95).[166] Chloride abstraction starting from $AsCl_3$ with TMSOTf in the presence of P(2-py)$_3$ yields [P(2-py)$_3$As][OTf]$_3$, in which the tricationic pnictogen complex adopts a C_{3v} symmetric structure. The reaction was shown to occur via formation of the dicationic intermediate [P(2-py)$_3$AsCl][OTf]$_2$, which then undergoes chloride metathesis to give the final products [P(2-py)$_3$As][OTf]$_3$ and [P(2-py)$_3$AsCl$_2$][OTf]. The analogous rearrangement reaction has been observed for the Sb derivative.

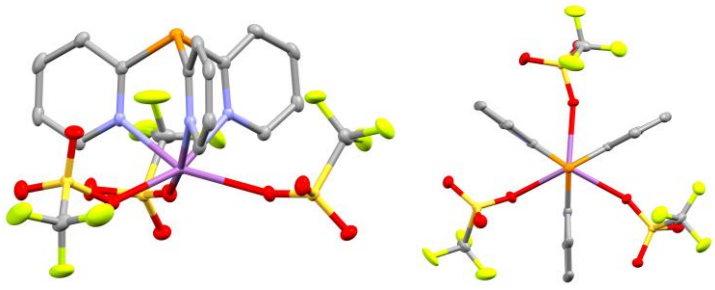

Figure 95: Different views of the solid state structure of [P(2-py)$_3$As][OTf]$_3$. Colour code: grey = C, blue = N, red = O, bright orange = P, purple = As/Sb, yellow = S, bright green = F.

The lone pair of trispyridyl phosphine can also be subjected to further functionalisation via oxidation with H_2O_2, elemental sulphur or selenium. Sundermeyer et al. used the nature of the pnictogen bridgehead to modify the photophysical properties in [E=Pn(2-

$py)_3CuI]$ complexes (E = O, S, Se; Pn = P, As).[167] The reported Cu(I) complexes were found to be potent emitter materials, exhibiting thermally activated delayed fluorescence (TADF) with relatively short phosphorescence decay times (T_1 -> S_0). This study nicely demonstrated how the nature of the bridgehead in $E=Pn(2\text{-}py)_3CuI$ and its oxidant can tune the electronic properties of the coordinated metal. Trispyridyl phosphine oxide also has been recently used by Miller et al. as a supporting ligand in $[O=P(2\text{-}py)_3Ru(bipy)(OH_2)]$ (bipy = bipyridine) which acted as a water-oxidation catalyst, with enhanced electrocatalytic activity compared to related systems.[168] Both of these studies highlight how moving to more robust Pn(V) bridgeheads leads can lead to real-world applications.

Although a plethora of trispyridyl main group ligands have been synthesised there are still gaps in this area. For example, there are no examples with Ga(III), Sb(III/V) or Bi(III/V) as the bridgehead. Seminal work by Gabbai et al. showed that such bridgeheads in P-donor ligands make transition metal reactivities possible that have few parallels in other coordination complexes.[169] As mentioned in the introduction, some trispyridyl main group ligands are largely unexplored in coordination chemistry, such as $RSi(2\text{-}py)_3$ or $As/O=As(2\text{-}py)_3$. Because of this the goal in this part of the thesis was to close these gaps in the synthesis of trispyridyl main group ligands and to explore the coordination chemistry of the unknown and underexplored derivatives. In addition, although there has been a lot of synthetic effort in the area of trispyridyl main group ligands, little is about the actual electronic consequences of changing the bridgehead and the result on coordination behaviour and reactivity of metal complexes. This is a further aim of the current study.

Chapter 7: How Can Changing the Bridgehead Affect the Properties of Trispyridyl Pnictogen Ligands?

Surprisingly, there are no previous reports of the synthesis or coordination chemistry of trispyridyl ligands of Sb or Bi. Our attempts to obtain the unsubstituted ligands E(2-py)$_3$ (E = Sb, Bi) using the in situ reactions of 2-lithio-pyridine with ECl_3 were only successful for E = As, apparently as a result of reductive elimination of bipyridine from E(2-py)$_3$ and the generation of elemental Sb or Bi for the heavier group 15 elements. Black reaction mixtures (due to the formation of Sb and Bi) are obtained which show a complex mixture of products by ^{1}H NMR analysis. Reductive elimination of bipyridine from the bridgehead is a problem which has been observed before for the tin(IV) analogue.[145] The failure of the initial attempts to obtain the Sb and Bi trispyridyl ligands in these initial studies is in line with a previous report which showed that the ligand Bi(2-py)$_3$ could not be obtained even from the reaction of $BiCl_3$ with the more stable 2-(ZnBr)-pyridine reagent.[170] A very recent study also failed to isolate the trispyrazolato bridged bismuth ligand.[171] Figure 96 summarises these results.

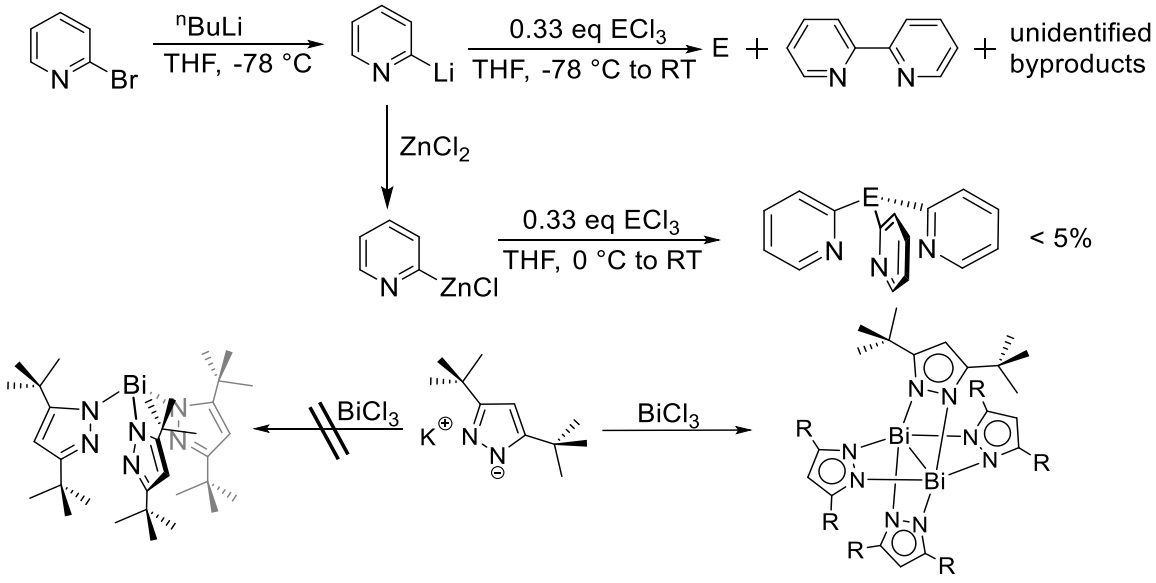

Figure 96: Synthetic efforts to afford heavy pnictogen E (E = Sb, Bi) trispodal ligands.

Results and Discussion

The use of 2-Li-6-Me-pyridine has allowed us here to synthesise the tripodal ligands E(6-Me-2-py)$_3$ [E = As **7.1**, Sb **7.2**, Bi **7.3**] in good yields (64-69%) after crystallisation from toluene (Figure 97), making all the group 15 (N, P, As, Sb, Bi) trispyridyl ligands synthetically available. Bi(6-Me-2-Py)$_3$ **7.3** is the heaviest member of the family of isovalent trispyridyl main group ligands to be reported

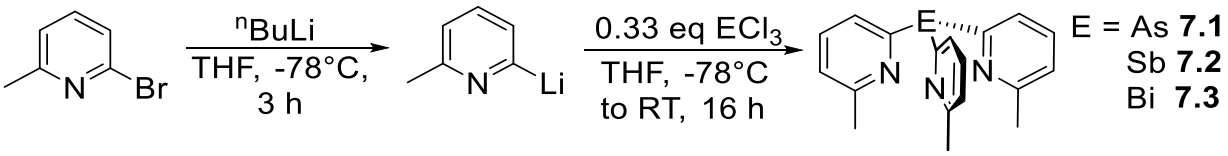

Figure 97: Synthesis of E(6-Me-2-py)$_3$ E = As **7.1**, Sb **7.2**, Bi **7.3**.

The increased stability of the pyridyl substituents in **7.2** and **7.3** can be ascribed to the electron donating effect of the Me-group, which suppresses reductive elimination. Also, we found that the lithiate 6-Me-2-Li-py is more stable during metathesis than the unsubstituted lithiate 2-Li-py.

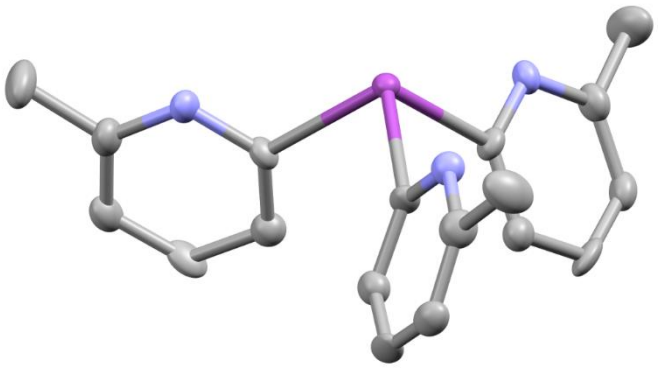

Figure 98: Solid-state structure of **7.3**; the structures of **7.2** and **7.1** are similar. Ellipsoids shown at 40% probability; hydrogen atoms omitted for clarity. Selected bond lengths [Å] and angles (º) for **7.1**-**7.3**: **7.1**, As-C 1.980(4), C-As-C 97.3(2), py-ring dihedral from perpendicular 35.3. **7.2**, Sb-C 2.160(10), C-Sb-C 95.3(4), py-ring dihedral from perpendicular 34.8. **7.3**, Bi-C 2.270(8), C-Bi-C 95.0(3), py-ring dihedral from perpendicular 22.8. Colour code: grey = C, blue = N, purple = Bi.

X-ray quality crystals of **7.1**, **7.2** and **7.3** could be grown from saturated toluene and THF solutions at -14 °C.The solid-state structures of **7.1**, **7.2** and **7.3** are similar to the previously structurally characterised P-counterpart P(6-Me-2-Py)$_3$, in which the 6-Me groups and N-atoms of the pyridyl ring units are orientated (‘upwards’) towards the lone pair on E.[158] As expected, the C$_{pyridyl}$-E distances increase moving down group

15 (by ca. 0.29 Å), matching the increase in atomic size of the group 15 atoms. The increase in the E-C bond lengths going from As to Sb to Bi is matched by the planes of the pyridyl rings becoming increasingly perpendicular to the bridgehead C-E bonds, as a result of the decreased steric repulsion between the 6-Me groups.

Our initial interest regarding the properties of **7.1**-**7.3** focused on the potential structural/functional effects of the increasing Lewis acidity of the bridgehead as group 15 is descended. At the top of the group (N and P) the higher electronegativity, combined with the presence of compact lone pairs, is known to lead to ambidentate character in which both the N-atoms of the 2-py groups and the group 15 atom E can donate to metal ions as shown in the introduction. However, the onset of electropositive character and relativistic stabilisation of the lone pair at Bi are anticipated to lead to increasing acceptor character for the bridgehead as the group is descended.[172,173]

The increase in the Lewis acidity of the bridgehead atoms in **7.1**-**7.3** was demonstrated by initial DFT (B3LYP/def2-TZVPP) calculations of their fluoride ion affinities (FIA). These calculations were carried out by Patrick Pröhm at FU Berlin. Firstly, the structures of the free ligands and their fluoride adducts were optimised and the binding energies of fluoride were compared. The As ligand **7.1** turned out to have the lowest FIA and was therefore set to 0 kJ/mol relative to the Sb and Bi ligands. For the heavier homologues the FIA increases with increasing atomic number (FIA **7.2** = -36.8 kJ/mol, FIA **7.3** = -58.2 kJ/mol), indicating a progressive increase in the Lewis acidity of the bridgehead atoms. From this we reasoned that the Sb and Bi ligands might be capable of simultaneous anion and cation coordination of metal salts (using their pyridyl-N and bridgehead E atoms).

The Cu(I) complexes $[E(6\text{-Me-2-Py})_3CuMeCN]PF_6$ [E = As **7.4**, Sb **7.5**, Bi **7.6**)] were obtained by the room temperature reactions of **7.1** - **7.3** with $[Cu(MeCN)_4]PF_6$ in MeCN and crystallised from the concentrated reaction mixtures after filtration (Figure 99). Isolated crystalline yields were 32% for **7.4**, 25% for **7.5** and 18% for **7.6**.

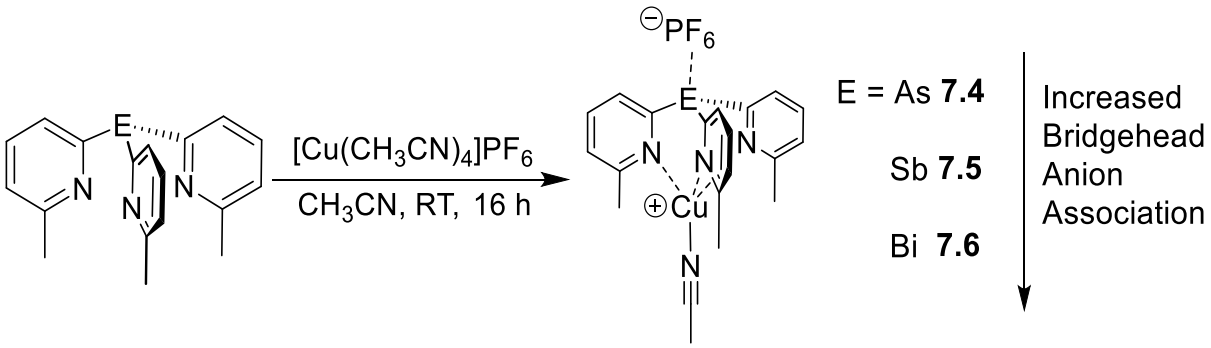

Figure 99: Synthesis and structural trend observed in the solid-state structures of **7.4**, **7.5** and **7.6**.

These crystals were suitable for X-ray diffraction studies (Figure 100). All of the complexes contain isostructural $[E(6\text{-Me-2-Py})_3CuMeCN]^+$ cations in the solid state, in which the trispyridyl ligands coordinate pseudo-tetrahedral Cu(I) centres using all three N-atoms**.** The increase in the size of the bridgehead atom (As-Bi, ca. 0.3 Å) has only a minor influence on the Cu(I) geometry because the ligand bite is maintained in **7.4**-**7.6** by the pivoting of the 6-Me-2-py groups towards the metal ions (about the ipso-C-atoms of the pyridyl rings). An important consequence of this, regarding later catalytic studies, is that the steric environments of the Cu(I) centres in **7.4**-**7.6** are very similar. A more noticeable structural influence, however, is the increase in Lewis acidity of the group 15 bridgehead atoms, resulting in increasing anion-cation interactions on descending group 15.

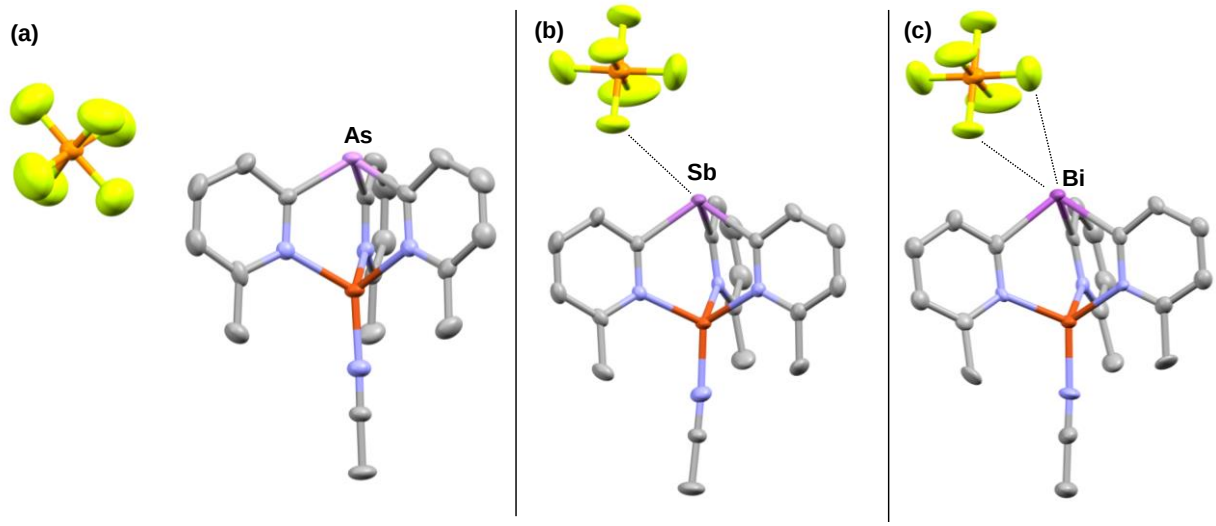

Figure 100: Solid-state structure of (a) **7.4**, (b) **7.5** and (c) **7.6**. Displacement ellipsoids shown at 40% probability; hydrogen atoms and PF_6-disorder omitted for clarity. As-C range 1.956(3)-1.970(3), $N_{pyridyl}$-Cu range 2.071(3)-2.091(2), NMeCN-Cu 1.945(3), C-As-C range 99.25(15)-99.94(9), $N_{pyridyl}$-Cu-$N_{pyridyl}$ range 97.51(8)-99.58(12). Sb-C range 2.155(3)-2.167(3), $N_{pyridyl}$-Cu range 2.070(2)-2.111(2), N_{MeCN}-Cu 1.954(3), C-Sb-C range 92.09(11)-98.93(11), $N_{pyridyl}$-Cu-$N_{pyridyl}$ range 94.33(9)-106.04(9). Bi-C range 2.244(6)-2.270(6), $N_{pyridyl}$-Cu range 2.057(5)-2.128(5), N_{MeCN}-Cu 1.965(5), C-Bi-C range 90.2(2)-97.0(2), $N_{pyridyl}$-Cu-$N_{pyridyl}$ range 95.15(17)-107.71(18). Colour code: grey = C, blue = N, purple = As/Sb/Bi, orange = P, bright green = F, dark orange = Cu.

In the As derivative **7.4** there are no close contacts between the As(III) bridgehead and the PF_6^- anions in the lattice. However, in the Sb derivative **7.5** the lattice arrangement consists of ion-pairs of the $[Sb(2\text{-}py)_3CuMeCN]^+$ cation and PF_6^- anion, with one short Sb•••F interaction linking each cation to a single anion [3.483 Å; cf. a maximum of ca. 3.53 Å expected for a van der Waals interaction].[80] The extent of these interactions increases further for the Bi complex **7.6**, in which a helical packing arrangement of the $[Bi(2\text{-}py)_3CuMeCN]^+$ cations and PF_6^- anions occurs through two close Bi•••F contacts [3.349 and 3.736 Å; cf. a maximum of 3.77 Å for a van der Waals interactions]. However, these bridgehead•••PF_6^- interactions do not persist in solution as the ^{31}P NMR spectra in CD_3CN are identical in **7.4**, **7.5** and **7.6**, showing free PF_6^- at -144.5 ppm.

In light of the observed effects of ion-pairing found in the solid-state structures of complexes **7.5** and **7.6**, we were intrigued by the potential effects of having a more strongly coordinating anion.

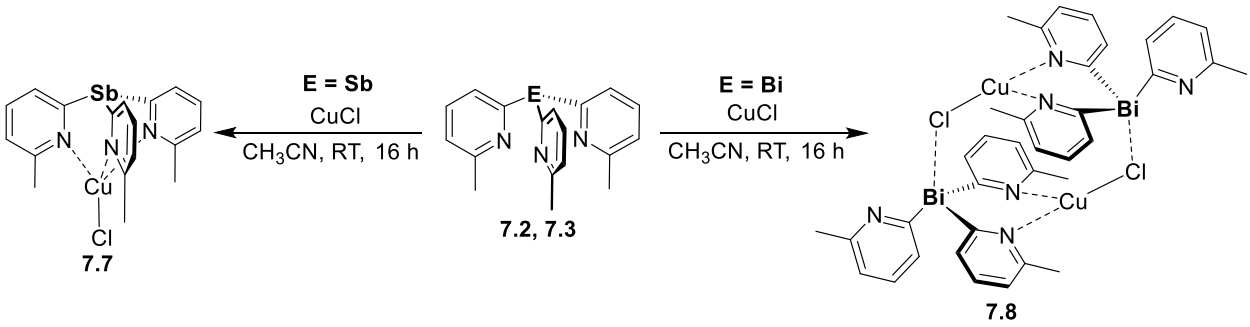

Figure 101: Reaction of **7.2** and **7.3** with CuCl yielding **7.7** and **7.8**.

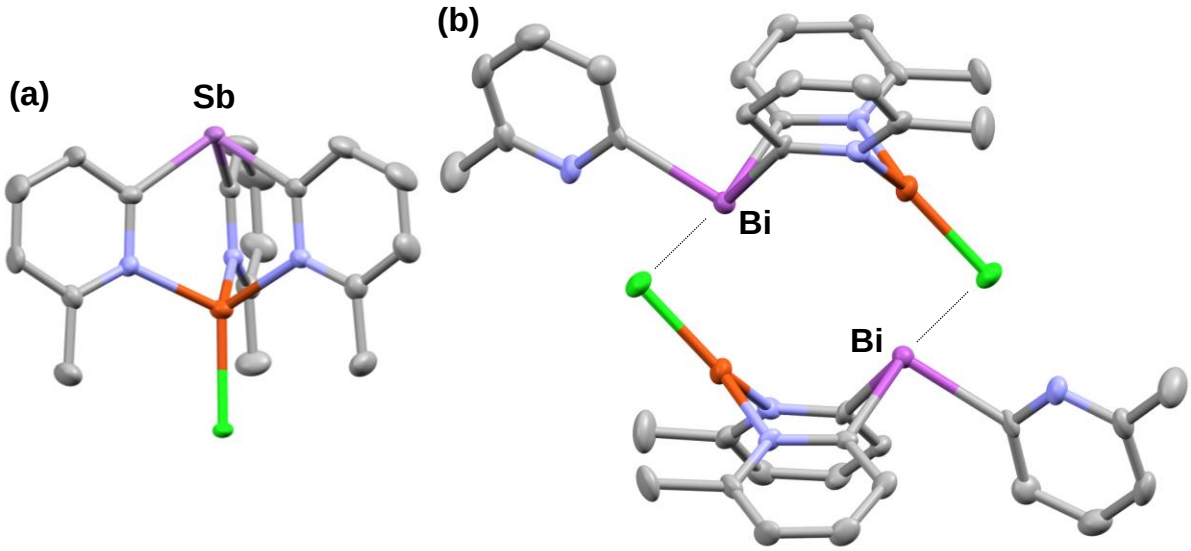

Figure 102: Solid-state structure of (a) **7.7** and (b) **7.8**; displacement ellipsoids set at 40% probability; hydrogen atoms omitted for clarity. Selected bond lengths [Å] and angles [°] for **7.7** and **7.8**: **7.7**, Sb-C range 2.133(6)-2.160(4), N-Cu range 2.126(3)-2.146(5), Cu-Cl 2.341(1), C-Sb-C 94.6(2)-97.7(2), N-Cu-N 98.4(2)-103.2(1). **7.8**, Bi-$C_{(bridging\ pyridyl)}$ range 2.269(8)-2.296(8), Bi-$C_{(terminal\ pyridyl)}$ 2.255(9), N-Cu 2.033(6), 2.033(7), Cu-Cl 2.188(2), Bi•••Cl 3.432(2), Bi•••Cu 3.271(1), C-Bi-$C_{(bridging\ pyridyl)}$ 89.5(3), $C_{(bridging\ pyridyl)}$-Bi-$C_{(terminal\ pyridyl)}$ 90.2(3)-101.5(3), Bi•••Cl-Cu 80.5(2). Colour code: grey = C, blue = N, purple = Sb/Bi, dark orange = Cu, bright green = F.

Accordingly, we prepared the corresponding CuCl complexes of **7.2** or **7.3** by the reactions of CuCl in MeCN (Figure 101). The Sb-ligand complex **7.7** was isolated as yellow crystals suitable for X-ray crystallography from the concentrated reaction mixture. As expected, Sb(6-Me-Py)$_3$ **7.2** forms a C_{3v}-symmetric complex in which all three pyridyl groups coordinate to the Cu(I) ion of a CuCl unit (Figure 102). However, an unprecedented dimeric arrangement [(6-Me-Py)Bi(6-Me-Py)$_2$CuCl]$_2$ **7.8** is observed for **7.3,** in which one of the intramolecular N-Cu bonds is effectively sacrificed for an intermolecular Cu-Cl•••Bi interaction and an intramolecular Cu•••Bi interaction, leaving the Cu centres in trigonal planar coordination environments (Figure

102). The Bi-Cl interaction of ca. 3.43 Å is around 0.7 Å shorter than the sum of the van der Waals radii of Bi and Cl and Bi•••Cu contact of ca. 3.27 Å in the monomer units of **7.8** is about 1.1 Å shorter than the sum of the van der Waals radii of Cu and Bi.[80] In order to investigate the electronic grounds for this structural change we turned to computational modelling. These computations were carried out by Patrick Pröhm at FU Berlin. A single-point DFT calculation (B3LYP hybrid functional, def2-TZVPP basis set) using the atom coordinates obtained from the solid- state structure shows that the inter-dimer Bi•••Cl interactions result from Cl lone-pair donation into the σ*-orbital of one of the $C_{pyridyl}$-Bi bonds in the HOMO-24 and HOMO-27. Additionally, AIM analysis reveals bond critical points in the Bi•••Cl axes between the monomers (Figure 103). The electronic overlap between copper and bismuth can be seen in the HOMO -12 and stems from donation of one of the copper d-orbitals into the σ*-orbital of one of the $C_{pyridyl}$-Bi bonds. Consequently, the energetic accessibility of the σ*-orbital of Bi drives the structural change going from Sb to Bi.

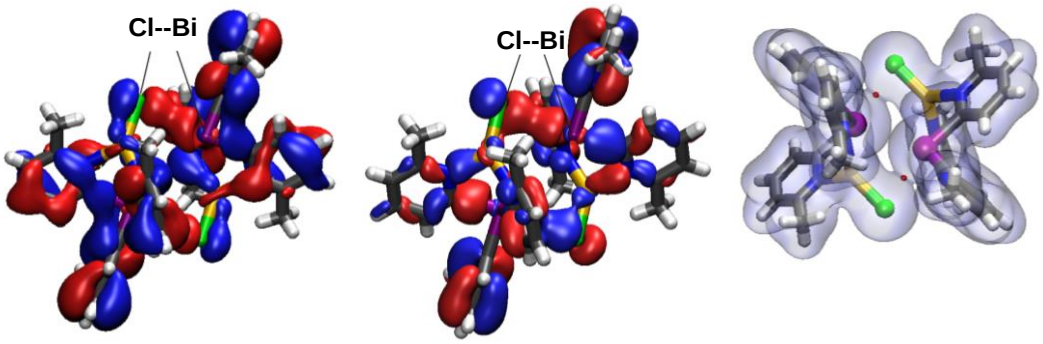

Figure 103: HOMO -24 and HOMO -27 and electron density plot of dimeric **7.8**.

The anion-mediated switching of the coordination mode of the trispyridyl ligand **7.3** from tris-N-donor in the $CuPF_6$ complex **7.6** to bis-N-donor/Bi-acceptor in **7.8** is not just a solid-state effect, but can be demonstrated by the addition of an excess of a chloride source (tetrabutylammonium chloride, TBACl) to **7.6** in MeCN, which gives **7.8** quantitatively (Figure 104). Variable-temperature ^{1}H NMR spectroscopic studies (253 – 313 K) show that **7.8** is involved in a monomer/dimer equilibrium in MeCN solution. In addition to the two sets of 2-pyridyl and Me-resonances expected for the Bi/Cu-bridging and terminal 6-Me-2-py groups of the dimer, the room temperature ^{1}H NMR spectrum of **7.8** in CD_3CN also shows resonances for the symmetric, tris-chelated monomer [Bi(6-Me-py)$_3$CuCl] **7.9** (i.e., isostructural with **7.7**, ca 10% of the

total at 298K), with the monomer increasing in abundance at higher temperatures. The presence of an intermolecular monomer-dimer equilibrium is confirmed by dilution experiments at room temperature, in which the equilibrium shifts towards the monomer at lower concentrations and towards the dimer at higher concentrations. Van't Hoff analysis of the variable-temperature data yields a dimerisation enthalpy of $\Delta H = -21 \pm 2$ kJ mol^{-1} and entropy of $\Delta S = -61 \pm 6$ J mol^{-1} K^{-1} (Figure 105).

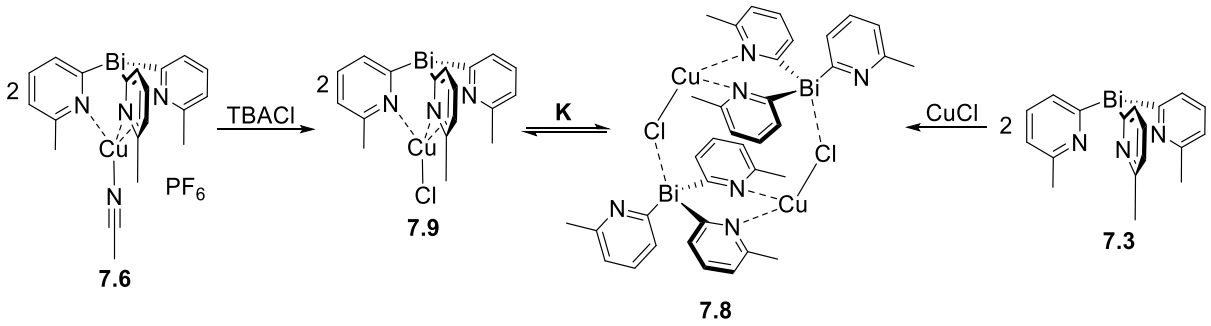

Figure 104: Anion dependent coordination chemistry and monomer/dimer equilibrium of **7.3** and its copper complexes.

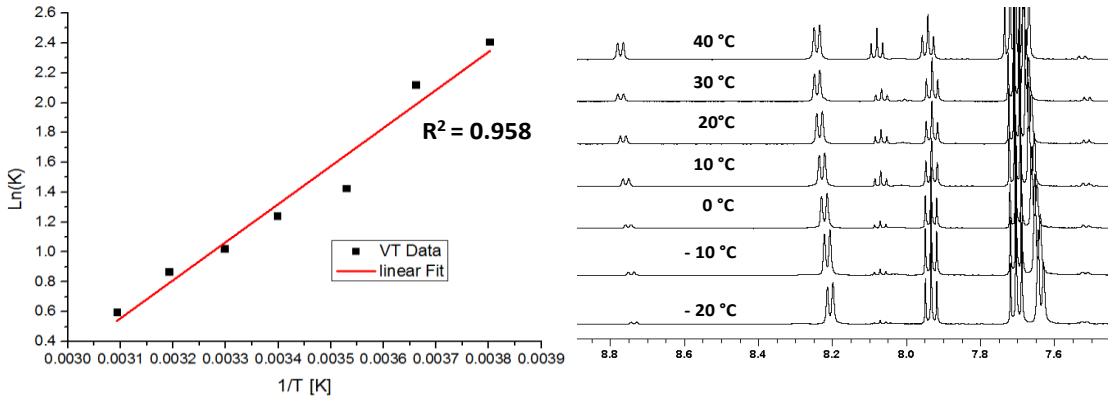

Figure 105: Variable temperature NMR analysis and van't Hoff plot of monomer/dimer equilibrium.

These data provide further evidence that the enthalpy gained in forming the dimer outweighs the entropic gain normally associated with the chelate effect at lower temperatures.

In addition to structural consequences, ligands **7.1**-**7.3** also provide a unique opportunity to explore the effects of incremental changes in the electronic character and size of the bridgehead on catalytic selectivity and reactivity. The impact of the decrease in electronegativity of the bridgehead atom is indicated by DFT calculations

(B3LYP/def2-TZVPP), which show a small but consistent trend towards greater negative charge at the N-atoms as group 15 is descended. Natural population analysis of the DFT optimised ligand structures reveals an increasing amount of negative charge at the nitrogen atoms as group 15 is descended, from -0.44877 a.u. for **7.1** to -0.46991 a.u. for **7.2** to -0.47737 a.u. for **7.3**.[174] An increase in negative charge should theoretically render the ligands better σ-donors as one moves down the pnictogen group. The resulting increase in the σ-donor character of the ligands is consistent with the trend towards lower Cu(I)/Cu(II) oxidation potential observed in the cyclic voltammograms of the $CuPF_6$ complexes **7.4**-**7.6** in MeCN [$E_{1/2}$(Cu(I)/Cu(II)) = 0.65 **7.4**; 0.56 **7.5**; 0.48 **7.6** V vs. Fc/Fc^+] (Figure 106). Here we refer to the maximum of the oxidative wave since the redox pair is only partially reversible, presumably due to structural rearrangement of the complex upon oxidation to Cu(II).

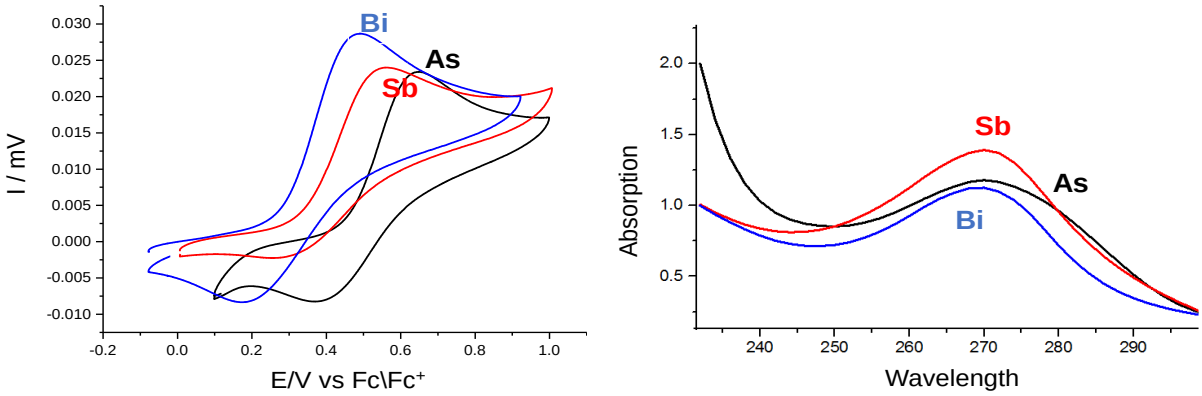

Figure 106: Left: Overlayed Cu(I)/Cu(II) redox cyclic voltamograms for **7.4**, **7.5** and **7.6** derivatives (2.5mM) in 0.1M $TBAPF_6$/MeCN electrolyte at a scan rate of 100 mVs^{-1}. Right: Overlayed UV-Vis spectra of **7.1** (As), **7.2** (Sb), **7.3** (Bi) (2.5 µM solution in DCM, x-Axis in nm).

At the same time, the bridgehead atom appears to have little effect on the acceptor character of the ligands, with the free ligands all exhibiting a π to π* transition at 270 nm in their UV-Vis spectra in DCM (Figure 106). This stems from the s-character of the bridgehead E lone pairs, which do not have the correct symmetry to interact with the π-orbitals of the pyridyl rings. From this we conclude that as one moves down the group the ligands **7.1**, **7.2** and **7.3** become better σ-donors and but have approximately equal π-acceptor ability.

With this information in hand we were curious to see how this change in the ligand properties affects the reactivity of the coordinated metal and turned to homogeneous catalysis as an experimental handle. As mentioned previously, facially coordinating

tripodal ligands are among the most commonly used auxiliary ligands in homogenous catalysis.[120] We investigated the bridgehead influence on the Cu(I)-mediated aziridination of styrenes as this reaction is one of the most reliable reactions catalysed by Cu(I). This reaction has been used previously as a mechanistic probe using Cu(I) trispyrazolyl borate complexes by Perez and coworkers, who showed that the polar contribution to the mechanism is increased by electron-poor Cu(I) centres, while the radical contribution is increased by electron rich Cu(I) centres.[175] In this case electronic modulation is achieved by conventional substitution of the pyrazolyl rings and the electronic effects were demonstrated by cyclovoltamery and the IR CO stretching frequency of the related Cu(I) carbonyl complexes.

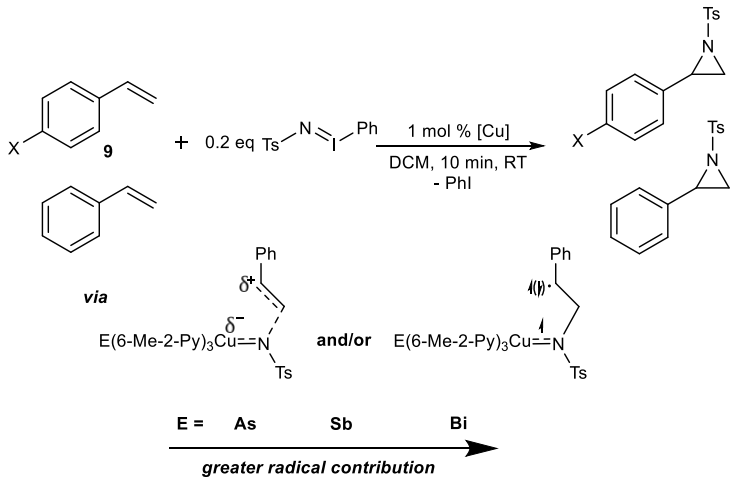

Figure 107: Competition experiments of the copper(I) catalysed aziridination. [Cu] = **7.4**, **7.5**, **7.6**.

We conducted a similar competitive study of the Cu(I)-mediated aziridination of a series of aryl alkenes with TsN=IPh (Ts = Tosyl) in the presence of styrene, using the $CuPF_6$ complexes **7.4**, **7.5** and **7.6** as the catalysts (Figure 107). All complexes show equally excellent activity with reaction times under 5 min and turnovers of >95% substrate at 1 mol% catalyst loading. However, when a 1:1 mixture of a X-para-substituted styrene and styrene was employed a change in the ratio of the two aziridine products is observed for a given X-group (X= MeO, Me, Ph, H, Cl, CF_3) moving from **7.4** to **7.6**. An example of the type of data that was obtained is shown in Figure 108.

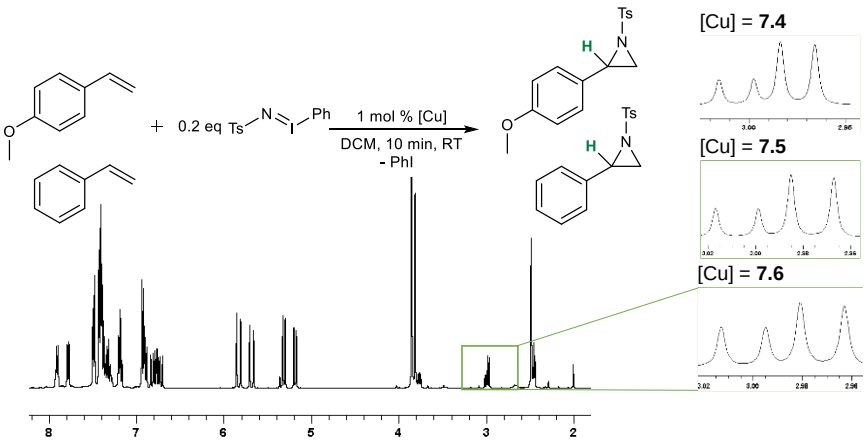

Figure 108: Ratio change of competitive aziridination catalysis by **7.4**, **7.5** and **7.6** using a 1:1 ratio of syrene and 4-methoxy-styrene.

Hammett analysis of the ratio of the two aziridination products produced (which represents the ratio of the reaction rate constants k_X/k_H) shows that while the data employing **7.4** (R^2 = 0.96) and **7.5** (R^2 = 0.95) can be fitted well to a single-parameter Hammett equation ($\log(k_X/k_H)$ vs. σ^+), the data for **7.6** as the catalyst are modelled better using a two-parameter equation ($\log(k_X/k_H)$ vs $\sigma^+ + \sigma^\bullet$) ($R^2$ single parameter fit 0.89, R^2 dual parameter fit 0.97). The ratio contribution of the polar with respect to the radical pathway is represented by the ratio of the partial slopes $\rho^+\backslash\rho^\bullet$ of the dual parameter fit. This ratio is 2.1 for As, 1.36 for Sb and 0.76 Bi. This is consistent with a shift from a polar mechanism for **7.4** towards a radical mechanism for **7.5** and **7.6**, and is in line with the decrease in the Cu(I)/Cu(II) oxidation potentials going from **7.4** to **7.6**, the decrease in electronegativity of the bridgehead atom, and the resulting increase in σ-donor character of ligands **7.1**-**7.3**. Thus, changing the bridgehead in $[E(6\text{-Me-2-py})_3CuMeCN]^+$ can be used to modulate the electronic character. Using this approach in conjunction with ligand substitution can potentially be used to fine-tune the electronic character of tripodal ligands.

Chapter Conclusion

We have obtained the first examples of trispyridyl ligands of Sb and Bi by 6-methyl substitution of the pyridyl rings. This has allowed us to assess the effects of incremental periodic changes in the electronic character and size of the bridgehead atom for the first time in this and related classes of tripodal main group ligands. The bridgehead atom does indeed have a considerable effect on structure and reactivity of complexes of $E(6\text{-Me-2-py})_3$, with a large influence being the electronegativity of the bridgehead atom and its impact on Lewis acidity and σ-donor character of the ligand set. This is seen in the unique, anion-dependent coordination character of the $Bi(6\text{-Me-2-py})_3$ ligand in which structural change is driven by σ* interactions. Additionally, changing the bridgehead can be used to alter the catalytic properties of a coordinated metal, not in direct electronic contact with the bridgehead.

Experimental Details

General experimental details involving techniques, instruments and materials employed are provided in the appendix at the end of this thesis.

NMR labelling Scheme

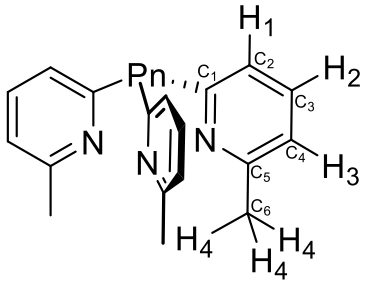

Synthesis of New Compounds

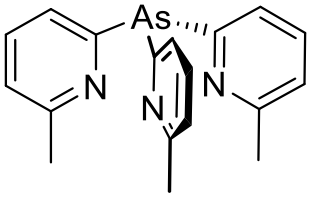

Synthesis of 7.1: 2-Bromo-6-methyl pyridine (2.28 ml, 20 mmol) was dissolved in 40 ml of THF. To this ^{n}BuLi (12.5 ml, 20 mmol, 1.6 M in hexanes) was added dropwise at −78 °C.The resulting dark orange solution was stirred for 3 h at −78 °C.$AsCl_3$ (558 µl, 6.66 mmol) in 5 ml THF was added dropwise to the dark red lithiated species. The resulting pale brown mixture was allowed to warm up to room temperature. After stirring overnight, a pale green solution with a light brown precipitate was formed. All volatiles were removed under vacuum and the resulting solid residue was extracted with 40 ml of warm toluene. The suspension was filtered through Celite to yield a clear pale green solution which was concentrated in vacuum until the precipitation of a white solid was observed, which was redissolved by gentle heating. Storage overnight at – 15 °C yielded **7.1** as colourless needles suitable for X-ray crystallography. The product was isolated by filtration and storage of the mother liquor yielded a second crop of crystals. Combined yield 1.62 g (4.61 mmol, 64%).**^{1}H NMR (25 °C, d_8-toluene, 500.12 MHz)**: δ(ppm) = 2.37 (s, 9H, H4), 6.58 (d, $^{3}J_{HH}$ = 7.76 Hz, 3H, H3), 7.00 (t, $^{3}J_{HH}$ = 7.76 Hz, 3H, H2), 7.32 (d, $^{3}J_{HH}$ = 7.76 Hz, 3H, H1); **^{13}C NMR (25 °C, d_8–toluene, 125.78 MHz)**: δ(ppm) = 23.9 (C6), 121.3 (C2), 125.8 (C4), 134.9 (C3), 158.2 (C5), 166.6(C1); **Elemental analysis (%)** calcd. for **7.1**: C 61.5%, H 5.1%, N 11.9%; found C 61.0%, H 5.2%, N 12.0%.

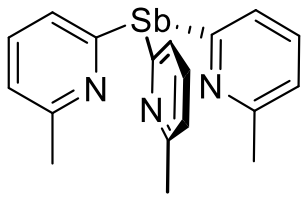

Synthesis of 7.2: 2-Bromo-6-methyl pyridine (2.28 ml, 20 mmol) was dissolved in 40 ml of THF. To this ^{n}BuLi (12.5 ml, 20 mmol, 1.6 M in hexane) was added dropwise at −78 °C.The resulting dark orange solution was stirred for 3 h at −78 °C.$SbCl_3$ (1.51 g, 6.66 mmol) in 5 ml THF was added dropwise to the dark red lithiated species. The resulting pale brown mixture was allowed to warm up to room temperature. After stirring overnight, a pale green solution with a light brown precipitate was formed. All volatiles were removed under vacuum and the resulting solid residue was extracted with 40 ml of warm toluene. The suspension was filtered through Celite to yield a clear pale green solution which was concentrated under vacuum until the precipitation of a white solid was observed which was redissolved by gentle heating. Storage overnight at -15 °C yielded **7.2** as colourless needles suitable for X-ray crystallography. The product was isolated by filtration and storage of the mother liquor yielded a second crop of crystals. Combined yield 1.60 g (4.00 mmol, 60%).**^{1}H NMR (25 °C, d_8-toluene, 500.12 MHz)**: δ(ppm) = 2.41 (s, 9H, H4), 6.58 (d, $^{3}J_{HH}$ = 7.76 Hz, 3H, H3), 7.00 (t, $^{3}J_{HH}$ = 7.76 Hz, 3H, H2), 7.53 (d, $^{3}J_{HH}$ = 7.76 Hz, 3H, H1); **^{13}C NMR (25 °C, d_8–toluene, 125.78 MHz)**: δ(ppm) = 24.0 (C6), 121.4 (C2), 128.3(C4), 134.5 (C3), 158.5 (C5), 169.9(C1); **Elemental analysis (%)** calcd. for **7.2**: C 54.3%, H 4.3%, N 9.1%; found C 54.0%, H 4.5%, N 8.8%.

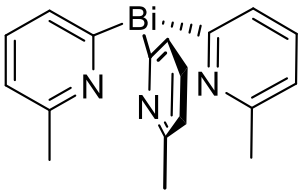

Synthesis of 7.3: 2-Bromo-6-methylpyridine (2.28 ml, 20 mmol) was dissolved in 40 ml of THF. To this ^{n}BuLi (12.5 ml, 20 mmol, 1.6 M in hexane) was added dropwise at −78 °C.The resulting dark orange solution was stirred for 3 h at −78 °C.$BiCl_3$ (1.51 g, 6.66 mmol) in 5 ml THF was added dropwise to the dark red lithiated species. The resulting pale brown mixture was allowed to warm up to room temperature. After stirring overnight, a pale green solution with a light brown precipitate was formed. All volatiles were removed under vacuum and the resulting solid residue was extracted with 40 ml of warm toluene. The suspension was filtered through Celite to yield a clear pale green solution which was concentrated in vacuum until the precipitation of a white solid was observed which was redissolved by gentle heating. Storage overnight at – 15 °C yielded **7.3** as colourless needles suitable for X-ray crystallography. The product was isolated by filtration and storage of the mother liquor yielded a second crop of crystals. Combined yield 1.84 g (4.62 mmol, 69%). **^{1}H**

NMR (25 °C, d_8-toluene, 500.12 MHz): δ(ppm) = 2.45 (s, 9H, H4), 6.63 (d, $^3J_{HH}$ = 7.76 Hz, 3H, H3), 7.16 (t, $^3J_{HH}$ = 7.76 Hz, 3H, H2), 7.75 (d, $^3J_{HH}$ = 7.76 Hz, 3H, H1); **^{13}C NMR (25 °C, d_8–toluene, 125.78 MHz)**: δ(ppm) = 23.9 (C6), 120.8 (C2), 131.1 (C4), 136.0 (C3), 160.4 (C5), 193.8(C1); **Elemental analysis (%)** calcd. for **7.3**: C 44.1%, H 3.7%, N 8.6%; found C 44.5%, H 3.7%, N 8.6%.

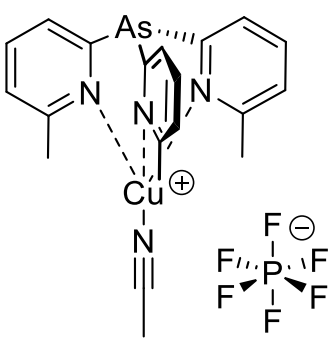

Synthesis of 7.4: Inside a N_2 filled glove box a Schlenk tube was charged with **7.1** (300 mg, 0.85 mmol) and $Cu(MeCN)_4PF_6$ (635 mg, 1.70 mmol, 2 eq). The Schlenk tube was transferred to a Schlenk line and 25 ml of CH_3CN was added. The resulting yellow solution was stirred at room temperature overnight during which a fine white precipitate formed. The suspension was filtered through Celite and the resulting clear yellow solution was concentrated in vacuum until the precipitation of a yellow solid was observed. The solid was redissolved by gentle heating. Storage overnight at -15 °C yielded yellow crystals of **7.4** suitable for X-ray crystallography which were isolated by filtration. Yield 166 mg (0.27 mmol, 32%). **^{1}H NMR (25 °C, CD_3CN, 500.12 MHz)**: δ(ppm) = 1.99 (s, 3H, CH_3CN), 2.83 (s, 9H, H4), 7.40 (d, $^3J_{HH}$ = 7.83 Hz, 3H, H3), 7.77 (t, $^3J_{HH}$ = 7.83 Hz, 3H, H2), 7.88 (d, $^3J_{HH}$ = 7.83 Hz, 3H, H1); **^{31}P NMR (25 °C, CD_3CN, 202.48 MHz)**: δ(ppm) = -144.6 (hpt, $^1J_{PF}$ = 705.69 Hz, PF_6); **^{13}C NMR (25 °C, CD_3CN, 125.78 MHz)**: δ(ppm) = 24.0 (C6), 121.4 (C2), 128.3(C4), 134.5 (C3), 158.5 (C5), 169.9(C1); **Elemental analysis (%)** calcd. for **7.4**: C 40.0%, H 3.5%, N 9.3%; found C 39.9%, H 3.4%, N 9.3%.

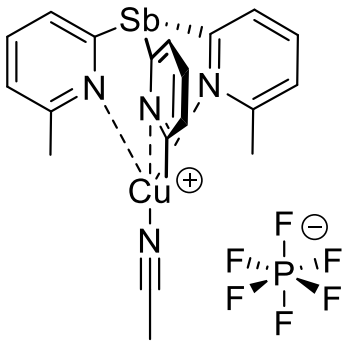

Synthesis of 7.5: Inside a N_2 filled glove box a Schlenk tube was charged with **7.2** (300 mg, 0.75 mmol) and $Cu(MeCN)_4PF_6$ (560 mg, 1.5 mmol, 2 eq). The Schlenk tube was transferred to a Schlenk line and 25 ml of CH_3CN was added. The resulting yellow solution was stirred at room temperature overnight during which a fine yellow precipitate formed. The suspension was filtered through Celite and the resulting clear yellow solution was concentrated under vacuum until the precipitation of a yellow solid was observed. The solid was redissolved by gentle heating. Storage overnight at -15 °C yielded yellow crystals of **7.5** suitable for

X-ray crystallography which were isolated by filtration. Yield 122 mg (0.19 mmol, 25%). **^{1}H NMR (25 °C, CD_3CN, 500.12 MHz)**: δ(ppm) = 1.99 (s, 3H, CH_3CN), 2.83 (s, 9H, H4), 7.35 (d, $^{3}J_{HH}$ = 7.83 Hz, 3H, H3), 7.70 (t, $^{3}J_{HH}$ = 7.83 Hz, 3H, H2), 7.83 (d, $^{3}J_{HH}$ = 7.83 Hz, 3H, H1); **^{31}P NMR (25 °C, CD_3CN, 202.48 MHz)**: δ(ppm) = -144.6 (hpt, $^{1}J_{PF}$ = 705.69 Hz, PF_6); **^{13}C NMR (25 °C, CD_3CN, 125.78 MHz)**: δ(ppm) = 25.2 (C6), 125.6 (C2), 133.5(C4), 136.4 (C3), 160.9 (C5), 164.8 (C1); **Elemental analysis (%)** calcd. for **7.5**: C 37.1%, H 3.3%, N 8.5%; found C 36.9%, H 3.3%, N 8.6%.

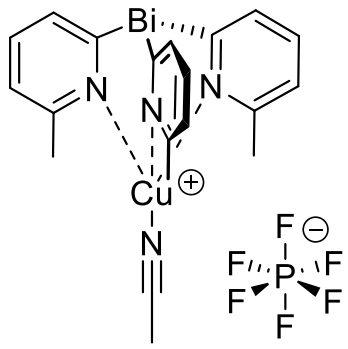

Synthesis of 7.6: Inside a N_2 filled glove box a Schlenk tube was charged with **7.3** (300 mg, 0.65 mmol) and $Cu(MeCN)_4PF_6$ (485 mg, 1.3 mmol, 2 eq). The Schlenk tube was transferred to a Schlenk line and 25 ml of CH_3CN was added. The resulting yellow solution was stirred at room temperature overnight during which a black precipitate formed. The suspension was filtered through Celite and the resulting clear yellow solution was concentrated under vacuum until the precipitation of a yellow solid was observed. The solid was redissolved by gentle heating. Storage overnight at -15 °C yielded yellow crystals of **7.6** suitable for X-ray crystallography which were isolated by filtration. Yield 85 mg (0.12 mmol, 18%). **^{1}H NMR (25 °C, CD_3CN, 500.12 MHz)**: δ(ppm) = 1.99 (s, 3H, CH_3CN), 2.83 (s, 9H, H4), 7.32 (d, $^{3}J_{HH}$ = 7.77 Hz, 3H, H3), 7.70 (t, $^{3}J_{HH}$ = 7.85 Hz, 3H, H2), 7.83 (d, $^{3}J_{HH}$ = 7.83 Hz, 3H, H1). **^{31}P NMR (25 °C, CD_3CN, 202.48 MHz)**: δ(ppm) = -144.5 (hpt, $^{1}J_{PF}$ = 706.96 Hz, PF_6);**^{13}C NMR (25 °C, CD_3CN, 125.78 MHz)**: δ(ppm) = 25.2 (C6), 124.7 (C2), 133.9(C4), 137.0 (C3), 162.1 (C5), 193.1 (C1, from ^{1}H-^{13}C HMBC); **Elemental analysis (%)** calcd. for **7.6**: C 32.7%, H 2.8%, N 7.6%; found C 33.0%, H 3.0%, N 8.0%.

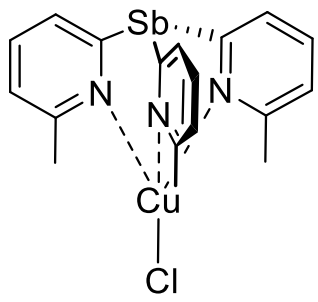

Synthesis of 7.7: Inside a N_2 filled glove box a Schlenk tube was charged with **7.2** (300 mg, 0.75 mmol) and CuCl (74 mg, 0.75 mmol, 1 eq). The Schlenk tube was transferred to a Schlenk line and 15 ml of CH_3CN and 10 ml of THF was added. The resulting yellow solution was stirred at room temperature overnight during which a fine yellow precipitate formed. The suspension was filtered over Celite and the resulting clear yellow solution

was concentrated in vacuum until the precipitation of a yellow solid was observed. The solid was redissolved by gentle heating. Storage overnight at -15 °C yielded yellow crystals of **7.7** suitable for X-ray crystallography which were isolated by filtration and washed with 10 ml diethyl ether. Yield 102 mg (0.21 mmol, 28%). Alternatively, this complex can obtained by addition of dry TBACl to **7.5**. **^{1}H NMR (25 °C, CD_3CN, 500.12 MHz)**: δ(ppm) = 2.68 (s, 9H, H4), 7.25 (d, $^{3}J_{HH}$ = 7.77 Hz, 3H, H3) , 7.49 (d, $^{3}J_{HH}$ = 7.83 Hz, 3H, H1), 7.60 (t, $^{3}J_{HH}$ = 7.85 Hz, 3H, H2); **^{13}C NMR (25 °C, CD_3CN, 125.78 MHz)**: δ(ppm) = 24.2 (C6), 123.9 (C2), 130.7(C4), 136.3 (C3), (due to the low solubility of the complex only CH and CH_3 carbons could be assigned by ^{1}H-^{13}C HSQC); **Elemental analysis (%) calcd. for 7.7**·Et_2O: C 45.2%, H 4.7%, N 7.5%; found C 45.1%, H 4.6%, N 7.4%.

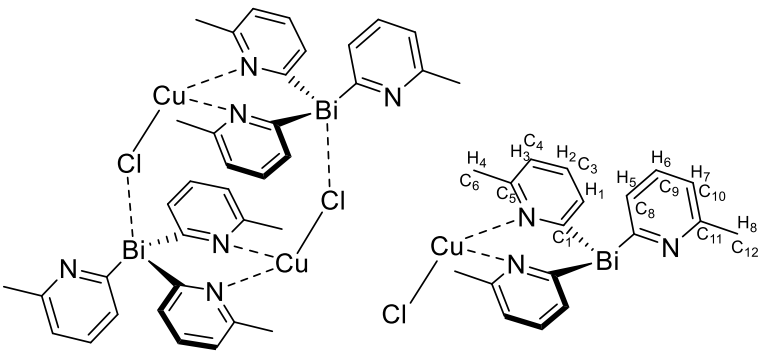

Synthesis of 7.8: Inside a N_2 filled glove box a Schlenk tube was charged with **7.3** (300 mg, 0.65 mmol) and CuCl (61 mg, 0.65 mmol, 1 eq). The Schlenk tube was transferred to a Schlenk line and 15 ml of CH_3CN and 10 ml of THF were added. The resulting yellow solution was stirred at room temperature overnight during which a fine white precipitate formed. The suspension was filtered through Celite and the resulting clear yellow solution was concentrated under vacuum until the precipitation of a yellow solid was observed. The solid was redissolved by gentle heating. Storage overnight at -15 °C yielded yellow crystals of **7.8** suitable for X-ray crystallography which were isolated by filtration. Yield 75 mg (0.10 mmol, 15.0% in terms of the monomer unit). Alternative this complex can also be obtained by addition of tetrabutylammonium chloride to **7.3**. For temperatures above -20 °C monomeric and dimeric molecules of $Bi(6\text{-Me-Py})_3CuCl$ **7.9** are observed in solution, as described in the main text. **7.8: ^{1}H NMR (25 °C, CD_3CN, 500.12 MHz)**: δ(ppm) = 2.69 (s, 6H, H4), 2.79 (s, 3H, H8), 7.25 (d, $^{3}J_{HH}$ = 7.61 Hz, 2H, H3) , 7.33 (d, $^{3}J_{HH}$ = 7.70 Hz, 1H, H7), 7.61 (d, $^{3}J_{HH}$ = 7.61 Hz, 2H, H1), 7.60 (t, $^{3}J_{HH}$ = 7.61 Hz, 3H, H2), 7.92 (t, $^{3}J_{HH}$ = 7.70 Hz, 1H, H6), 8.17 (d, $^{3}J_{HH}$ = 7.70 Hz, 1H, H5); **^{13}C NMR (25 °C, CD_3CN, 125.78 MHz)**: 24.11 (C6), 24.9 (C12), 122.9 (C4), 123.3 (C10), 132.4 (C3), 134.8 (C6), 137.2 (C2), 137.8 (C8), 161.4 (C5), 162.4 (C11), 192.6

(C1), 196.1 (C7 from from ^{1}H-^{13}C HMBC); **7.9: ^{1}H NMR (-40 °C, CD_3CN, 500.12 MHz)**: δ(ppm) = 2.37 (s, 9H, H4), 7.37 (d, $^{3}J_{HH}$ = 7.70 Hz, 3H, H3) , 8.00 (t, $^{3}J_{HH}$ = 7.85 Hz, 3H, H2), 8.76 (d, $^{3}J_{HH}$ = 7.70 Hz, 3H, H1); **^{13}C NMR (-40 °C, CD_3CN, 125.78 MHz)**: δ(ppm) = 25.1 (C6), 124.0 (C2), 134.1(C4), 139.2 (C3), 158.5 (C5), C6 could not be assigned due to the low solubility of the compound in CD_3CN; **Elemental analysis (%)** calcd. for **7.8/7.9**: C 37.0%, H 3.1%, N 7.2%; found C 37.9%, H 3.5%, N 7.0%.

Catalytic studies: Catalytic reactions were carried out in an N_2 filled Saffron type α glovebox. The Cu(I) catalyst **7.3**, **7.5** or **7.6** (1 mol%) and the olefin (para-substituted-styrene and styrene in equimolar ratio, 0.5 mmol each) were dissolved in CD_2Cl_2 (0.8 ml). After 2 min of shaking, PhINTs was introduced in one portion (0.1 mmol), and the mixture was shaked for another 2 min. No solid PhINTs was observed in the reaction mixture after this time. The aziridine products were identified by ^{1}H NMR spectroscopy and the ratio of the two products was obtained by integration of highlighted peaks in Figure 107. Hammett plots were obtained from single parameter linear regression of $\log(k_x/k_h)$, which represents the logarithm of the relative ratio obtained from ^{1}H NMR integration to the polar Hammet σ^{+} values reported in the literature.[175] Dual parameter Hammet plots are obtained by dual parameter linear regression of $\log(k_x/k_h)$ of the polar Hammet (σ^{+}) and radical Hammet parameters ($\sigma\cdot$).

Chapter 8: Comparison of the Coordination Chemistry of As(6-Me-2-py)$_3$, O=As(6-Me-2-py)$_3$ and Sb(6-Me-2-py)$_3$

As we noted in the previous chapter, the incorporation of the 6-Me group into the 2-pyridyl units of the heavier Group 15 ligands E(6-Me-2-py)$_3$ [E = As **7.1**, Sb **7.2**, Bi **7.3**] leads to a significant increase in their stability compared to unsubstituted 2-pyridyl groups. Although the parent As(III)-bridged trispyridyl ligand As(2-py)$_3$ has been prepared previously, the unsubstituted Sb and Bi homologues are unstable and ligands **7.2** and **7.3** are the first stable examples of their type.[176] During the initial stages of the work presented in this chapter we have found, contrary to our initial expectations, that all three ligands **7.1**, **7.2** and **7.3** are indefinitely stable in air under ambient conditions.

Since we had shown in the previous chapter that changes in the Lewis acidity of the group 15 element had a major effect on the donor strength and coordination mode of the parent ligands **7.1** - **7.3**, we were also interested in assessing the potential effects of oxidation of the As(III) atom of **7.1** on charge distribution and coordination preference. Such oxidation will have the effect of further increasing the electronegativity of the group 15 bridgehead atoms.

Results and Discussion

The arsenic oxide ligand O=As(6-Me-2-py)$_3$ **8.1** is obtained in 72% yield by the oxidation of As(6-Me-2-py)$_3$ **7.1** with H_2O_2 in THF, after removal of the solvent under vacuum. This new ligand was characterised using ^{1}H, ^{13}C NMR, IR, UV-Vis and elemental analysis, prior to obtaining its single crystal X-ray structure. Comparison of the IR spectrum with that of **7.1** allowed the assignment of the As=O stretching frequency in **8.1** at 902 cm^{-1} (in comparison Ph$_3$As=O 880 cm^{-1}).[177] Oxidation of the As bridgehead in **7.1** has a large effect on the solubility of the ligand. While **7.1** and **8.1** are indefinitely stable under ambient conditions in air, **8.1** is also soluble and stable in water as a solvent (as shown by ^{1}H NMR spectroscopy). The solid-state structure of **8.1** shows that the incorporation of the O-atom at the bridgehead position, not unexpectedly, pushes the 6-Me substituents away from repulsion with the As=O bond

(Figure 109). The orientation of the 6-Me-2-py groups in **8.1** can be compared to that in the parent ligand **7.1**, in which the 6-Me-groups are all orientated (upwards) towards the As(III) atom. Oxidation also has the effect of reducing the bridgehead As-C bond lengths by approximately 0.04 Å and increasing the bridgehead C-As-C angles compared to the parent ligand **7.1** (from 92.3(2) in **7.1** to 102.4(1)-106.3(1)^{o} in **8.1**). The latter can be seen as a direct consequence of the more sterically congested orientation of the 6-Me groups in **8.1**, but is also in line with VSEPR arguments concerning the effect of the increase in the electronegativity of the As centre on C-As/C-As bonding-pair repulsion.

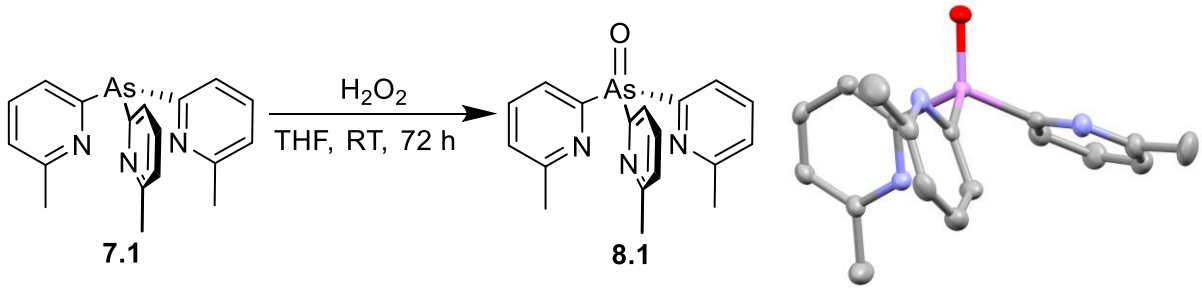

Figure 109: Synthesis and molecular structure of the ligand **8.1**, showing displacement ellipsoids at 40% probability, with H-atoms omitted. Selected bond lengths [Å] and angles [°]: As=O 1.644(2), As–$C_{pyridyl}$ range 1.882(2)–1.886(2), $C_{pyridyl}$–As–$C_{pyridyl}$ range 102.4 (1)–106.3(1), As–$C_{pyridyl}$–N range 113.7 (2)–114.4(2). Colour code: pink = As, blue = N, grey = C, red = O.

Coordination studies of **7.1** and **8.1** were undertaken with a range of transition metal salts. The new complexes [(**8.1**)Cu(CH_3CN)]PF_6 **8.2**, [Ag@Ag_4(**8.1**)$_4$](O_2CCF_3)$_5$ **8.3**, [(**8.1**)Ag(O_2CCF_3)] **8.4**, [(**8.1**)$CoBr_2$] **8.5**, [(**8.1**)$_2$CoBr]($CoBr_3NCCH_3$) **8.6**, [(**8.1**)$NiBr_2$] **8.7** and [(**8.1**)$NiBr_2$] **8.8** have been successfully synthesised and were fully characterised by ^{1}H and ^{13}C NMR (where applicable), IR, UV-Vis and elemental analysis. Their single crystal X-ray structures were also obtained.

The reaction of [Cu(CH_3CN)$_4$]PF_6 with **8.1** in CH_3CN at room temperature yields the complex [(**8.1**)Cu(CH_3CN)]PF_6 **8.2** in 31% isolated yield after crystallisation from the concentrated reaction mixture at -14 °C.The ^{1}H NMR spectrum at room temperature shows a single pyridyl environment, but with very broad resonances that sharpen upon cooling to -30 °C.This is in contrast to the $CuPF_6$ complex of the unoxidised ligand **7.1**, [(**7.1**)Cu(CH_3CN)]PF_6 **7.4**, for which sharp resonances are observed even at room temperature and might suggest that a fluxional process is occurring in **8.2** in which the coordination of a pyridyl-N atom to Cu(I) is exchanging with As=O coordination. This

N,O-coordination mode is observed later in a number of other complexes of **8.1**. In the solid state, **8.2** adopts an ion-separated structure containing [{O=As(6-Me-2-py)$_3$}CuCH$_3$CN]$^+$ cations, in which the Cu(I) atom is chelated by all three of the pyridyl-N atoms (Figure 110). This metal coordination mode is commonplace for trispyridyl ligands and is the same as that found in the previously reported series of CuPF$_6$ complexes of **7.1**, **7.2** and **7.3** (see previous chapter). The only noticeable differences between the cations [(**7.1**)Cu(CH$_3$CN)]$^+$ and [(**8.1**)Cu(CH$_3$CN)]$^+$ stem from the larger bridgehead bite angles in **8.1**, the bridgehead C-As-C angles for **8.1** being ca. 5^o greater than in the [(**8.1**)Cu(CH$_3$CN)]$^+$ cation, resulting in an associated large increase in the N$_{pyridyl}$Cu-N$_{pyridyl}$ angles (by ca. 15-23^o) compared to the [(**8.1**)Cu(CH$_3$CN)]$^+$ cation.

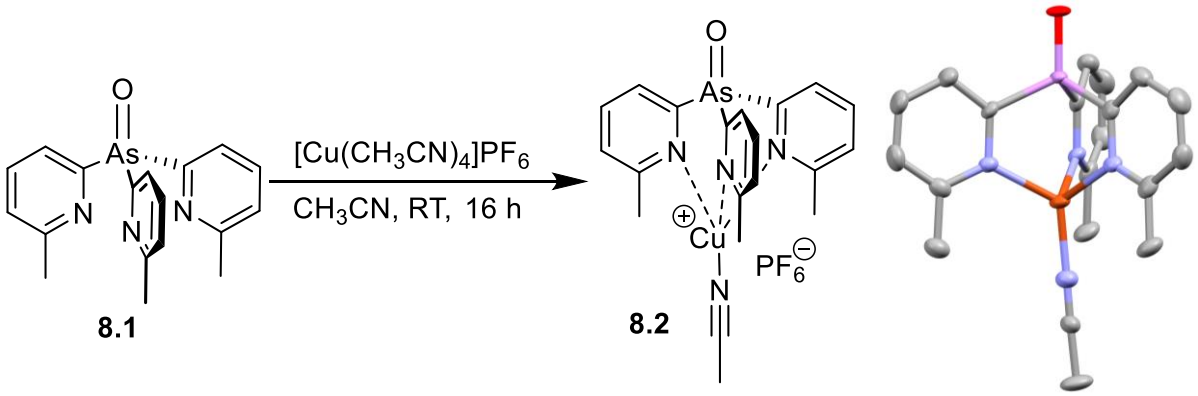

Figure 110: Synthesis and solid-state structure of the cation of **8.2**. H-atoms and the PF$_6^-$ anion omitted for clarity. Thermal ellipsoids at 40% probability. Selected bond lengths [Å] and angles [°]: As=O 1.641(2), As–C$_{pyridyl}$ range 1.932(3)–1.939(4), Cu–N$_{pyridyl}$ range 2.076(4)–2.132(5), Cu–N$_{MeCN}$ 1.949(6), C$_{pyridyl}$–As–C$_{pyridyl}$ range 105.5(2)–105.9(3), As–C$_{pyridyl}$–N range 115.7(5)–116.5(6), N$_{pyridyl}$–Cu–N$_{pyridyl}$ range 116.2(3)–122.8(5). Colour code: orange = Cu, pink = As, blue = N, red = O, grey = C.

The UV-Vis absorption spectrum of the Cu(I) complex **8.2** shows two distinct bands at 265 nm and 333 nm which can be assigned to a ligand π–π* transition and a Cu(I)-to-ligand charge transfer transition (MLCT). These values compare to 270 nm and 359 nm, respectively, in the previously reported As(III) analogue **7.4** and the π–π* transitions in the ligands **7.1** (269 nm) and **8.1** (265 nm). While the π–π* bands are identical to those of the ligands themselves, the MLCT band shows a small red shift going from **7.4** to **8.2**. This can be attributed to an increase in ligand-field strength, similar to conclusions made by Kodera et al. for the family of [RC(6-Me-2-py)$_3$)Cu(CH$_3$CN)]PF$_6$ complexes (R = H, Me, Et).[178]

The reaction of AgO_2CCF_3 with **7.1** in CH_3CN at room temperature yields the cluster $[Ag@Ag_4(\mathbf{7.1})_4](O_2CCF_3)_5$ **8.3** in an isolated crystalline yield of 21%, after layering the concentrated reaction mixture with Et_2O. The identity of **8.3** was confirmed via X-ray single crystal diffraction. Although the crystals only diffracted weakly, the overall connectivity could be clearly established (Figure 111). However, this precludes a detailed discussion of the metric parameters. The cluster **8.3** has a very similar structural arrangement to the previously reported $[Ag@Ag_4(P(2\text{-}py)_3)_4](OTf)_5$, being composed of a Ag-centred Ag_4 tetrahedral core.[164] Similarly to this previously described $P(2\text{-}py)_3$ complex, the four As(III) ligands in **8.1** coordinate four Ag^+ cations over each of the four faces of the Ag_4 tetrahedron using their pyridyl-N atoms. The As centres define another tetrahedron themselves. However, unlike $[Ag@Ag_4(P(2\text{-}py)_3)_4](OTf)_5$ in which the Ag^+ cations are also coordinated by OTf^- anions or solvent molecules, the presence of the sterically blocking 6-Me groups in the trispyridyl ligands of **8.1** prevents further coordination of the Ag centres, so that they remain three coordinate (trigonal planar).

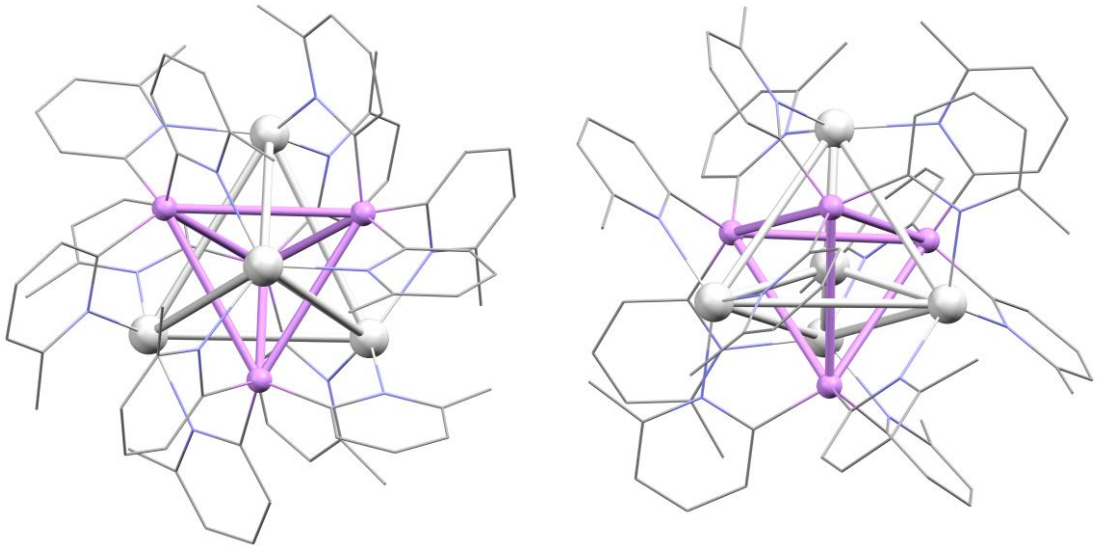

Figure 111: Different views on the solid-state structure of the cluster compound $[Ag@Ag_4(\mathbf{7.1})_4](O_2CCF_3)_5$ **8.3**, CF_3COO^- and H atoms omitted for clarity. Low quality of the data set precludes detailed structural discussion. Colour code: silver = Ag, blue = N, pink = As, grey = C.

Although **8.3** is compositionally pure, as confirmed by elemental analysis, the ^1H and ^{13}C spectra at room temperature in MeCN show multiple, broad pyridyl environments indicating that the cluster disassembles in solution. This is in contrast to the previously reported $P(2\text{-}py)_3$ complex which stays intact in MeCN, suggesting that the steric

repulsion between the 6-Me groups and the weaker As-Ag interactions at the periphery of the cluster results in weaker ligand bonding.

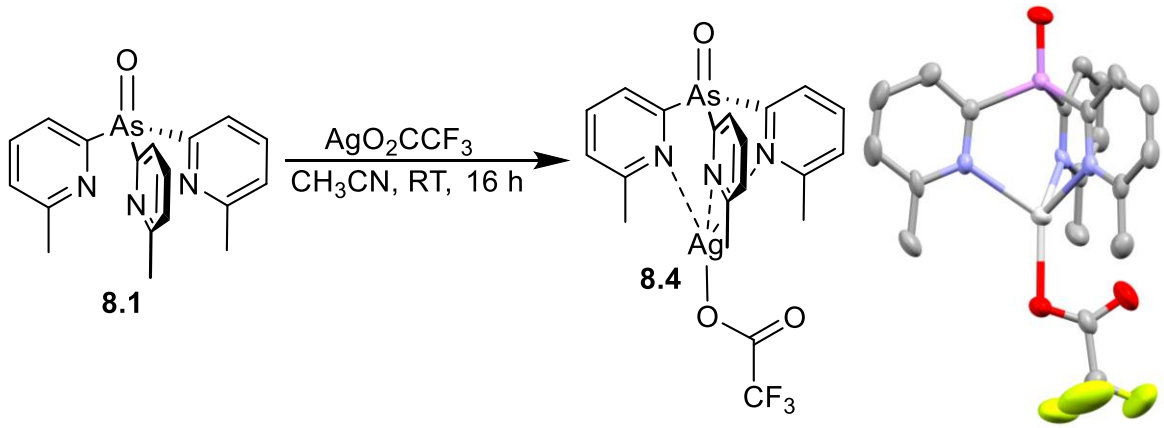

Figure 112: Synthesis and solid-state structure of **8.4**, H-atoms omitted for clarity. Thermal ellipsoids are shown at the 40% probability. Selected bond lengths [Å] and angles [°]: As=O 1.639(3), As– $C_{pyridyl}$ range 1933(7) - 1.938(4), Ag–$N_{pyridyl}$ range 2.315(5) – 2.461(4), Ag–O 2.248(6), $C_{pyridyl}$–As–$C_{pyridyl}$ range 106.9(2) – 108.9(2), As–$C_{pyridyl}$–N range 117.5(4) – 118.8(4), $N_{pyridyl}$–Ag–$N_{pyridyl}$ range 87.6(2) – 94.3(2). Colour code: silver = Ag, pink = As, blue = N, red = O, bright green = F.

The reaction of AgO_2CCF_3 with **8.1** in CH_3CN at room temperature gives the complex [(**8.1**)Ag(O_2CCF_3)] **8.4** in 21% isolated yield after crystallisation from the concentrated reaction mixture at -14 °C.The C_3-symmetric (N,N,N) coordination of Ag^+ is apparent from the ^{1}H NMR spectrum for **8.4** which shows only one sharp 6-Me-2-py environment. The single crystal X-ray structure is that of an ion-paired complex in which the $O_2CCF_3^-$ anion also coordinates the metal centre (Figure 112). The structure of **8.4** resembles the previously reported Ag(I) complex [{O=P(2-py)$_3$P=O}AgPPh$_3$]BF_4. In both cases, the presence of the As/P=O substituent precludes the unusual (Pn,N,N,N) ligand bonding mode present in the clusters [Ag@Ag$_4$(P(2-py)$_3$)$_4$] and **8.3**.

The 1:1 stoichiometric reactions of $CoBr_2$ and $NiBr_2$ with **7.1** and subsequent crystallisation from the concentrated reaction mixtures at -14 °C give the corresponding 1:1 complexes [(**7.1**)$NiBr_2$] **8.5** (27% yield) and [(**7.1**)$CoBr_2$] **8.6** (22% yield), respectively. The solid-state structures of both show bidentate coordination of the metal centres using two of the three pyridyl-N atoms of **7.1** (Figure 113). The complexes are isostructural with the complexes [{PhSi(6-Me-2-py)$_3$}$CoCl_2$] **9.4** and [{PhSi(6-Me-2-py)$_3$}$FeCl_2$] **9.5** containing the PhSi(6-Me-2-py)$_3$ **9.1** ligand described in the next chapter of this thesis. Similarly, to these complexes, the adoption of a bidentate coordination mode is probably a consequence of the steric congestion of the

6-Me substituents, which prevents the coordination of smaller metal ions by all three of the pyridyl-N atoms.

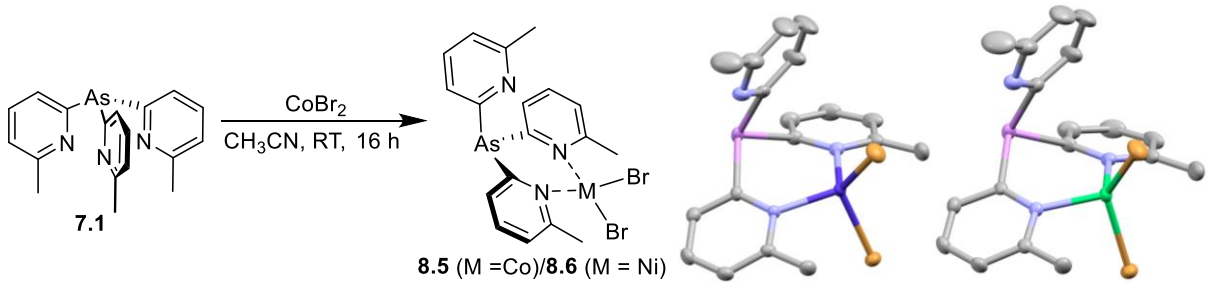

Figure 113: Synthesis and solid-state structure of the complex [(**7.1**)$CoBr_2$] **8.5** and [(**7.1**)$NiBr_2$] **8.6**. Displacement ellipsoids shown at 40% probability, with H atoms omitted for clarity. Selected bond lengths [Å] and angles [°]: **8.5**, As– $C_{pyridyl}$ range 1.959(3)–1.964(3), Co–$N_{pyridyl}$ range 2.051(3)–2.053(4), Co–Br range 2.3682(7)–2.4080(5), $C_{pyridyl}$–As–$C_{pyridyl}$ range 96.0(1)–104.2(1), As–$C_{pyridyl}$–N range 122.5(2)–123.8(2) (coordinating pyridyl groups), As–$C_{pyridyl}$–N 115.1(3) (non-coordinating pyridyl group), N–Co–N 109.1(1), Br–Co–Br 120.47(3). 6, As–$C_{pyridyl}$ range 1.950(4)–1.975(5), Ni–$N_{pyridyl}$ range 2.017(4)–2.023(5), Ni–Br range 2.349(1)–2.4039(8), $C_{pyridyl}$–As–$C_{pyridyl}$ range 96.0(2)–103.0(2), As–$C_{pyridyl}$–N range 122.3(4)–124.2(4) (coordinating pyridyl groups), As–$C_{pyridyl}$–N 115.4(4) (non-coordinating pyridyl group), N–Ni–N 107.0(2), Br–Ni–Br 130.24(4). Colour code: pink = As, blue = N, dark blue = Co, orange = Br, green = Ni.

Oxidation of the bridgehead atom of **7.1** has a marked effect on the coordination preferences of ligand **8.1**. The 1:1 stoichiometric reaction of $CoBr_2$ with **8.1** in CH_3CN and subsequent crystallisation from the concentrated reaction mixture at -14 °C yields blue crystals of [(**8.1**)$_2$CoBr][$CoBr_3CH_3CN$] **8.7** in 74% yield. Surprisingly, the solid-state structure reveals an ion-separated arrangement containing [(**8.1**)$_2$CoBr]$^+$ cations and [$CoBr_3CH_3CN$]$^-$ anions (Figure 114). Within the [(**8.1**)$_2$CoBr]$^+$ cations the Co(II) centre adopts a trigonal bipyramidal geometry in which two 2-pyridyl-N atoms of separate ligands **8.1** bond at the axial positions. The Co(II) cation is further coordinated in the equatorial plane by the bridgehead O-atoms of the ligands and by a Br^- ion. The anion (which is not shown in Figure 114) has a tetrahedral Co(II) centre that is bonded to three Br^- anions and a MeCN molecule. The paramagnetic ^{1}H NMR spectrum of **8.7** at room temperature in MeCN shows two sets of pyridyl resonances, indicating that the solid-state structure is maintained in solution.

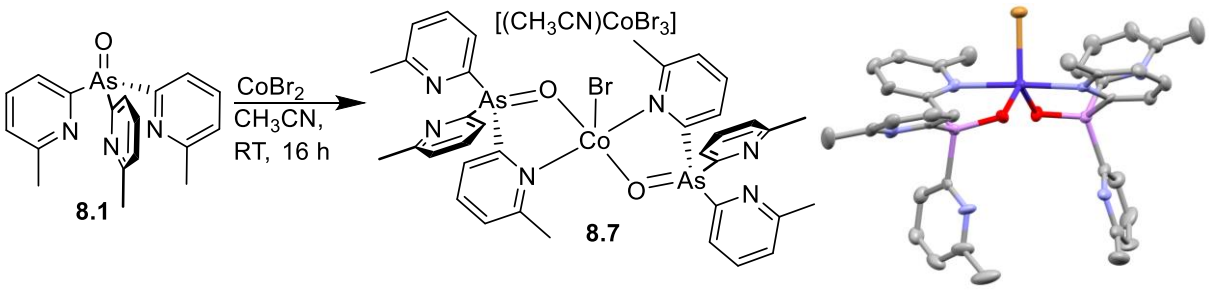

Figure 114: Synthesis and solid-state structure of the complex [(**8.1**)$_2$CoBr](CoBr$_3$CH$_3$CN) **8.7**. Showing displacement ellipsoids at 40% probability, with H-atoms, lattice-bound CH$_3$CN and the counteranion omitted for clarity. Selected bond lengths [Å] and angles [°]: As–C$_{pyridyl}$ range 1.91(1)–1.94(1), Co–N$_{pyridyl}$ range 2.244(8)–2.318(8), Co–Br 2.430(3), Co-O range 1.966(9)–1.971(8), C$_{pyridyl}$–As–C$_{pyridyl}$ range 106.4(5)–112.6(5), As–C$_{pyridyl}$–N range 110.0(8)–113.2(8) (coordinating pyridyl groups), As–C$_{pyridyl}$–N range 109.4(8)–113.0(8) (non-coordinating pyridyl group), N–Co–N 177.3(3), O–Co–O 117.3(3), O-Co-Br range 121.3(3)-121.4(3), Co-Br range 2.372(2)–2.391(3) (CoBr$_3$CH$_3$CN fragment), Co-CH$_3$CN 2.04(1), Br-Co-Br range 109.(1)–115.8(1), CH$_3$CN-Co-Br range 102.8(4) – 108.9(4). Colour code: pink = As, blue = N, red = O, dark blue = Co, brown = Br.

The same N,O-coordination mode as seen in **8.7** is also observed in the Ni(II) complex [(**8.1**)NiBr$_2$] **8.8**, obtained from the reaction of NiBr$_2$ with **8.1** in CH$_3$CN in low yield (2%). In the solid-state structure (Figure 115), the Ni(II) centre is chelated by the bridgehead-O and a pyridyl-N atom of the ligand **8.1** and further bonded to two Br$^-$ anions, giving a distorted tetrahedral geometry at the metal centre. The formation of **8.7** and **8.8** highlight that bridgehead oxidation can drastically change the ligand character of trispyridyl arsine ligands. This switch in coordination character from all-N to N,O (e.g., comparing the Co(II) complexes **8.5** and **8.7**) is no doubt largely a consequence of the relative hardness or softness of the ligand modes with respect to the metal coordinated. However, there may also be a more subtle influence of the steric effect of the 6-Me-substution of the pyridyl groups in **8.1** on the preference for N-chelation versus N,O-chelation. It is noteworthy in this regard that the closely related, unsubstituted P(III) ligand O=P(2-py)$_3$ (which has been studied extensively) has been observed to bond almost exclusively using its pyridyl-N atoms, the only example of N,O-chelation similar to that seen in **8.7** and **8.8** being seen in [MoBr(CO)$_2$(CH$_2$CHCH$_2$){O=P(2-py)$_3$}].[179]

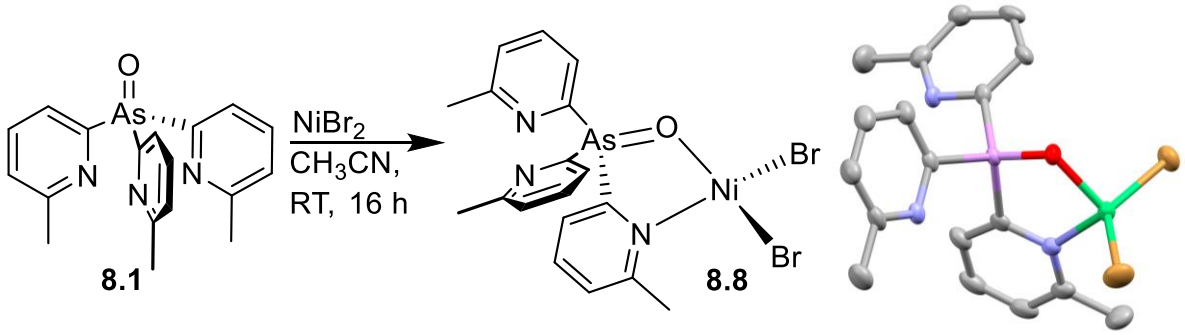

Figure 115: Synthesis and solid-state structure of [(**8.1**)$NiBr_2$] **8.8**. Displacement ellipsoids are shown at 40% probability. H-atoms and lattice bound CH_3CN are omitted. Selected bond lengths [Å] and angles [°]: As–$C_{pyridyl}$ range 1.910(8)–1.941(6), As=O 1.668(5), Ni–$N_{pyridyl}$ 2.022(6), Ni–Br range 2.342(2)–2.368(1), Ni-O 1.964(5), $C_{pyridyl}$–As–$C_{pyridyl}$ range 106.2(3)–112.3(3), As–$C_{pyridyl}$–N 111.(5) (coordinating pyridyl groups), As–$C_{pyridyl}$–N range 111.0(5)–114.3(5) (non-coordinating pyridyl group), O–Ni–N 93.0(2), Br-Ni-Br 134.01(6). Colour code: pink = As, blue = N, green = Ni, brown = Br, red = O.

Having probed the coordination preferences of the arsines **7.1** and **8.1**, we moved on to explore the Sb- and Bi-bridged ligands **7.2** and **7.3**. In both cases, attempted oxidation of the bridgehead atoms with H_2O_2 resulted in complicated mixtures of products. This was not pursued further since in neither case would localised Sb=O or Bi=O bonding arrangements (analogous to **8.1**) be expected, on the basis of the low bond energies of Sb-O and Bi-O π-bonds.[40] Attempts to coordinate harder transition metal ions with **7.2** and **7.3** often lead to the formation of intractable mixtures preventing further analysis. This appears to be due to the greater polarity of the bridgehead C-Sb and C-Bi bonds (which leads to 2-pyridyl transfer to the metal rather than coordination) and to greater sensitivity to hydrolysis even where dried solvents are employed. For example, in the case of reaction of the Sb-ligand **7.2** with $CoBr_2$ only the decomposition product [(6-Me-2-pyH)$_2$$CoBr_2$] could be isolated (as shown by X-ray crystallography). A similar but more interesting outcome is observed when **7.3** is reacted with $FeCl_2$, which leads to the formation of Bi metal and the complex [ClBi(6-Me-2-Py)$_2$$FeCl_2$] **8.9**, which was only characterised by X-ray crystallography owing to the low yield (Figure 116). The molecular arrangement of **8.9** shows that one of the 6-Me-2-py groups of the ligand **7.3** has been lost, presumably by transfer to another Fe(II) centre. **8.9** consists of a bimetallic arrangement in which an Fe(II) and Bi(III) atoms are bridged by the two remaining 6-Me-2-py groups and by a μ-Cl atom.

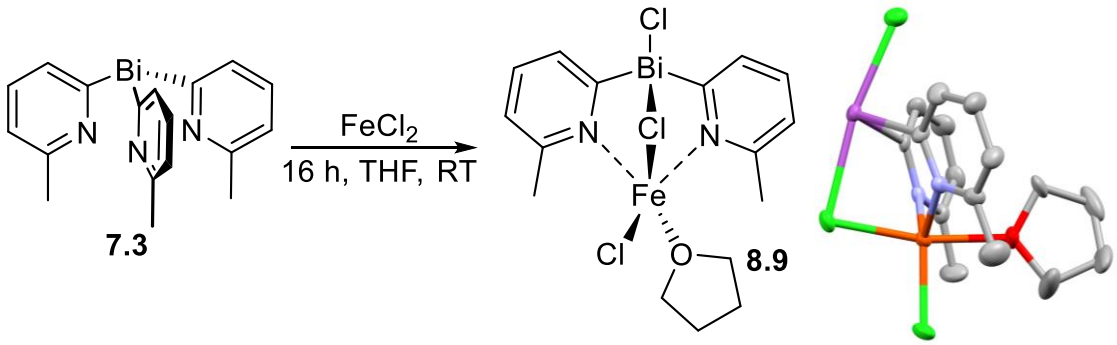

Figure 116: Synthesis and molecular structure of [ClBi(6-Me-2-Py)$_2$FeCl$_2$] **8.9**. H-atoms have been omitted for clarity. Thermal ellipsoids at 50% probability. Bi–C$_{pyridyl}$ range 2.112(2) – 2.141(4), Fe–N$_{pyridyl}$ 2.052(5), Bi–Cl range 2.334(7) – 2.668(3), C$_{pyridyl}$–Bi–C$_{pyridyl}$ 95.6(4), Bi–C$_{pyridyl}$–N 112.1(3). Colour code: purple = Bi, light blue = N, orange = Fe, oxygen = O, green = Cl.

Reactions with softer transition metal centres were more successful, although under these circumstances metal coordination is observed to occur exclusively by the bridgehead atoms (reflecting the softness of the atoms involved). The room temperature, 1:1 stoichiometric reactions of the arsenic ligand **7.1** and the antimony ligand **7.2** with [(Cymene)RuCl$_2$]$_2$ in DCM result in quantitative formation of [(**7.1**)(Cymene)RuCl$_2$] **8.10** and [(**7.2**)(Cymene)RuCl$_2$] **8.11**, respectively, within 5 minutes, as monitored via in situ ^{1}H NMR spectroscopy. Layering of the concentrated reaction mixtures with pentane yielded red crystalline **8.10** and **8.11** in 66% and 64% yield, respectively. The complexes are isostructural in the solid-state, in which the As and Sb bridgehead atoms coordinate the Ru(II) centres (Figure 117). There are only minor structural changes in the ligands upon coordination, with the pnictogen-ruthenium bond lengths increasing from 2.450(7) to 2.597(2)Å in line with the increase in the atomic radii of the heavier Group 15 elements. In both cases, room temperature ^{1}H and ^{13}C NMR spectra in CD$_2$Cl$_2$ confirm that the C$_3$ ligand symmetry is retained in solution, showing only one pyridyl environment. The aromatic cymene proton resonances in **8.10** are found in the region δ = 5.92-5.58 ppm whereas those in **8.11** are in the range between δ = 6.15-6.00 ppm. This indicates that the Sb atom in **8.11** donates more electron density to the Ru atom in **8.10** than the As atom does in **8.10**, resulting in less π-aryl-donation in the former. This somewhat counterintuitive observation presumably reflects the relative softness of the Sb(III) centre of **8.10** in respect to the soft Ru(II) centre.

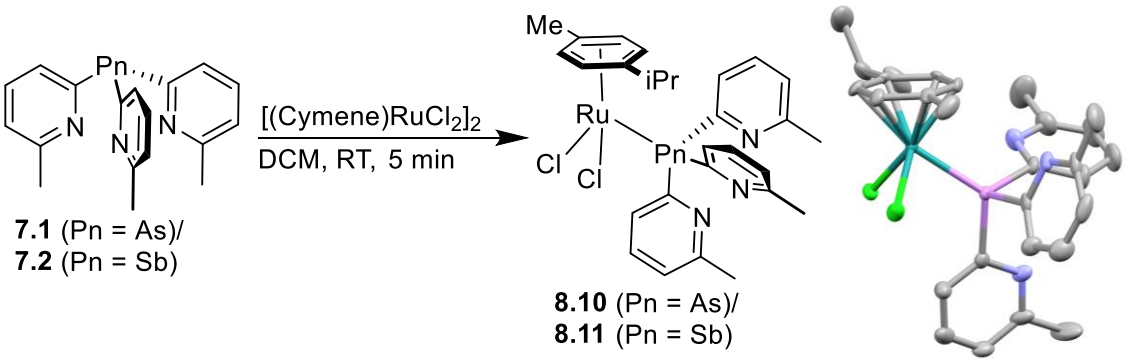

Figure 117: Synthesis and solid-state structure of [(**7.1**)(Cymene)$RuCl_2$] **8.10**; [(**7.2**)(Cymene)$RuCl_2$] **8.11** is isostructural in the solid-state. Showing displacement ellipsoids at 40% probability; with H-atoms omitted. Selected bond lengths [Å] and angles [°]: **8.10**, As–$C_{pyridyl}$ range 1.954(9)–1.97(1), Ru–As 2.450(1), Ru–Cl range 2.417(3)–2.420(3), Ru-C range 2.17(1)–2.23 (1), $C_{pyridyl}$–As–$C_{pyridyl}$ range 100.0(4)–100.8(4), As–$C_{pyridyl}$–N range 112.2(7)–115.4(8), Ru–As–C range 112.4(3) – 121.3(3), As–Ru–Cl range 83.93(6)–88.58(7), Cl-Ru-Cl 89.27(8). **8.11**, Sb–$C_{pyridyl}$ range 2.147(4)–2.157(4), Ru–Sb 2.5972(4), Ru–Cl range 2.406(1)–2.411(1), Ru-C range 2.173(5)–2.210(5), $C_{pyridyl}$–Sb–$C_{pyridyl}$ range 99.5(2)–102.3(2), Sb–$C_{pyridyl}$–N range 113.0(3)–114.6(3), Ru–Sb–C range 113.4(1)–121.4(1), Sb–Ru–Cl range 84.45(3)–85.91(3), Cl-Ru-Cl 87.38(4). Colour code: pink = As, blue = N, dark green = Ru, green = Cl.

Similar observations are made in regard to coordination of $PtCl_2$. Reactions of **7.1** or **7.2** with (benzonitrile)$_2PtCl_2$ in DCM for 5 minutes and subsequent layering of the concentrated reaction mixtures with pentane give the platinum complexes [(**7.1**)$_2PtCl_2$] **8.12** and [(**7.2**)$_2PtCl_2$] **8.13** as yellow crystals in 59% and 30% yields, respectively. The complexes are isostructural in the solid-state, in which the square-planar Pt(II) atoms are bonded to two As- or Sb-atoms of **8.12** or **8.13** (Figure 118). Again, there are only minor changes in the structural parameters of the ligands compared to the isolated ligands themselves. The observed elongation of the pnictogen-Pt bonds is consistent with the increase in the atomic radius of the group 15 atoms involved (2.3415(6)–2.3501(5) in **8.12** to 2.4945(6)–2.4977(7) in **8.13**).

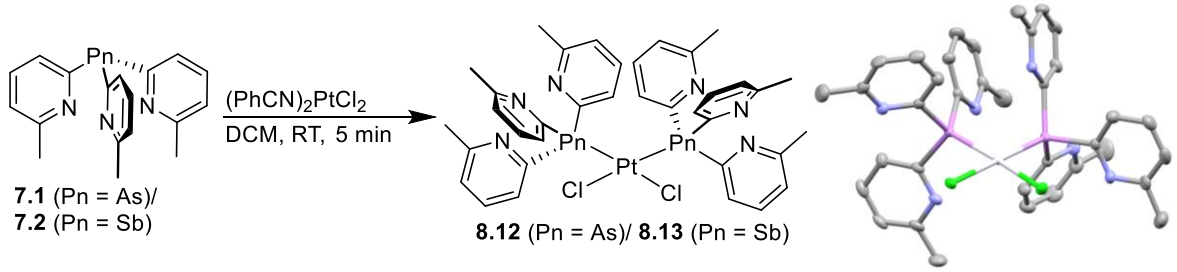

Figure 118: Synthesis and solid-state structure of [(**7.1**)$_2$PtCl$_2$] **8.12**; [(**7.2**)$_2$PtCl$_2$] **8.13** is isostructural in the solid-state. Showing displacement ellipsoids at 50% probability; with H-atoms omitted. Selected bond lengths [Å] and angles [°]: **8.12**, As–C$_{pyridyl}$ range 1.947(5)–1.965(4), Pt–As range 2.3415(6)–2.3501(5), Pt–Cl range 2.332(1)–2.352(1), C$_{pyridyl}$–As–C$_{pyridyl}$ range 100.6(2)–109.4(2), As–C$_{pyridyl}$–N range 111.7(3)–19.5(3), Pt–As–C range 109.7(1)–121.4(1), As–Pt–Cl range 83.75(3)–90.09(3) (on same side), As-Pt-As 96.25(2), Cl-Pt-Cl 89.92(4). **8.13**, Sb–C$_{pyridyl}$ range 2.13(1)– 2.151(9), Pt–Sb range 2.4945(6)–2.4977(7), Pt–Cl range 2.335(2)–2.354(2), C$_{pyridyl}$–Sb–C$_{pyridyl}$ range 98.1(3)–109.1(4), As–C$_{pyridyl}$–N range 111.4(6)–114.9(6), Pt–Sb–C range 112.0(2)–121.1(2), Sb–Pt–Cl range 84.03(5)–88.47(6) (on same side), Sb-Pt-Sb 96.88(2), Cl-Pt-Cl 90.61(8). Colour code: pink = As, light blue = N, white = Pt, green = Cl.

Employing the bismuth ligand **7.3** in the coordination of the same ruthenium(II) and platinum(II) precursors resulted either in the formation of inseparable mixtures, preventing further analysis, or in the precipitation of elemental bismuth.

Conclusions

In contrast to the more well studied phosphine ligands of the type $P(2\text{-py})_3$, the 6-Me-2-pyridyl ligands **7.1**, **7.2** and **7.3** are all indefinitely air and moisture stable, making them not only easy to make but also easy to use. While the bismuth ligand **7.3** is sensitive to reduction or ligand transfer, **7.1** and **7.2** are robust enough to transfer to a range of transition metal centres. Oxidation of the bridgehead atom of the arsenic ligand **7.1** can drastically change its coordination preferences, leading to a greater tendency for N,O-coordination involving with the bridgehead O-atom. This tendency may well also be influenced by the presence of substituents on the 2-pyridyl groups in our case and can be compared to the related unsubstituted $O=P(2\text{-py})_3$ ligand, which is observed to bond almost exclusively using a chelating N-coordination mode.

Experimental Details

General experimental details involving techniques, instruments and materials employed are provided in the appendix at the end of this thesis.

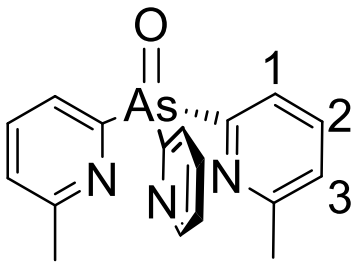

Synthesis of 8.1: Inside a N_2 filled glovebox a Schlenk tube was charged with the **7.1** (900 mg, 2.56 mmol) and transferred to a Schlenk line. 50 ml of THF were added. 324 µL H_2O_2 (30% w/v, 1.1 equiv., 2.81 mmol) were added. The resulting clear solution was stirred for 3 days at room temperature. The solvent was removed in vacuo and the resulting solid mixture was washed with 20 ml of hexane. The product was dried in vacuo to yield **8.1** as a colourless powder (675 mg, 1.83 mmol, 72%). A solution of 20 mg of the product in 0.5 ml of THF was transferred to a crystallisation tube and layered with 10 ml of pentane. After 10 days at room temperature colourless crystals formed which were suitable for X-ray crystallography. **^{1}H NMR (25 °C, CD_3Cl, 400 MHz):** δ [ppm] =7.95 (d, $^3J_{HH}$ = 6.7 Hz, 1H, H-1), 7.66 (t, $^3J_{HH}$ = 6.8 Hz, 3H, H-2), 7.22 (d, $^3J_{HH}$ = 7.1 Hz, 3H, H-3), 2.54 (s, 9H, CH_3); **^{13}C NMR (25 °C, CD_3Cl, 100.48 MHz):** δ [ppm] = 159.99 (C_q, 1C, CH_3-**C**), 156.80 (C_q, 1C, As-C), 136.37 (C_t, 1C, C-2), 125.63 (C_t, 1C, C-1), 125.54 (C_t, 1C, C-3), 24.51 (C_p, 1C, CH_3);**Elemental analysis (%)** calcd. for **8.1:** calcd. C 58.9%, H 4.9%, N 11.4%; found C 58.2%, H 4.9%, N 11.1%; **IR**: v [cm^{-1}] = 3106 (w), 3075 (w), 3035 (w), 3004 (w), 2962 (w), 2923 (w), 2854 (w), 2732 (w), 1770 (w), 1582 (s), 1551 (s), 1443 (s), 1377 (w), 1259 (s), 1176 (w), 1163 (w), 1135 (w), 1082 (s), 1034 (s), 981 (s), 902 (s), 845 (w), 802 (s), 784 (s), 733 (s), 706 (w), 667 (w), 557 (s), 545 (s), 533 (s), 422 (w).

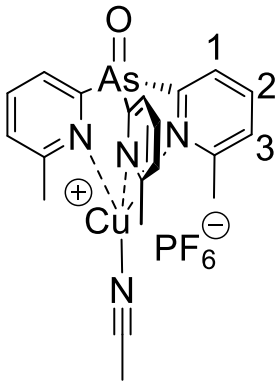

Synthesis of 8.2: Inside a N_2 filled glovebox a Schlenk tube was charged with **8.1** (100 mg, 0.27 mmol) and tetrakis(acetonitrile)copper(I)hexafluorophosphate (101 mg, 0.27 mmol) and transferred to a Schlenk line. 20 ml of acetonitrile were added. The resulting yellow solution was stirred overnight at room temperature. A colourless precipitate formed overnight and was removed by filtration. The clear yellow filtrate was concentrated in vacuo until the precipitation of a yellow solid was observed which was dissolved into solution by gentle heating. Storage at -20 °C

yielded a yellow crystalline solid which was washed twice with hexane to yield **8.2** as yellow crystals suitable for single crystal X-ray diffraction (52 mg, 0.08 mmol, 31%). **^{1}H NMR (-30 °C, CD_3CN, 500 MHz):** δ [ppm] =8.05 (d, $^{3}J_{HH}$ = 7.0 Hz, 3H, H-3), 8.00 (t, $^{3}J_{HH}$ = 7.6 Hz, 3H, H-2), 7.58 (d, $^{3}J_{HH}$ = 7.7 Hz, 3H, H-1), 2.81 (s, 9H, CH_3), 1.99 (s, 3H, Cu-NC-CH_3); **^{1}H NMR (50 °C, CD_3CN, 500 MHz):** δ [ppm] =8.08 (3H), 8.03 (3H), 7.60 (3H), 2.83 (s, 9H, CH_3), 1.99 (s, 3H, Cu-NC-CH_3); **Elemental analysis (%)** calcd. for **8.2:** calcd. C 38.9%, H 3.4%, N 9.1%; found C 38.5%, H 3.3%, N 9.1%; **IR**: v [cm^{-1}] = 3067 (w), 2940 (w), 2308 (w), 2273 (w), 2155 (w), 2030 (w), 2008 (w), 1986 (w), 1936 (w), 1731 (w), 1589 (w), 1550 (w), 1446 (w), 1384 (w), 1368 (w), 1257 (w), 1173 (w), 1165 (w), 1132 (w), 1092 (w), 1038 (w), 1002 (w), 927 (w), 878 (w), 834 (s), 796 (s), 734 (w), 675 (w), 556 (s), 481 (w), 449 (w), 430 (w).

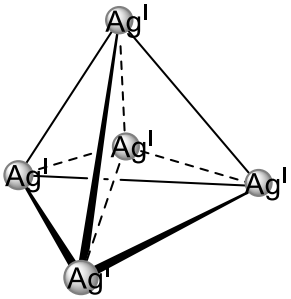

Synthesis of 8.3: Inside a N_2 filled glovebox a Schlenk tube was charged with **7.1** (50 mg, 0.14 mmol) and silvertrifluoroacetate (39 mg, 0.17 mmol) and transferred to a Schlenk line. 20 ml of dry acetonitrile were added. The solution was stirred overnight at room temperature. A colourless precipitate was removed by filtration. The filtrate was concentrated in vacuo and then layered with 15 ml of diethyl ether. After 3 days at room temperature colourless crystals formed which were suitable for X-ray crystallography (34 mg, 0.01 mmol, 38%). **^{1}H NMR (25 °C, CD_3CN, 500 MHz):** δ [ppm] =7.77 (s, 1H, H-Ar), 7.27 (s, 1H, H-Ar), 6.98 (s, 1H, H-Ar), 2.24 (s, 3H, CH_3); ^{13}C NMR shows multiple overlapping signals; **Elemental analysis (%)** calcd. for **8.3:** calcd. C 39.3%, H 2.9%, N 6.7%; found C 40.5%, H 2.9%, N 7.5%; **IR**: v [cm^{-1}] = 3416 (w), 3058 (w), 2918 (w), 1686 (s), 1591 (w), 1550 (w), 1448 (s), 1389 (w), 1197 (s), 1156 (s), 1108 (s), 1038 (w), 1003 (s), 847 (w), 816 (w), 795 (s), 784 (s), 728 (w), 714 (s), 674 (w), 596 (w), 556 (w), 541 (w), 516 (w), 412 (w).

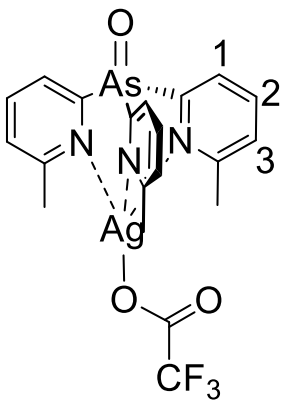

Synthesis of 8.4: Inside a N_2 filled glovebox a Schlenk tube was charged with **8.1** (50 mg, 0.13 mmol) and silvertrifluoroacetate (30 mg, 0.13 mmol) and transferred to a Schlenk line. 10 ml of acetonitrile were added. The resulting clear solution was stirred overnight at room temperature. The clear solution was concentrated in vacuo until the precipitation of a white solid was observed which was dissolved into solution by gentle heating. Storage at -20 °C yielded colourless crystals suitable for X-ray crystallography (16 mg, 0.03 mmol, 20%). **^{1}H NMR (25 °C, CD_3CN, 500 MHz):** δ [ppm] = 8.06 (d, $^3J_{HH}$ = 7.5 Hz, 3H, H-3), 7.94 (t, $^3J_{HH}$ = 7.8 Hz, 3H, H-2), 7.55 (d, $^3J_{HH}$ = 7.9 Hz, 3H, H-1), 2.74 (s, 9H, CH_3); **^{13}C NMR (25 °C, CD_3CN, 125 MHz):** δ [ppm] = 160.93 (C_q, 1C, C-CH_3), 157.14 (C_q, 1C, C-As), 138.85 (C-H, 1C, C-2), 127.13 (C-H, 1C, C-1), 125.24 (1C, C-H, C-3), 24.82 (CH_3, 1C, CH_3). (The two C_q were determined from the HMBC); **Elemental analysis (%) calcd. for 8.4:** calcd. C 40.8%, H 3.1%, N 7.1%; found C 39.5%, H 2.8%, N 5.7%; **IR**: v [cm^{-1}] = 3063 (w), 3009 (w), 2980 (w), 2962 (w), 2929 (w), 2301 (w), 1704 (w), 1668 (s), 1589 (s), 1551 (w), 1445 (s), 1418 (w), 1383 (w), 1254 (w), 1198 (s), 1177 (s), 1132 (s), 1089 (w), 1038 (w), 996 (w), 916 (s), 834 (w), 795 (s), 732 (w), 721 (s), 672 (w), 597 (w), 555 (w), 520 (w), 454 (w), 406 (w).

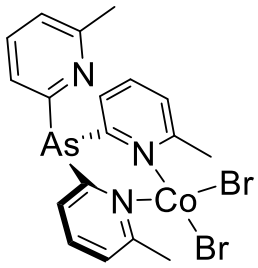

Synthesis of 8.5: Inside a N_2 filled glovebox a Schlenk tube was charged with **7.1** (200 mg, 0.57 mmol) and cobalt(II)bromide (124 mg, 0.57 mmol) and transferred to a Schlenk line. 20 ml of acetonitrile were added. The resulting dark blue solution was stirred overnight at room temperature. Dark blue crystals formed overnight. Storage at -20 °C yielded **8.5** as blue crystals suitable for single crystal X-ray diffraction (88 mg, 0.15 mmol, 27%). **^{1}H NMR (25 °C, CD_3CN, 500 MHz):** δ [ppm] = 49.63, 37.10, 12.69, 7.17; **Elemental analysis (%)** calcd. for **8.5:** calcd. C 37.9%, H 3.2%, N 7.4%; found C 37.8%, H 3.1%, N 7.2%; **IR**: v [cm^{-1}] = 3066 (w), 3049 (w), 2989 (w), 2923 (w), 1588 (s), 1578 (s), 1551 (s), 1435 (s), 1373 (s), 1307 (s), 1231 (s), 1186 (s), 1169 (s), 1123 (s), 1095 (s), 1014 (s), 990 (s), 984 (s), 841 (w), 809 (s), 790 (s), 771 (s), 737 (s), 730 (s), 682 (w), 660 (w), 561 (w), 545 (s), 426 (s), 414 (s).

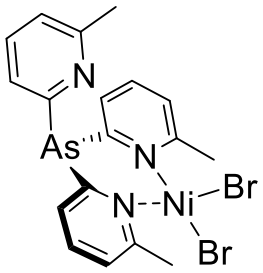

Synthesis of 8.6: Inside a N_2 filled glovebox a Schlenk tube was charged with **7.1** (200 mg, 0.57 mmol) and nickel(II)bromide (124 mg, 0.57 mmol) and transferred to a Schlenk line. 20 ml of acetonitrile were added. The resulting clear green solution was stirred overnight at room temperature. A colourless precipitate formed overnight and was removed by filtration. The clear green filtrate was stored for 5 days at -20 °C and yielded **8.6** as purple crystals suitable for single crystal X-ray diffraction (70 mg, 0.123 mmol, 22%). **Elemental analysis (%)** calcd. for **8.6:** calcd. C 37.9%, H 3.2%, N 7.4%; found C 37.7%, H 3.1%, N 7.5%; **IR**: v [cm^{-1}] = 3604 (w), 3344 (w), 3065 (w), 3050 (w), 3002 (w), 2922 (w), 2678 (w), 2097 (w), 2004 (w), 1912 (w), 1777 (w), 1706 (w), 1625 (w), 1590 (s), 1578 (s), 1552 (s), 1436 (s), 1371 (s), 1253 (w), 1245 (w), 1227 (w), 1187 (w), 1170 (w), 1133 (w), 1124 (w), 1100 (w), 1091 (w), 1018 (s), 994 (w), 975 (w), 914 (w), 842 (w), 809 (s), 790 (s), 772 (s), 731 (w), 684 (w), 661 (w), 562 (w), 545 (w), 448 (w), 428 (w), 415 (s).

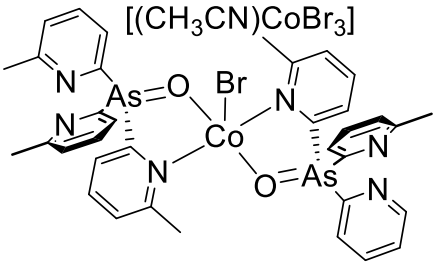

Synthesis of 8.7: Inside a N_2 filled glovebox a Schlenk tube was charged with **8.1** (150 mg, 0.41 mmol) and cobalt(II)bromide (89 mg, 0.41 mmol) and transferred to a Schlenk line. 20 ml of acetonitrile were added. The resulting blue solution was stirred overnight at room temperature. The clear blue solution was concentrated in vacuo until the precipitation of a blue solid was observed which was dissolved into solution by gentle heating. Storage at -20 °C yielded blue crystals suitable for X-ray crystallography (188 mg, 0.15 mmol, 74%).**^{1}H NMR (25 °C, CD_3CN, 500 MHz):** δ [ppm] = 34.02, 28.14, 13.43, 11.10, 7.42, 6.57, 3.67, -1.54, -3.98; **Elemental analysis (%)** calcd. for **8.7·CH_3CN:** calcd. C 37.6%, H 3.2%, N 8.0%; found C 37.5%, H 3.0%, N 7.9%;**IR**: v [cm^{-1}] = 3371 (w), 3050 (w), 2988 (w), 2957 (w), 2922 (w), 2306 (w), 2279 (w), 2248 (w), 2026 (w), 2003 (w), 1914 (w), 1584 (w), 1549 (w), 1443 (s), 1389 (w), 1375 (w), 1308 (w), 1248 (w), 1232 (w), 1170 (w), 1129 (w), 1089 (w), 1036 (w), 983 (w), 914 (w), 858 (w), 829 (s), 790 (s), 774 (w), 728 (w), 674 (w), 543 (w), 448 (s), 424 (w).

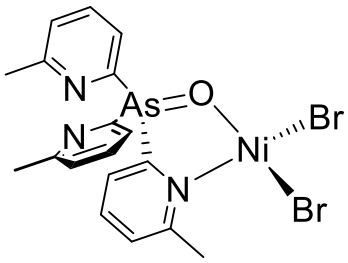

Synthesis of 8.8: Inside a N_2 filled glovebox a Schlenk tube was charged with **8.1** (150 mg, 0.41 mmol) and nickel(II)bromide (89 mg, 0.41 mmol) and transferred to a Schlenk line. 20 ml of acetonitrile were added. The resulting pale orange solution was stirred overnight at room temperature. A red solution with a small amount of brown precipitate formed overnight and was removed by filtration. The clear red filtrate was concentrated in vacuo until the precipitation of a yellow solid was observed which was dissolved into solution by gentle heating. Storage at -20 °C yielded a yellow crystalline solid which was washed twice with hexane to yield **8.8** as yellow crystals (7 mg, 0.01 mmol, 2%). 0.5 ml of the solution were transferred to a crystallisation tube and layered with 10 ml of Et_2O. After 3 days at room temperature yellow crystals formed which were suitable for X-ray crystallography. **Elemental analysis (%)** calcd. for **8.8 · DCM:** calcd. C 34.0%, H 3.0%, N 6.3%; found C 34.8%, H 2.9%, N 6.6%. **IR**: v [cm^{-1}] = 3351 (w), 3281 (w), 3050 (w), 3006 (w), 2951 (w), 2921 (w), 2025 (w), 1910 (w), 1748 (w), 1705 (w), 1586 (s), 1547 (s), 1443 (s), 1402 (w), 1378 (w), 1335 (w), 1249 (w), 1182 (w), 1170 (w), 1133 (w), 1104 (w), 1085 (w), 1039 (w), 1005 (w), 993 (w), 860 (s), 830 (s), 789 (s), 761 (s), 729 (s), 674 (w), 554 (s), 526 (w), 455 (s), 423 (w).

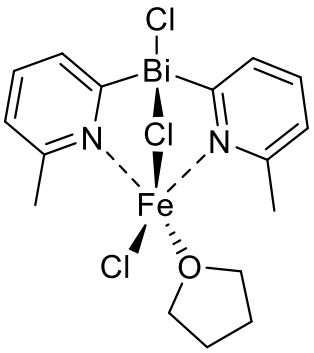

Synthesis of 8.9: Inside a N_2 filled glovebox a Schlenk tube was charged with **7.3** (200 mg, 0.41 mmol) and iron(II)chloride (52 mg, 0. 0.41 mmol) and transferred to a Schlenk line. 20 ml of tetrahydrofuran were added. The resulting pale orange solution was stirred overnight at room temperature. An orange solution with a small amount of brown precipitate formed overnight and was removed by filtration. The clear orange filtrate was concentrated in vacuo to approximately 5 ml volume. Storage at -20 °C yielded a few yellow crystals suitable for X-ray crystallography.

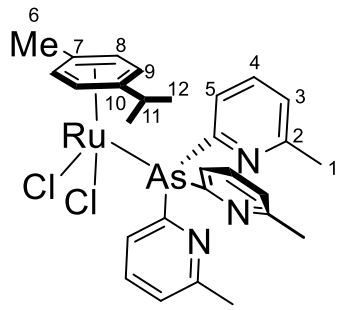

Synthesis of 8.10: Inside a N_2 filled glovebox a Schlenk tube was charged with **7.1** (34 mg, 0.10 mmol) and dichloro(cymene)ruthenium(II)dimer (30 mg, 0.05 mmol) and transferred to a Schlenk line. 1 ml of DCM was added. The resulting red solution was stirred for 10 min at room temperature. The solution was layered with approximately 10 ml of pentane. After 3 days at room temperature red crystals formed which were suitable for X-ray crystallography (42 mg, 0.06 mmol, 66%); **^{1}H NMR (25 °C, CD_2Cl_2, 500 MHz):** δ [ppm] = 7.66 (d, $^3J_{HH}$ = 7.7 Hz, 3H, H-5), 7.54 (t, $^3J_{HH}$ = 7.7 Hz, 3H, H-4), 7.18 (d, $^3J_{HH}$ = 7.7 Hz, 3H, H-3), 5.85 (d, $^3J_{HH}$ = 5.9 Hz, 2H, H-8), 5.68 (d, $^3J_{HH}$ = 5.9 Hz, 2H, H-9), 2.71 (sept, $^3J_{HH}$ = 6.9 Hz, 1H, H-11), 2.54 (s, 9H, H-1), 1.94 (s, 3H, H-6), 1.06 (d, $^3J_{HH}$ = 6.9 Hz, 6H, H-12). **^{13}C NMR (25 °C, CD_2Cl_2, 125 MHz):** δ [ppm] = 158.54 (C_q, 1C, C-As), 158.37 (C_q, 1C, C-2), 135.19 (C-H, 1C, C-4), 128.45 (C-H, 1C, C-5), 123.38 (1C, C-H, C-3), 106.60 (C_q, 1C, C-10), 94.53 (C_q, 1C, C-7), 86.87 (1C, C-H, C-8), 82.04 (1C, C-H, C-9), 30.13 (C-H, 1C, C-11), 24.04 (CH_3, 1C, C-1), 21.44 (CH_3, 2C, C-12), 17.15 (CH_3, 1C, C-6); **Elemental analysis (%)** calcd. for **8.10:** calcd. C 51.2%, H 4.9%, N 6.4%; found C 51.1%, H 4.8%, N 6.3%; **IR**: v [cm^{-1}] = 3037 (w), 2962 (w), 2921 (w), 2866 (w), 1579 (s), 1555 (s), 1496 (w), 1469 (w), 1438 (s), 1389 (w), 1375 (w), 1361 (w), 1327 (w), 1265 (w), 1248 (w), 1169 (w), 1120 (w), 1085 (w), 1060 (w), 1034 (w), 987 (w), 924 (w), 890 (w), 874 (w), 799 (s), 784 (w), 775 (s), 731 (s), 702 (w), 668 (w), 633 (w), 569 (w), 555 (w), 548 (w), 517 (w), 451 (w), 426 (w).

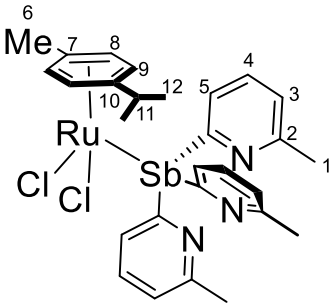

Synthesis of 8.11: Inside a N_2 filled glovebox a Schlenk tube was charged with **7.2** (39 mg, 0.10 mmol) and dichloro(cymene)ruthenium(II)dimer (30 mg, 0.05 mmol) and transferred to a Schlenk line. 1 ml of DCM was added. The resulting red solution was stirred for 10 minutes at room temperature. The solution was layered with approximately 10 ml of pentane. After 3 days at room temperature red crystals formed which were suitable for X-ray crystallography (44 mg, 0.0625 mmol, 64%);**^{1}H NMR (25 °C, CD_2Cl_2, 500 MHz):** δ [ppm] = 7.77 (d, $^3J_{HH}$ = 7.6 Hz, 3H, H-5), 7.49 (t, $^3J_{HH}$ = 7.7 Hz, 3H, H-4), 7.14 (d, $^3J_{HH}$ = 7.7 Hz, 3H, H-3), 6.08 (d, $^3J_{HH}$ = 6.0 Hz, 2H, H-8), 6.00 (d, $^3J_{HH}$ = 6.0 Hz, 2H, H-9), 2.81 (sept, $^3J_{HH}$ = 7.0 Hz, 1H, H-11), 2.56 (s, 9H, H-1), 2.06 (s, 3H, H-6), 1.16 (d, $^3J_{HH}$ = 7.0 Hz, 6H, H-12); **^{13}C NMR (25 °C, CD_2Cl_2, 125 MHz):** δ [ppm] =

160.34 (C_q, 1C, C-As), 159.13 (C_q, 1C, C-2), 135.14 (C-H, 1C, C-4), 130.38 (C-H, 1C, C-5), 123.49 (1C, C-H, C-3), 105.22 (C_q, 1C, C-10), 95.30 (C_q, 1C, C-7), 84.67 (1C, C-H, C-8), 81.54 (1C, C-H, C-9), 34.01(), 30.40 (C-H, 1C, C-11), 24.12 (CH_3, 1C, C-1), 21.60 (CH_3, 2C, C-12), 17.77 (CH_3, 1C, C-6); **Elemental analysis (%)** calcd. for **8.11:** calcd. C 47.8%, H 4.6%, N 6.0%; found C 48.5%, H 5.1%, N 5.7%; **IR**: v [cm^{-1}] = 3066 (w), 3046 (w), 2956 (w), 2919 (w), 2868 (w), 2127 (w), 2121 (w), 2097 (w), 2088 (w), 1615 (w), 1576 (s), 1550 (s), 1504 (w), 1464 (w), 1435 (s), 1385 (w), 1370 (w), 1322 (w), 1246 (w), 1219 (w), 1200 (w), 1169 (s), 1118 (w), 1081 (s), 1056 (w), 1033 (w), 988 (s), 890 (w), 871 (w), 840 (w), 786 (s), 742 (w), 730 (w), 692 (w), 669 (w), 658 (w), 548 (w), 539 (s), 525 (w), 517 (w), 448 (w), 423 (w), 410 (w).

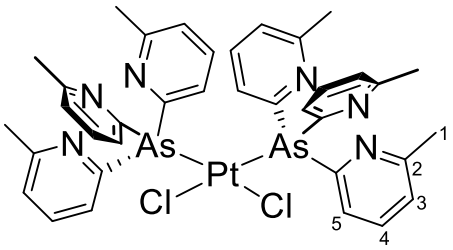

Synthesis of 8.12: Inside a N_2 filled glovebox a Schlenk tube was charged with **7.1** (45 mg, 0.12 mmol) and cis-bis(benzonitrile)dichloroplatinum(II) (30 mg, 0.06 mmol) and transferred to a Schlenk line. 1 ml of DCM was added. The resulting yellow solution was stirred for 10 minutes at room temperature. The solution was layered with approximately 10 ml of pentane. After 3 days at room temperature yellow crystals formed which were suitable for X-ray crystallography (36 mg, 0.03 mmol, 59%). **^{1}H NMR (25 °C, CD_2Cl_2, 500 MHz):** δ [ppm] = 8.04 (d, $^3J_{HH}$ = 7.7 Hz, 3H, H-5), 7.50 (t, $^3J_{HH}$ = 7.7 Hz, 3H, H-4), 7.05 (d, $^3J_{HH}$ = 7.5 Hz, 3H, H-3), 2.27 (s, 9H, CH_3); **^{13}C NMR (25 °C, CD_2Cl_2, 125 MHz):** δ [ppm] = 158.20 (C_q, 1C, C-2) 156.29 (C_q, 1C, As-C**),** 135.42 (t, 1C, C-4), 127.77 (t, 1C, C-5), 123.64 (t, 1C, C-3), 23.59 (p, 1C, CH_3); **Elemental analysis (%)** calcd. for **8.12:** calcd. C 44.6%, H 3.8%, N 8.7%; found C 43.8%, H 3.7%, N 8.3%; **IR**: v [cm^{-1}] = 3046 (w), 2960 (w), 2922 (w), 2103 (w), 1911 (w), 1813 (w), 1793 (w), 1679 (w), 1580 (s), 1553 (s), 1438 (s), 1374 (w), 1247 (w), 1168 (w), 1128 (w), 1089 (w), 1031 (w), 989 (w), 921 (w), 903 (w), 781 (s), 729 (s), 698 (w), 666 (w), 559 (w), 548 (s), 535 (w), 421 (w), 402 (s).

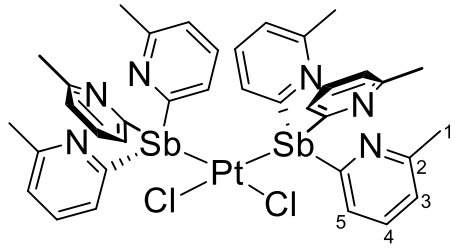

Synthesis of 8.13: Inside a N_2 filled glovebox a Schlenk tube was charged with **7.2** (51 mg, 0.12 mmol) and cis-bis(benzonitrile)dichloroplatinum(II) (30 mg,

0.06 mmol) and transferred to a Schlenk line. 1 ml of DCM was added. The resulting yellow solution was stirred for 10 minutes at room temperature. The solution was layered with approximately 10 ml of pentane. After 3 days at room temperature yellow crystals formed which were suitable for X-ray crystallography (21 mg, 0.02 mmol, 29%). **^{1}H NMR (25 °C, CD_2Cl_2, 500 MHz):** δ [ppm] = 7.99 (d, $^{3}J_{HH}$ = 7.5 Hz, 3H, H-5), 7.51 (t, $^{3}J_{HH}$ = 7.7 Hz, 3H, H-4), 7.03 (d, $^{3}J_{HH}$ = 7.5 Hz, 3H, H-3), 2.24 (s, 9H, CH_3); **^{13}C NMR (25 °C, CD_2Cl_2, 125 MHz):** δ [ppm] = 159.10 (C_q, 1C, C-2) 158.00 (C_q, 1C, Sb-C), 135.33 (t, 1C, C-4), 129.63 (t, 1C, C-5), 123.84 (t, 1C, C-3), 23.55 (p, 1C, CH_3); **Elemental analysis (%)** calcd. for **8.13:** calcd. C 38.7%, H 3.3%, N 7.3%; found C 39.4%, H 3.4%, N 7.4%; **IR**: v [cm^{-1}] = 3048 (w), 2961 (w), 2924 (w), 2007 (w), 1977 (w), 1681 (w), 1622 (w), 1576 (s), 1549 (s), 1435 (s), 1389 (w), 1372 (w), 1272 (w), 1247 (w), 1168 (s), 1122 (w), 1083 (w), 1035 (w), 990 (w), 980 (w), 901 (w), 840 (w), 780 (s), 728 (s), 696 (w), 659 (w), 546 (w), 529 (w), 416 (w).

Chapter 9: The Coordination Chemistry of the Neutral Trispyridyl Silicon Ligand PhSi(6-Me-2-py)$_3$

There are no in-depth reports on the coordination of Si(IV) ligands of the type RSi(2-py)$_3$ and its derivatives, which we anticipate to be more robust than other heavier group 14 analogues. The main obstacle to developing this area is the low yielding synthesis of ligands containing unsubstituted pyridyl groups from 2-Li-pyridine and RSiCl$_3$. As a result, the only coordination compound obtained so far in this area has been MeSi(2-py)$_3$LiCl, which was isolated in low yield .[144] However, a clue to a way around this problem is provided by an early study which reported that the 6-bromo-substituted Si(IV) ligand MeSi(6-Br-2-py)$_3$ can be obtained in 54% yield from the reaction of MeSiCl$_3$ and monolithiated 2,6-dibromo-pyridine.[180] We showed in Chapter 7 of this thesis that 6-methyl substitution at the pyridyl substituents not only leads to cleaner lithiation of the corresponding 6-methyl-2-bromo-pyridine, but also stabilises the trispyridyl products themselves by suppressing the reductive elimination of bipyridine. This also makes the resulting ligands more air and moisture stable, making them more suitable to applications such as in catalysis.

Results and Discussion

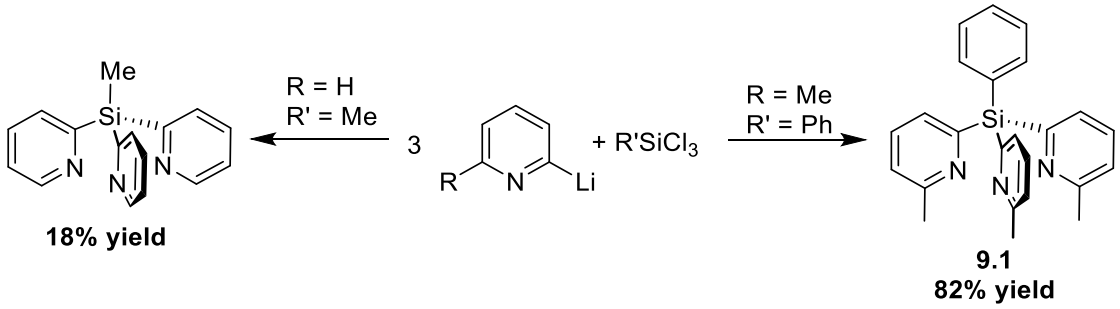

Figure 119: Synthetic approaches for trispyridyl silicon(IV) ligands.

We were able to obtain the new Si(IV) ligand PhSi(6-Me-2-py)$_3$ **9.1** in high yield (82%) and purity from the reaction of PhSiCl$_3$ with 6-Me-2-Li-py in THF (Figure 119), providing gram quantities for the further investigation of its coordination chemistry. In contrast, the reaction between unmethylated 2-Li-pyridine and PhSiCl$_3$ yields a mixture of products, as apparent from the ^{1}H NMR spectrum of the crude reaction mixture.

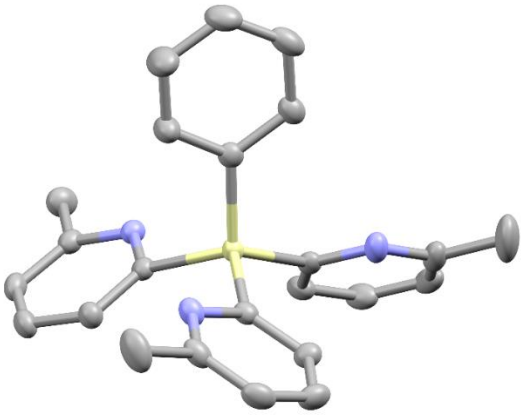

Figure 120: Solid-state structure of **9.1** showing displacement ellipsoids at 40% probability. Hydrogen atoms omitted for clarity. Selected bond lengths [Å] and angles [°]: Si–C_{phenyl} 1.879(2), Si–$C_{pyridyl}$ range 1.882(2)-1.886(2), $C_{pyridyl}$-Si-$C_{pyridyl}$ range 107.25(8)-110.18(8), Si-$C_{pyridyl}$-N range 114.15(13)-114.61(14). Colour code: grey = C, blue = N, yellow = Si.

Elemental analysis confirms that unlike the previously reported Si(IV) system only trace lithium halide coordination occurs for **9.1** in crystalline samples. This is further confirmed by the single crystal X-ray structure, which shows a C_3-symmetric molecular arrangement in the solid state in which the pyridyl-N atoms are orientated towards the Si(IV) bridgehead atom (Figure 120). The absence of LiX (X= Cl, Br) coordination in **9.1** presents a technical advantage (in addition to the high yield of the ligand) because there is no need to separate LiX from reaction products after transfer of the ligand to other metal centres. It can be noted also that although **9.1** is prepared under inert-atmosphere conditions, it is in fact air-stable and only hygroscopic.

The reaction of $[Cu(CH_3CN)_4]PF_6$ with **9.1** in CH_3CN at room temperature gives the crystalline complex $[\{PhSi(6\text{-}Me\text{-}2\text{-}py)_3\}CuCH_3CN]PF_6$ **9.2** in 31% isolated yield. The single crystal X-ray structure of **9.2** shows that it is an ion-separated complex containing $[\{PhSi(6\text{-}Me\text{-}2\text{-}py)_3\}CuCH_3CN]^+$ cations (Figure 121) and PF_6^- anions.

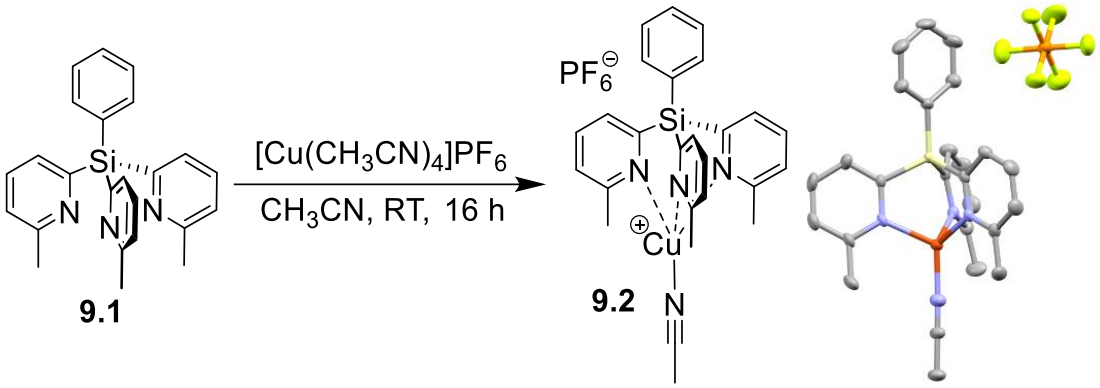

Figure 121: Reaction scheme and solid-state structure of **9.2.** Displacement ellipsoids at 40% probability. Hydrogen atoms omitted for clarity. Selected bond lengths [Å] and angles [°]: Si–C_{phenyl} 1.871(5), Si–$C_{pyridyl}$ range 1.888(5)-1.892(5), Cu-$N_{pyridyl}$ range 2.061(4)-2.121(4), Cu-N_{MeCN} 1.936(4), $C_{pyridyl}$-Si-$C_{pyridyl}$ range 104.0(2)-110.0(2), Si-$C_{pyridyl}$-N range 114.0(3)-117.4(3), $N_{pyridyl}$-Cu-$N_{pyridyl}$ 97.65(16)-100.65(16). Colour code: grey = C, blue = N, yellow = Si, orange = P, bright yellow = F, dark orange = Cu.

The previously reported ion-separated complexes [{RC(6-Me-2-py)$_3$}CuCH$_3$CN]PF$_6$ (R = H, Me), containing C-bridged pyridyl ligands, are closely related to **9.2** (containing C-bridged analogues of ligand **9.1**, with the same 6-Me-2-py substituents).[178] There are noticeable effects in changing the bridgehead atom from the smaller C- to the larger Si-atom. In particular, the Cu-$N_{pyridyl}$ bonds in the cation of **9.2** [2.061(4)-2.121(4) Å] are on average longer than those in the [{RC(6-Me-2-py)$_3$}CuCH$_3$CN]$^+$ cations [1.993(8)-2.088(7) Å]. There is also a large expansion of the internal $N_{pyridyl}$-Cu-$N_{pyridyl}$ coordination angles from 90.23(9)-91.8(3)° in the [{RC(6-Me-2-py)$_3$}CuCH$_3$CN]$^+$ cations to 97.65 (16)-100.65(16)° in the cation of **9.2**. Both of these changes can be traced to the increase in the bridgehead Si-C bond length in the Si analogue.

Interestingly, the 1:1 stoichiometric reaction of **9.1** with Cu(II)Cl$_2$ in CH$_3$CN initially forms a green solution characteristic of Cu(II) before slowly turning yellow at room temperature. The yellow all-Cu(I) complex [{PhSi(6-Me-2-py)$_3$}CuCH$_3$CN]$^+$Cu(I)Cl$_2^-$ **9.3** is the only solid product that could be isolated. Since this was only obtained in low yield it was only characterised by single crystal X-ray crystallography (Figure 122). The reduction of Cu(II) in the presence of metal or semi-metal bridged trispyridyl ligand frameworks has been seen before and is probably coupled to the reductive elimination of 6,6'-di-methyl-bipyridine, although the precise mechanism involved is not certain.

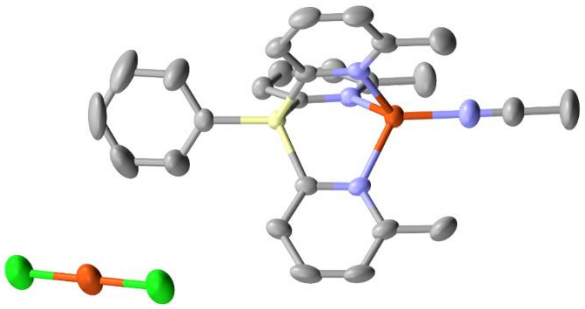

Figure 122: Solid-state structure of **9.3**, the decomposition product of **9.1** and CuCl**.** Hydrogen atoms omitted for clarity; displacement ellipsoids shown at 40% probability. Selected bond lengths [Å] and angles [°]: Si–C_{phenyl} 1.867(4), Si–$C_{pyridyl}$ range 1.877(4)-1.894(3), Cu-$N_{pyridyl}$ range 2.068(3)-2.089(2), Cu-N_{MeCN} 1.948(4), $C_{pyridyl}$-Si-$C_{pyridyl}$ range 104.48(17)-108.61(11), Si-$C_{pyridyl}$-N range 114.0(2)-116.6(3), $N_{pyridyl}$-Cu-$N_{pyridyl}$ 95.38(13)-101.28(9).). Colour code: grey = C, blue = N, yellow = Si, green= Cl, dark orange = Cu.

For example, the attempted coordination of the Sn(IV) trispyridyl ligand ^{n}BuSn(2-py)$_3$ to Cu(II) results in a Cu(I) complex.[145] This redox instability contrasts with C-bridged trispyridyl ligands which can be transferred intact to the Cu(II) cation without breakdown of the ligand framework, e.g., as in the case of the complex [HC(6-Me-2-py)$_3$CuBr$_2$].[181]

The 1:1 stoichiometric reactions of $CoCl_2$ and $FeCl_2$ with **9.1** give clean transfer of the transition metal ions into the corresponding complexes [{PhSi(6-Me-2-py)$_3$}$CoCl_2$] **9.4** and [{PhSi(6-Me-2-py)$_3$}$FeCl_2$] **9.5**, respectively. Satisfactory elemental analyses were obtained for both compounds. However, room temperature ^{1}H NMR spectroscopy proved unhelpful in their characterisation owing to the paramagnetic nature of the high-spin d^6 and d^7 electronic configurations of the transition metal ions and the presence of a fluxional process (described later). Unambiguous characterisation was made by single crystal X-ray diffraction (Figure 123). Both complexes are isostructural, consisting of molecules in which the trispyridyl ligand **9.1** adopts a bidentate coordination mode in which only two of the three N-atoms are bonded to the transition metal ions.

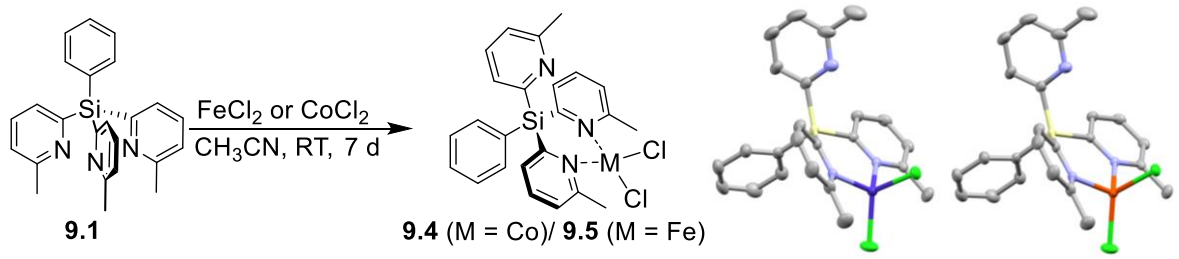

Figure 123: Reaction scheme and solid-state structure of **9.4** and **9.5**. Displacement ellipsoids shown at 40% probability; hydrogen atoms are omitted for clarity**.** Selected bond lengths [Å] and angles [°]: **9.4**, Si–C_{phenyl} 1.866(2), Si–$C_{pyridyl}$ range 1.872(2)-1.885(2), Co-$N_{pyridyl}$ range 2.0505(18)-2.0589(19), Co-Cl 2.2339(7)-2.2623(6), $C_{pyridyl}$-Si-$C_{pyridyl}$ range 105.67(11)-115.78(10), Si-$C_{pyridyl}$-N range 119.81(17)-122.80(16) (coordinating pyridyl groups), Si-$C_{pyridyl}$-N 113.26(17) (non-coordinating pyridyl group), N-Co-N 110.47(7), Cl-Co-Cl 118.50(3). **9.5**, Si–C_{phenyl} 1.866(3), Si–$C_{pyridyl}$ range 1.874(3)-1.884(3), Fe-$N_{pyridyl}$ range 2.106(2)-2.118(2), Fe-Cl range 2.2486(8)-2.2885(7), $C_{pyridyl}$-Si-$C_{pyridyl}$ range 105.60(12)-117.09(10), Si-$C_{pyridyl}$-N range 119.90(18)-122.11(17) (coordinating pyridyl groups), Si-$C_{pyridyl}$-N 113.57(18) (non-coordinating pyridyl group), N-Fe-N 108.88(8), Cl-Fe-Cl 124.58(3).). Colour code: grey = C, blue = N, yellow = Si, green= Cl, blue = Co, orange = Fe.

There are no closely related analogues of **9.4** and **9.5** containing C-bridged trispyridyl ligands, the closest relatives being the 2:1 'sandwich' complexes $[\{MeC(2\text{-}py)_3\}_2M]^{2+}$ (M = Co(II),Fe(II)).[182] However, the bis-coordination of two of the N-atoms of ligand **9.1** found in both complexes is the same as that observed for the isoelectronic P(6-Me-2-py)$_3$ ligand in the complex $[\{P(6\text{-}Me\text{-}2\text{-}py)_3\}FeCl_2]$, which has a very similar structural arrangement.[158] The reasons behind this bis-coordination of the metal cations in **9.4** and **9.5**, rather than tris-coordination in the potential alternative ionisation isomer $[\{P(6\text{-}Me\text{-}2\text{-}py)_3\}FeCl]^+[Cl]^-$, are likely to stem from the combined effects of the presence of sterically constraining 6-Me substituents (which also make the formation of 2:1 sandwich complexes unfavourable with small metal cations) and the greater strength of M-Cl bonds compared to M-N bonds. The metal-N bond lengths in **9.4** and **9.5** are as expected for tetrahedral Co(II) and Fe(II) cations.

As noted before, the ^{1}H NMR spectra of **9.4** and **9.5** at 298 K were unintelligible due to unusually broad resonances, even for paramagnetic complexes of Co(II) and Fe(II). However, reducing the temperature of solutions of **9.4** and **9.5** in toluene results in significant sharpening of the ^{1}H NMR resonances for both compounds. The sharpening of the spectra strongly indicates a dynamic (fluxional) process is occurring. In the case of **9.4**, gradual sharpening of the signals is observed between 353 and 253 K to show eventually the same 2:1 desymmetrisation of the 6-Me-2-py substituents that is present in the solid-state structure. At the same time, the linewidths

of the Ph-resonances remain unchanged in this temperature interval, showing that fluxionality of the pyridyl groups alone is responsible for the observed effect. Additional information is obtained from the temperature-dependent behaviour of **9.5** which shows similar behaviour as **9.4** between 230 and 298 K. However, increasing the temperature above 298K also results in sharpening of the 6-Me- and 2-py resonances into a C_3-symmetric arrangement containing only one 6-Me-2-py environment. This behaviour is consistent with an intramolecular fluxional process involving precession of the bis-coordinating pyridyl groups in both complexes (Figure 124).

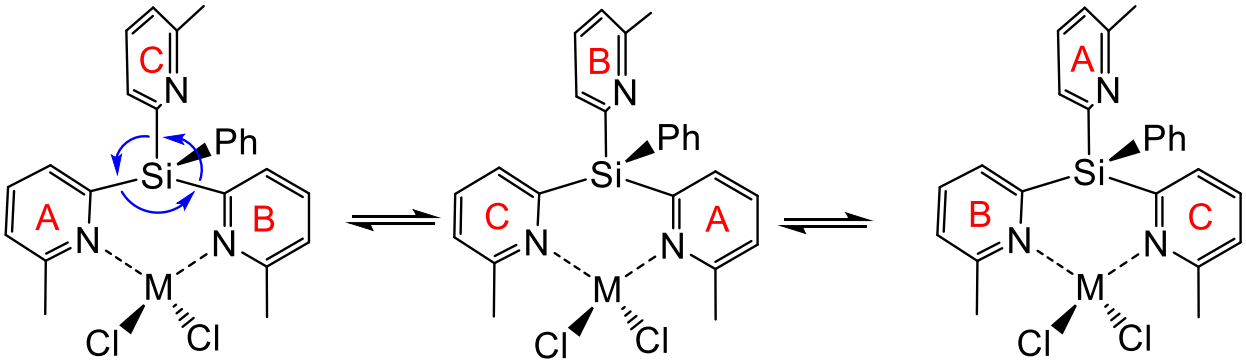

Figure 124: Precession of the pyridyl groups, as potential explanation for the fluxional behaviour of **9.4** and **9.5**.

The low-temperature (230 K) ^{1}H NMR signals of the coordinated pyridyl groups in **9.4** and **9.5** can be assigned using calculated DFT spin-densities at the B3LYP/6-311G(d) level of theory.[183] This work has been done by our collaborator in Heidelberg Markus Enders. However, the correlation of the calculated NMR shifts using Fermi-contact and orbital shifts alone is not satisfactory. EXSY NMR spectroscopy allows the assignment of H^2 (see experimental details for assignment) of the non-coordinated pyridyl at 12 ppm (exchange peak with H^2_c at –28 ppm). This atom is seven bonds away from the paramagnetic centre and therefore no Fermi-contact shift contributes to the observed NMR value, only orbital and pseudocontact shifts. Using the molecular structure and a magnetic axis that bisects the N-Fe-N angle gives an axial magnetic anisotropy ($\Delta\chi_{ax}$) of 7 x 10^{-32} m^3 for **9.4**. In a similar way $\Delta\chi_{ax}$ was determined for **9.5** (8 x 10^{-32} m^3). Including both Fermi-contact and pseudo-contact shifts leads to a much better agreement with the experimental ^{1}H NMR spectrum. The anisotropy of **9.4** compares well with a known 4-coordinate Fe(II) complex whereas in octahedral Co(II) compounds much larger anisotropies compared to **9.5** have been observed.[184,185]

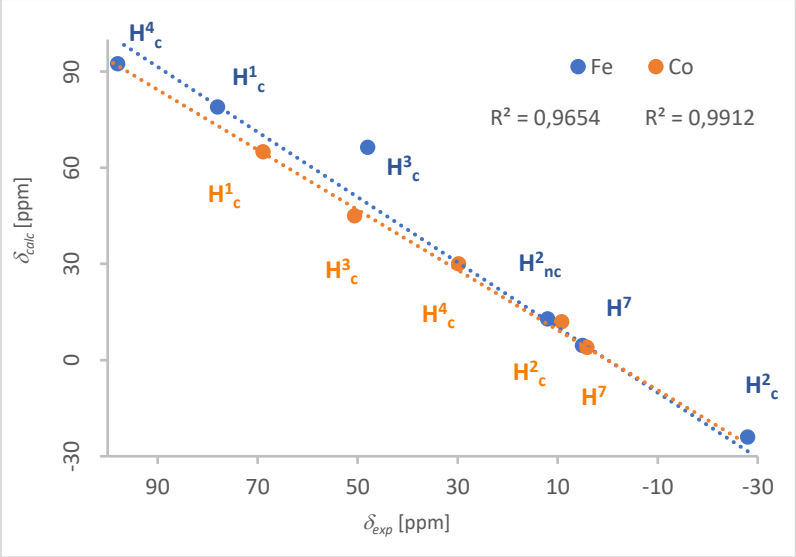

Figure 125: Correlation of experimental with calculated ^{1}H NMR shifts of **9.4** and **9.5** (at 230 K), considering orbital, Fermi-contact and pseudo-contact shifts. H^{x}_{c} and H^{x}_{nc} denotes atoms of coordinated and non-coordinated pyridyl units, respectively. For the numbering scheme see experimental part.

The 1:1 stoichiometric reaction of $Mo(CO)_6$ with **9.1** in MeCN at reflux produces the complex [{PhSi(6-Me-2-py)$_3$}Mo(CO)$_3$] **9.6** in 21% yield after crystallisation from DCM (as the DCM mono-solvate) (Figure 126).

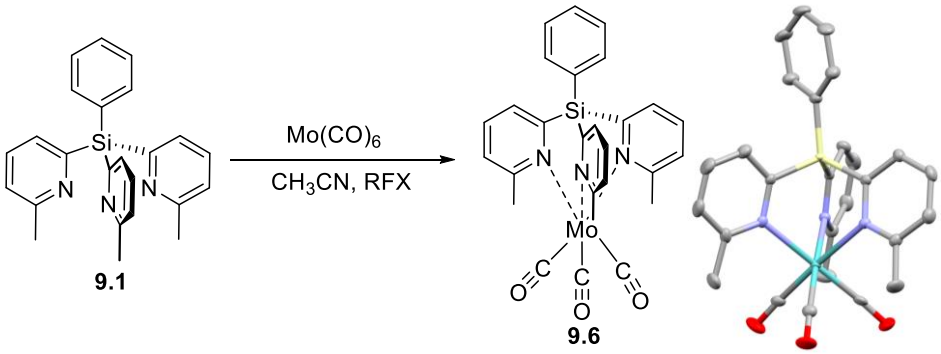

Figure 126: Reaction scheme and solid-state structure of **9.6;** hydrogen atoms omitted for clarity; displacement ellipsoids shown at 40% probability. Selected bond lengths [Å] and angles [°]: Si–C_{phenyl} 1.876(3), Si–$C_{pyridyl}$ range 1.870(3)-1.874(3), Mo-$N_{pyridyl}$ range 2.343(2)-2.424(2), Mo-C range 1.921(3)-1.933(3), $C_{pyridyl}$-Si-$C_{pyridyl}$ range 103.96(13)-112.88(13), Si-$C_{pyridyl}$-N range 115.9(2)-120.4(2), $N_{pyridyl}$-Mo-$N_{pyridyl}$ 86.87(8)-90.05(8), C-Mo-C range 79.91(13)-86.28(13). Colour code: grey = C, blue = N, yellow = Si, red = O, turquois = Mo.

The solid-state structure of **9.6** shows the expected triscoordination of **9.6** to a $Mo(CO)_3$ unit within its molecular arrangement. This is similar to that of the previously reported complex [{^{n}BuSn(2-py)$_3$}Mo(CO)$_3$], containing a Sn-bridged ligand.[186] The IR spectrum of solid **9.6** shows two CO stretching bands at 1893 and 1750 cm^{-1}. This can

be compared to the solid-state IR spectra reported previously for [{HC(2-py)$_3$}Mo(CO)$_3$] (1897 and 1769 cm^{-1}) and [{^{n}BuSn(2-py)$_3$}Mo(CO)$_3$] (1900 and (averaged) 1763 cm^{-1}).[186,187] Unfortunately, it is impossible on this basis to delineate the effect of the electronegativity of the bridgehead atom from the additional effect of the electron-donating 6-Me groups present in **9.1**, since the decrease in electronegativity going down group 14 and the electron-donating Me substituents should both result in greater σ-donor character. This said, it appears that **9.6** has similar σ-donor/π-acceptor properties to the [HC(2-py)$_3$] and [^{n}BuSn(2-py)$_3$] ligands.

Chapter Conclusion

In conclusion, substitution at the 6-position of the pyridyl ring units makes the synthesis of the resulting [PhSi(6-Me-2-py)] ligand much more amenable and produces usable amounts for further coordination studies. This has allowed access to the first examples of transition metal complexes of this type of Si(IV) trispyridyl ligand. Synthetic studies show that, while these ligands function similarly to their C-bridged relatives, they nonetheless exhibit some redox instability, depending on the metal coordinated; a characteristic of related Sn(IV) trispyridyl ligands. During the coordination studies with **9.1** it was noted that **9.1** was a lot more stable compared to many other ligands presented in this thesis and decomposition was not observed either by reduction of the Si bridgehead or by pyridyl transfer. This hints at the applicability of **9.1** under harsher catalytic reaction conditions. Encouragingly, in preliminary tests we have found that the $CuPF_6$ complex of **9.1** (complex **9.2**) shows good activity in the copper(I) catalysed cyclopropanation and aziridination of styrenes. One advantage in moving from the C-bridged to the Si-bridged trispyridyl ligands is the greater flexibility of ligand site, which can expand or contract during reaction to a greater extent than the C-based system.

Experimental Details

General experimental details involving techniques, instruments and materials employed are provided in the appendix at the end of this thesis.

NMR labelling Scheme

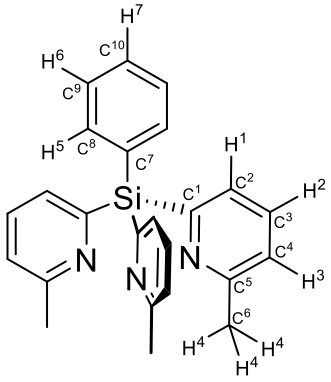

Synthesis of New Compounds

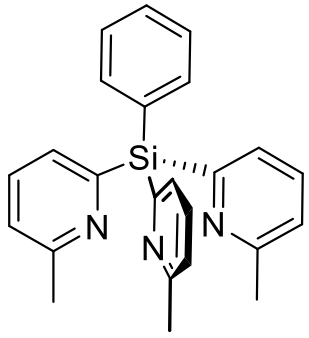

Synthesis of 9.1: 2-Bromo-6-methyl pyridine (2.28 ml, 20 mmol) was dissolved in 40 ml of THF. To this ^{n}BuLi (12.5 ml, 20 mmol, 1.6 M in hexane) was added dropwise at −78 °C.The resulting dark orange solution was stirred for 3 h at −78 °C.$PhSiCl_3$ (1.4 g, 6.66 mmol) in 5 ml of THF was added dropwise to the dark red lithiated species. The resulting pale brown mixture was allowed to warm to room temperature. After stirring overnight, a dark brown solution with a light brown precipitate was formed. All volatiles were removed under vacuum and the resulting solid residue was extracted with 40 ml of warm toluene. The suspension was filtered through Celite to yield a clear-brown solution which was concentrated under vacuum until the precipitation of a white solid was observed, which was redissolved by gentle heating. Storage overnight at -15 °C yielded **9.1** as colourless needles suitable for X-ray crystallography. The product was isolated by filtration and storage of the mother liquor yielded a second crop of crystals. Combined yield 2.10g (4.61 mmol, 82%). **^{1}H NMR (25 °C, d_8-toluene, 500 MHz):** δ(ppm) = 8.20 (d, J = 7.0 Hz, 2H, H-5), 7.86 (d, J = 7.4 Hz, 3H, H-1), 7.24 (m, 3H, H-6, H-7), 7.11 (t, J = 7.7 Hz, 3H, H-2), 6.68 (d, J = 7.8 Hz, 3H,H-3), 2.40 (s, 9H, H-4); **^{13}C NMR (25 °C, d_8–toluene, 125 MHz):** δ(ppm) = 162.7 (C-1), 157.9 (C-2), 136.7 (C-4), 134.3 (C-7), 133.6 (C-3), 129.8 (C-9), 129.0 (C-5) , 127.3 (C-8), 122.2 (C-

10), 24.0 (C-6); **Elemental analysis (%)** calcd. for **9.1**: C 75.5, H 6.1, N 11.0 found: C 74.5, H 5.9, N 10.5.

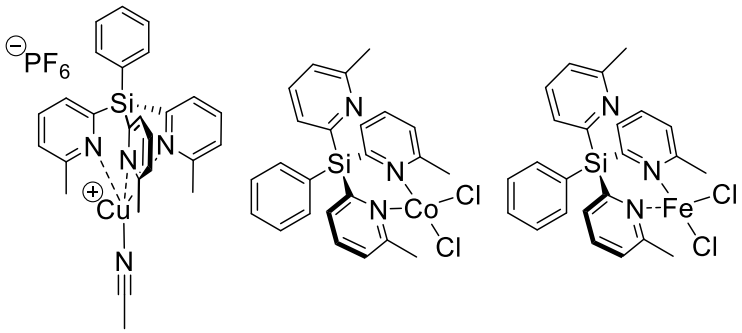

Synthesis of 9.2, 9.4 and 9.5: A Schlenk tube was charged with **9.1** (300 mg, 0.78 mmol, 1 eq.) and 1 equivalent of the transition metal source $[Cu(MeCN)_4]PF_6$ (314 mg, 0.78 mmol) for **9.2**, $CoCl_2$ (100 mg, 0.78 mmol, 1 eq) for **9.4**, $FeCl_2$ (100 mg, 0.78 mmol) for **9.5** in a glovebox. The Schlenk tube was transferred to a vacuum line and 25 ml of CH_3CN was added. The resulting solution (yellow for **9.2**, green for **9.4** and yellow for **9.5**) was stirred at room temperature overnight and then concentrated under vacuum until the precipitation of a solid was observed (yellow for **9.2** and **9.5**, blue for **9.4**). The solid was redissolved by gentle heating. Storage overnight at -15 °C yielded crystals of **9.2** (yellow), **9.4** (blue) or **9.5** (yellow) suitable for X-ray crystallography which were isolated by filtration. **For 9.2**: Yield 152 mg (0.24 mmol, 31%); **^{1}H NMR (25 °C, CD_3CN, 500 MHz)**: δ(ppm) = 8.08 (d, J = 6.9 Hz, 2H, H-5), 7.78 (t, J = 7.5 Hz, 1H, H-7), 7.72 (m, 5H, H-6, H-2), 7.60 (d, J = 7.5 Hz, 3H, H-1), 7.40 (d, J = 7.8 Hz, 3H, H-3), 2.83 (s, 9H, H-4), 1.99 (s, 3H, Acetonitrile); **^{31}P NMR (25 °C, CD_3CN, 202.48 MHz)**: δ(ppm) = -144.6 (hpt, $^1J_{PF}$ = 705.69 Hz, PF_6); **^{13}C NMR (25 °C, CD_3CN, 125.78 MHz)**: δ(ppm) = 160.2 (C-1), 158.6 (C-2) ,148.9 (C-4), 136.7 (C-7), 136.1 (C-3), 131.6 (C-9), 130.2 (C-5), 128.9 (C-8), 125.3 (C-10), 24.7 (C-6); **Elemental analysis (%)** calcd. for **9.2**: C 49.5, H 4.2, H 8.9, found: C 49.2, H 4.2, N 9.1. For **9.4**: Yield 210 mg (0.55 mmol, 70%); **Elemental analysis (%)** calcd. for **9.4**: C 49.5, H 4.2, H 8.9, found: C 49.2, H 4.2, N 9.1; **For 9.5**: Yield 195 mg (0.50 mmol, 65%); **Elemental analysis (%)** calcd. for **9.5**: C 56.7, H 4.5, N 8.3, found C 55.3, H 4.5, N 8.8.

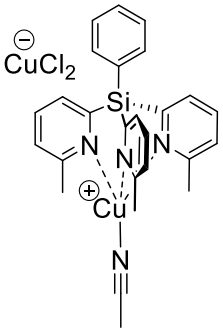

Synthesis of 9.3: A Schlenk tube was charged with **9.1** (50 mg, 0.13 mmol, 1 eq.) and 1 equivalent of $CuCl_2$ (16 mg, 0.13 mmol) in a glovebox. The Schlenk tube was transferred to a vacuum line and 5 ml of CH_3CN was added. The resulting solution green solution was stirred at room temperature overnight and then concentrated and layered with Et_2O. Over the course of 2 weeks a few yellow crystals grew which could be analysed via X-ray diffraction.

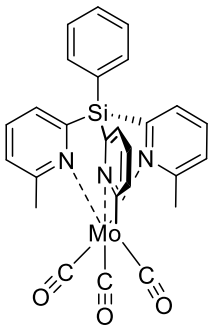

Synthesis of 9.6: A Schlenk tube was charged with **9.1** (500 mg, 1.30 mmol) and $Mo(CO)_6$ (343 mg, 1.30 mmol, 1 eq) inside a N_2-filled glovebox. The Schlenk tube was transferred to a vacuum line and 25 ml of CH_3CN was added. The resulting solution was brought to reflux overnight during which the colour changed to brown/red. The solvent was removed and the solid brown residue was dissolved in 25 ml of DCM and stirred for 2 hours. The solution was concentrated under vacuum until the precipitation of a red solid was observed which, was redissolved by gentle heating. Storage overnight at -15 °C yielded red crystals of **9.6**•DCM suitable for X-ray crystallography which were isolated by filtration. Isolation of this solvate under vacuum (1 bar) results in loss of ca. 0.5 DCM molecules per molecular unit, give a final product with formula **9.6**•0.5DCM. Yield 150 mg (0.27 mmol, 21%). **^{1}H NMR (25 °C, 500 MHz, $CDCl_3$):** δ[ppm] = 8.06 (d, J = 6.8 Hz, 2H, H-5), 7.72 (m, 3H, H-6, H-7), 7.50 (m, 6H, H-1, H-2), 7.27 (d, J = 8.9 Hz, 3H, H-3), 3.34 (s, 9H, H-4) (DCM also present at 5.3 (s)]; **^{13}C NMR (25 °C, 125 MHz, $CDCl_3$)**: δ[ppm] = 228.16 (CO), 166.03 8 (C-1), 159.33 (C-2) , 137.01 (C-4), 134.35 (C-7), 131.56 (C-3), 130.13 (C-9), 129.21 (C-5), 128.44 (C-8), 126.24 (C-10), 29.04 (C-6); Elemental analysis (%) calcd. for **9.6**•0.5DCM C 54.7, H 4.0, N 7.0; found, C 54.9, H 4.1, N 8.0; **IR (Solid)**: CO stretch: 1893 cm^{-1} and 1750 cm^{-1}.

Chapter 10: Deprotonation, Insertion and Isomerisation in the Post-functionalisation of Trispyridyl aluminates

In light of the applications of the aluminate complex [EtAl(6-Me-2-py)$_3$Li] **10.1** in the chiral discrimination of alcohols (discussed in the introduction to this part of the thesis),[135] we sought in this chapter of the thesis to extend this work to other acidic and electrophilic organic analytes.

Results and Discussion

We first explored the reactions of **10.1** (which was synthesised via the literature procedure) with aldehydes.[132] Monitoring the 1:1 stoichiometric reaction between **10.1** and benzaldehyde (PhCH=O) by ^{1}H NMR in d$_8$-THF shows the exclusive formation of a single product **10.2** after 5 min at room temperature (Figure 127). Several observations support the nucleophilic addition of a 6-Me-2-pyridyl group to the aldehyde carbonyl. In particular, the aldehyde CH proton of PhCH=O disappears completely and is replaced by a CH singlet at δ = 6.55 ppm, supporting the generation of a secondary alcoholate. In the ^{1}H-^{1}H NOESY NMR a cross-peak between the tertiary CH proton and the bridgehead Et-Al group of aluminate anion is also observed. While there is no change in the position of the broad singlet found in the ^{127}Al NMR spectrum compared **10.1** (δ = 127 ppm), the ^{7}Li NMR spectrum shows a diagnostic change from 3.5 ppm in **10.1** to 2.6 ppm in **10.2**.

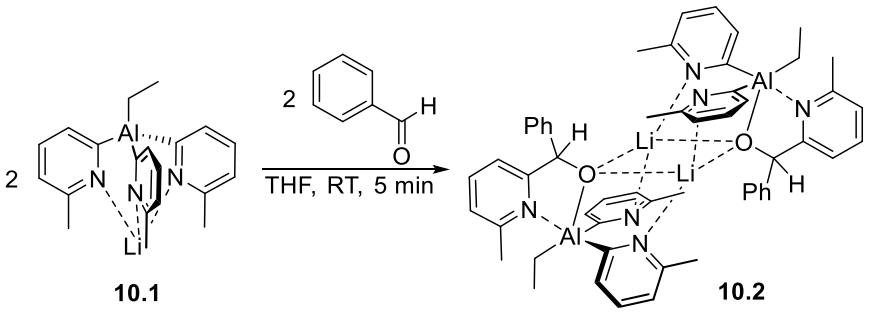

Figure 127: Selective reaction of the trispyridyl-aluminate **10.1** with one equivalent benzaldehyde yielding **10.2**.

X-ray quality crystals of the product [{EtAl(6-Me-2-py)$_2$(OCHPh(6-Me-2-py))}Li]$_2$ **10.2** were grown from a saturated toluene solution at -14 °C in 30% yield. The single crystal

X-ray structure confirms the selective functionalisation of [EtAl(6-Me-2-py)$_3$Li(THF)] (Figure 128). The solid-state structure is that of a dimer containing a central Li_2O_2 core involving the O-atoms of the [(6-Me-2-py)$_2$(OCHPh(6-Me-2-py)]$^-$ anions (Li-O range 1.942(6)-2.309(7) Å). The aluminate anions use their two 2-py-N atoms to coordinate the separate Li^+ cations of the core [2.022(7) Å], resulting in a pseudo-tetrahedral geometry at Li^+. The pyridyl-N atom of the OCHPh(6-Me-2-py) group within each of aluminate anion is involved in a secondary N•••Al interaction with the bridgehead Al(III) atom [2.482(4) Å]. This results in a roughly pentagonal coordination geometry for the Al atoms.

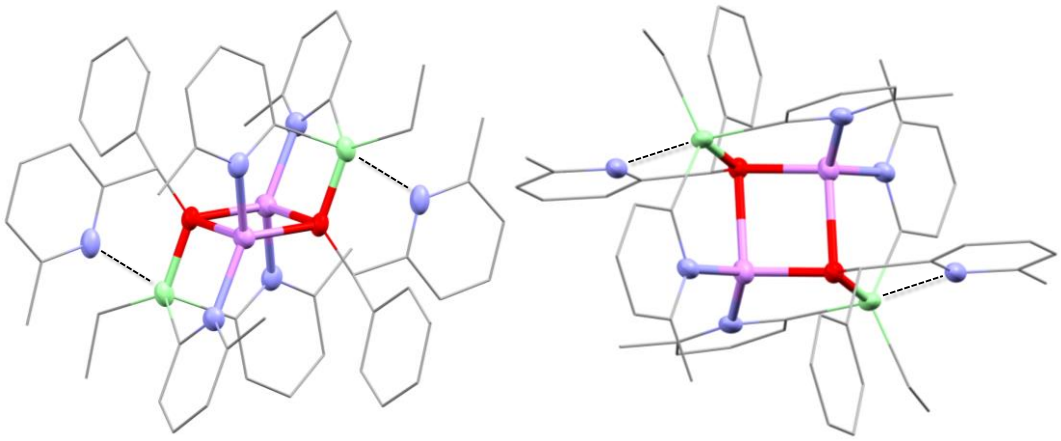

Figure 128: Different views on the solid-state structure of the dimer [{EtAl(6-Me-2-Py)2(OCHPh(6-Me-2-py))}Li]$_2$ **10.2** in the toluene solvate. H-atoms and the lattice toluene molecules have been omitted for clarity. Displacement ellipsoids set at 40% probability. Selected bond lengths [Å] and angles [°]; Li-O range 1.942(6)-2.309(7), Li-N range 2.021(7)-2.022(7), Al-O 1.828(3), Al-$C_{pyridyl}$ 2.023(4)-2.076(4), Al-C_{Et} 2.004(4), Al•••N 2.482(4), Li-O-Li 85.6(3), O-Li-O 94.4(3). Colour code: grey =C, blue = N, red = O, purple = Li, green = Al.

A chiral tertiary carbon atom is generated upon nucleophilic addition of the 6-Me-2-py substituent of **10.1** to the prochiral aldehyde carbonyl centre of PhCH=O. However, dimers of **10.2** are non-chiral as a result of the presence of both R- and S-enantiomers of the OCHPh(6-Me-2-py) groups. The presence of the secondary N•••Al interactions with the pyridyl-N atoms of the OCHPh(6-Me-2-py) groups means that no free rotation of the C-O bond can occur and results in desymmetrizing the 6-Me-2-py groups of each of the anions **10.2**. This is evident in the room temperature ^{1}H NMR spectra of **10.2** in d_8-toluene and d_8-THF, which both show two 6-Me-2-py environments. The corresponding ^{7}Li NMR spectra, however, show a large change in chemical shift moving from toluene (sharp singlet at 3.7 ppm) to THF (broad singlet at 2.6 ppm),

which we ascribe to the presence of a dimer in toluene and a (most likely THF solvated) monomer in THF. In either case, the presence of a N/O-chelating OCHPh(6-Me-2-py) groups will result in the desymmetryisation of the 6-Me-2-py groups. The observation of only two 6-Me-2-py groups in the ^{1}H NMR spectrum and only a singlet in the ^{7}Li NMR spectrum of dimeric **10.2** in toluene strongly supports the retention of the RS-stereochemistry found in the solid-state structure, since equilibration to the SS- and RR-dimers would give additional ^{1}H and ^{7}Li resonances (as found previously in studies of the reactions of **10.1** with mixtures of chiral alcohols containing an entantiometric excess of one isomer).[135] The room temperature 2:1 reaction of **10.1** with benzaldehyde is unselective, presumably because the remaining 2-py groups are less nucleophilic. Increasing the temperature only led to a complicated mixture of products.

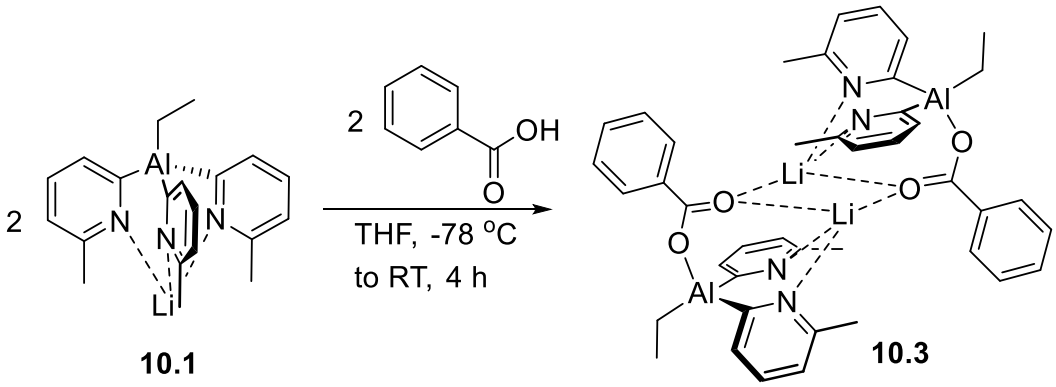

Figure 129: Functionalisation of **10.1** with benzoic acid yielding **10.3**.

While a range of other aldehydes react with **10.1** in a similar way, ketones, isonitriles and imines, which contain less electrophilic C-centres, do not react. However, unsurprisingly on the basis of previous studies, carboxylic acids react readily with **10.1** even at low temperature. The ^{1}H NMR spectrum of the room-temperature 1:1 reaction of **10.1** with benzoic acid $PhCO_2H$ in THF showed the formation of a mixture of products. Significantly, these included 6-Me-pyH and EtH, indicating that both the 6-Me-2-py and bridgehead Et groups of **10.1** are involved in deprotonation of the acid. Although the same reaction at -78°C in toluene leads to a ca. 1:1:1 mixture of unreacted **10.1** and the lithium complexes of the mono- and disubstituted anions $[EtAl(6\text{-Me-py})_2(PhCO_2)]^-$ **10.3** and $[EtAl(6\text{-Me-py})(PhCO_2)_2]^-$ **10.4**, respectively, the reaction of the bridgehead Et group is largely supressed. The ^{1}H NMR spectrum shows

that the 1:2 reaction of **10.1** with $PhCO_2H$ at -78ºC in toluene leads to exclusive formation of **10.4**.

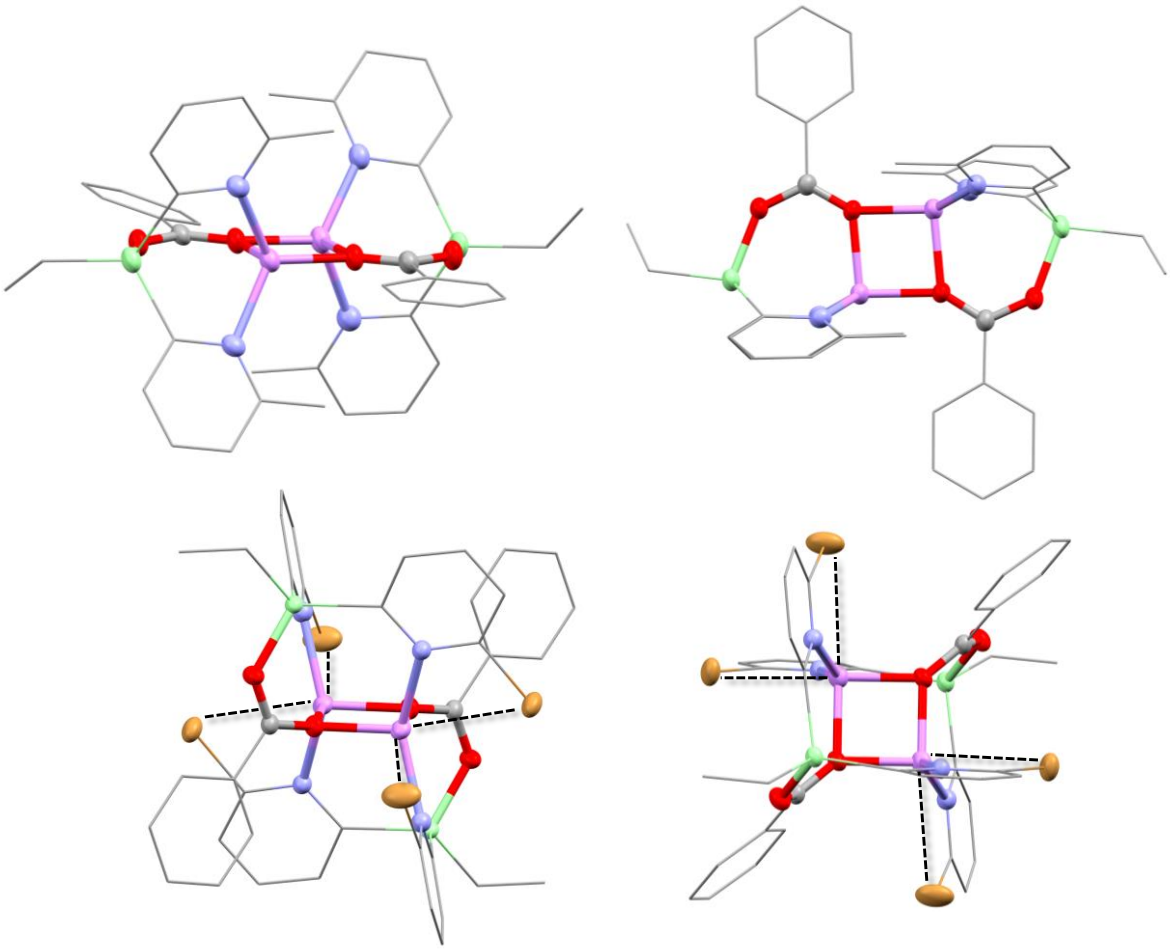

Figure 130: Dimeric structure of top: **10.3** and bottom: **10.7**. The H-atoms and the toluene molecules present in the lattices of the solvates **10.3** have been omitted for clarity; displacement ellipsoids set at 40% probability. Selected bond lengths [Å] and angles [°]: **10.3**: Li-O range 1.943(4)-1.998(4), Li-N range 2.079(4)-2.104(4), Al-O range 1.837(2)-1.840(2), Al-$C_{pyridyl}$ range 1.978(3)-2.007(3), Al-C_{Et} range 1.975(3)-1.978(3), Li-O-Li range 85.6(2), O-Li-O 94.3(2)-94.5(2). **10.7**: Li–O range 1.930(6)–1.956(7), Li–N range 2.093(6)–2.124(6), Al–O range 1.814(2)–1.833(2), Al–$C_{pyridyl}$ range 2.015(3)–2.030(4), Al–C_{Et} range 1.976(4)–1.999(4), Li–O–Li range 88.3(3)–90.2(3), O–Li–O 88.3(3)–90.1(3). Colour code: grey =C, blue = N, red = O, purple = Li, green = Al, brown = Br.

On the basis of the previous NMR experiments, we scaled up the 1:1 and 1:2 reactions using the same conditions to obtain the solid lithium salts of **10.3** and **10.4** (in 23% and 34% yields, respectively). Although **10.4** could only be obtained as a powder (which was characterised by multinuclear NMR and elemental analysis), in the case of the lithium complex of **10.3** crystals of the mono-toluene solvate were obtained directly from the reaction mixture by layering with hexane and storage at −15 °C for

16 h. The single crystal X-ray structure reveals an approximately centrosymmetric dimeric arrangement and confirms the substitution of one of the 6-Me-2-py groups (Figure 130). Interestingly, the coordination mode of the anions in **10.3** is distinctly different from that of the anions in **10.2** and in previously reported alkoxy-aluminate dimers of the type [{EtAl(6-Me-2-py)$_2$(OR)}Li]$_2$. Whereas in all the latter the two 6-Me-2-py groups coordinate separate Li$^+$ cations within their Li$_2$O$_2$ cores, in **10.3** both of the 6-Me-2-py groups of each anion are coordinated to a single Li$^+$ cation of the Li$_2$O$_2$ ring unit. The formation of the dimer effectively results from the 'side-on' association of the monomers, with the Li$_2$O$_2$ ring, PhCO$_2$ groups and Al atoms of the aluminate ligands being almost coplanar.

As background to this study, we also explored the selectivity of the reactions of benzoic acid with other aluminate ions [{EtAl(6-R-2-py)$_3$}Li] [R = CF$_3$ **10.5**, Br **10.6**]. The presence of electron-withdrawing substituents on the pyridyl rings makes these anions considerably less reactive than **10.1** and a greater amount of EtH was observed by ^{1}H NMR in their 1 : 1 and 1 : 2 reactions with PhCO$_2$H at −78 °C in toluene. The observed order of reactivity (**10.1** > **10.6** > **10.5**) is in line with the electron-withdrawing ability of the substituent on the pyridyl ring units (and the resulting reduction in the polarity of the C–Al bonds). A ca. 3 : 1 mixture of unreacted anion **10.6** and the new anion [EtAl(6-Br-2-py)$_2$(PhCO$_2$)]$^-$ **10.7** is formed under these conditions, from which a low yield of the crystalline lithium salt was isolated. Owing to the low yield, the complex was only characterised using X-ray crystallography. The solid-state structure again shows a centrosymmetric dimer arrangement (Figure 130), with the overall structural features being similar to those found in **10.2** and **10.3**. However, a particular point of interest is the coordination mode of the anion [EtAl(6-Br-2-py)$_2$(PhCO$_2$)]$^-$ to the Li$^+$ cations, which involves bonding of the pyridyl-N atoms to the two separate Li$^+$ cations within the Li$_2$O$_2$ ring, and is therefore like that found in **10.2** rather than that in the more chemically-related dimer **10.3**. The 'face-on' association of the monomer units of **10.7** places the Al atoms of the aluminate ligands above and below the Li$_2$O$_2$ ring unit, with the PhCO$_2$ groups being perpendicular to the ring. The origin of the coordination isomerism observed in **10.3** and **10.7** may in part be due to the presence of stabilising Br···Li interactions which are in the range 3.040(6)–3.066(6) Å in **10.7**, although this is not fully understood at this stage.

Chapter Conclusions

We have shown that the aluminate anion **10.1** can function either as nucleophile, adding to polar C=O groups of aldehydes, or as a base, deprotonating the OH groups of carboxylic acids. Depending on the organic reaction partner, dimers with different coordination connectivity are obtained. Whereas electrophilic attack of benzaldehyde occurs selectively in a quantitative fashion, deprotonation of benzoic acid is not selective for the 1:1 but selective for the 2:1 reaction highlighting the fact that the basicity/nucleophilicity of the pyridyl substituents depends on the other aluminate substituents. Although pentacoordination of the bridgehead in pyridyl aluminates has been observed before,[136] the combination of chiral self-sorting and bridgehead coordination might open up further avenues in enantiomeric discrimination.

Experimental Details

General experimental details involving techniques, instruments and materials employed are provided in the appendix at the end of this thesis.

[{EtAl(6-R-2-py)$_3$}Li] [R = Me **10.1**, CF_3 **10.5**, Br **10.6**] were synthesized according to the literature procedure.[132]

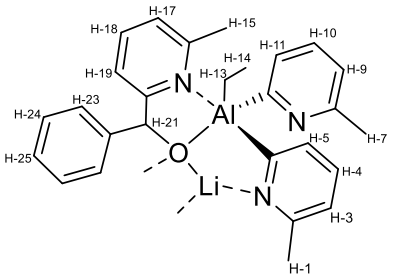

Synthesis of 10.2: To a stirred solution of **10.1** (300 mg, 0.89 mmol) in 5 ml of THF was added neat benzaldehyde (89 µL, 0.89 mmol). The mixture was stirred for 5 min and the solvent was then removed in vacuo. The oily residue was dissolved in 2 ml of toluene and stored at - 15 °C for 1 week to yield **10.2** as colourless crystals (160 mg, 0.36 mmol, 40%). **^{1}H NMR (25 °C, 500 MHz, d_8-toluene) δ[ppm] =** 7.66 (d, J = 7.2 Hz, 1H, H-5), 7.58 (d, J = 7.2 Hz, 1H, H-11), 7.27 (d, J = 7.3 Hz, 2H, H-23), 7.15 – 7.00 (m, 5H, H-4, H-10, H-24, H-25), 6.82 (t, J = 7.7 Hz, 1H, H-18), 6.62 (d, J = 7.7 Hz, 1H, H-3), 6.55 (pt, J = 8.5 Hz, 2H, H-9, H-17), 6.41 (d, J = 7.8 Hz, 1H, H-19), 5.73 (s, 1H, H-21), 2.62 (s, 3H, H-15), 2.50 (s, 3H, H-1), 2.36 (s, 3H, H-15), 1.46 (t, J = 8.2 Hz, 3H, H-14), 0.55 (q, J = 8.1 Hz, 2H, H-13); **^{13}C NMR (25 °C, 126 MHz, d_8-toluene):** δ[ppm] = 187.97, 167.41, 155.50, 155.08, 154.90, 146.09, 136.67, 132.45, 129.86, 129.35, 128.80, 128.68, 127.90, 127.75, 126.97, 120.61, 119.64, 119.61, 119.50, 77.08, 25.04, 24.61, 24.59, 9.59, -1.99; **^{127}Al NMR (25 °C, 130 MHz, d_8-toluene):** δ[ppm] = 130.9; **^{7}Li NMR (25 °C,194 MHz, d_8-toluene, 25 °C):** δ[ppm] = 3.68. **Elemental analysis** (%) calcd. for **10.2**: C 73.2%, H 7.4%, N 8.8%; found C 72.8%, H 7.2%, N 8.9%.

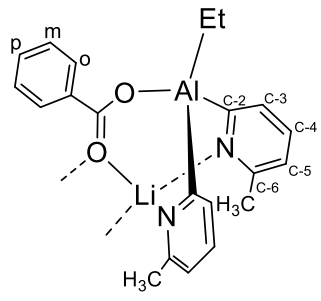

Synthesis of 10.3: **10.1** (200 mg, 0.59 mmol,) was dissolved in toluene (5 ml) and the solution was cooled to -78 °C.After addition of benzoic acid (72 mg, 0.59 mmol) the reaction mixture was stirred at -78 °C for 3 min and subsequently allowed to warm up to room temperature. The resulting clear solution was stirred at

room temperature for further 4 h. The solution was concentrated in vacuo until the precipitation of a colourless solid was observed. The precipitate was redissolved by gently heating the solution. Layering with hexane and storage at -15 °C overnight afforded colourless crystals of **10.3** (100 mg, 271 µmol, 46%). **^{1}H-NMR (25 °C, d$_8$-toluene, 500 MHz):** δ[ppm] **=** 8.18 (d, J = 5.1 Hz, 2H, o-C_6H_5), 7.80 (d, J = 7.1 Hz, 2H, H-3 py), 7.11 (t, J = 7.6 Hz, 2H, H-4 py), 6.91 (t, J = 6.7 Hz, 1H, p-C_6H_5), 6.73 (m, 2H, m-C_6H_5), 6.47 (t, J = 7.6 Hz, 2H, H-5 py), 1.90–1.87 (m, 9H, 2-py-CH_3 and Al-CH_2-CH_3), 1.02 (q, J = 8.0 Hz, 2H, Al-CH_2); **^{13}C-NMR (25 °C, d$_8$-toluene, 126 MHz):** δ[ppm] = 184.4 (br, C_q, C-2 py), 174.4 (br, C_q, COO), 158.2 (C_q, C-6 py), 135.6 (C_q, C_6H_5), 133.8 (CH, C-4 py), 133.0 (CH, p-C_6H_5), 131.1 (CH, o-C_6H_5), 131.0 (CH, C-3 py), 125.6 (CH, m-C_6H_5), 122.1 (CH, C-5 py), 23.7 (CH_3, py), 10.4 (CH_3, Al-CH_2CH_3), -1.4 (CH_2, Al-CH_2); **^{7}Li-NMR (25 °C, d$_8$-toluene, 194 MHz):** δ[ppm] = 3.03 ppm. **Elemental analysis** calcd. for **10.3:** calcd. C 68.5%, H 6.0%, N 7.6%, found: C 68.5%, H 6.1%, N 7.0%.

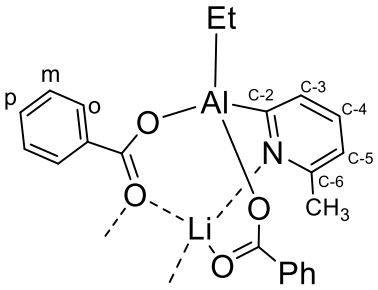

Synthesis of 10.4: 10.1 (200 mg, 0.59 mmol) was dissolved in toluene (5 ml) and the solution was cooled to -78 °C.After addition of benzoic acid (144 mg, 1.18 mmol), the reaction mixture was stirred at -78 °C for 3 min and subsequently allowed to warm up to room temperature. The resulting clear solution was stirred at room temperature for further 4 h. The solution was concentrated in vacuo to a volume of 1 ml and layered with hexane. Storage at -15 °C overnight afforded **10.4** as a colourless solid (155 mg, 390 µmol, 66%). **^{1}H-NMR (25 °C, d$_8$-toluene, 500 MHz):** δ[ppm] = 8.47 (m, 4 H, o-C_6H_5), 7.69 (d, J = 7.2 Hz, 1H, H-3 py), 7.11–7.07 (m, 5H, m-C_6H_5 and H-4 py), 7.02–7.00 (m, 2H, p-C_6H_5), 6.30 (d, J = 7.3 Hz, 1H, H-5 py), 1.85 (t, J = 8.2 Hz, 3H, Al-CH_2-CH_3), 1.69 (br s, 3H, 2-py-CH_3), 0.89 (q, J = 8.1 Hz, 2 H, Al-CH_2); **^{7}Li-NMR (25 °C, d$_8$-toluene, 194 MHz):** δ[ppm] = 2.55 ppm; **Elemental analysis** calcd. for **10.4**: C 66.5%, H 5.3%, N 3.5%, found: C 66.3%, H 5.7%, N 3.5%.

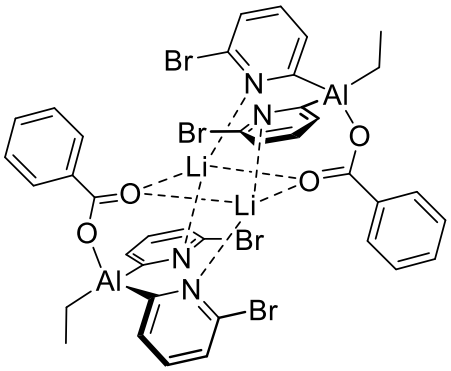

Synthesis of 10.7: Compound **10.7** was only isolated as a few crystals that were characterised by X-ray crystallography and no NMR data could be recorded. In a glove box, **10.6** (40 mg, 0.07 mmol) and benzoic acid (9.1 mg, 0.07 mmol, 1 eq.) were dissolved in toluene (0.6 ml). The solution was concentrated and stored at −15 °C overnight, affording **10.7** as a few colourless crystals.

Chapter 11: Future Work

Although work by Stahl et al. and others demonstrated the potential of diaminophophazanes as supporting ligands for main group and transitions metals, the potential has not been fully unlocked.[16]

Phosphazanes as Ligands in Catalysis: As this work has shown, the four membered P_2N_2 framework is robust enough for applications under ambient conditions once either oxidised or coordinated to a metal, this might allow research into applications in homogeneous catalysis under normal conditions. Diamidophosphazanes $[RN(\mu\text{-}NR)P]_2^{2-}$ could in principle function as six electron donor providing a chiral environment via their endo and exocyclic substituents with chiral R-groups, distinctly different from established ligands sets such as diketimides. Aldridge et al. recently used a bulky xanthene based N,N,O-dianionic six electron donor set to stabilise a aluminium(I) anion in which the aluminium centre is nucleophilic.[188] Phosphazane based six electron donor ligands could provide the necessary steric bulk via the exocyclic substituents and a chiral environment via the endocyclic amine substituents. This could enable enantioselective reactivity of aluminium(I). In addition, diamidophosphazane ligands feature orthogonal chemically hard amido donor centres and soft phophine donor centres which could allow simultaneous coordination to soft and hard metals. Such bimetallic complexes could function as tandem catalysts where one system is catalytically active in a series of orthogonal reactions. A particularly interesting aspect of such multimetallic phosphazane complexes would be to what extent the catalytic activity of one metal type is affected by the other. Another approach which would in principle make use of the intrinsic geometrical features of the phosphazane framework could be the integration of additional donor substituents as shown below (Figure 131). Either quinolyl or CR_2pyridyl substituents on the endocyclic nitrogen centres ideally positioned for the construction of tetradentate N,N,N,N donor sets.

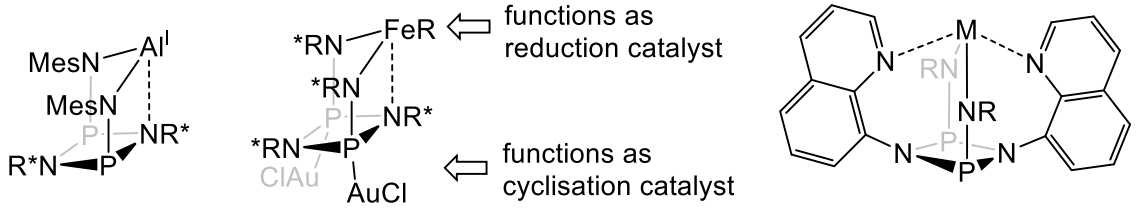

Figure 131: Proposed ligand set for functional phosphazane ligands.

Anion Binding and Transport: In the realm of anion binding a future possible development could be the construction of larger H-bonding phosphazanes with more donor sites. As mentioned earlier in the introduction choosing smaller endocyclic substituents results in expansion of the phosphazane ring.[8] Hence a tridentate anion receptor could be accessed from a six member phosphazane trimer $[RNHP(\mu\text{-}NR)]_3$ with endocyclic ethyl substituents as shown below (Figure 132). Such systems could again prove valuable in anion binding, abstraction catalysis and transport after chalcogen oxidation. However we anticipate the phosphorus(III) derivatives to be viable receptors already because of the increase of H-bond donor sites. Having a potent receptor which features phosphine centres might prove valuable in organocatalysis since both H-bond donors as well as phosphines are active catalysts.[189,190]

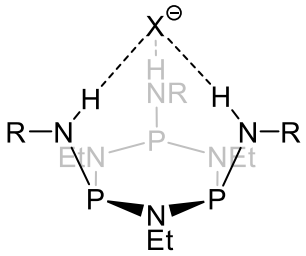

Figure 132: Tridentate Phosphazane Anion receptor.

Macrocyclic Chemistry: The recent advances in synthetic methodologies for phosphazane macrocycles pave the way for future investigation into their functional behaviour. Since work in the thesis demonstrated binding to alkynes and kinetic locking of guests, one possible avenue could be the design of a capture-release systems for acetylene storage, as shown below (Figure 133). Oxidation in presence of acetylene could lead to similar entrapment of acetylene as seen for halides discussed earlier. Addition of a reductant could then reverse the steric distortion responsible for entrapment and release the acetylene guest.

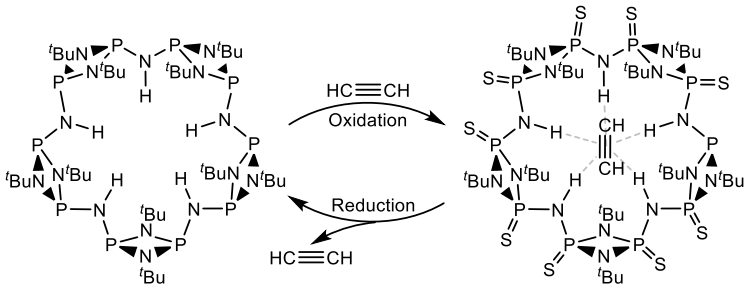

Figure 133: Capture release system of acetylene based on the pentameric macrocycle **5.1**.

The oxidation discussed above confirmed that host-guest complexes of phosphazane macrocycles retain backbone reactivity. Hence the pentameric macrocycle **5.1** could serve as a ligand for transition metals which could display a change in the electronic ligand properties upon guest binding, as shown below (Figure 134). Upon anion encapsulation **5.1** would transform from a neutral into an anionic ligand which potentially modulates the metal-ligand interaction and consequently the electronic properties of the coordinated metal. This process could be potentially applied in switchable catalysis, with catalytically active metals, or anion sensing with luminescent coordinated complex fragments. Further oxidation of the remaining free phosphine centres could enhance this process.

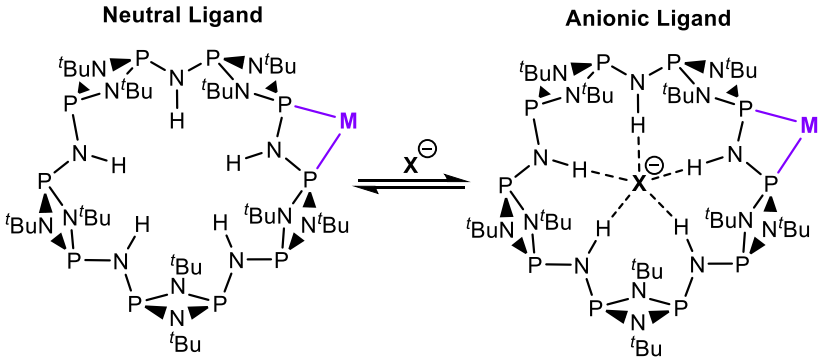

Figure 134: Proposed ligands switching based on macrocyle **5.1**.

On a similar note, we anticipate **5.1** may have potential in materials chemistry. In principle reaction of the pentamer with transition metal salts could result in the formation of porous coordination networks. Choosing the right counter anion (e.g., large weakly coordinating anions) would leave the cavities of the **5.1** empty and accessible for applications such as gas storage. Since the work in this thesis shows **5.1** to be size selective, integration of **5.1** into coordination networks could provide rational tools for the design of functional materials.

Pyridyl Ligands in Catalysis: One future avenue for the application of pyridyl main group ligands could be the involvement of the bridgehead reactivity in homogenous catalysis. One potential ligand design is shown in Figure 135. It features a bispyridyl antimony based ligand set for metal coordination featuring a tuneable Lewis acidic main group centre in proximity to a transition metal catalyst close enough to cooperatively react with a substrate but spatially separated enough not to quench each other's reactivity. This principle has been recently developed for main group systems in the context of frustrated Lewis-base pairs (FLPs).[191]

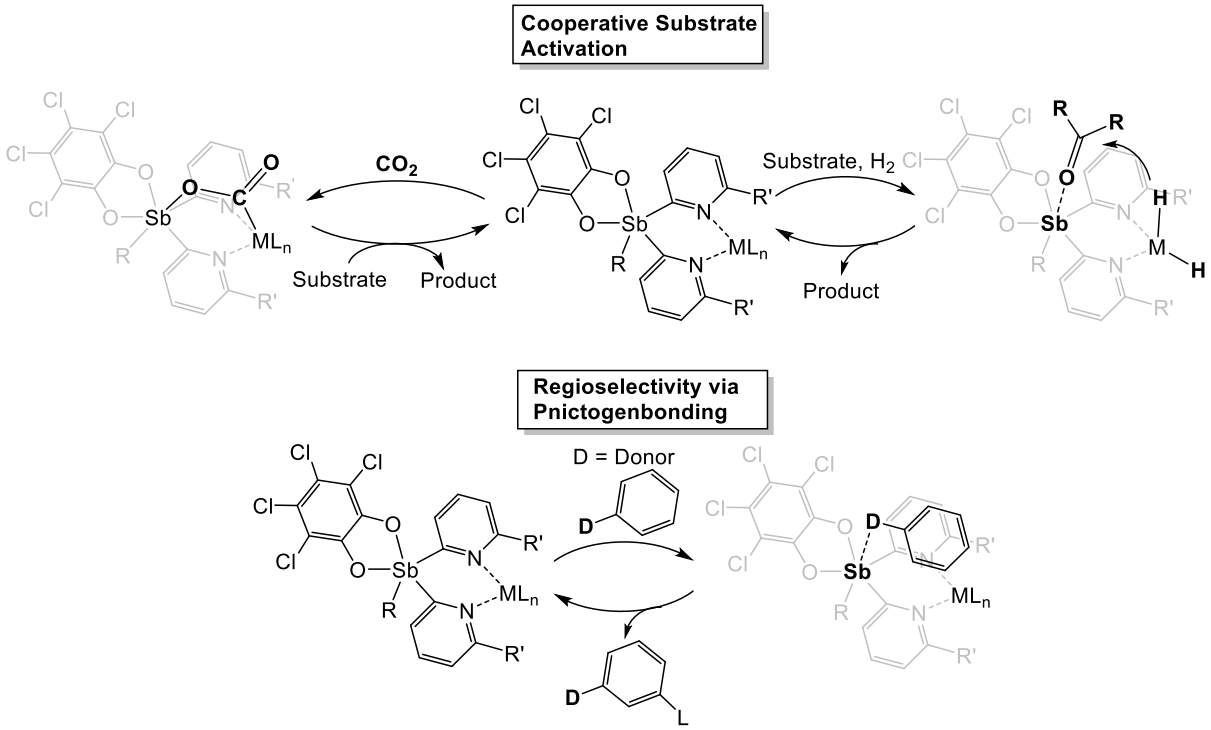

Figure 135 : Ligand design and cooperative activity.

The key structural feature of the proposed design involves the choice of coordinating groups attached to the main group Lewis acid which prevent Z-type metal ligand interaction between the coordinated metal and the main group Lewis acid. This will enable different types of reactivity such as cooperative FLP type activation via electron donation from the transition metal and electron withdrawal from the Lewis acid, activation of substrates via coordination to the Lewis acidic main group site via electron donation of substrate lone pairs to main group centre and orientation via pnictogen bonding of substrates to induce regioselectivity in reactions with the transition metal. Since the work in this thesis established further that N-donor main group ligands are particularly accessible, there is great potential for ligand tuning in the proposed design. This involves tuning of the Lewis acidity via the substituent R' as well as the main

group element to B, Al, In, Bi, etc. and the oxidation state. The distance between the main group Lewis acid and the transition metal centre could be modified by change of the donor groups from pyridyl to CH_2Pyridyl, quinolyl or oxazolyl which is expected to play a central role in the catalyst's reactivity. Finally, the ligand can be rendered chiral via the use of chiral pyridyl and oxazolyl donor functionalities.

Trispyridyl pnictogen ligands also have the potential to be further used in the synthesis of polycationic pnictogen ligands. Alcazaro et al. have shown that the monopyridyl phosphines and arsines R_2Pn(2-py) can be synthesised as their quarternised pyridinium derivatives, which act as particularly potent π-accepting ligands in, e.g., gold catalysis.[192,193] Trispyridyl Pn-ligands could in theory be used to access the mono-, di- or tri-cationic versions after methylation of the pyridine N-atoms. This could be used to tune the electronic environment of the ligands for metal coordination. Quarternisation of the pnictogen bridgehead might also useful in this respect to change the donor properties of the N-atoms for the coordination to metal centres. Since Artem'ev et al. have shown that metal coordination to trispyridyl phosphonium halides is possible, it might be interesting to explore how oxidation of the bridgehead atoms with 'F^+" or 'RO^+" sources affect the electronics of the coordinated metal.[165] Particularly a fluorophosphonium bridgehead might be a good candidate as these cations are catalytically active themselves which, in combination with an coordinated metal, could lead to applications in tandem catalysis.[194] Another possible direction could be the chemistry of the 3-pyridyl and 4-pyridyl derivatives for the build-up of larger multimetallic coordination capsules. Stang, Fujita and others showed how polypyridyl ligands with rationally chosen angles between the coordination vector of the pyridyl functionalities leads to the formation of large cage structures.[195] The same principle could be in theory applied to trispyridyl main group ligands since Stang et al. showed that methoxy-tris-4-pyridyl methane forms coordination cages.[196] Introduction of functional main group centres such as Lewis acidic Sb(V) or B(III) in such cages could lead to, e.g., enhanced host-guest chemistry or catalytic activity of such capsules. Having shown in Chapters 7 and 8 that either bridgehead or pyridyl coordination of trispyridyl arsines and stibines can be addressed with different metals one could envisage the formation of heterobimetallic coordination cages with such systems.

Bibliography

[1] *Phosphorus-Nitrogen Compounds*, Elsevier, **1972**.

[2] R. Schwesinger, C. Hasenfratz, H. Schlemper, L. Walz, E.-M. Peters, K. Peters, H. G. V. Schnering, *Angew. Chem.* **1993**, *105*, 1420–1422.

[3] H. R. Allcock, R. M. Wood, *J. Polym. Sci. Part B Polym. Phys.* **2006**, *44*, 2358–2368.

[4] G.-X. Xu, Q. Lu, B.-T. Yu, L. Wen, *Solid State Ion.* **2006**, *177*, 305–309.

[5] R. Keat, in *Inorg. Ring Syst.*, Springer Berlin Heidelberg, **1982**.

[6] N. Burford, T. S. Cameron, K. D. Conroy, B. Ellis, M. Lumsden, C. L. B. Macdonald, R. McDonald, A. D. Phillips, P. J. Ragogna, R. W. Schurko, *J. Am. Chem. Soc.* **2002**, *124*, 14012–14013.

[7] N. Burford, K. D. Conroy, J. C. Landry, P. J. Ragogna, M. J. Ferguson, R. McDonald, *Inorg. Chem.* **2004**, *43*, 8245–8251.

[8] F. García, R. A. Kowenicki, L. Riera, D. S. Wright, *Dalton Trans.* **2005**, *24*, 2495-2500.

[9] A. Michaelis, G. Schroeter, *Berichte Dtsch. Chem. Ges.* **1894**, *27*, 490–497.

[10] M. Lehmann, A. Schulz, A. Villinger, *Struct. Chem.* **2011**, *22*, 35–43.

[11] T. Roth, H. Wadepohl, D. S. Wright, L. H. Gade, *Chem. – Eur. J.* **2013**, *19*, 13823–13837.

[12] T. Beweries, R. Kuzora, U. Rosenthal, A. Schulz, A. Villinger, *Angew. Chem. Int. Ed.* **2011**, *50*, 8974–8978.

[13] I. Silaghi-Dumitrescu, I. Haiduc, *Phosphorus Sulfur Silicon Relat. Elem.* **1994**, *91*, 21–36.

[14] C. G. M. Benson, V. Vasilenko, R. García-Rodríguez, A. D. Bond, S. González Calera, L. H. Gade, D. S. Wright, *Dalton Trans.* **2015**, *44*, 14242–14247.

[15] M. S. Balakrishna, *Dalton Trans.* **2016**, *45*, 12252–12282.

[16] L. Stahl, *Coord. Chem. Rev.* **2000**, *210*, 203–250.

[17] J. K. Brask, T. Chivers, M. L. Krahn, M. Parvez, *Inorg. Chem.* **1999**, *38*, 290–295.

[18] G. G. Briand, T. Chivers, M. Krahn, *Coord. Chem. Rev.* **2002**, *23*, 237–254.

[19] G. R. Lief, C. J. Carrow, L. Stahl, R. J. Staples, *Organometallics* **2001**, *20*, 1629–1635.

[20] Y. Sim, D. Tan, R. Ganguly, Y. Li, F. García, *Chem. Commun.* **2018**, *54*, 6800–6803.

[21] Y. X. Shi, R. Z. Liang, K. A. Martin, N. Weston, S. Gonzalez-Calera, R. Ganguly, Y. Li, Y. Lu, A. J. M. Ribeiro, M. J. Ramos, et al., *Inorg. Chem.* **2015**, *54*, 6423–6432.

[22] A. Nordheider, T. Chivers, R. Thirumoorthi, K. S. Athukorala Arachchige, A. M. Z. Slawin, J. D. Woollins, I. Vargas-Baca, *Dalton Trans* **2013**, *42*, 3291–3294.

[23] A. Nordheider, K. Hüll, J. K. D. Prentis, K. S. Athukorala Arachchige, A. M. Z. Slawin, J. D. Woollins, T. Chivers, *Inorg. Chem.* **2015**, *54*, 3043–3054.

[24] A. Nordheider, K. Hüll, K. S. A. Arachchige, A. M. Z. Slawin, J. Derek Woollins, R. Thirumoorthi, T. Chivers, *Dalton Trans.* **2015**, *44*, 5338–5346.

[25] A. J. Plajer, R. Garcia-Rodriguez, F. J. Rizzuto, D. S. Wright, *Chem. – Eur. J.* **2018**, *24*, 2013–2019.

[26] J. W. Steed, J. L. Atwood, *Supramolecular Chemistry*, John Wiley & Sons, **2013**.

[27] V. Böhmer, *Angew. Chem. Int. Ed. Engl.* **1995**, *34*, 713–745.

[28] M. A. Pitt, D. W. Johnson, *Chem. Soc. Rev.* **2007**, *36*, 1441–1453.

[29] F. Diederich, P. J. Stang, R. R. Tykwinski, *Modern Supramolecular Chemistry: Strategies for Macrocycle Synthesis*, John Wiley & Sons, **2008**.

[30] M. F. Hawthorne, Z. Zheng, *Acc. Chem. Res.* **1997**, *30*, 267–276.

[31] G. C. Forbes, A. R. Kennedy, R. E. Mulvey, R. B. Rowlings, W. Clegg, S. T. Liddle, C. C. Wilson, *Chem. Commun.* **2000**, *10*, 1759–1760.

[32] A. R. Kennedy, J. Klett, R. E. Mulvey, S. Newton, D. S. Wright, *Chem. Commun.* **2008**, *2*, 308–310.

[33] T. W. Hudnall, C.-W. Chiu, F. P. Gabbaï, *Acc. Chem. Res.* **2009**, *42*, 388–397.

[34] A. J. Martínez-Martínez, A. R. Kennedy, R. E. Mulvey, C. T. O'Hara, *Science* **2014**, *346*, 834–837.

[35] H. P. Calhoun, N. L. Paddock, J. N. Wingfield, *Can. J. Chem.* **1975**, *53*, 1765–1774.

[36] J. S. Ritch, T. Chivers, *Angew. Chem. Int. Ed.* **2007**, *46*, 4610–4613.

[37] M. R. Churchill, C. H. Lake, S.-H. L. Chao, O. T. Beachley, *J. Chem. Soc. Chem. Commun.* **1993**, *6*, 1577–1578.

[38] S. Chanmungkalakul, V. Ervithayasuporn, P. Boonkitti, A. Phuekphong, N. Prigyai, S. Kladsomboon, S. Kiatkamjornwong, *Chem. Sci.* **2018**, *9*, 7753–7765.

[39] G. B. Kaufman, *J. Chem. Educ.* **1993**, *70*, 279.

[40] Y.-R. Luo, *Comprehensive Handbook of Chemical Bond Energies*, CRC Press, **2007**.

[41] M. A. Beswick, M. K. Davies, M. A. Paver, P. R. Raithby, A. Steiner, D. S. Wright, *Angew. Chem. Int. Ed.* **1996**, *35*, 1508–1510.

[42] R. Bryant, S. C. James, J. C. Jeffery, N. C. Norman, A. G. Orpen, U. Weckenmann, *J. Chem. Soc. Dalton Trans.* **2000**, *17*, 4007–4009.

[43] A. Bashall, E. L. Doyle, C. Tubb, S. J. Kidd, M. McPartlin, A. D. Woods, D. S. Wright, *Chem. Commun.* **2001**, *10*, 2542–2543.

[44] A. Bashall, A. D. Bond, E. L. Doyle, F. García, S. Kidd, G. T. Lawson, M. C. Parry, M. McPartlin, A. D. Woods, D. S. Wright, *Chem. – Eur. J.* **2002**, *8*, 3377–3385.

[45] F. García, J. M. Goodman, R. A. Kowenicki, I. Kuzu, M. McPartlin, M. A. Silva, L. Riera, A. D. Woods, D. S. Wright, *Chem. – Eur. J.* **2004**, *10*, 6066–6072.

[46] J. P. Richard, *Advances in Physical Organic Chemistry*, Academic Press, **2011**.

[47] F. García, R. A. Kowenicki, I. Kuzu, M. McPartlin, L. Riera, D. S. Wright, *Inorg. Chem. Commun.* **2005**, *8*, 1060–1062.

[48] E. L. Doyle, F. García, S. M. Humphrey, R. A. Kowenicki, L. Riera, A. D. Woods, D. S. Wright, *Dalton Trans.* **2004**, *9*, 807–812.

[49] S. G. Calera, D. J. Eisler, J. M. Goodman, M. McPartlin, S. Singh, D. S. Wright, *Dalton Trans.* **2009**, *11*, 1293–1296.

[50] W. T. K. Chan, D. Eisler, F. García, S. Gonzalez-Calera, M. McPartlin, J. V. Morey, R. E. Mulvey, S. Singh, A. Steiner, D. S. Wright, *Chem. Commun.* **2008**, *20*, 2251–2253.

[51] C. G. M. Benson, A. J. Plajer, R. García-Rodríguez, A. D. Bond, S. Singh, L. H. Gade, D. S. Wright, *Chem. Commun.* **2016**, *52*, 9683–9686.

[52] A. J. Plajer, R. García-Rodríguez, C. G. M. Benson, P. D. Matthews, A. D. Bond, S. Singh, L. H. Gade, D. S. Wright, *Angew. Chem. Int. Ed.* **2017**, *56*, 9087–9090.

[53] A. Nordheider, T. Chivers, R. Thirumoorthi, I. Vargas-Baca, J. Derek Woollins, *Chem. Commun.* **2012**, *48*, 6346–6348.

[54] D. Bawari, B. Prashanth, S. Ravi, K. R. Shamasundar, S. Singh, D. S. Wright, *Chem. – Eur. J.* **2016**, *22*, 12027–12033.

[55] S. González-Calera, D. J. Eisler, J. V. Morey, M. McPartlin, S. Singh, D. S. Wright, *Angew. Chem.* **2008**, *120*, 1127–1130.

[56] P. Kommana, K. C. Kumara Swamy, *Inorg. Chem.* **2000**, *39*, 4384–4385.

[57] F. García, R. A. Kowenicki, I. Kuzu, L. Riera, M. McPartlin, D. S. Wright, *Dalton Trans.* **2004**, *15*, 2904–2909.

[58] F. Dodds, F. García, R. A. Kowenicki, M. McPartlin, A. Steiner, D. S. Wright, *Chem. Commun.* **2005**, *30*, 3733–3735.

[59] F. Dodds, F. García, R. A. Kowenicki, M. McPartlin, L. Riera, A. Steiner, D. S. Wright, *Chem. Commun.* **2005**, *34*, 5041–5043.

[60] C. R. Wade, F. P. Gabbaï, *Organometallics* **2011**, *30*, 4479–4481.

[61] C. R. Wade, I.-S. Ke, F. P. Gabbaï, *Angew. Chem. Int. Ed.* **2012**, *51*, 478–481.

[62] E. Galbraith, T. D. James, *Chem. Soc. Rev.* **2010**, *39*, 3831–3842.

[63] A. M. Christianson, F. P. Gabbaï, *Organometallics* **2017**, *36*, 3013–3015.

[64] A. G. Schafer, J. M. Wieting, T. J. Fisher, A. E. Mattson, *Angew. Chem. Int. Ed.* **2013**, *52*, 11321–11324.

[65] D. Uraguchi, Y. Ueki, T. Ooi, *Science* **2009**, *326*, 120–123.

[66] M. A. Martínez-Aguirre, A. K. Yatsimirsky, *J. Org. Chem.* **2015**, *80*, 4985–4993.

[67] C.-H. Chen, F. P. Gabbaï, *Angew. Chem. Int. Ed.* **2018**, *57*, 521–525.

[68] P. B. Cranwell, J. R. Hiscock, C. J. E. Haynes, M. E. Light, N. J. Wells, P. A. Gale, *Chem. Commun.* **2013**, *49*, 874–876.

[69] S. Grabowsky, M. F. Hesse, C. Paulmann, P. Luger, J. Beckmann, *Inorg. Chem.* **2009**, *48*, 4384–4393.

[70] V. Chandrasekhar, R. Boomishankar, S. Nagendran, *Chem. Rev.* **2004**, *104*, 5847–5910.

[71] H. Klare, S. Hanft, J. M. Neudörfl, N. E. Schlörer, A. Griesbeck, B. Goldfuss, *Chem. – Eur. J.* **2014**, *20*, 11847–11855.

[72] H. Klare, J. M. Neudörfl, B. Goldfuss, *Beilstein J. Org. Chem.* **2014**, *10*, 224–236.

[73] F. F. Wolf, J.-M. Neudörfl, B. Goldfuss, *New J. Chem.* **2018**, *42*, 4854–4870.

[74] P. A. Gale, E. N. W. Howe, X. Wu, M. J. Spooner, *Coord. Chem. Rev.* **2018**, *375*, 333–372.

[75] V. Amendola, G. Bergamaschi, M. Boiocchi, L. Fabbrizzi, M. Milani, *Chem. – Eur. J.* **2010**, *16*, 4368–4380.

[76] D. Tan, Z. X. Ng, Y. Sim, R. Ganguly, F. García, *CrystEngComm* **2018**, *20*, 5998–6004.

[77] M. P. Williamson, *Prog. Nucl. Magn. Reson. Spectrosc.* **2013**, *73*, 1–16.

[78] P. Thordarson, *Chem. Soc. Rev.* **2011**, *40*, 1305–1323.

[79] R. G. Parr, R. G. Pearson, *J. Am. Chem. Soc.* **1983**, *105*, 7512–7516.

[80] M. Mantina, A. C. Chamberlin, R. Valero, C. J. Cramer, D. G. Truhlar, *J. Phys. Chem. A* **2009**, *113*, 5806–5812.

[81] A. Scherer, T. Mukherjee, F. Hampel, J. A. Gladysz, *Organometallics* **2014**, *33*, 6709–6722.

[82] T. Mukherjee, C. Ganzmann, N. Bhuvanesh, J. A. Gladysz, *Organometallics* **2014**, *33*, 6723–6737.

[83] V. Amendola, L. Fabbrizzi, *Chem. Commun.* **2009**, *7*, 513–531.

[84] V. Amendola, D. Esteban-Gómez, L. Fabbrizzi, M. Licchelli, E. Monzani, F. Sancenón, *Inorg. Chem.* **2005**, *44*, 8690–8698.

[85] H. Schmidbaur, A. Schier, *Chem Soc Rev* **2012**, *41*, 370–412.

[86] A. J. Plajer, K. Bold, F. J. Rizzuto, R. García-Rodríguez, T. K. Ronson, D. S. Wright, *Dalton Trans.* **2017**, *46*, 12775–12779.

[87] P. A. Gale, *Coord. Chem. Rev.* **2003**, *240*, 191–221.

[88] M. S. Balakrishna, D. Suresh, G. S. Ananthnag, J. T. Mague, *Dalton Trans.* **2014**, *43*, 8835–8848.

[89] V. Amendola, D. Esteban-Gómez, L. Fabbrizzi, M. Licchelli, *Acc. Chem. Res.* **2006**, *39*, 343–353.

[90] P. A. Gale, *Acc. Chem. Res.* **2011**, *44*, 216–226.

[91] B. A. McNally, A. V. Koulov, T. N. Lambert, B. D. Smith, J.-B. Joos, A. L. Sisson, J. P. Clare, V. Sgarlata, L. W. Judd, G. Magro, et al., *Chem. – Eur. J.* **2008**, *14*, 9599–9606.

[92] B. A. McNally, A. V. Koulov, B. D. Smith, J.-B. Joos, A. P. Davis, *Chem. Commun.* **2005**, *8*, 1087–1089.

[93] A. Hennig, L. Fischer, G. Guichard, S. Matile, *J. Am. Chem. Soc.* **2009**, *131*, 16889–16895.

[94] T. Saha, M. S. Hossain, D. Saha, M. Lahiri, P. Talukdar, *J. Am. Chem. Soc.* **2016**, *138*, 7558–7567.

[95] N. Busschaert, M. Wenzel, M. E. Light, P. Iglesias-Hernández, R. Pérez-Tomás, P. A. Gale, *J. Am. Chem. Soc.* **2011**, *133*, 14136–14148.

[96] N. Busschaert, I. L. Kirby, S. Young, S. J. Coles, P. N. Horton, M. E. Light, P. A. Gale, *Angew. Chem. Int. Ed.* **2012**, *51*, 4426–4430.

[97] X. Wu, E. N. W. Howe, P. A. Gale, *Acc. Chem. Res.* **2018**, *51*, 1870–1879.

[98] S. Oi, K. Kashiwagi, Y. Inoue, *Tetrahedron Lett.* **1998**, *39*, 6253–6256.

[99] J. Manzur, A. Vega, A. M. García, C. Acuña, M. Sieger, B. Sarkar, M. Niemeyer, F. Lissner, T. Schleid, W. Kaim, *Eur. J. Inorg. Chem.* **2007**, *117*, 5500–5510.

[100] F. W. Patureau, S. de Boer, M. Kuil, J. Meeuwissen, P.-A. R. Breuil, M. A. Siegler, A. L. Spek, A. J. Sandee, B. de Bruin, J. N. H. Reek, *J. Am. Chem. Soc.* **2009**, *131*, 6683–6685.

[101] J. R. Gispert, *Coordination Chemistry*, Wiley, **2008**.

[102] D. W. Allen, B. F. Taylor, *J. Chem. Soc. Dalton Trans.* **1982**, 51–54.

[103] A. Idrissi, P. Damay, K. Yukichi, P. Jedlovszky, *J. Chem. Phys.* **2008**, *129*, 164512.

[104] D. Milano, B. Benedetti, M. Boccalon, A. Brugnara, E. Iengo, P. Tecilla, *Chem. Commun.* **2014**, *50*, 9157–9160.

[105] M.-H. Chen, Y. Zheng, X.-J. Cai, H. Zhang, F.-X. Wang, C.-P. Tan, W.-H. Chen, L.-N. Ji, Z.-W. Mao, *Chem. Sci.* **2019**, *10*, 3315–3323.

[106] D. F. Moser, I. Schranz, M. C. Gerrety, L. Stahl, R. J. Staples, *J. Chem. Soc. Dalton Trans.* **1999**, *12*, 751–758.

[107] G. D. Andreetti, R. Ungaro, A. Pochini, *J. Chem. Soc. Chem. Commun.* **1979**, *15*, 1005–1007.

[108] D. S. Kim, J. L. Sessler, *Chem. Soc. Rev.* **2014**, *44*, 532–546.

[109] J. M. Goicoechea, H. Grützmacher, *Angew. Chem. Int. Ed.* **2018**, *57*, 16968–16994.

[110] A. Hinz, R. Labbow, C. Rennick, A. Schulz, J. M. Goicoechea, *Angew. Chem. Int. Ed.* **2017**, *56*, 3911–3915.

[111] K. H. Møller, A. S. Hansen, H. G. Kjaergaard, *J. Phys. Chem. A* **2015**, *119*, 10988–10998.

[112] A. S. Hansen, L. Du, H. G. Kjaergaard, *J. Phys. Chem. Lett.* **2014**, *5*, 4225–4231.

[113] J.-Y. L. Questel, M. Berthelot, C. Laurence, *J. Phys. Org. Chem.* **2000**, *13*, 347–358.

[114] D. Mootz, A. Deeg, *J. Am. Chem. Soc.* **1992**, *114*, 5887–5888.

[115] D. A. Roberts, B. S. Pilgrim, J. R. Nitschke, *Chem. Soc. Rev.* **2018**, *47*, 626–644.

[116] B. Breiner, J. K. Clegg, J. R. Nitschke, *Chem. Sci.* **2010**, *2*, 51–56.

[117] V. Marcos, A. J. Stephens, J. Jaramillo-Garcia, A. L. Nussbaumer, S. L. Woltering, A. Valero, J.-F. Lemonnier, I. J. Vitorica-Yrezabal, D. A. Leigh, *Science* **2016**, *352*, 1555–1559.

[118] I. A. Riddell, M. M. J. Smulders, J. K. Clegg, Y. R. Hristova, B. Breiner, J. D. Thoburn, J. R. Nitschke, *Nat. Chem.* **2012**, *4*, 751–756.

[119] S. J. Edwards, H. Valkenier, N. Busschaert, P. A. Gale, A. P. Davis, *Angew. Chem.* **2015**, *127*, 4675–4679.

[120] L. H. Gade, P. Hofmann, *Molecular Catalysts: Structure and Functional Design*, John Wiley & Sons, **2014**.

[121] I. Kuzu, I. Krummenacher, J. Meyer, F. Armbruster, F. Breher, *Dalton Trans.* **2008**, *64*, 5836–5865.

[122] Swiatoslaw. Trofimenko, *Chem. Rev.* **1972**, *72*, 497–509.

[123] N. Kitajima, W. B. Tolman, in *Prog. Inorg. Chem.*, John Wiley & Sons, Ltd, **2007**.

[124] A. Caballero, M. M. Díaz-Requejo, M. R. Fructos, J. Urbano, P. J. Pérez, in *Ligand Des. Met. Chem.*, John Wiley & Sons, Ltd, **2016**.

[125] H. R. Simmonds, D. S. Wright, *Chem. Commun.* **2012**, *48*, 8617–8624.

[126] F. García, A. D. Hopkins, R. A. Kowenicki, M. McPartlin, M. C. Rogers, D. S. Wright, *Organometallics* **2004**, *23*, 3884–3890.

[127] T. H. Bullock, W. T. K. Chan, D. J. Eisler, M. Streib, D. S. Wright, *Dalton Trans.* **2009**, *10*, 1046–1054.

[128] C. S. Alvarez, F. García, S. M. Humphrey, A. D. Hopkins, R. A. Kowenicki, M. McPartlin, R. A. Layfield, R. Raja, M. C. Rogers, A. D. Woods, et al., *Chem. Commun.* **2005**, *3*, 198–200.

[129] F. García, A. D. Hopkins, R. A. Kowenicki, M. McPartlin, M. C. Rogers, J. S. Silvia, D. S. Wright, *Organometallics* **2006**, *25*, 2561–2568.

[130] T. H. Bullock, W. T. K. Chan, D. S. Wright, *Dalton Trans.* **2009**, *20*, 6709–6711.

[131] R. García-Rodríguez, T. H. Bullock, M. McPartlin, D. S. Wright, *Dalton Trans.* **2014**, *43*, 14045–14053.

[132] R. García-Rodríguez, D. S. Wright, *Chem. – Eur. J.* **2015**, *21*, 14949–14957.

[133] R. García-Rodríguez, D. S. Wright, *Dalton Trans.* **2014**, *43*, 14529–14532.

[134] A. F. Holleman, E. Wiberg, N. Wiberg, *Lehrbuch der anorganischen Chemie*, De Gruyter, **1995**.

[135] R. García-Rodríguez, S. Hanf, A. D. Bond, D. S. Wright, *Chem. Commun.* **2017**, *53*, 1225–1228.

[136] Á. García-Romero, A. J. Plajer, L. Álvarez-Miguel, A. D. Bond, D. S. Wright, R. García-Rodríguez, *Chem. – Eur. J.* **2018**, *24*, 17019–17026.

[137] R. García-Rodríguez, H. R. Simmonds, D. S. Wright, *Organometallics* **2014**, *33*, 7113–7117.

[138] R. García-Rodríguez, S. Kopf, D. S. Wright, *Dalton Trans.* **2018**, *47*, 2232–2239.

[139] G. M. Pawar, J. B. Sheridan, F. Jäkle, *Eur. J. Inorg. Chem.* **2016**, *16*, 2227–2235.

[140] C. Cui, R. A. Lalancette, F. Jäkle, *Chem. Commun.* **2012**, *48*, 6930–6932.

[141] S. Y. Jeong, R. A. Lalancette, H. Lin, P. Lupinska, P. O. Shipman, A. John, J. B. Sheridan, F. Jäkle, *Inorg. Chem.* **2016**, *55*, 3605–3615.

[142] G. M. Pawar, R. A. Lalancette, E. M. Bonder, J. B. Sheridan, F. Jäkle, *Macromolecules* **2015**, *48*, 6508–6515.

[143] P. O. Shipman, C. Cui, P. Lupinska, R. A. Lalancette, J. B. Sheridan, F. Jäkle, *ACS Macro Lett.* **2013**, *2*, 1056–1060.

[144] F. García, A. D. Hopkins, S. M. Humphrey, M. McPartlin, M. C. Rogers, D. S. Wright, *Dalton Trans.* **2004**, *7*, 361–362.

[145] M. A. Beswick, C. J. Belle, M. K. Davies, M. A. Halcrow, P. R. Raithby, A. Steiner, D. S. Wright, *Chem. Commun.* **1996**, *24*, 2619–2620.

[146] M. A. Beswick, M. K. Davies, P. R. Raithby, A. Steiner, D. S. Wright, *Organometallics* **1997**, *16*, 1109–1110.

[147] K. Zeckert, S. Zahn, B. Kirchner, *Chem. Commun.* **2010**, *46*, 2638–2640.

[148] F. Reichart, M. Kischel, K. Zeckert, *Chem. – Eur. J.* **2009**, *15*, 10018–10020.

[149] K. Zeckert, *Organometallics* **2013**, *32*, 1387–1393.

[150] K. Zeckert, *Dalton Trans.* **2012**, *41*, 14101–14106.

[151] K. Zeckert, J. Griebel, R. Kirmse, M. Weiß, R. Denecke, *Chem. – Eur. J.* **2013**, *19*, 7718–7722.

[152] I. Schrader, K. Zeckert, S. Zahn, *Angew. Chem. Int. Ed.* **2014**, *53*, 13698–13700.

[153] K. Zeckert, *Inorganics* **2016**, *4*, 19.

[154] J. G. Woollard-Shore, J. P. Holland, M. W. Jones, J. R. Dilworth, *Dalton Trans.* **2010**, *39*, 1576–1585.

[155] T. Astley, H. Headlam, M. A. Hitchman, F. R. Keene, J. Pilbrow, H. Stratemeier, E. R. T. Tiekink, Y. C. Zhong, *J. Chem. Soc. Dalton Trans.* **1995**, *32*, 3809–3818.

[156] A. V. Artem'ev, A. V. Kashevskii, A. S. Bogomyakov, A. Yu. Safronov, A. O. Sutyrina, A. A. Telezhkin, I. V. Sterkhova, *Dalton Trans.* **2017**, *46*, 5965–5975.

[157] R. P. Schutte, S. J. Rettig, A. M. Joshi, B. R. James, *Inorg. Chem.* **1997**, *36*, 5809–5817.

[158] S. Hanf, R. García-Rodríguez, A. D. Bond, E. Hey-Hawkins, D. S. Wright, *Dalton Trans.* **2015**, *45*, 276–283.

[159] J. A. Casares, P. Espinet, J. M. Martín-Álvarez, V. Santos, *Inorg. Chem.* **2006**, *45*, 6628–6636.

[160] I. Jacobs, A. C. T. van Duin, A. W. Kleij, M. Kuil, D. M. Tooke, A. L. Spek, J. N. H. Reek, *Catal. Sci. Technol.* **2013**, *3*, 1955–1963.

[161] V. Bocokić, M. Lutz, A. L. Spek, J. N. H. Reek, *Dalton Trans.* **2012**, *41*, 3740–3750.

[162] A. W. Kleij, M. Kuil, D. M. Tooke, A. L. Spek, J. N. H. Reek, *Inorg. Chem.* **2005**, *44*, 7696–7698.

[163] S. Hanf, R. García-Rodríguez, S. Feldmann, A. D. Bond, E. Hey-Hawkins, D. S. Wright, *Dalton Trans.* **2017**, *46*, 814–824.

[164] A. V. Artem'ev, I. Y. Bagryanskaya, E. P. Doronina, P. M. Tolstoy, A. L. Gushchin, M. I. Rakhmanova, A. Y. Ivanov, A. O. Suturina, *Dalton Trans.* **2017**, *46*, 12425–12429.

[165] A. V. Artem'ev, E. A. Pritchina, M. I. Rakhmanova, N. P. Gritsan, I. Y. Bagryanskaya, S. F. Malysheva, N. A. Belogorlova, *Dalton Trans.* **2019**, *48*, 2328–2337.

[166] R. Suter, H. Sinclair, N. Burford, R. McDonald, M. J. Ferguson, E. Schrader, *Dalton Trans.* **2017**, *46*, 7681–7685.

[167] T. Gneuß, M. J. Leitl, L. H. Finger, N. Rau, H. Yersin, J. Sundermeyer, *Dalton Trans.* **2015**, *44*, 8506–8520.

[168] A. G. Walden, A. J. M. Miller, *Chem. Sci.* **2015**, *6*, 2405–2410.

[169] J. S. Jones, F. P. Gabbaï, *Acc. Chem. Res.* **2016**, *49*, 857–867.

[170] K. Urgin, C. Aubé, C. Pichon, M. Pipelier, V. Blot, C. Thobie-Gautier, E. Léonel, D. Dubreuil, S. Condon, *Tetrahedron Lett.* **2012**, *53*, 1894–1896.

[171] M.-G. Zhao, T.-T. Hao, X. Zhang, J.-P. Ma, J.-H. Su, W. Zheng, *Inorg. Chem.* **2017**, *56*, 12678–12681.

[172] T.-P. Lin, I.-S. Ke, F. P. Gabbaï, *Angew. Chem.* **2012**, *124*, 5069–5072.

[173] C. Tschersich, S. Hoof, N. Frank, C. Herwig, C. Limberg, *Inorg. Chem.* **2016**, *55*, 1837–1842.

[174] A. E. Reed, R. B. Weinstock, F. Weinhold, *J. Chem. Phys.* **1985**, *83*, 735–746.

[175] L. Maestre, W. M. C. Sameera, M. M. Díaz-Requejo, F. Maseras, P. J. Pérez, *J. Am. Chem. Soc.* **2013**, *135*, 1338–1348.

[176] A. Steiner, D. Stalke, *Organometallics* **1995**, *14*, 2422–2429.

[177] G. B. Deacon, J. H. S. Green, *Spectrochim. Acta Part Mol. Spectrosc.* **1969**, *25*, 355–364.

[178] M. Kodera, Y. Kajita, Y. Tachi, K. Kano, *Inorg. Chem.* **2003**, *42*, 1193–1203.

[179] P. Espinet, R. Hernando, G. Iturbe, F. Villafañe, A. G. Orpen, I. Pascual, *Eur. J. Inorg. Chem.* **2000**, *20*, 1031–1038.

[180] J. E. Parks, B. E. Wagner, R. H. Holm, *J. Organomet. Chem.* **1973**, *56*, 53–66.

[181] M. Kodera, Y. Tachi, T. Kita, H. Kobushi, Y. Sumi, K. Kano, M. Shiro, M. Koikawa, T. Tokii, M. Ohba, et al., *Inorg. Chem.* **2000**, *39*, 226–234.

[182] A. Santoro, C. Sambiagio, P. C. McGowan, M. A. Halcrow, *Dalton Trans.* **2014**, *44*, 1060–1069.

[183] P. Fernández, H. Pritzkow, J. J. Carbó, P. Hofmann, M. Enders, *Organometallics* **2007**, *26*, 4402–4412.

[184] V. V. Novikov, A. A. Pavlov, Y. V. Nelyubina, M.-E. Boulon, O. A. Varzatskii, Y. Z. Voloshin, R. E. P. Winpenny, *J. Am. Chem. Soc.* **2015**, *137*, 9792–9795.

[185] M. Kruck, H. Wadepohl, M. Enders, L. H. Gade, *Chem. – Eur. J.* **2013**, *19*, 1599–1606.

[186] D. Morales, J. Pérez, L. Riera, V. Riera, D. Miguel, *Organometallics* **2001**, *20*, 4517–4523.

[187] J. W. Faller, Y. Ma, *J. Am. Chem. Soc.* **1991**, *113*, 1579–1586.

[188] J. Hicks, P. Vasko, J. M. Goicoechea, S. Aldridge, *Nature* **2018**, *557*, 92.

[189] P. R. Schreiner, *Chem. Soc. Rev.* **2003**, *32*, 289–296.

[190] H. Guo, Y. C. Fan, Z. Sun, Y. Wu, O. Kwon, *Chem. Rev.* **2018**, *118*, 10049–10293.

[191] D. W. Stephan, G. Erker, *Angew. Chem. Int. Ed.* **2015**, *54*, 6400–6441.

[192] J. W. Dube, Y. Zheng, W. Thiel, M. Alcarazo, *J. Am. Chem. Soc.* **2016**, *138*, 6869–6877.

[193] H. Tinnermann, L. D. M. Nicholls, T. Johannsen, C. Wille, C. Golz, R. Goddard, M. Alcarazo, *ACS Catal.* **2018**, *8*, 10457–10463.

[194] C. B. Caputo, L. J. Hounjet, R. Dobrovetsky, D. W. Stephan, *Science* **2013**, *341*, 1374–1377.

[195] R. Chakrabarty, P. S. Mukherjee, P. J. Stang, *Chem. Rev.* **2011**, *111*, 6810–6918.

[196] B. Olenyuk, M. D. Levin, J. A. Whiteford, J. E. Shield, P. J. Stang, *J. Am. Chem. Soc.* **1999**, *121*, 10434–10435.

Appendix: Methods

General

All solvents were freshly distilled over appropriate drying agents under nitrogen. Deuterated solvents were dried over molecular sieves and degassed via three freeze pump/thaw cycles prior to use. All pyridine and amine derivatives were distilled from calcium hydride and dried over molecular sieves before use. Phosphorus trichloride was distilled. All other reagents were purchased from the supplier and used without any further purification. Unless stated otherwise, manipulations were carried out using standard Schlenk line techniques or inside a nitrogen-filled glovebox.

Nuclear Magnetic Resonance (NMR) spectroscopy

NMR spectra were recorded using a 400 MHz Avance III HD Smart Probe, DCH 500 MHz dual cryoprobe, DPX S5 500 MHz BB ATM or 500 MHz TCI-ATM cryo NMR spectrometers. Chemical shifts for ^{1}H, ^{13}C, ^{31}P, ^{77}Se, ^{27}Al, ^{7}Li, ^{127}I and ^{19}F are reported in ppm on the δ scale; ^{1}H and ^{13}C were referenced to the residual solvent peak and other nuclei where referenced to an external. Coupling constants (J) are reported in Hertz (Hz). All proton signals of diamagnetic compounds were assigned with the aid of 2D NMR spectra (COSY, NOESY, HSQC, HMBC). Wide-sweep paramagnetic NMR spectra were recorded in the analogue digitisation mode with a spectral width (SW) of 999.98 ppm, a transmitter frequency offset (O1P) of 100.00 ppm and the line width set to 10.0 Hz.

Mass spectrometry (MS)

Low-resolution electrospray ionisation mass spectrometry (LR-ESI-MS) was undertaken on a Micromass Quattro LC mass spectrometer (cone voltage 10-30 eV; desolvation temperature 313 K; ionisation temperature 313 K) infused from a Harvard syringe pump at a rate of 10 μL min^{-1}. High-resolution electrospray ionisation mass spectrometry (HRMS-ESI) was performed on a Waters LCT Premier Mass Spectrometer featuring a Z spray source with electrospray ionisation and modular LockSpray interface.

X-ray crystallography

Data were collected using either a Bruker D8 VENTURE diffractometer equipped with high-brilliance IμS Cu-Kα radiation (1.54178 Å), with ω and ψ scans at 180(2) K, or at Beamline I19 of The Diamond Light Source employing silicon double-crystal monochromated synchrotron radiation (0.6889 Å) with ω scans at 100(2) K. Data integration and reduction were undertaken with SAINT13 in the APEX3 software suite for data collected on the Bruker diffractometer; data integration and reduction on synchrotron collections were undertaken with either CrysalisPRO14 or xia2.[1-3] Multi-scan empirical absorption corrections were applied to the data using SADABS16 or xia2.[3,4] Subsequent computations were carried out using the WinGX-32 graphical user interface.[5] Structures were solved by direct methods using SHELXT-201318 then refined and extended with SHELXL-2013.[6] In general, non-hydrogen atoms with occupancies greater than 0.5 were refined anisotropically. Carbon- and nitrogen-bound hydrogen atoms were included in idealised positions and refined using a rigid model. Disorder was modelled using standard crystallographic methods including constraints, restraints and rigid bodies where necessary. In cases involving the use of SQUEEZE19, molecular formulas were determined firstly from the required number of charge-balancing anions, and then confirmed from the number of electrons identified in the disordered portion of the crystal by SQUEEZE.[7]

Computational modelling

All calculations in carried out by Sanha Lee, Jonathan Goodman and Markus Enders were carried out with Gaussian 16 and NBO program package. The geometry optimisations were performed with the M06-2X functional and 6-31G(d,p) basis sets.[8-12] For chloride and iodide complexes, def2svp basis sets were used. Frequency calculations were used to characterise the stationary points and to ensure the structures were optimised to minima.

All calculations carried out by Patrick Pröhm were performed using the Turbomole V7.0.1 program package. Structure optimisations at the DFT level have been performed by the B3LYP hybrid functional with the triple-ζ basis set def2-TZVPD at an m5 grid.[13-16] Dispersion correction by Grimme (D3) and Becke-Johnson (BJ) damping was employed for the calculations as implemented. Atoms in molecules (AIM) analysis

and natural population analysis (NPA) were performed as implemented.[15,17] NBO analysis was carried out using the NBO7.0 program in the Gaussian 16 interface.[8-12] Minimized structures have been confirmed by frequency analysis within the harmonic approximation as implemented in the Turbomole code.[13] For visualisation the program VMD V1.9.7 was used.[18]

UV-Vis spectroscopy

UV-Visible absorption spectroscopy was performed using a Perkin Elmer Lambda 750 or Agilent Cary 5000 UV-Vis-NIR spectrophotometer. Spectra were obtained in double-beam mode using only the (front) analyte beam to record spectra, with air in the (rear) reference path. A background spectrum of the neat solvent was recorded using the analyte beam prior to each experiment and a baseline correction applied using the Perkin Elmer WinLab software suite. Samples were analysed using quartz cuvettes with optical path lengths of 10 mm.

Cyclic voltammetry

Solution-state cyclic voltammetry (CV) was performed using a BioLogic SP-150 potentiostat with ferrocene (Fc) as an internal reference. Measurements were conducted under an Ar atmosphere using a conventional three-electrode cell: a glassy carbon working electrode, a Pt wire auxiliary electrode, and a Ag/Ag^+ quasi-reference electrode. A 0.1 M $^nBu_4NPF_6/CH_3CN$ electrolyte was used, with scan rates in the range 25–1000 mV/s.

Infrared Spectroscopy

A Perkin-Elmer FT IR instrument with an ATR sample setting was used for the IR measurements. Compounds were either employed in powdered form on the ATR window or deployed as solutions, followed by evaporation of the solvent under a stream of air.

Elemental Analysis

Carbon, hydrogen and nitrogen contents of the compounds were determined using an Exeter Analytical CE-440 Elemental Analyser. Air- and moisture-sensitive samples were sealed inside pre-weighed aluminium capsules under an inert atmosphere inside a nitrogen filled glovebox.

Bibliography Methods

[1] Bruker, *SAINT.* **2012**, Bruker ASX Inc.

[2] Agilent*, Crysalis PRO.* **2014**, Agilent Technologies, Ltd.

[3] G. J. Winter, *Appl. Crystallogr.* **2010**, *43*, 186-190.

[4] Bruker, *SADABS.* **2001**, Bruker AXS, Inc.

[5] L. J. Farrugia, Appl. Crystallogr. **2012**, *45*, 849-854.

[6] G. M. Sheldrick, *Acta Crystallogr. Sect. A* **2015**, *71*, 3-8.

[7] A. L. Spek, *Acta Crystallogr. Sect C* **2015**, *71*, 9-18.

[8] Gaussian, *Gaussian 16 Revision B.01* **2016**, Gaussian Inc.

[9] Y. Zhao, D. Truhlar, *Theor. Chem. Acc.* **2008**, *120*, 215.

[10] W. J. Hehre, R. F. Stewart, J. A. Pople*, J. Chem. Phys.* **1969**, *51*, 2657

[11] F. Weinhold, C. R. Landis, *Chem. Educ. Res. Prac.* **2001**, *2*, 91-104.

[12] S. J. Grabowski, *Chem. Rev.* **2011**, *111*, 2597-2625.

[13] TURBOMOLE, *TURBOMOLE V7.0.1* **2015**, TURBOMOL GmbH.

[14] a) A. D. Becke, *J. Chem. Phys.* **1993**, *98*, 5648; b) C. Lee, W. Yang, R. G. Parr, *Phys. Rev. B* **1988**, *37*, 785.

[15] A. E. Reed, R. B. Weinstock, F. Weinhold*, J. Chem. Phys.* **1985**, *83*, 735.

[16] F. Weigend, M. Häser, H. Patzelt, R. Ahlrichs, *Chem. Phys. Lett.* **1998**, *294*, 143.

[17] *Atoms in molecules. A quantum theory*, Clarendon Press, **1994**.

[18] W. Humphrey, A. Dalke, K. Schulten, *Journal of Molecular Graphics* **1996**, 14, 33.